Spectral and temporal studies of accretion and ejection processes around supermassive black holes

DANIEL KYNOCH

Spectral and temporal studies of accretion and ejection processes around supermassive black holes

Daniel Kynoch

A Thesis presented for the degree of
Doctor of Philosophy

Centre for Extragalactic Astronomy
Department of Physics
Durham University
United Kingdom

July 2019

Spectral and temporal studies of accretion and ejection processes around supermassive black holes

Daniel Kynoch

Submitted for the degree of Doctor of Philosophy

July 2019

Abstract: In the centre of every major galaxy is a supermassive black hole. Some of these power an active galactic nucleus (AGN) in which the black hole is growing by accreting the luminous disc of material around it. As well as consuming matter, AGN can eject it in the form of powerful jets travelling at relativistic velocities. I present detailed studies of two narrow-line Seyfert 1 galaxies which exhibit powerful jets and high-energy γ-ray emission. I explore the relationship between the disc and jet in these sources and suggest that their jets are relatively underpowered.

Although AGN are too small and distant to be spatially resolved, temporal studies can reveal information about the processes occurring within the central engine. I conduct a temporal spectroscopic study of a hypervariable AGN which dimmed and rebrightened by a factor of three over four years. I demonstrate that the event is due to an intrinsic change within the accretion disc, and is not due to obscuration by an external body. Such dramatic variability poses a challenge to our current models of accretion discs. I draw attention to some new models which confront this problem.

Finally, I place my findings in the context of the current literature and discuss some of its limitations and open questions. I highlight how future, planned observatories will help us to address these issues and deepen our understanding of AGN.

Declaration

The work in this thesis is based on research carried out in the Department of Physics at Durham University. No part of this thesis has been submitted elsewhere for any degree or qualification. Material from this thesis has appeared in the published papers:

- *On the black hole mass of the γ-ray emitting narrow-line Seyfert 1 galaxy 1H 0323+342* by Landt, Ward, Baloković, Kynoch, Storchi-Bergmann, Boisson, Done, Schimoia and Stern, 2017, MNRAS, 464, 2265

- *The relativistic jet of the γ-ray emitting narrow-line Seyfert 1 galaxy 1H 0323+342* by Kynoch, Landt, Ward, Done, Gardner, Boisson, Arrieta-Lobo, Zech, Steenbrugge and Pereira Santaella, 2018, MNRAS, 475, 404

- *The relativistic jet of the γ-ray emitting narrow-line Seyfert 1 galaxy PKS J1222+0413* by Kynoch, Landt, Ward, Done, Boisson, Baloković, Angelakis and Myserlis, 2019, MNRAS, 487, 181

- *The 'Big Dipper': The nature of the extreme variability of the AGN SDSS J2232−0806* by Kynoch, Ward, Lawrence, Bruce, Landt and MacLeod, 2019, MNRAS, 485, 2573

In Chapter 4, the black hole mass determination was done by Dr. Hermine Landt. The *Spitzer* IRS spectrum was provided by Dr. Miguel Pereira Santaella. The SPEX analysis of the *XMM-Newton* RGS spectrum was performed by Dr. Katrien Steenbrugge. In Chapters 4 and 5 the *Fermi* data reduction was performed by Prof. Catherine Boisson and the *NuSTAR* data reduction by Dr. Mislav Baloković. In Chapter 5 the Effelsberg radio data were reduced and provided by Dr. Emmanouil Angelakis and Dr. Ioannis Myserlis. In Chapter 6 the reduced WHT and MMT spectra were provided by Dr. Alastair Bruce and Dr. Chelsea MacLeod, respectively. The radio data in Appendix C were provided by Mr. Jake Mitchell.

This research was made possible by the support of a UK Science and Technology Facilities Council studentship (ST/N50404X/1) and a Postgraduate Award from Van Mildert College.

Acknowledgements

I owe thanks to a great many people. Firstly, to my family for their love and support. In particular to Mam, Dad, Grams, Nana and Aunty Viv who have encouraged me to follow my interests and have always had faith in my abilities.

I am grateful to my supervisors (both official and unofficial) at Durham for their guidance over the years. Thanks to Martin Ward for his wealth of knowledge, experience and relaxed supervision; Chris Done for her boundless enthusiasm; Hermine Landt for all of her ideas and those 'trips' to Hawaii; and Tim Roberts and Paula Chadwick for their sage advice and reassurance. To Andy Lawrence, Alastair Bruce and David Homan in Edinburgh, thanks for donating the 'Big Dipper' to me, and giving me the opportunity to go observing for the first time. Thanks also to James Collinson for getting me started and setting such a high bar in matplotlibbing, and to Emma Gardner for patient instruction in the intricacies of jets.

I have been taught by some wonderful science teachers, without whom I might not have embarked on this path. So thanks Mr. O'Neil, Mr. Batey, Paula Williams and Bob Robson for teaching the subject with such enthusiasm and excellent humour.

To all of my friends at Van Mildert College, which has been a home away from home for the last eight years: thanks so much for your companionship and good humour through the good times and the bad. To PhD office mates past and present, particularly Ra'ad, Raj, Greg and Lizelke, thanks for making turning up to work each morning (and sometimes evenings ... and weekends) such a pleasure.

Finally, a supermassive thanks to Alice who has been my very best friend these last three-and-a-half years. Thank you so much for always supporting me and believing in me, and for all of the happy memories of Durham and beyond.

Black holes are the bits of space that you can't see because they're black. Most of space is quite black, but black holes are really black. Even though nobody can see them because they're black on a black background, scientists know that black holes are there because when they ask for money to research them, nobody tells them to —— off.

— from *Cunk on Everything* by Philomena Cunk

Dedicated to

Mam and Dad

and

Nana, Grams and Aunty Viv

Contents

Abstract ii

List of Figures xv

List of Tables xix

1 Introduction 1

1.1 Supermassive black holes and active galactic nuclei 1

1.1.1 Dark stars and the shadow of the colossus 1

1.1.2 The Eddington luminosity 4

1.1.3 The accretion disc 6

1.1.4 The X-ray emission regions 12

1.1.5 The broad line region 14

1.1.6 The narrow line region 15

1.1.7 The dust torus 17

1.1.8 Jets 18

1.2 Putting it all together 24

1.2.1 The unification of AGN 24

1.2.2 Narrow-line Seyfert 1s 27

2 Methods and models **33**

2.1 Weighing black holes . . . 33

2.1.1 Dynamical methods . . . 34

2.1.2 Reverberation mapping . . . 34

2.1.3 Single-epoch virial methods . . . 35

2.1.4 Other methods . . . 36

2.2 Reddening and absorption . . . 40

2.2.1 Reddening by dust . . . 41

2.2.2 Photoelectric absorption by the interstellar medium . . . 43

2.3 Modelling the accretion flow emission . . . 43

2.4 Modelling the jet emission . . . 47

3 Astronomical facilities and surveys **49**

3.1 Radio to sub-mm . . . 49

3.1.1 NVSS . . . 49

3.1.2 FIRST . . . 50

3.1.3 Effelsberg . . . 50

3.1.4 Planck . . . 50

3.2 Infrared . . . 51

3.2.1 WISE . . . 51

3.2.2 2MASS . . . 52

3.2.3 UKIDDS . . . 52

3.2.4 Gemini . . . 52

3.2.5 Spitzer . . . 53

3.3 Optical and ultraviolet . . . 53

3.3.1 Sloan Digital Sky Survey . . . 54
3.3.2 Pan-STARRS . . . 54
3.3.3 William Herschel Telescope . . . 55
3.3.4 Liverpool Telescope . . . 55
3.3.5 MMT . . . 56
3.3.6 Keck . . . 56
3.3.7 Very Large Telescope . . . 57
3.3.8 Hubble Space Telescope . . . 58
3.3.9 GALEX . . . 58
3.4 X-ray . . . 60
3.4.1 ROSAT . . . 60
3.4.2 XMM-Newton . . . 61
3.4.3 Neil Gehrels Swift Observatory . . . 63
3.4.4 NuSTAR . . . 64
3.5 Gamma-ray . . . 64
3.5.1 Fermi . . . 64
3.5.2 Cherenkov Telescope Array . . . 65

4 The γ-ray NLS1 1H 0323+342 67

4.1 Introduction . . . 68
4.2 The multiwavelength data set . . . 70
4.2.1 Quasi-simultaneous data sampling the external photon field . 70
4.2.2 Additional data sampling the external photon field . . . 74
4.2.3 Data sampling the jet emission . . . 77
4.2.4 Supplementary X-ray data . . . 79

4.3 The black hole mass . . . 81
4.4 X-ray analysis . . . 85
4.4.1 Variability . . . 85
4.4.2 X-ray spectral analysis . . . 88
4.5 The origin of the γ-ray emission . . . 91
4.5.1 Determining the external photon field . . . 92
4.5.2 Determining the jet parameters . . . 102
4.5.3 Jet emission models . . . 106
4.6 Discussion . . . 108
4.6.1 Is 1H 0323+342 a typical NLS1? . . . 108
4.6.2 Contribution of the jet to the IR and X-ray emission . . . 113
4.6.3 The external photon field . . . 115
4.6.4 The impact of variability . . . 117
4.6.5 The origin of the γ-ray emission . . . 118
4.6.6 Where does 1H 0323+342 lie in the blazar sequence? . . . 120
4.6.7 A comparison of jet powers . . . 121
4.7 Summary and conclusions . . . 123

5 The γ-ray emitting NLS1 PKS J1222+0413 126

5.0.1 The source PKS J1222+0413 . . . 127
5.1 X-Shooter spectroscopy . . . 128
5.1.1 The observations and data reduction . . . 128
5.1.2 Estimates of the black hole mass . . . 131
5.2 The multiwavelength data set . . . 135
5.2.1 Data quasi-simultaneous with X-shooter . . . 135

5.2.2 Radio monitoring data . . . 142
5.2.3 Additional archival data . . . 143
5.3 The origin of the γ-ray emission . . . 153
5.3.1 Determining the external photon field . . . 153
5.3.2 The broadband SED . . . 156
5.4 Discussion . . . 159
5.4.1 PKS J1222+0413 as a NLS1 . . . 159
5.4.2 The jet of PKS J1222+0413 . . . 164
5.4.3 Comparison with 1H 0323+342 . . . 165
5.5 Conclusions . . . 170

6 The 'Big Dipper': A study of a hypervariable AGN 172

6.1 Introduction . . . 173
6.1.1 The source SDSS J2232−0806 . . . 174
6.1.2 The aims of this study . . . 174
6.2 The optical monitoring campaign . . . 177
6.2.1 Observations and data reduction . . . 177
6.2.2 Optical spectral analysis . . . 179
6.2.3 Measurement of the continuum and the emission lines . . . 184
6.2.4 The black hole mass . . . 187
6.3 Multiwavelength data . . . 190
6.3.1 X-ray and UV observation with *XMM-Newton* . . . 190
6.3.2 Archival photometric data . . . 191
6.3.3 The spectral energy distribution . . . 196
6.4 The nature of the variability . . . 200

6.4.1 Obscuration interpretation 200
6.4.2 Intrinsic change interpretation 206
6.5 Discussion 210
6.5.1 An extrinsic cause of variability 210
6.5.2 An intrinsic cause of variability 211
6.5.3 SDSS J2232−0806 in the context of other hypervariable AGN 214
6.6 Conclusions 219

7 Summary and future work 221
7.1 Synopsis of findings 222
7.1.1 γ-ray emitting NLS1s 222
7.1.2 The hypervariable AGN SDSS J2232−0806 223
7.2 Future work 224
7.2.1 A long, hard look at 1H 0323+342, and future studies of γ-NLS1s 224
7.2.2 Future high-energy and multimessenger studies of SMBHs . 231
7.2.3 Variability studies 232

A Complexity in the X-ray spectrum of 1H 0323+342 235

B Optical spectral fitting of SDSS J2232−0806 242

C A large sample of optical/X-ray quasars 246
C.1 Introduction 246
C.2 Sample selection 249
C.2.1 The parent catalogues 249
C.2.2 Source selection criteria 251

C.3 Optical spectral fitting 253

C.4 Determinations of SMBH masses 263

C.4.1 Some problematic spectra 263

C.4.2 SMBH masses for 573 AGN 264

C.5 Source luminosities 265

C.6 The quasar main sequence 271

C.7 Summary 271

List of Figures

1.1 The shadow of the supermassive black hole in M87 4

1.2 AGN accretion disc radius-temperature profiles 7

1.3 Model AGN accretion disc spectral energy distribution 8

1.4 The effect of black hole spin on characteristic radii and radiative efficiency 10

1.5 Composite AGN optical spectrum 16

1.6 The relativistic jet of M87 19

1.7 Fanaroff-Riley type I and II sources 21

1.8 The blazar sequence 24

1.9 Cartoon illustration of AGN jet structure and emission components 25

1.10 Seyfert 1, Seyfert 2 and narrow-line Seyfert 1 optical spectra . . . 26

1.11 The unification model of AGN 27

1.12 Eigenvector 1 29

2.1 Black hole mass estimates by line or continuum luminosity 37

2.2 Black hole mass estimates by SED fitting and SE relations 39

2.3 Milky Way, LMC and SMC reddening curves 42

2.4 Transmission of X-rays through the interstellar medium 44

2.5 The OPTXCONV accretion flow model 46

3.1 The Milky Way behind the William Herschel Telescope 56

3.2 Ultraviolet to mid-infrared photometric bands 59

3.3 High-energy observatories 60

4.1 The multiwavelength SED of 1H 0323+342 72

4.2 *Spitzer* spectroscopy and photometry of 1H 0323+342 77

4.3 Paschen and Balmer lines in the spectra of 1H 0323+342 83

4.4 The X-ray RMS spectrum of 1H 0323+342 86

4.5 The X-ray variability of 1H 0323+324 87

4.6 The *XMM-Newton* X-ray spectrum of 1H 0323+342 90

4.7 Iron lines in the X-ray spectrum of 1H 0323+342 92

4.8 Accretion flow SEDs of 1H 0323+342 99

4.9 Jet and accretion flow modelling of the broadband SED 110

5.1 VLT X-shooter spectra of PKS J1222+0413 130

5.2 Mg II, Hα and Hβ emission line profiles 134

5.3 The multiwavelength SED of PKS J1222+0413 137

5.4 *XMM-Newton* X-ray spectra 140

5.5 *Fermi* count map 141

5.6 *Fermi* γ-ray spectra 142

5.7 *WISE* infrared lightcurve 146

5.8 *HST* COS spectrum 148

5.9 Accretion flow models 157

5.10 Comparison of PKS J1222+0413 and 1H 0323+342 jet models . . . 160

5.11 Jet and accretion powers of BL Lacs, FSRQs and RL-NLS1s . . . 168

5.12 $M_{\rm BH}$ and $\dot{m}$ for BL Lacs, FSRQs and RL-NLS1s 169

6.1 Optical and infrared lightcurves of SDSS J2232−0806 176

6.2 Optical spectra of SDSS J2232−0806 181

6.3 The mean and RMS optical spectra of SDSS J2232−0806 183

6.4 Emission line fits 188

6.4 Emission line fits (continued) 189

6.5 The spectral energy distribution of SDSS J2232−0806 201

6.6 Fractional variations in fluxes and emission line equivalent widths . 203

6.7 Balmer decrement vs. continuum colour 204

6.8 Optical lightcurve and simulated infrared dust response 209

6.9 Comparisons of variability amplitude with other quasars 215

6.10 Comparisons of Eddington ratio with other types of quasar 218

7.1 Iron line in the X-ray spectra of 1H 0323+342 225

7.2 Various SEDs of 1H 0323+342 230

7.3 Future astronomical observatories 234

A.1 Complexity in the X-ray spectra of 1H0323+342 237

A.2 Tests of different absorbers in the EPIC-pn spectrum of 1H 0323+342 238

A.3 The *XMM-Newton* RGS spectrum of 1H 0323+342 240

C.1 Optical-X-ray source separations 252

C.2 Sample selection criteria 254

C.3 Examples of low S/N optical spectra 255

C.4 Emission line FWHMs of sources in the sample 257

C.5 Comparison of broad emission line FWHMs 258

C.6 Examples of AGN types within the sample 261

C.7 Narrow-line Seyfert 1s in the sample 262

C.8 FWHM(Hβ) distributions from QSFIT and Shen et al. (2011) . . 263

C.9 Comparison of SMBH mass estimates 266

C.10 Examples of spectral fits giving discrepant SMBH mass estimates . 267

C.11 Optical, ultraviolet and X-ray luminosities 268

C.12 Ratios of bolometric luminosities and Eddington ratios 269

C.13 Radio fluxes, luminosities and radio-loudness 270

C.14 Broad Hβ FWHM versus $R_{\mathrm{Fe\,II}}$ 272

List of Tables

1.1 Some key AGN emission lines 17

1.2 Known γ-ray emitting narrow-line Seyfert 1 galaxies 31

3.1 SDSS spectrograph parameters 54

4.1 The multiwavelength data set 71

4.2 Summary of *XMM-Newton* exposures 75

4.3 Estimates of the black hole mass of 1H 0323+342 85

4.4 Results of X-ray spectral fits 89

4.5 Results from spectral fits to the deabsorbed IR to hard X-ray SED . 97

4.6 External photon field parameters 101

4.7 Constraints on jet model parameters 105

4.8 The jet model parameters of 1H 0323+342 109

4.9 Comparison of 1H 0323+342 jet powers 122

5.1 Estimates of the black hole mass of PKS J1222+0413 133

5.2 Results of *XMM-Newton* X-ray spectral fits 139

5.3 Radio monitoring data from Effelsberg 143

5.4 The multiwavelength data set 150

5.4 The multiwavelength data set (continued) 151

5.4 The multiwavelength data set (continued) 152

5.5 Accretion flow model parameters 155

5.6 Jet model parameters for PKS J1222+0413 and 1H 0323+342 . . . 161

6.1 Black hole mass estimates from optical spectra 189

6.2 X-ray spectral models 192

6.3 The multiwavelength photometric dataset 195

6.4 Multiwavelength SED model parameters 199

7.1 Jet model parameters and powers determined for 1H 0323+342 . . 229

B.1 Balmer, [O III] and [N II] emission line measurements 243

B.1 Balmer, [O III] and [N II] emission line measurements (continued) . 244

B.2 Mg II emission line measurements 245

C.1 Coverage of emission lines in optical spectra 256

C.2 Emission line FWHMs from spectral fits 257

Chapter 1

Introduction

In the centre of every major galaxy lies a supermassive black hole (SMBH). In a small fraction of galaxies, the black hole is actively growing by accreting the matter within its gravitational well. The infall of this material releases a tremendous amount of energy in the form of radiation spanning many wavelengths which can be detected even over cosmological distances. Galaxies with growing SMBHs are said to contain an active galactic nucleus (AGN).

In this chapter, I give some historical background to the discovery of AGN and the subsequent studies of the phenomenon which have been undertaken. I also summarise some of the key physical principles and processes that are relevant to the rest of this thesis.

1.1 Supermassive black holes and active galactic nuclei

1.1.1 Dark stars and the shadow of the colossus

In the Eighteenth Century, the English natural philosopher John Michell and the French mathematician Pierre-Simon Laplace both independently conceived the idea

of 'dark stars': suns so massive that not even light can escape their gravitational pull. Michell's idea was formulated in the Newtonian scheme of gravity, and supposed that particles of light ('corpuscles') were affected by gravity in the same manner as ordinary matter. Michell (1784) said that if the escape velocity at the star's surface, $v_{\rm esc} = \sqrt{GM/R}$, exceeds the speed of light then light would fall back onto the star. To an outside observer, the star would therefore be dark. Presciently, Michell (1784) noted that although we may not be able to see these dark stars directly, we would be able to infer their presence by their observable effects on neighbouring bodies. However, in the Nineteenth Century the nature of light as an electromagnetic wave (rather than a stream of particles with mass) emerged in the theory of electromagnetism.

The idea of strongly-gravitating dark bodies returned in Einstein's general theory of relativity, developed in the early Twentieth Century (Einstein 1915a; Einstein 1915b). Rather than in Newtonian gravity in which gravity acts between two massive bodies, in general relativity, gravity is the distortion of the fabric of space and time caused by mass-energy. Therefore, even though light has no mass, it is affected by gravity because it travels in straight lines through space which is curved[1]. Immensely massive objects, such as black holes (BHs), warp spacetime so extremely that the paths of all light rays near to the mass are bent towards it. Schwarzschild (1916) presented the first analytic, mathematical description of a BH based on Einstein's field equations. Much later, Kerr (1963) generalised Schwarzschild's solution for the case of a spinning BH.

Compelling evidence for the existence of BHs only began to appear in the middle of the Twentieth Century. In the mid-Sixties, a bright Galactic X-ray source in the constellation of Cygnus (catalogued as Cyg X-1) was discovered as a result of mapping the sky with rocket-borne detectors (Bowyer et al. 1965). Optical

[1]The light-bending properties of massive objects means they can act as lenses, magnifying or distorting the images of background objects. Chang & Refsdal (1979) showed that the double quasar QSO 0957+561 A, B is a single object, doubly imaged because its light is split by the gravitational well of a star in an intervening galaxy.

observations later identified a large-mass companion star (Bolton 1972, Webster & Murdin 1972). The orbital motion of the star implied that its dark companion had a mass several times that of the Sun, much too massive to be a neutron star, implying instead the existence of a BH in the binary system. Cyg X-1 is considered to be the first astrophysical object widely accepted to be a BH. Populations of such stellar-mass BHs (with masses $\approx$ 3–20 $M_\odot$), the remnants of dead stars, are now widely believed to exist in all galaxies. A key piece of evidence for the existence of *supermassive* BHs (SMBHs: those with a mass 10^5–10^5 $M_\odot$) was the discovery of quasars.

Schmidt (1963) was investigating 3C 273[2] which was known to be a bright radio source by observations made with the Cambridge Interferometer and the Parkes radio telescope. Its radio emission is coincident with a point-like (or star-like) optical source. This was unusual on its own, because stars are not strong radio emitters. The optical spectrum of this 'star' was also puzzling and the emission lines could not be identified at first. Schmidt realised that the lines were Hydrogen lines, but redshifted by $z = 0.158$ – then a huge amount. This implied a very large distance to the source, which must be incredibly luminous to appear so bright in the sky. Its short-timescale variability also indicated that the emission region must be very compact. Clearly this was no star, but a quasi-stellar radio source or 'quasar'. But how could something as small and distant as a quasar appear so bright? The accretion of matter onto SMBHs was identified as an efficient way of generating this incredible power (Salpeter 1964, Zel'dovich 1965). We now know that quasars are a type of galaxy in which the central SMBH is actively accreting matter and growing: they have active galactic nuclei (AGN).

Despite decades of evidence supporting the existence of BHs, until recently, nobody could claim to have actually *seen* one. The pioneering work of the Event Horizon Telescope (EHT) group applied interferometry methods, linking several radio telescopes around the globe to effectively create one 'Earth-sized' telescope. Over four

[2] 3C 273 makes a cameo appearance in Chapter 5.

Figure 1.1: The shadow of the supermassive black hole in the centre of the active galaxy M87, seen against a rotating ring of hot, infalling matter. As imaged by the Event Horizon Telescope in April 2017 (Event Horizon Telescope Collaboration et al. 2019).

days in April 2017, the EHT observed the active nucleus of the nearby elliptical galaxy Messier 87 (M87, $z = 0.004$). After combining the data recorded at each individual telescope, the team were able to reconstruct the image of the SMBH's shadow against the luminous material around it. The image shown in Figure 1.1 was released by the EHT group on 10 April 2019 and is our first direct image of a BH.

1.1.2 The Eddington luminosity

The Eddington luminosity, named for the Twentieth Century astronomer Sir Arthur Eddington, is the luminosity at which hydrostatic equilibrium is achieved for material falling towards a star. The principle may be applied more generally to other massive, accreting bodies such as BHs or neutron stars. In the case of spherical accretion ('Bondi accretion': Bondi & Hoyle 1944) of a pure hydgrogen gas falling onto a BH of mass $M_{\rm BH}$, the gravitational force acting on a particle of mass m at a distance r

from the singularity is

$$F_{\rm G} = \frac{GM_{\rm BH}m}{r^2}. \tag{1.1.1}$$

Protons are ≈ 2000 times more massive than electrons and so they experience a greater gravitational force (although the Coulomb attraction means that electrons are 'dragged along' with the protons). The gravitational potential energy of the infalling material is converted into radiation so the inflow radiates outward with a luminosity L. The force due to the radiation pressure acting on a particle is

$$F_{\rm rad} = \frac{\sigma_{\rm t}L}{4\pi cr^2} \tag{1.1.2}$$

where $\sigma_{\rm t}$ is the Thomson scattering cross-section for a particle of charge q and is

$$\sigma_{\rm t} = \frac{8\pi}{3}\left(\frac{q}{mc^2}\right)^2 \tag{1.1.3}$$

in cgs units. Radiation pressure acts mostly on the electrons, because their smaller mass results in a greater $\sigma_{\rm t}$ than for protons. For an electron, $q = e$ and $m = m_{\rm e}$ and we denote the Thomson cross-section for the electron $\sigma_{\rm T}$. The Eddington luminosity is defined to be the luminosity at which radiation pressure balances the gravitational force pulling the material inwards. Equating (1.1.1) and (1.1.2), we determine the Eddington luminosity,

$$L_{\rm Edd} = \frac{4\pi cGM_{\rm BH}m_{\rm p}}{\sigma_{\rm T}}. \tag{1.1.4}$$

The Eddington luminosity depends upon the mass of the BH and the composition of the infalling gas. For a pure hydrogen gas, we determine that numerically

$$L_{\rm Edd} \approx 1.28 \times 10^{38}\left(\frac{M_{\rm BH}}{M_\odot}\right) {\rm erg\,s^{-1}}. \tag{1.1.5}$$

Associated with the Eddington luminosity is the mass accretion rate required to meet it, $\dot{M}_{\rm Edd}$. We can therefore express the luminosity or mass accretion rate of an accretor in terms of the normalised mass accretion rate

$$\dot{m} = \frac{\dot{M}}{\dot{M}_{\rm Edd}} = \frac{L}{L_{\rm Edd}}. \tag{1.1.6}$$

1.1.3 The accretion disc

Accretion onto BHs tends not to occur in the spherical geometry described above, but rather in the form of accretion discs. Infalling gas from the galactic centre will reach the nucleus with some angular momentum that prevents it from falling directly into the BH. If the gas can cool on timescales shorter than its infall time then thermal pressure is unable to support it and the material will collapse into a flattened disc. Viscous torques within the disc transfer angular momentum outwards, allowing the gas to move inwards. The radiative dissipation of heat within the disc produces observable emission. So, although we are unable to see the BH directly, we can see its 'shadow' against this glowing ring (Figure 1.1).

The physical theory of accretion discs is a somewhat complex description of the properties of the infalling material including its radial and angular momentum, radial and vertical geometry, and its temperature, pressure and viscosity. Shakura & Sunyaev (1973) were able to make some reasonable physical assumptions to simplify the theory into a set of tractable equations. Having a workable theory with which to make predictions about the observable properties of accretion discs greatly increased our understanding of the phenomenon. Even today, much of our understanding of accretion discs is based on the work of Shakura & Sunyaev (1973). However, this may soon have to change as I discuss later in Chapter 6. A general relativistic treatment of accretion discs was made by Novikov & Thorne (1973). Importantly, the general relativistic version incorporates the effects of BH spin.

The accretion disc may be thought of as a series of concentric annuli (rings) of rotating gas. If the gas rotates in Keplerian orbits, then the inner annuli will be rotating faster than the outer parts of the disc. It is assumed that the motion of neighbouring rings is coupled by some sort of viscosity or fiction. The friction between neighbouring annuli heats the disc material, so that the disc temperature increases with decreasing radius. Netzer (2013) evaluates the radial temperature

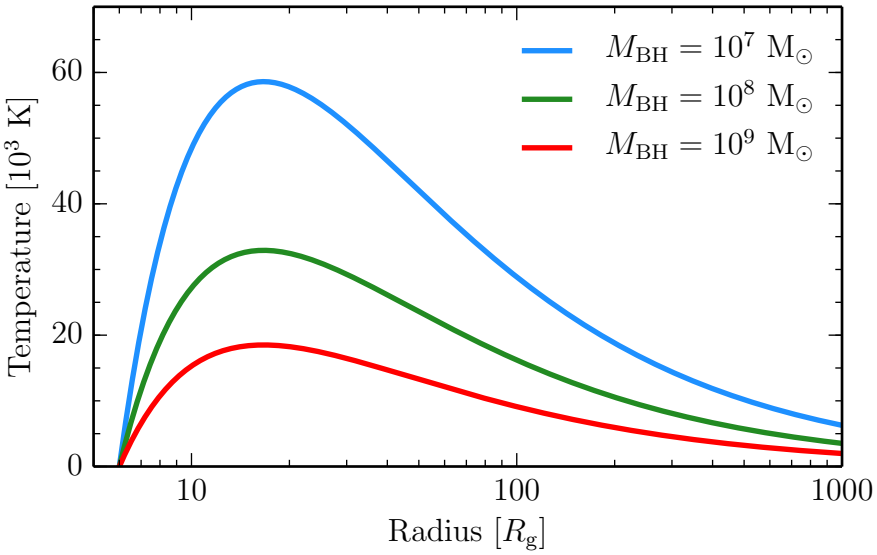

Figure 1.2: Radius-temperature profiles of AGN accretion discs around Schwarzchild BHs of different masses. All are calculated for a normalised accretion rate $L/L_{\rm Edd} = 0.1$.

profile of the disc as

$$T(R) \approx 8.6 \times 10^5 \left(\frac{\dot{M}}{\mathrm{M}_\odot\ \mathrm{yr}^{-1}}\right)^{\frac{1}{4}} \left(\frac{M_{\rm BH}}{10^8 \mathrm{M}_\odot}\right)^{-\frac{1}{2}} \left(1 - \left[\frac{R_{\rm isco}}{R}\right]^{\frac{1}{2}}\right) \left(\frac{R}{R_{\rm g}}\right)^{-\frac{3}{4}} \ \mathrm{K}, \quad (1.1.7)$$

where the mass-scaled gravitational radius

$$R_{\rm g} = \frac{GM_{\rm BH}}{c^2} \quad (1.1.8)$$

and the radius of the innermost stable circular orbit is denoted $R_{\rm isco}$, inside of which matter plunges rapidly into the BH. Examples of accretion disc radius-temperature profiles are plotted in Figure 1.2. Each annulus of the disc emits as a blackbody, with brightness following Planck's law:

$$B(\nu, T) = \frac{2h\nu^3}{c^2} \frac{1}{e^{h\nu/kT} - 1}. \quad (1.1.9)$$

Wien's law tells us that the characteristic (or peak) frequency of the blackbody emission is proportional to its temperature, and the Stefan-Boltzmann law that the radiant power is proportional to T^4. Therefore, with decreasing radius, the accretion disc emission becomes brighter and bluer. A 10^8 M$_\odot$ SMBH accreting 0.4 M$_\odot$ yr^{-1}

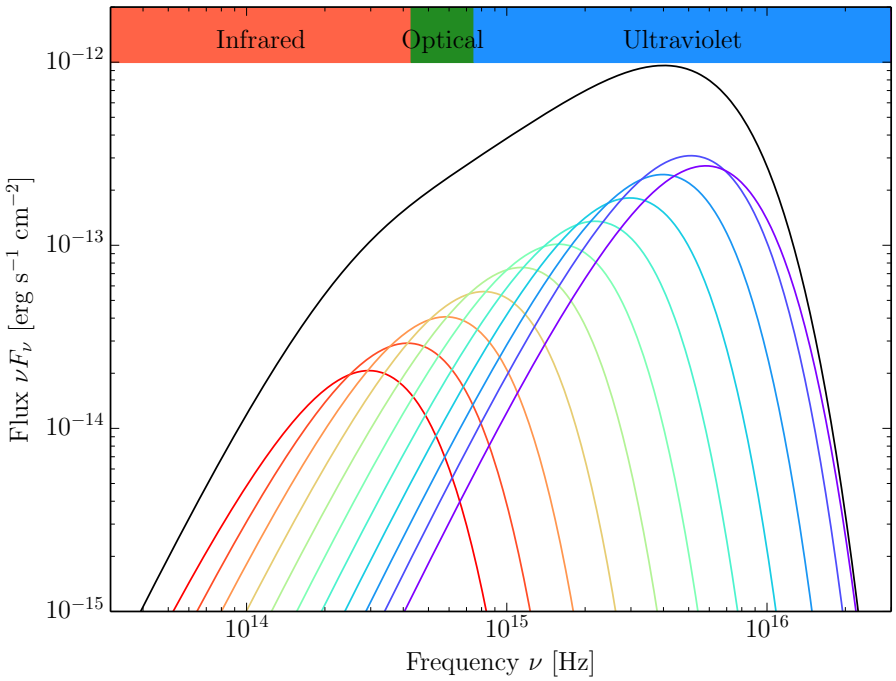

Figure 1.3: Model AGN accretion disc spectral energy distribution. The total disc spectrum (black) is the sum of many blackbodies, representing the emission from many disc annuli (coloured curves).

has an accretion disc with a peak temperature $\sim 3 \times 10^5$ K (see Figure 1.2), which corresponds to a far-ultraviolet photon with $\lambda \approx 50$ nm. By integrating the disc brightness over all radii one can determine that, in a limited frequecncy range, if $R_{\rm out} \gg R_{\rm isco}$ then the luminosity L at frequency ν

$$L_\nu \propto \dot{M}^{\frac{2}{3}} M^{\frac{2}{3}} \nu^\alpha, \tag{1.1.10}$$

where the spectral index $\alpha = 1/3$. This 'canonical' disc spectral shape, $L_\nu \propto \nu^{1/3}$, holds around the optical band. At lower frequencies, the Rayleigh-Jeans tail has a stronger $L_\nu \propto \nu^2$ frequency dependence and the Wien tail is the exponential cutoff at high frequencies (see Figure 1.3). Observationally, AGN accretion disc spectra are generally redder than predicted by models. This is likely because of reddening in the interstellar medium of the AGN host galaxies (Baron et al. 2016).

Since angular momentum must be conserved, the angular momentum of the infalling matter is imparted to the BH. The BH therefore gains both mass and angular

momentum from the accretion disc, causing the BH to spin. The spin of the BH is often expressed by the dimensionless quantity

$$a_\star = \frac{a}{M_{\rm BH}} = \frac{|\mathbf{J}|}{cM_{\rm BH}R_{\rm g}} = \frac{|\mathbf{J}|c}{GM_{\rm BH}^2}, \tag{1.1.11}$$

where $\mathbf{J}$ is the angular momentum of the BH. The dimensionless spin ranges from -1 to $+1$, where the negative sign indicates the accretion disc is spinning in the opposite sense to the BH itself. An accretion episode which increases the mass of the BH by a factor ~ 1.5 will also increase its spin from 0 to $+1$ (Thorne 1974; King & Kolb 1999). The spin of the BH determines the location of the event horizon $R_{\rm eh}$ (the maximum radius from which light can escape) and of the innermost stable circular orbit $R_{\rm isco}$, the latter of which sets the radiative efficiency η of the accretion disc. The event horizon $R_{\rm eh} = 1 + \sqrt{1 - a_\star^2}$ and is at 2 $R_{\rm g}$ for a non-spinning ('Schwarzchild') BH and is smaller in the case of a spinning ('Kerr') BH, reaching a minimum of 1 $R_{\rm g}$ for maximal spin. The innermost stable circular orbit and hence the radiative efficiency have a more complicated dependence on the spin; much of the relevant formalism was developed by Bardeen et al. (1972) (see also section 5.4 of Novikov & Thorne 1973). The quantities $R_{\rm isco}$, $R_{\rm eh}$ and η are plotted as a function of $a_\star$ in Figure 1.4; we see from the figure that a Schwarzchild BH has $R_{\rm isco} = 6$ $R_{\rm g}$ and $\eta \approx 6\%$. For $a_\star = +1$, a Kerr BH has $R_{\rm isco} \approx 1$ $R_{\rm g}$ and $\eta \approx 40\%$. Physically however, the counteracting torque provided by accretion disc photons prevent the BH being spun up beyond $a_\star \approx 0.998$ (Thorne 1974). Taking the maximum (physically-allowed) $a_\star = 0.9982$, Thorne (1974) calculated the maximum radiative efficiency to be $\eta \approx 30\%$. Figure 1.4 also shows that $R_{\rm isco}$ is always exterior to $R_{\rm eh}$ (i.e. in principle the 'plunging region' is always visible), and the two approach equality at $R_{\rm isco} = R_{\rm eh} = 1$ $R_{\rm g}$ as $a_\star \to +1$.

The outer radius of AGN accretion discs is unknown. Commonly, the accretion disc's greatest extent is taken to be the self-gravity radius, beyond which the disc fragments (Shlosman & Begelman 1987). The self-gravity radius was calculated by

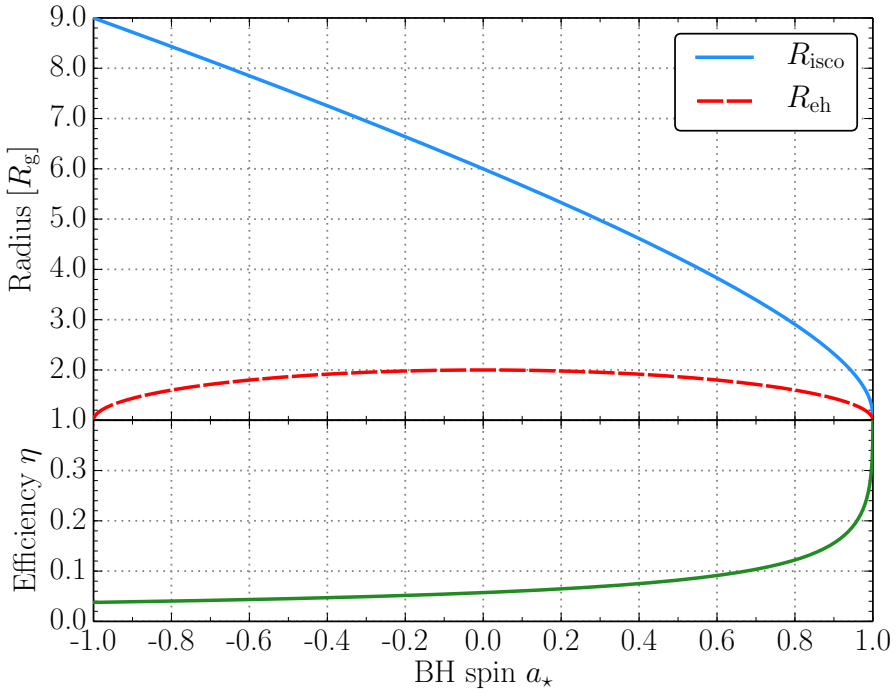

Figure 1.4: *Top:* The effect of black hole spin on the location of the innermost stable circular orbit $R_{\rm isco}$ and the event horizon $R_{\rm eh}$. *Bottom:* The variation of the accretion disc radiative efficiency η with black hole spin.

Laor & Netzer (1989) as

$$R_{\rm sg} = 2150 \left(\frac{M_{\rm BH}}{10^9 \ {\rm M}_\odot} \right)^{-2/9} \dot{m}^{4/9} \alpha^{2/9} \ R_{\rm g}, \tag{1.1.12}$$

where α is the disc viscosity parameter introduced by Shakura & Sunyaev (1973). $R_{\rm sg}$ is $\approx 800 \ R_{\rm g}$ for a 10^8 $\rm M_\odot$ SMBH with $\dot{m} = 0.1$ and $\alpha = 0.1$. The outer annuli of the accretion disc will emit in the infrared (Figure 1.3), but the disc flux is lower than the the flux of thermal emission from the hot dust in the surrounding torus (Section 1.1.7) at wavelengths longer than ~ 1 µm. Kishimoto et al. (2008) studied the polarised, near-infrared light scattered by material above the disc. They found a blue spectral shape indicative of emission from the large, outer annuli of accretion discs. However, they did not significantly detect a bluer spectral shape toward longer wavelengths which would result from a turnover at the truncation radius of the disc. Hao et al. (2010) found discs exceeding $R_{\rm sg}$ by a factor of 10–23 in a sample of 'hot-dust-poor' AGN in which the weakness of the hot dust emission exposed more

of the disc emission at longer wavelengths. Contrarily, Collinson et al. (2017) found that when the outer disc could be constrained by spectral energy distribution (SED) modelling, the outer radius was correlated with $R_{\rm sg}$ but systematically *smaller* by a factor ≈ 5.

1.1.3.1 Variability timescales for accretion discs

Variability is a ubiquitous property of AGN and is seen across all observed wavelengths. In the optical/ultraviolet the variability must result from changes in the accretion disc. Generally, AGN variability is characterised as a damped, random walk with small-amplitude, stochastic variability being observed on short timescales and large-amplitude, systematic changes in luminosity occurring over much longer timescales. These variations are driven by different physical processes and their characteristic timescales are described below.

The dynamical timescale relates to the circular motion of material within the disc. Since in Keplerian motion the period $P^2 \propto R^3$, the dynamical timescale,

$$t_{\rm dyn} = \sqrt{\frac{GM_{\rm BH}}{R^3}} \approx 0.006 \left(\frac{M_{\rm BH}}{10^8\ {\rm M}_\odot}\right)\left(\frac{R}{R_{\rm g}}\right)^{\frac{3}{2}}\ {\rm days}, \tag{1.1.13}$$

has a $R^{3/2}$ dependence.

The sound-crossing timescale is determined by the radial speed of sound waves through the disc and is

$$t_{\rm s} \approx t_{\rm dyn}\left(\frac{H}{R}\right)^{-1}, \tag{1.1.14}$$

where

$$\frac{H}{R} = \frac{c_{\rm s}}{v_{\rm K}} \tag{1.1.15}$$

is the disc scale height, equal to the ratio of the sound speed $c_{\rm s} = \sqrt{kT/m_{\rm p}}$ to the Keplerian velocity $v_{\rm K} = c\sqrt{R_{\rm g}/R}$.

The thermal timescale is determined by the rate of transmission of heat through the disc and is

$$t_{\rm th} \approx \frac{t_{\rm dyn}}{\alpha}. \tag{1.1.16}$$

The viscous timescale is the characteristic timescale of the radial inflow of the accreting mass. It is

$$t_{\rm vis} \approx \frac{t_{\rm dyn}}{\alpha}\left(\frac{H}{R}\right)^{-2}, \tag{1.1.17}$$

which (for a thin disc with $H/R \ll 1$) is very much longer than the previous timescales. For some typical numbers, the optical-emitting region ($\sim 100\ R_{\rm g}$) of the disc around a 10^8 $M_\odot$ SMBH has a dynamical timescale of ~ 6 days, a thermal timescale of ~ 2 months and a viscous timescale of $\sim 10^6$ years. This implies that large, systematic changes in the mass accretion rate of an AGN should not occur on observable timescales.

The cold accretion disc reprocesses rapidly-variable X-ray emission from a compact, hot corona near the SMBH (see below). So, another relevant timescale is the light-crossing time, simply the time for light to travel from the corona to the optical emitting part of the disc; typically this is a few hours. This reprocessing is responsible for the low-amplitude, high-frequency optical variability of accretion discs.

1.1.4 The X-ray emission regions

The peak frequency of the accretion disc emission is set by its maximum temperature. This cannot exceed ~ 20 eV (Shakura & Sunyaev 1973) in discs around SMBHs so AGN disc emission typically peaks in the ultraviolet, with an exponential decline in brightness toward shorter wavelengths (see Figure 1.3). However, we observe that significant fraction of the accretion power is emitted in X-rays[3]. This power is not emitted by the disc directly but is attributed to emission from a hot, optically thin Comptonising corona. The optical/ultraviolet photons from the accretion disc are scattered by energetic electrons in the corona, and the electrons impart some of their energy to the photons. It can be shown that, after multiple photon scatterings in the corona, the emergent X-ray spectrum has a power-law shape. This power-law is characterised by its slope Γ[4], dependent on the temperature and optical depth of

[3] Around 20–30 % in low-luminosity AGN, and less for high-luminosity sources.
[4] Γ relates to the spectral index α used in Equation (1.1.10) as $\Gamma = \alpha + 1$.

the electrons, and normalisation A, such that

$$N(E) = AE^{-\Gamma}, \tag{1.1.18}$$

where N is the number of X-ray photons with energy E emitted in unit time. This power-law of X-ray emission holds over the energy range $\sim$ 0.1–150 keV, with the lower energy turnover set by the energy of the accretion disc seed photons and the high-energy cutoff by the temperature of the coronal electrons (e.g. Pahari et al. 2017, Molina et al. 2019).

Extrapolating the 2–10 keV coronal power-law down to lower energies, an excess of soft X-ray emission is often found. The origin of this 'soft X-ray excess' is debated. Some proposed possibilities include a blend of reflection features (Czerny & Zycki 1994, Crummy et al. 2006) or strongly smeared absorption by an ionised accretion disc wind (Gierliński & Done 2004). When modelled as a thermal component, it has a remarkably consistent temperature, $\approx$ 0.12 keV, between sources (Gierliński & Done 2004, Jin et al. 2012a). In this thesis, the soft X-ray excess emission is attributed to Compton scattering of accretion disc seed photons within a warm, optically thick region of the inner accretion flow.

The X-ray emission from the hot corona may reflect off the colder accretion disc. The resulting reflection spectrum contains fluorescence line features as well as a smoother reflection continuum, peaking in a 'Compton hump' at $\sim$ 30 keV. Among the line features, the Fe Kα line at 6.4 keV is most commonly seen in AGN X-ray spectra. This emission is produced following the ejection of a K-shell electron when a neutral iron atom absorbs an X-ray photon. An L-shell electron drops into the K-shell vacancy and emits its excess energy as a Kα photon. The high cosmic abundance and fluorescent yield of iron make Fe Kα the most prominent X-ray fluorescence line. When the line emission results from reflection from the inner accretion disc, Doppler and relativistic effects broaden and distort its profile. The distortions due to relativistic effects are stronger the nearer the line emission region is to the SMBH. In the case of a highly spinning SMBH, the inner accretion disc approaches the event

horizon (see Figure 1.4) and the relativistic effects are extreme. It has been claimed that by modelling the observed iron line profiles in AGN X-ray spectra, the spin of the SMBH can be precisely determined (e.g. Brenneman & Reynolds 2006).

1.1.5 The broad line region

Edward Fath is credited with recording the first spectrum of an AGN (NGC 1068) in 1908, during his PhD studies. Its spectrum exhibited very strong high-excitation emission lines. Later, Seyfert (1943) identified a number of high-surface brightness spiral nebulae with very broad emission lines: these sources are now classed as Seyfert galaxies. The breadth of the lines in these spectra suggested very high Doppler motion, but the significance of this was not fully appreciated. We now know that these lines are emitted by high-velocity gas in the vicinity of SMBHs.

Radiation from the accretion disc and its corona ionises clouds of gas orbiting the SMBH. Radiative de-excitation of ions in the clouds produces a series of emission lines which are visible in the spectra of AGN. The widths of the emission lines (usually characterised by their full width at half maximum: FWHM) can be very large ($\approx$ 1000–10000 km s^{-1}) because of the very high velocities of the gas.

Properties of the emission lines can yield important information about the SMBH and the physical conditions of the material in its vicinity. The ionisation parameter

$$\xi = \frac{L}{r^2 n} \tag{1.1.19}$$

relates the luminosity L of ionising radiation to the density n of gas at distance r from the continuum source. Line emission will only be produced if the gas is in the appropriate ionisation state for that transition to occur. A particular ionisation state can be achieved at different radii, as long as there is gas of the appropriate density. For example, for a given luminosity L the ionisation state ξ' could occur at both r_1 and $r_2 = 2r_1$ provided there is gas at r_2 which has a density 1/4 of that at r_1. For this reason, in AGN spectra the permitted emission lines exhibit both

broad components (emitted in close-in, dense gas) and narrow components (from more distant, less dense gas, which has a smaller orbital velocity).

The Balmer emission lines of Hydrogen occur in the (rest frame) optical waveband and have therefore been studied extensively. The Balmer series results from the transition of electrons from excited states in the atom to the $n' = 2$ level[5]. Other Hydrogen transition series are also well-studied, for example the Lyman ($n' = 1$) series in the ultraviolet and Paschen ($n' = 3$) series in the infrared. Some of the strongest emission lines in the ultraviolet, optical and infrared bands relevant to the work in this thesis are listed in Table 1.1.

In addition to clearly-identifiable line features, AGN also exhibit complexes of blended lines such as Fe II. Strong Fe II complexes around Hβ can be seen in the composite AGN spectrum shown in Figure 1.5. The similarity of Fe II and Hβ FWHMs suggests that they originate from the same location (Boroson & Green 1992). However, unlike the Balmer lines, modelling has shown that the observed Fe II emission is too strong to be explained by photoionisation. Rather, Fe II emission may originate from collisional excitations due to turbulence in high-density gas clouds (e.g. Baldwin et al. 2004, and see Collin & Joly 2000 for a review).

1.1.6 The narrow line region

Some electronic transitions within ions are forbidden by quantum selection rules and as such they have very long lifetimes. The high-density gas clouds within the BLR do not produce forbidden line emission because in a high-density gas the ion will be collisionally de-excited before the forbidden radiative transition has had time to occur. Therefore forbidden emission lines originate from an ensemble of lower-density gas at large distances from the SMBH. The widths of permitted lines are narrow (typically a few hundred km s^{-1}) because of the lower orbital velocities at these larger radii. Forbidden emission lines are stylised with square parentheses, e.g.

[5]Where n is the principal quantum number and transitions occur between $n \rightarrow n'$.

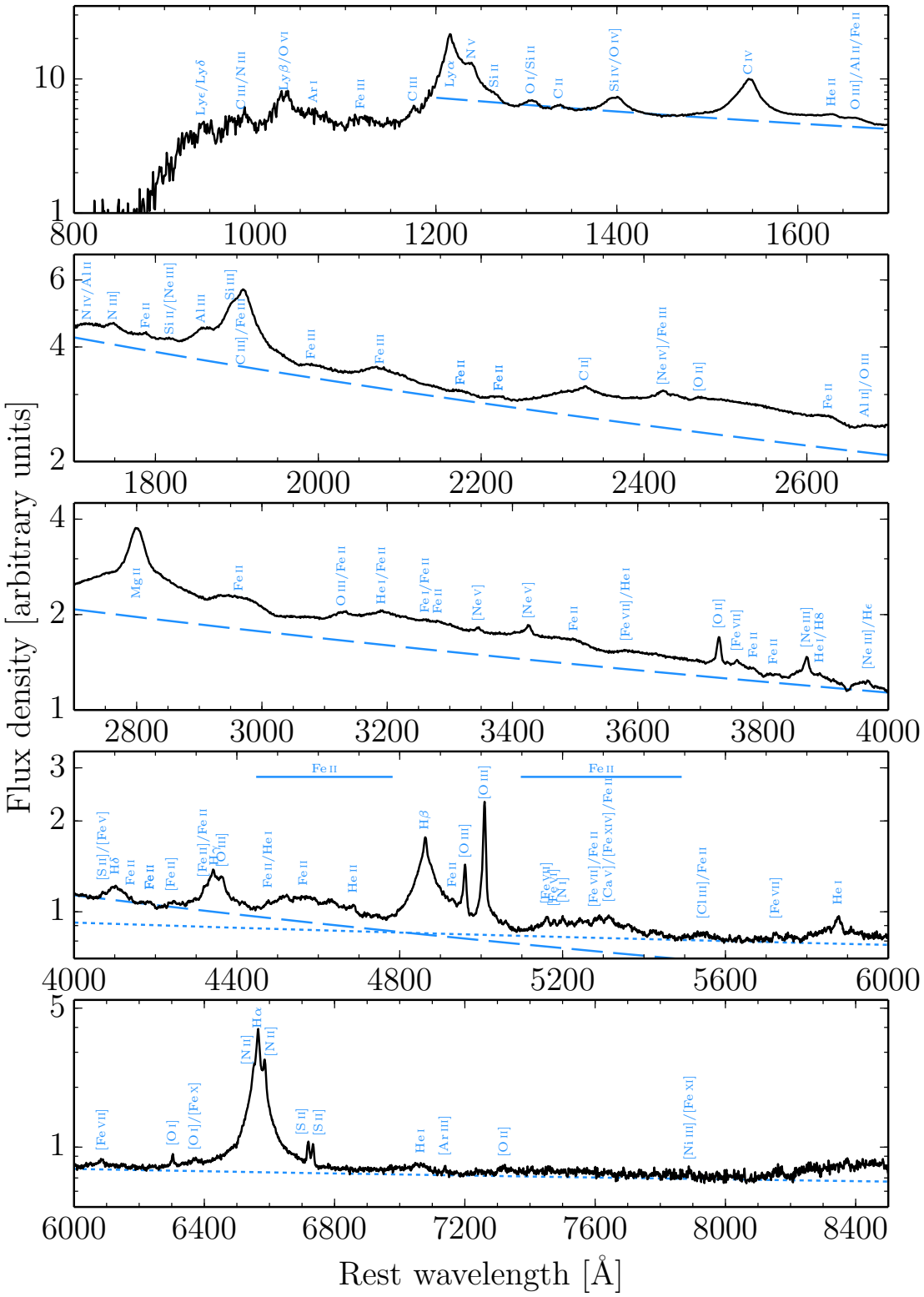

Figure 1.5: The composite AGN optical spectrum of Vanden Berk et al. (2001).

Table 1.1: Some key AGN emission lines

Line	λ [Å]	Band	Strength
Lyβ	1026	UV	9.6
Lyα	1216	UV	100
Mg II	2800	Opt.	15
[Ne V]	3427	Opt.	0.41
[Ne III]	3870	Opt.	0.35
Hδ	4101	Opt.	1.1
Hγ	4340	Opt.	2.6
He II	4687	Opt	0.14
Hβ	4861	Opt.	8.6
[O III]	5007	Opt.	2.5
He I	5877	Opt.	0.80
Hα	6564	Opt.	31
Paδ	10050	IR	1.0
Paγ	10940	IR	1.9
Paβ	12820	IR	3.1
Paα	18750	IR	3.4

Notes: Strength of the UV/optical lines is 100 times the line flux over the line flux of Lyα. Values for the UV/optical lines are taken from Vanden Berk et al. (2001); those for the Paschen lines are estimated from Kim et al. (2010) and Herbig & Vacca (2008).

[O III]λ5007. Some examples of strong forbidden lines in the optical band are given in Table 1.1.

1.1.7 The dust torus

Surrounding the central engine on parscec-scales is a vast reservoir of accretion material. This structure is thought to take the shape of a large flattened torus, coplanar with the accretion disc. Being distant from the central, UV-bright continuum source, the torus is beyond the dust sublimation radius of the AGN. The material in the torus therefore consists of dust and molecular gas as well as plasma. The torus intercepts light from the accretion disc and re-radiates it as thermal infrared emission over a range of temperatures.

The radius of the torus scales approximately with the square root of the AGN luminosity; higher AGN luminosity results in a more distant torus, which has a smaller solid angle as seen by the central source: this is the 'receding torus model' (Lawrence 1991). Being much larger than the accretion disc, it is just about possible

to spatially resolve the torus in nearby AGN using high-resolution imagers (e.g. Packham et al. 2005) and mid-infrared interferometers such as ALMA (e.g. Burtscher et al. 2013; Izumi et al. 2018; Carilli et al. 2019). However, many of these studies are still only able to place upper limits on the size of the structure. Another method to investigate the the size and geometry of the torus is that of reverberation (e.g. Barvainis 1992; Landt et al. 2019, MNRAS submitted): studying the temporal response of the infrared emission to that of the nuclear continuum which heats it. The dust torus is an important component of the unified model of AGN (Section 1.2.1).

1.1.8 Jets

As well as accreting matter, AGN can also eject it. In the case of jets, this expulsion can be spectacular. Observing the 'nebula' M87[6], Curtis (1918) noticed "a curious straight ray ... apparently connected with the nucleus by a thin line of matter" (Figure 1.6). We now know that Curtis had made the first discovery of an astrophysical jet and was observing luminous matter streaming out of the active nucleus of M87. Biretta et al. (1999) observed the jet with *Hubble* and were able to track bright knots moving at superluminal velocities of ≈ 4–$6c$. Of course, these features are not really travelling faster than light, rather their *apparent* superluminal motion results from the effects of their relativistic (near-lightspeed) velocity at an angle to the line of sight. When talking about relativistic motion, the normalised velocity $\beta = v/c$ and the Lorentz factor

$$\gamma = \sqrt{\frac{1}{1-\beta^2}} \tag{1.1.20}$$

are often used. The knots in M87 were found to have bulk Lorentz factors[7] $\Gamma_{\rm BLF} \geqslant 6$. Biretta et al. (1999) also determined that the M87 jet is inclined 19° to the line of

[6]The notion of other, distant galaxies was controversial at the time and many astronomers believed that objects such as M87 were small nebulae within the Milky Way. In 1920 a 'Great Debate' between Curtis and fellow astronomer Harlow Shapley was held. Shapley purported that the Universe consists of only one galaxy: the Milky Way, whilst Curtis argued in favour of the interpretation of some nebulae as very distant, independent galaxies (Shapley & Curtis 1921).

[7]When referring to the bulk motion of a clump of matter (rather than the individual motions of its constituent particles) it is common to use Γ for the bulk Lorentz factor. In this thesis, I use the notation $\Gamma_{\rm BLF}$.

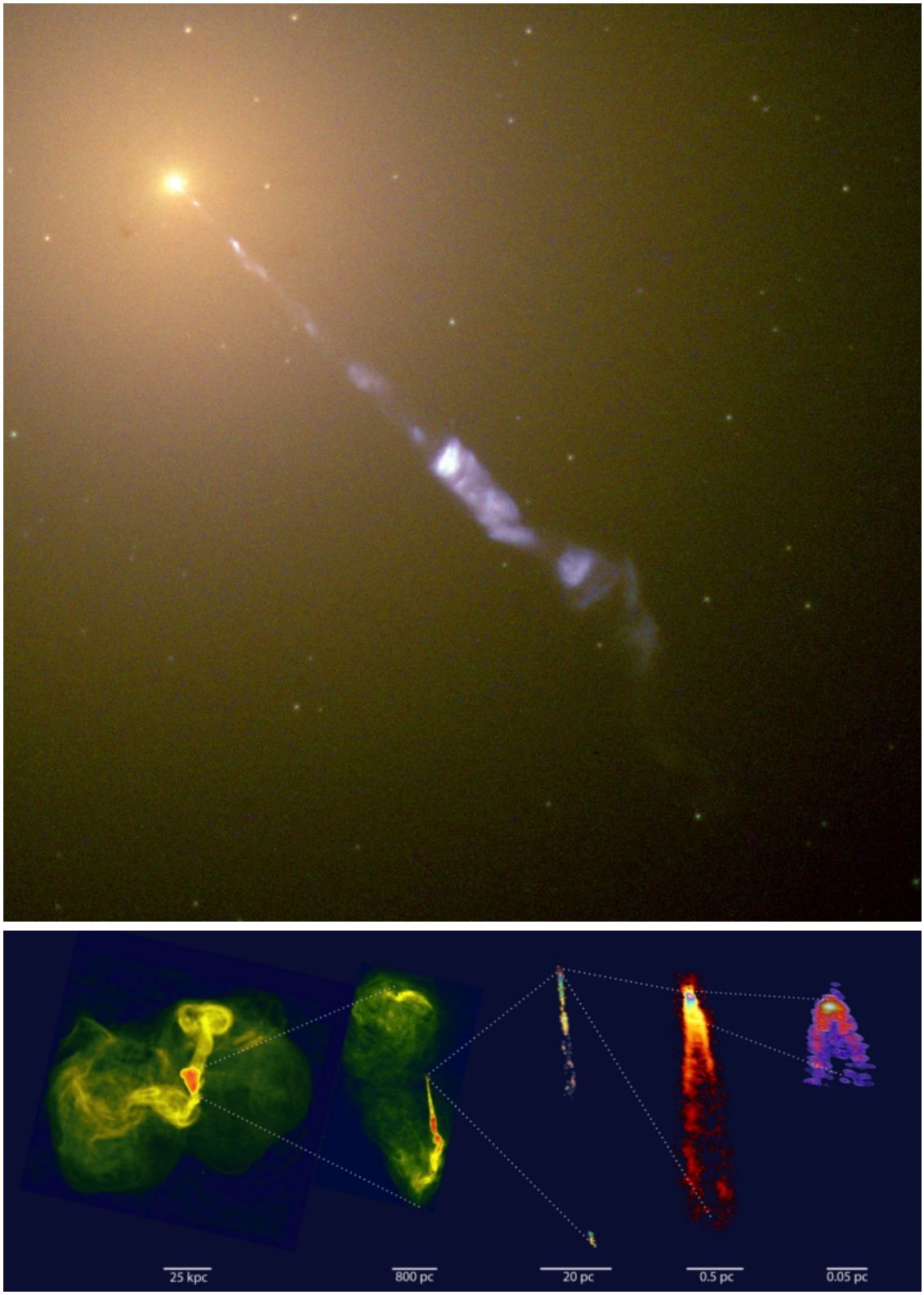

Figure 1.6: The relativistic jet of the AGN M87. *Top:* Composite image from the *Hubble* Legacy Archive. The visible jet has an angular size of approximately 20 arcseconds, equivalent to a length ≈ 1.5 kpc at the distance of M87. *Bottom:* The jet at different scales, from tens of kpc to fractions of a pc. Montage from Blandford et al. (2018).

sight, implying a de-projected jet size of ≈ 5 kpc.

Whilst accretion discs produce relatively little radio emission, the radio synchrotron emission from jets is very strong. Historically, the radio loudness parameter $R = F_{5\mathrm{GHz}}/F_B$[8] has been used to divide radio-loud ($R > 10$), jetted sources from radio quiet, non-jetted ones. A minority of AGN are radio-loud ($\sim$ 15–20 per cent, Kellermann et al. 1989). Nearby radio galaxies were divided into two types by Fanaroff & Riley (1974). Low radio luminosity Fanaroff-Riley type-I sources (FR-Is) such as M87 are *edge-darkened*, with the brightest emission coming from the jet core, beyond which the jet fizzles out into low-power lobes. High radio luminosity Fanaroff-Riley type-II sources (FR-IIs) are *edge-brightened*, with fainter jets ending in giant, bright lobes (see Figure 1.7 for a comparison). FR-Is have been found to commonly reside in clusters and are often the first ranked galaxy; FR-IIs on the other hand are more isolated (e.g. Owen & Laing 1989). Differences in their radio morphology may be understood in this context: the weaker and less well-collimated jets of FR-Is interact with a richer environment as they emerge, so they are more easily slowed by entrainment and suffer radiative losses of energy. The greater power and collimation of FR-II jets enables them to carry their energy out to greater distances, eventually dumping their energy when they collide with external gas clouds, creating the hot spots and bow shocks seen in Figure 1.7.

When jets are aligned close to our line of sight (with small angle of inclination i), the relativistic effect Doppler boosting amplifies the flux of the emission as $F_\nu^{\mathrm{obs}} = F_\nu^{\mathrm{em}} \delta^{3+\alpha} \nu^{-\alpha}$ where α is the spectral index of the emitted radiation and

$$\delta = \frac{1}{\Gamma_{\mathrm{BLF}}(1 - \beta \cos i)} \tag{1.1.21}$$

(Marscher 2009). Therefore, even though jets are radiatively inefficient, their emission can overwhelm that of the accretion flow across the entire SED.

The SEDs of blazars consist of two broad humps of emission (see Figure 1.8, left-hand

[8]Here the common definition of R as the radio of radio 5 GHz band flux to the optical B band flux is given, although sometimes other bands are used.

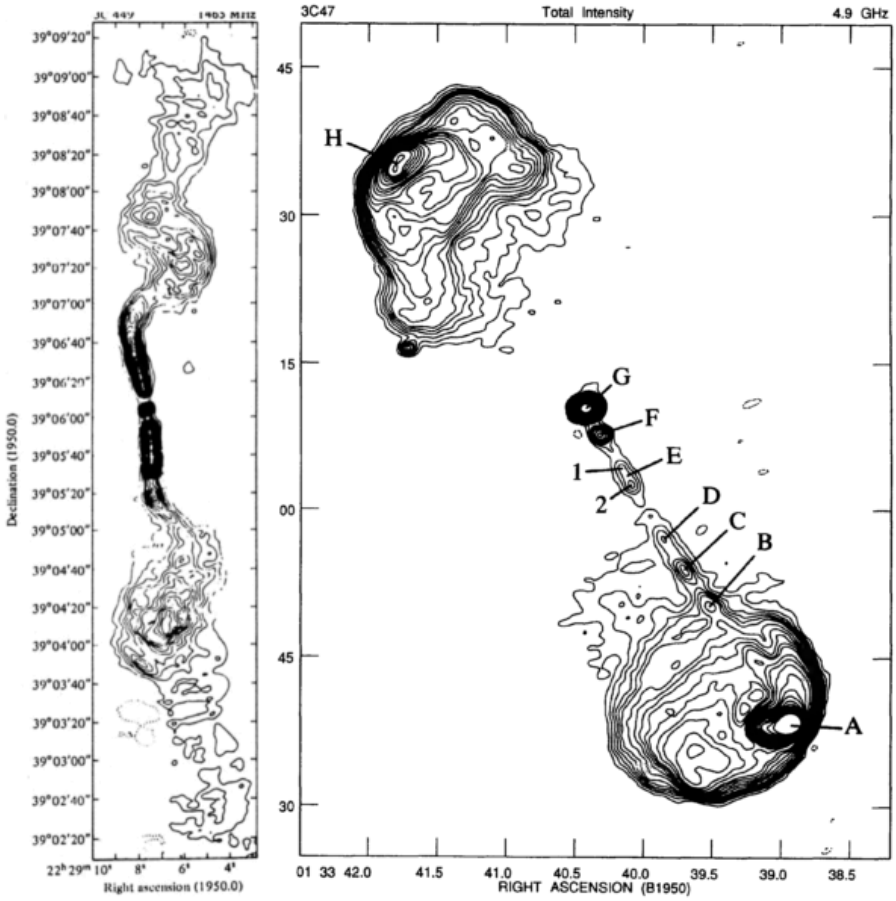

Figure 1.7: Radio intensity maps of Fanaroff-Riley type I and II sources. *Left:* The FR-I source 3C 449 (from Perley et al. 1979). *Right:* The FR-II source 3C 47 (from Bridle et al. 1994).

panel) and can be used to distinguish between two types of blazar: BL Lacertae objects (BL Lacs) and flat spectrum radio quasars (FSRQs). The BL Lac SEDs show two broad humps of emission that are roughly equal in luminosity. One hump arises from synchrotron processes (generally peaking in the radio/IR/optical) and the other from the synchrotron self-Compton mechanism ('SSC', generally peaking in the GeV range) from the same population of highly relativisitic electrons (with Lorentz factors of up to $\gamma \sim 10^{5-6}$) accelerated within the jet. The entire SED is dominated by this emission, boosted along the line of sight by the relativisitic bulk Lorentz factor ($\Gamma_{\rm BLF} \sim 10 - 20$) of the jet. In contrast, the FSRQs have GeV Compton humps that are considerably more luminous than their synchrotron emission humps, and they additionally show a clear accretion disc spectrum as a third hump in the

region between the two jet emission components, together with an associated broad line region (BLR). These differences can be understood in the context of a change in the nature of the accretion flow, with the BL Lacs having low accretion rates so the accretion flow is in the hot, advection dominated state with little intrinsic UV emission and hence a very weak or absent BLR. These advection-dominated accretion flows (ADAFs) collapse into a standard disc at luminosities above a few percent of the Eddington luminosity. The higher luminosity FSRQs therefore have UV bright discs which provides the ionisation to produce a BLR. This in turn gives an additional source of seed photons external to the jet for Comptonisation (via the external Compton 'EC' mechanism), leading to the observed much brighter Compton hump (Ghisellini et al. 2009). The BH mass can be derived from standard BLR scaling relations for the FSRQ, and is always found to be very high, with $M_{\rm BH} \gtrsim 10^8$ $\rm M_\odot$ (e.g. Ghisellini & Tavecchio 2015). Conversely, it is much more difficult to constrain in BL Lacs as these have very weak (or no) lines, but studies of the host galaxies conclude that these are powered by similarly high mass SMBHs (e.g. Plotkin et al. 2011; Falomo et al. 2003). Together the BL Lacs and FSRQs form a standard 'blazar sequence' of increasing accretion power onto the most massive SMBHs (Ghisellini et al. 2017; Fossati et al. 1998; and see Figure 1.8).

Whilst jet emission processes are relatively well-understood, the mechanisms by which jets are launched and powered are still areas of intense research. Ghisellini et al. (2014) found a clear correlation between jet powers and accretion disc luminosities, but with the jet power exceeding the accretion power by as much as a factor of ten (see Figure 1.8, right-hand side). The jet launching mechanism must therefore be very efficient and in some way linked to the accretion flow. The initial launching and acceleration of the jet requires some confinement at the base and a steep pressure gradient along the jet axis. Gas pressure was considered, but if this were provided by (e.g.) a wind from the accretion disc, it would require a gas so hot and dense that it would be implausibly X-ray bright (Blandford & Rees 1974). Instead, magnetic fields are often invoked. Differential rotation of the accretion disc or the ergosphere

of spinning SMBH, or both, could cause the magnetic field lines to wind up into a helix, providing a pinching force near the base of the jet. The magnetic field lines diverge with increasing distance from the SMBH, creating a pressure gradient which accelerates particles along the jet axis. The magnetic field energy is converted to the kinetic energy of the particles within the jet and acceleration of the jet continues until a balance is reached between the kinetic and magnetic energy densities (Marscher 2009).

The observed emission from the jet likely originates downstream from the launching site. The emission mechanisms require a population of highly relativistic electrons travelling in the bulk flow of the jet. The electrons are thought to be accelerated by the first order Fermi mechanism (i.e. the multiple reflections of particles across shock fronts). The population of relativistic electrons then radiatively cools by emitting synchrotron radiation, or by Compton processes as described above. The cartoon shown in Figure 1.9 illustrates the jet structure of an FSRQ-type jet (with a luminous disc, corona and BLR) in which the γ-ray emission site is located at $\sim 10^5$ Schwarzschild radii from the launching site.

Whilst the above description of jets (and that in the rest of this thesis) considers them to be *leptonic* in nature (i.e. the relativistic emitting particles within the jet are electrons/positrons), there is a case to be made for *hadronic* jets containing relativistic protons. IceCube Collaboration et al. (2018) reported the detection of a neutrino arriving from a position consistent with that of the blazar TXS 0506+056, which was in a flaring state at the time. Neutrinos may be produced if the protons in the jet are relativistic. Proton collisions can create charged pions, $\pi^{\pm}$, that decay into $e^{\pm}$ plus an electron-neutrino or electron-antineutrino. Neutral pions, π^0, decay into γ-rays. Additionally, p-γ interactions can result in electron-positron pair production,

$$\mathrm{p} + \gamma \rightarrow \mathrm{p}' + \mathrm{e}^- + \mathrm{e}^+,$$

and the resultant $e^{\pm}$ will emit synchrotron radiation.

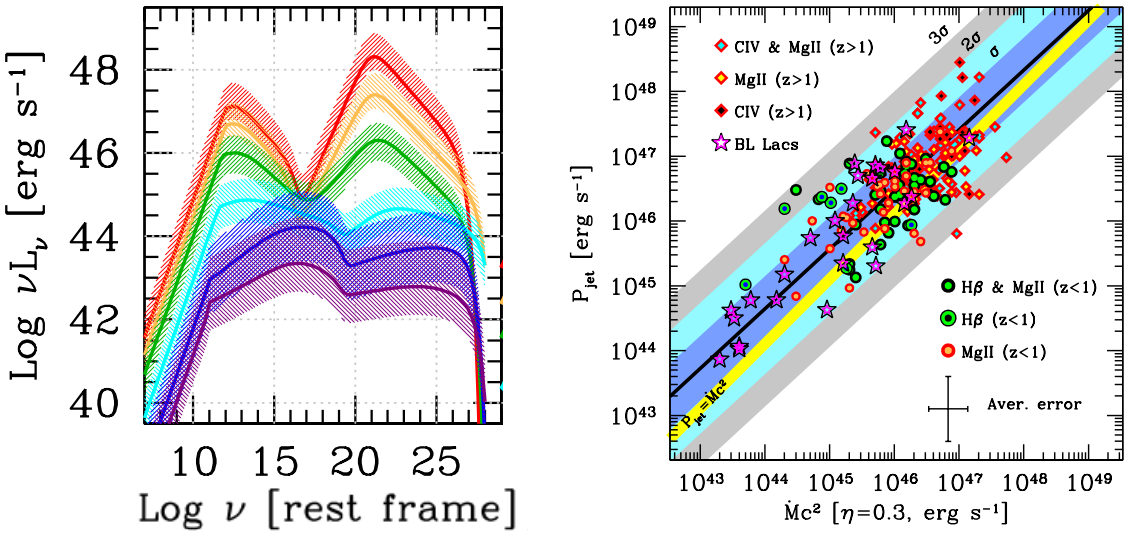

Figure 1.8: *Left:* The 'blazar sequence' showing jet SEDs from low-power, high-frequency peaked BL Lacs (purple) to high-power, low-frequency peaked FSRQs (red). From Ghisellini et al. (2017). *Right:* Jet power $P_{\rm jet}$ versus accretion power $\dot{M}c^2$ (assuming a radiative efficiency $\eta = 0.3$) for a sample of blazars. BL Lacs (shown as stars) typically have lower powers than the FSRQs (other symbols). The one-to-one relation is shown as a yellow line, and the best fit relation (indicating that generally $P_{\rm jet} > \dot{M}c^2$) is shown by a black line. From Ghisellini et al. (2014).

1.2 Putting it all together

1.2.1 The unification of AGN

The optical spectra of some AGN show a rising, blue component attributed to the sum-of-blackbodies emission from the accretion disc (Section 1.1.3) as well as both broad and narrow emission lines from the BLR and NLR, respectively (Sections 1.1.5 and 1.1.6). In the optical spectra of many other sources, the broad emission lines and blue continuum are absent and only the narrow emission lines can be seen. Local AGN have been classified as either Seyfert 1s or Seyfert 2s depending on whether or not the broad lines and continuum can be seen (Khachikian & Weedman 1974; and see Figure 1.10). More generally, we may divide Seyferts, quasars and other AGN into Type 1 and Type 2 sources by the same criteria. The unified model of AGN (Antonucci 1993, Urry & Padovani 1995), posits that Type 1 and Type 2 AGN are

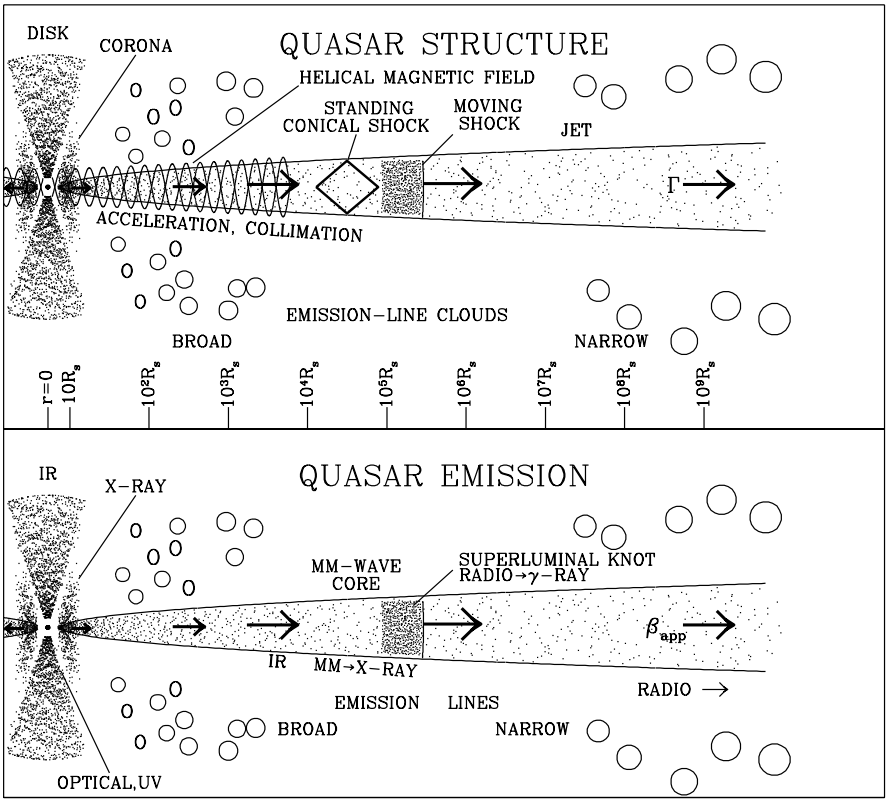

Figure 1.9: A cartoon illustration of AGN jet structure and emission regions. The length scale in the upper panel is logarithmic and given in terms of the black hole Schwarzschild radii. From Marscher (2009).

intrinsically exactly the same phenomenon, just viewed from different angles. In the case of Type 1 AGN we have a clear line-of-sight to the nucleus and BLR; because of a shallower viewing angle, the nucleus and BLR of Type 2 AGN are obscured by the thick, dusty torus (see Figure 1.11). Evidence for this picture comes from polarimetry studies of the scattered light from Type 2 AGN. The polarised spectra of Type 2 AGN do contain broad emission line features, but we cannot see these in direct light (Antonucci & Miller 1985). This strongly suggests that Type 2 AGN harbour hidden broad line regions illuminated by bright accretion discs. The ratio of Seyfert 2s to Seyfert 1s ($\approx$ 3:1) suggests that the AGN torus must cover $\approx$ $^3/_4$ of the sky seen by the central source.

Whilst orientation is certainly an important factor in observed properties, this simple picture may not tell the whole story about the differences between Type 1 and Type 2

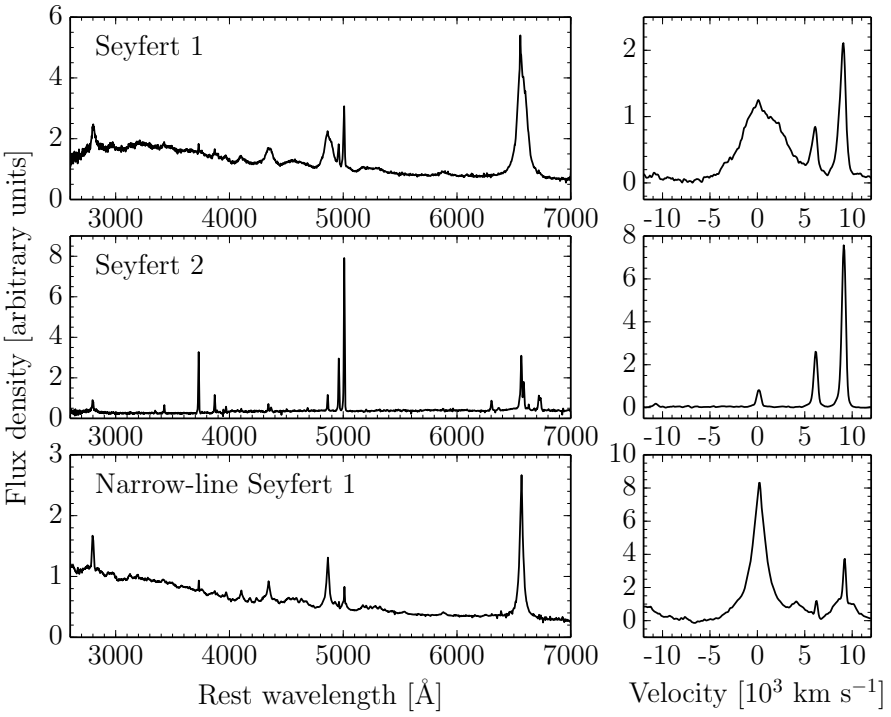

Figure 1.10: Examples of the optical spectra of a Seyfert 1, a Seyfert 2 and a narrow-line Seyfert 1 AGN, taken from the Sloan Digital Sky Survey. The left-hand panels show the optical spectrum shifted to the rest-frame wavelengths. The right-hand panels show the Hβ λ4861 and the [O III] $\lambda\lambda$4959, 5007 emission lines in velocity space.

AGN. Obscured Type 2 AGN may evolve into Type 1 sources following the accretion or ejection of the surrounding obscuring material (e.g. Sanders et al. 1988, Hopkins et al. 2008). In addition, it is increasingly it is being recognised that a number of AGN change their type on observable timescales, with their broad lines appearing or disappearing over years / decades (e.g. LaMassa et al. 2015, Rumbaugh et al. 2018, Stern et al. 2018, MacLeod et al. 2019). This second point is discussed further in Chapter 6.

Orientation also plays a role in the radio classification of AGN. It is thought that FR-IIs are the parent population of FSRQs (i.e. FSRQs are FR-IIs with their jets pointed towards us). Similarly, FR-Is are thought to be misaligned BL Lacs (see Figure 1.11 again).

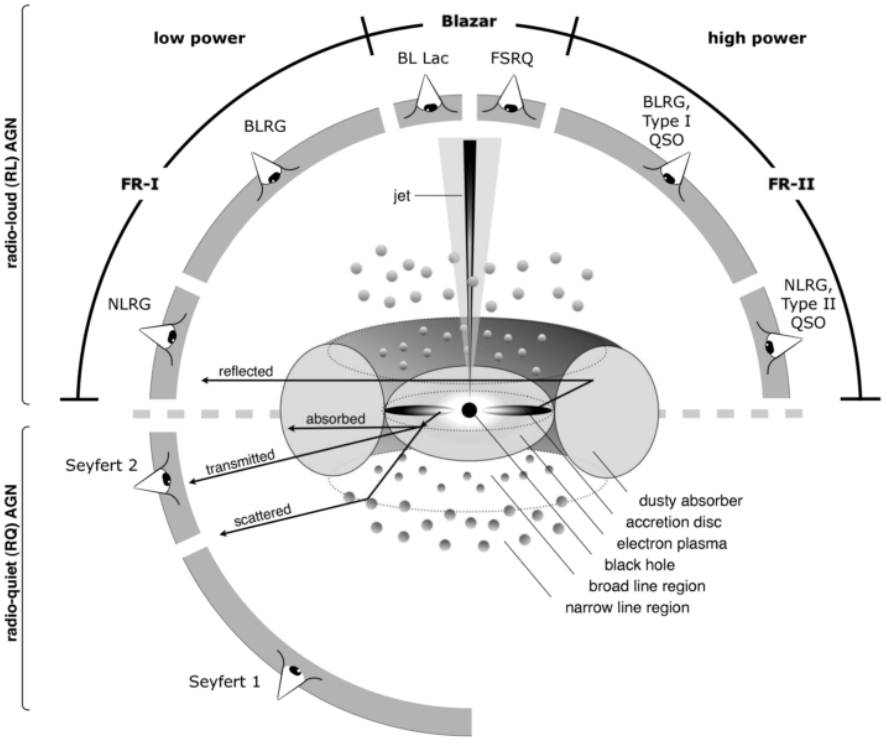

Figure 1.11: Cartoon illustrating the unified model of AGN. The classification of an AGN depends upon the angle at which it is observed. From Beckmann & Shrader (2012).

1.2.2 Narrow-line Seyfert 1s

1.2.2.1 Identification from optical and multiwavelength properties

Osterbrock & Pogge (1985) identified a subset of 'narrow-line' Seyfert 1s (NLS1s), in which the broad permitted lines were relatively narrow. Sometimes the FWHMs of the Balmer lines are only a few hundred km s^{-1} (similar to typical forbidden line widths and the permitted lines of S2s), as in the case of the first NLS1 to be discovered, Mrk 359 (Davidson & Kinman 1978). The distinction of NLS1s from broad-line Seyferts and S2s is often made with reference to three optical spectral properties set out by Goodrich (1989):

- a FWHM of permitted emission lines (usually Hβ) < 2000 km s^{-1};
- a line luminosity ratio $L_{[\mathrm{O\,III}]\lambda5007}/L_{\mathrm{H}\beta} < 3$;

- strong Fe II emission.

The first criterion distinguishes NLS1s from their more common broad-line counterparts. The second and third criteria separate NLS1s from S2s, which also have narrow permitted lines. Because the emission from the BLR is obscured in S2s, their total permitted line luminosities are lower than those in S1s. Forbidden line emission from the NLR is visible in the spectra of both S1s and S2s, so S2s will have lower permitted to forbidden line ratios than S1s. The line ratio above is commonly used to divide S1s and S2s (Shuder & Osterbrock 1981). Fe II emission is thought to originate from the BLR and so is absent in the spectra of S2s. Being type 1 AGN with unobscured nuclei, the accretion disc continuum emission can be seen in the optical spectra of NLS1s, but not S2s (see Figure 1.10).

Boroson & Green (1992) conducted a principal component analysis of a sample of 87 quasars, exploring how the optical spectral parameters varied together, and with the radio and X-ray properties. They identified a number of trends in the correlation space (see Figure 1.12, left). Firstly, a strong anticorrelation of Fe II[9] and [O III] λ5007 strength was evident. These relations are said to describe 'Eigenvector 1'[10]. It is possible to see a 'main sequence' connecting quasars across the Eigenvector 1 optical plane (see Figure 1.12, right). Sulentic et al. (2000) noted that the properties of NLS1s were continuous with those of broad-line sources, so NLS1s do not represent a distinct population of AGN, but the extreme end of this sequence.

The widths of the permitted lines in NLS1s imply low SMBH masses (see Section 2.1). Indeed, Rakshit et al. (2017) found that a sample of 11101 NLS1s had $\langle \log M_{\rm BH} \rangle = 6.9$ M$_\odot$, compared with $\langle \log M_{\rm BH} \rangle = 8.0$ M$_\odot$ for BLS1s. It follows that since NLS1s have similar luminosities to broad-line AGN, but lower masses, they must have a greater $L/L_{\rm Edd}$. It has been suggested that $L/L_{\rm Edd}$ is one of the main drivers of Eigenvector 1 (e.g. Sulentic et al. 2000).

[9] The Fe II strength is often characterised as $R_{\rm Fe\,II}$, the ratio of the integrated flux of the Fe II λ4570 complex to the flux of broad Hβ.

[10] A second eigenvector relates the optical luminosity with the strength of He II and the optical-X-ray spectral slope $\alpha_{\rm ox}$.

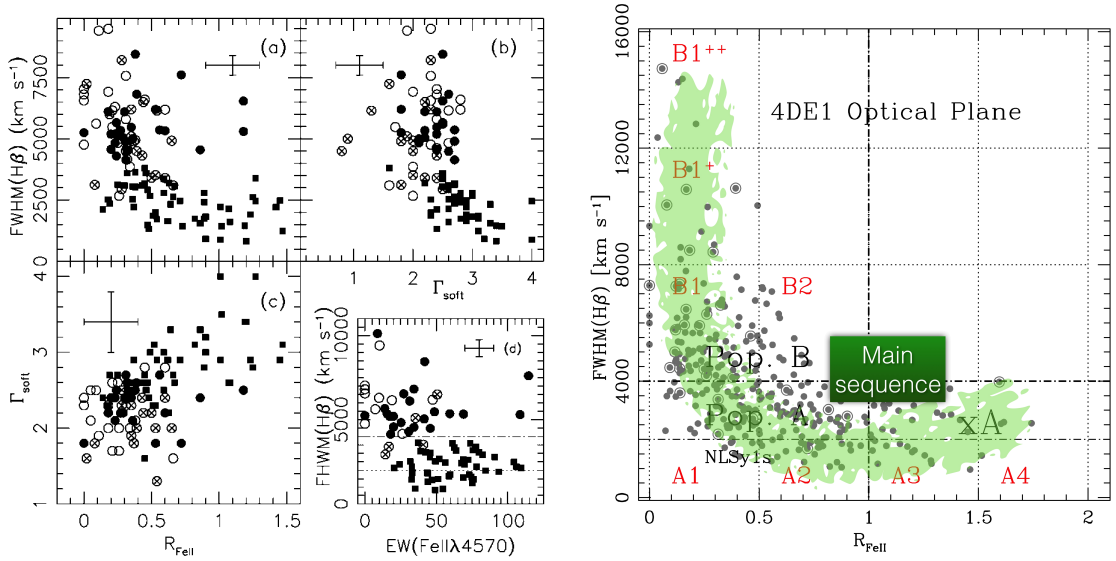

Figure 1.12: The optical plane Eigenvector 1 and the quasar main sequence. *Left:* Correlations between FWHM(Hβ), soft X-ray photon index Γ, $R_{\rm Fe\,II}$ and the equivalent width of Fe II λ4570. From Sulentic et al. (2000). *Right:* A dark horizontal dot-dashed line separates broad-line (FWHM(Hβ)$>$ 4000 km s^{-1}) Population B sources from narrower-line Population A sources. The light horizontal dot-dashed line indicates the 2000 km s^{-1} limit for NLS1s. NLS1s with strong Fe II emission ($R_{\rm Fe\,II} > 1$) form part of the extreme tail of Population A sources (xA). From Marziani et al. (2018).

Boroson & Green (1992) found that sources with strong Fe II emission have soft X-ray photon indices and narrower broad Hβ (see Figure 1.12). These observations have been supported by other studies. For example, Leighly (1999) studied a sample of NLS1s with *ASCA* and found that their X-ray spectral indices were significantly steeper $\Gamma \approx 2$–2.5 than those measured in other Seyferts. A correlation between the broad Hβ line width and X-ray photon index was also noted.

With regard to the radio properties, Boroson & Green (1992) found a distinction between radio-loud and radio-quiet sources with respect to their Fe II emission. Radio-loud sources tended to have weak Fe II, while the opposite was true for radio-quiet sources. The incidence of radio-loudness among NLS1s has been found to be very low (≈ 7 per cent, Komossa et al. 2006 or ≈ 5 per cent, Rakshit et al. 2017). This compares with a radio-loud fraction of 15–20 per cent among quasars generally (Kellermann et al. 1989).

It should be noted that NLS1s were first identified from observations of luminous AGN in the local Universe ($z \sim 0.01$, Osterbrock & Pogge 1985). As noted by McHardy et al. (2006), that NLS1s are found to have low SMBH masses is a selection effect, because AGN with greater $M_{\rm BH}$ would have to be accreting above the Eddington limit to be luminous enough to produce broad emission lines narrower than 2000 km s^{-1} (see also e.g. Czerny et al. 2018). Indeed, some AGN have been found to have many similar characteristics as NLS1s, but do not qualify as such because of their broader emission lines, resulting from their higher SMBH mass; PDS 456 is one such example (Reeves et al. 2003). McHardy et al. (2006) point out the linewidth depends not upon $\dot{m}$ or $M_{\rm BH}$ alone, but their ratio $\dot{m}/M_{\rm BH}$. This may motivate the introduction of 'NLQ1s': higher-mass, broader-line quasar analogues of NLS1s. Perhaps instead it would be better to do away with arbitrarily classifying type 1 AGN by linewidth altogether.

1.2.2.2 The γ-ray emitters

As noted above, the incidence of radio-loudness among NLS1s is rare, and their radio-loud fraction is much smaller than is found for BLS1s and AGN in general. However, Zhou et al. (2007), Yuan et al. (2008), Foschini et al. (2009) and others noted that several of the radio-loudest NLS1s exhibited blazar-like properties (e.g. flat radio spectra, compact one-sided jet structures seen in radio images and strong optical, UV and X-ray variability behaviour), suggesting the presence of a relativistic jet. Foschini et al. (2009) thought that the evidence for relativistic jets in NLS1s was compelling but not conclusive; however, they said that the detection in γ-rays by the *Fermi Gamma-Ray Space Telescope*, which had recently been launched (see Section 3.5.1), would provide confirmation of the blazar nature of these sources. Indeed, γ-ray emission from the NLS1 PMN 0948+0022 was detected with high significance by *Fermi* shortly after its launch in 2008 (Abdo et al. 2009a). This discovery was soon followed by the γ-ray detection of three more NLS1s, 1H 0323+342, PKS 1502+036 and PKS 2004−447 (Abdo et al. 2009b).

Table 1.2: Known γ-ray emitting narrow-line Seyfert 1 galaxies

Source name	RA	Dec.	z	Reference
1H 0323+342	03 24 41.16	+34 10 45.8	0.0625	Abdo et al. (2009b)
SBS 0846+513	08 49 75.983	+51 08 29.08	0.5840	Donato & Perkins (2011)
J0932+5306	09 32 41.1	+53 06 33.3	0.5970	Paliya et al. (2018)
J0937+5008	09 37 12.33	+50 08 52.1	0.2754	Paliya et al. (2018)
SDSS J0946+1017	09 46 35.06	+10 17 06.11	1.004	Yao et al. (2019)
PMN J0948+0022	09 48 57.319	+00 22 25.52	0.5836	Abdo et al. (2009a)
B2 0954+25A	09 56 49.880	+25 15 16.05	0.7076	Calderone et al. (2012)
J0958+3224	09 58 20.9	+32 24 01.6	0.5306	Paliya et al. (2018)
J1102+2239	11 02 23.36	+22 39 20.7	0.453	Foschini et al. (2015)
J1146+3236	11 46 54.30	+32 36 52.2	0.465	AB
PKS J1222+0413	12 22 22.548	+04 13 15.75	0.9662	Yao et al. (2015a)
J1238+3942	12 38 52.15	+39 42 27.6	0.623	Foschini et al. (2015)
SDSS J1246+0238	12 46 34.649	+02 38 09.02	0.3623	Foschini et al. (2015)
J1305+5116	13 05 22.749	+51 16 40.26	0.7876	FL8Y
U1575-03416792	14 10 45.83	+74 05 11.1	0.429	Marchesini et al. (2016)
J1421+2824	14 21 14.07	+28 24 52.2	0.538	Paliya et al. (2018)
B3 1441+476	14 43 18.561	+47 25 56.71	0.6972	D'Ammando et al. (2016)
PKS 1502+036	15 05 06.476	+03 26 30.83	0.4083	Abdo et al. (2009b)
B3 1518+423	15 20 39.610	+42 11 08.90	0.4847	Paliya et al. (2018)
J1641+3452	16 41 00.11	+34 54 52.68	0.1641	Lähteenmäki et al. (2018)
FBQS J1644+2619	16 44 42.536	+26 19 13.25	0.1440	D'Ammando et al. (2015)
PKS 2004−447	20 07 55.18	−44 34 44.4	0.240	Abdo et al. (2009b)
PMN J2118+0013	21 18 17.4	+00 13 16.8	0.4629	Paliya et al. (2018)
J2118−0732	21 18 52.97	−07 32 27.55	0.260	Yang et al. (2018a)

Notes: FL8Y is the *Fermi* LAT 8-year source list. AB: The γ-ray detection of this RL-NLS1 was made by Dr. Anthony Brown of the Gamma Ray Astronomy Group at Durham University.

Over the last decade, more γ-ray emitting NLS1s (γ-NLS1s) have been found. The increasing depth of *Fermi* data over time has made the detection of fainter γ-NLS1s possible, and allowed more time for usually faint sources to flare above the detection threshold. In the case of PKS J1222+0413, the optical counterpart of a known γ-ray source was identified as a NLS1 (Yao et al. 2015a). To date, only 24 γ-NLS1s are known; a list of those sources is given in Table 1.2.

Early studies (e.g. Laor 2000; McLure & Dunlop 2001) found no evidence of a RL-AGN population with BH masses $M_{\rm BH} \lesssim 10^8$ M$_\odot$ and RL-AGN were not among the Population A (FWHM(Hβ) < 4000 km s^{-1}) sources of Marziani et al. (2001). High-mass SMBHs are almost exclusively found in elliptical galaxies with large bulges, leading to ideas that there is something about the evolutionary history of

these systems which triggers jet production such as SMBH spin (Blandford & Znajek 1977) or the history of concentration of magnetic flux (Sikora & Begelman 2013), or both. The discovery of γ-NLS1s and lower-mass RL-AGN (Ho 2002; Yuan et al. 2008) which are hosted by spiral galaxies has broken this simple paradigm. This has opened up a new region of parameter space in which to explore the relationship between jets and accretion discs.

In this thesis, detailed multiwavelength studies of the nearest (1H 0323+342, $z = 0.063$) and second-most distant (PKS J1222+0413, $z = 0.967$) γ-NLS1s are made in Chapter 4 and Chapter 5, respectively.

Chapter 2

Methods and models

In this chapter I outline some of the methods and models which are used throughout this thesis. Section 2.1 discusses different methods to measure SMBH masses; the single-epoch virial method (Section 2.1.3) is most commonly used in the following chapters. Section 2.2 describes methods to deal with observations in which the flux is attenuated by reddening or absorption. Sections 2.3 and 2.4 describe two of the models which are applied to multifrequency spectral energy distributions in order to determine the physical parameters of the system.

2.1 Weighing black holes

Astrophysical BHs have masses which span approximately ten orders of magnitude. Stars with a mass greater than the Tolman-Oppenheimer-Volkoff limit (≈ 3 M$_\odot$) may collapse into BHs[1]. In X-ray binary systems, the masses of the BHs have been determined to be in the range $\approx$ 3–20 M$_\odot$ (Remillard & McClintock 2006). The gravitational wave signature of two merging BHs, detected by LIGO on 14 September 2015, implied masses greater than this at 36^{+5}_{-4} and 29 ± 4 M$_\odot$ (Abbott et al. 2016). The SMBHs in the centres of galaxies have masses $\sim 10^5$–10^{10} M$_\odot$. However, the

[1]Collapsing stars with a mass lower than this, but greater than the Chandrasekhar limit ($\approx$ 1.4 M$_\odot$), will form neutron stars.

existence of intermediate mass black holes (IMBHs) in the range 10^2–10^5 $M_\odot$ is currently debated (see Koliopanos 2017 for a recent review). There is evidence that BH accretion flows are scale-invariant (e.g. McHardy et al. 2006, Svoboda et al. 2017, Ruan et al. 2019). Since it is the mass which sets the scale, it is an important quantity to determine.

2.1.1 Dynamical methods

If one can track the motions of masses (e.g. stars) in orbit around a SMBH, then the mass enclosed in the orbit can easily be determined from its period and geometry. Motions of the stars in the Galactic centre imply that Sagittarius A* has a mass of $\approx 4 \times 10^6$ $M_\odot$ (Ghez et al. 2008, Gillessen et al. 2009, Schödel et al. 2009). However, because of the limited spatial resolution of our telescopes, it is not possible to map the motions of individual stars in the centres of other galaxies. Therefore, to estimate the masses of more distant SMBHs, we must rely on other methods such as those outlined below.

2.1.2 Reverberation mapping

Although we cannot spatially resolve AGN components, we can infer size scales using the temporal variability. The gas in the broad line region (BLR) is within the sphere of influence of the SMBH's gravity. If the BLR is virialised (i.e. the dynamics of the BLR gas clouds are governed by the gravitational influence of the SMBH) then we can apply the virial theorem to calculate the mass of the SMBH. The theorem relates the kinetic and gravitational potential energies of a system as

$$E_\mathrm{K} = -\frac{1}{2}E_\mathrm{G} \quad \rightarrow \quad \frac{1}{2}m\langle v^2\rangle = \frac{1}{2}\frac{GM_\mathrm{BH}m}{R}, \tag{2.1.1}$$

where $\langle v^2\rangle$ is the mean square velocity of a virial mass m. Rearranging Equation 2.1.1 for M_BH we have

$$M_\mathrm{BH} = f\frac{R\langle v^2\rangle}{G} \tag{2.1.2}$$

where the factor $f \sim 1$ (Collin et al. 2006, Onken et al. 2004) is introduced, which incorporates our ignorance of the orientation and kinematics of the BLR. Instead of $\langle v^2 \rangle$, the FWHM of the broad emission line is used as a proxy for the speed of the gas motion.

The relevant radius is that of the BLR. This can be determined by measuring the time lag of the response of broad lines to changes in the accretion disc continuum emission (e.g. Blandford & McKee 1982, Peterson 1993, Peterson & Horne 2006). In practice this is complicated because the BLR is extended, so different elements of the emission line respond with different lag times. By calculating the root mean square spectrum from the reverberation mapping campaign, it is possible to isolate just the variable part of the emission line (i.e. that which is responding to changes in the continuum, Peterson et al. 2004). To make a robust estimate of the lag times it is necessary to several of them. Since the BLR is typically $\sim$ 1 light month in size, reverberation mapping campaigns must take place over at least several months. This is observationally expensive, and prohibitively impractical for obtaining the BH masses of large samples of AGN. Therefore, 'single-epoch' techniques have been devised from which a BH mass can be determined from a single spectroscopic observation.

2.1.3 Single-epoch virial methods

Reverberation mapping has enabled a characterisation of the radius-luminosity relationship of the BLR. The size (radius) of the BLR has been found to be well-correlated with luminosity of the ionising continuum, i.e. $R_{\rm BLR} \propto L^{\alpha}$, where $\alpha \approx 1/2$. It has been shown that the BLR lags obtained from reverberation mapping campaigns correlate with the optical, UV and near-IR luminosity (of the ionising component) largely as expected from simple photoionisation arguments (e.g. Peterson 1993; Wandel et al. 1999; Kaspi et al. 2000; Bentz et al. 2009; Landt et al. 2011a).

If one can calculate the BLR radius (from the observed luminosity) and $\langle v^2 \rangle$ (from

an emission line FWHM) then Equation 2.1.2 can be applied to determine the SMBH mass. This method is very efficient for calculating the BH masses for large samples of AGN, since it requires only a single spectrum. However, the method is less precise than reverberation mapping. Uncertainties are introduced by scatter in the radius-luminosity relation and errors on the measured quantities. Park et al. (2012) has estimated that masses calculated by the single epoch virial method are accurate to within a factor ~ 3.

It is common to use the monochromatic continuum luminosity measured at 5100 Å or 3000 Å (in the rest frame) to make a SMBH mass estimate using the Balmer lines (Hα and Hβ) or Mg II, respectively. Relations have also been presented with make use of the integrated broad line luminosity. For example, Greene et al. (2010b) presented a relation which uses the broad Hα luminosity to calculate $R_{\rm BLR}$ and Mejía-Restrepo et al. (2016) presented a relation using Hβ to calculate the mass directly. These methods would be especially useful in cases where the AGN optical/ultraviolet continuum measurement may be very uncertain (e.g. in radio-loud sources where it may be contaminated by emission from a jet, or low-luminosity AGN with relatively strong starlight contribution). These methods are used in this thesis, to supplement mass estimates made the 'conventional' way, using the continuum luminosity. However, I have used large AGN samples to compare the results obtained by both methods and it appears that using the line luminosity systematically gives smaller mass estimates (see Figure 2.1).

2.1.4 Other methods

2.1.4.1 Host galaxy scaling relations

Magorrian et al. (1998) found that dynamical models of the bulges of nearby galaxies required massive dark objects (i.e. SMBHs) at their centres, with $\langle M_{\rm BH}/M_{\rm bulge}\rangle = 0.006$. Ferrarese & Merritt (2000) and Gebhardt et al. (2000) found correlations of $M_{\rm BH}$ with the velocity dispersion σ of stars in the bulge. This $M_{\rm BH}$-σ relation is a

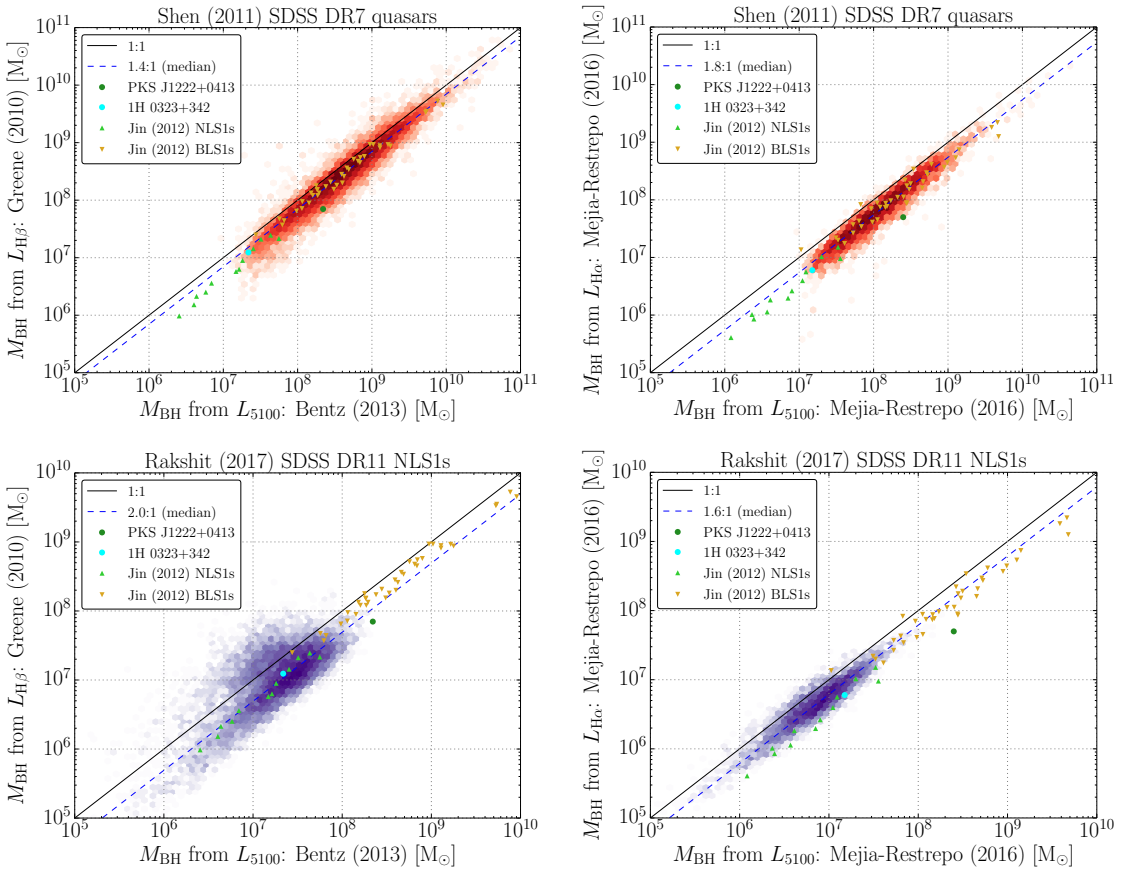

Figure 2.1: A comparison of single-epoch virial BH mass estimates made using either the continuum luminosity or emission line luminosity. The left panels are calculated using the FWHM of Hβ and the right using the FWHM of Hα. The top panels show a density plot for 22644 sources from the Shen et al. (2011) sample of SDSS DR7 quasars. The bottom panels show a density plot for the Rakshit et al. (2017) sample of 11101 SDSS DR7 NLS1s. Overlaid are the NLS1s and BLS1s from the sample of Jin et al. (2012a). The masses of the γ-NLS1s 1H 0323+342 (Chapter 4) and PKS J1222+0413 (Chapter 5), estimated in this thesis, are shown as cyan and green circles, respectively. The 1:1 relation is shown as a black solid line. The blue dashed line indicates the median ratio of the masses estimated by each method. It can be seen that masses estimated using the line luminosity are generally lower than those using the continuum luminosity.

key piece of evidence for the co-evolution of SMBHs and their host galaxies, and suggests that a feedback mechanism regulates their growth (Silk & Rees 1998, King 2003, Croton et al. 2006).

The near-infrared host galaxy bulge luminosity, $L_{\rm bul}$, is also correlated with the SMBH mass and the scatter in the $M_{\rm BH}$-$L_{\rm bul}$ relation is similar to that in $M_{\rm BH}$-σ (Marconi & Hunt 2003). The $M_{\rm BH}$-σ and $M_{\rm BH}$-$L_{\rm bul}$ relations can be used to estimate a SMBH mass in galaxies which do not contain an active nucleus, for which reverberation mapping and single-epoch virial methods are not applicable. D'Ammando et al. (2017) and D'Ammando et al. (2018) obtained high spatial resolution images of the γ-NLS1s FBQS J1644+2619 and PKS 1502+036, respectively. They were able to separate the host galaxy and nuclear components, then, using the Marconi & Hunt (2003) relation, they calculated SMBH masses of $(2.1 \pm 0.2) \times 10^8$ and $\approx 7 \times 10^8$ $M_\odot$, both of which are much greater than the masses calculated by the single epoch virial method.

2.1.4.2 Accretion disc SED fitting

If the emission near the peak of accretion disc spectrum is observed, then it is possible to fit an accretion disc model to the continuum data, from which the SMBH mass can be determined[2]. Calderone et al. (2013) used an SED fitting method to measure the masses of 23 RL-NLS1s. They found that the calculated masses were larger, on average, by a factor ~ 6 compared with those determined by the single-epoch virial method. However, Calderone et al. (2018) note that the SED-fit mass estimates may be reconciled with virial estimates if the inner part of the accretion disc becomes radiatively inefficient, lowering η to ~ 1 per cent from the ~ 10 per cent commonly assumed. If the mass accretion rate is sufficiently high then energy may be advected into the SMBH rather than being radiated.

[2]It is possible to use the luminosities of broad emission lines to estimate the bolometric ionising luminosity.

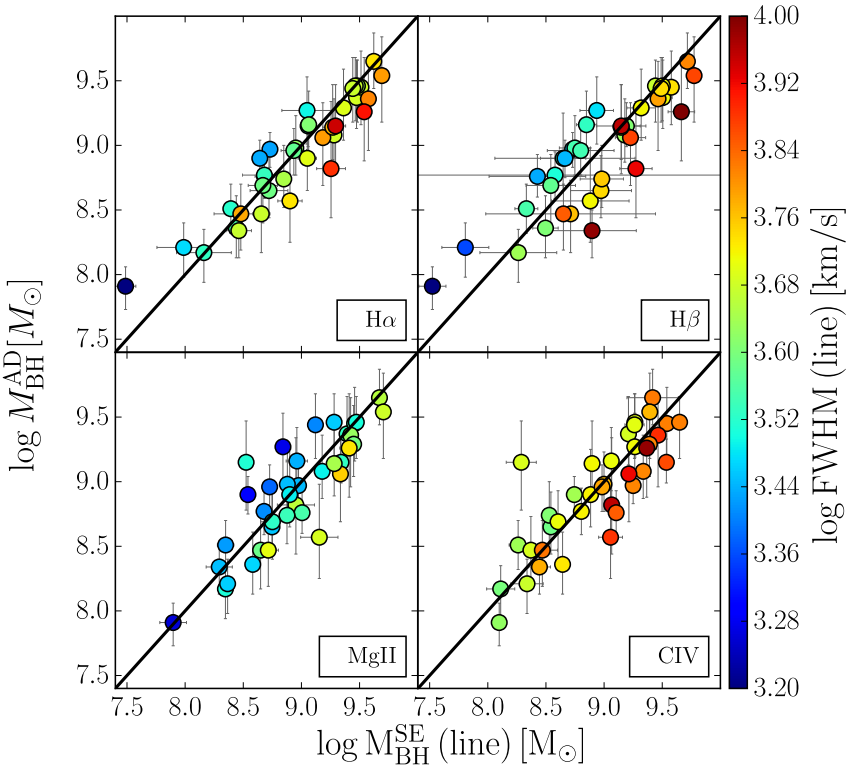

Figure 2.2: BH masses determined from accretion disc SED fitting are on the ordinate axis, and from single-epoch virial (SE) methods on the abscissa. Points are coloured according to the width of the broad line from narrow (blue) to very broad (red). From Mejía-Restrepo et al. (2018).

Mejía-Restrepo et al. (2018) compared masses estimated by accretion disc SED fitting and from single-epoch virial method. They found that a gradient with line width, indicating that for sources with relatively narrow broad lines, the SED fitting method gives a higher mass estimate (see Figure 2.2). They suggested that the orientation of the BLR was driving this effect.

2.1.4.3 Megamasers

A maser (microwave amplification by the stimulated emission of radiation) is the microwave equivalent to an optical laser. In an astrophysical context they are often called megamasers to distinguish them from laboratory masers. Like lasers, they rely on an electronic population inversion (and subsequent coherent radiative de-

excitation) within atoms or molecules; the megamasers around AGN are usually water masers. The light amplification requires a long path length through the maser disc, so the maser emission we observe comes from discs we view nearly edge-on. By tracking the motion of bright maser spots around the disc, a very precise estimate of the BH mass can be made. However, the method is only applicable in the very few systems which are both viewed edge-on and exhibit detectable maser emission. For examples of this technique, see Greenhill et al. 1995, Miyoshi et al. 1995 and Greene et al. 2010a.

2.2 Reddening and absorption

Diffuse dust and gas in interstellar medium (ISM) of the Milky Way can absorb the light of extragalactic sources, complicating our studies of them since we are generally interested in their *intrinsic* emission, rather than simply the light which we can observe. Correcting for the effects of intervening material requires a knowledge of how much 'stuff' there is in the Milky Way along a particular line of sight. Many surveys have been undertaken in different wavebands to map the Milky Way ISM; a few are listed below.

- Radio: cold, neutral Hydrogen emits an emission line with a wavelength of 21 cm via a 'spin-flip' transition in its ground state. By mapping this emission line, radio surveys have been able to trace the distribution of cold gas in the ISM (e.g. Kalberla et al. 2005).

- Infrared: the warm phase of the ISM can be mapped by observing thermal infrared emission from dust (e.g. Schlegel et al. 1998).

- X-ray: The *ROSAT* all-sky survey (Snowden et al. 1997) was able to map the soft X-ray emission of hot gas in the ISM with greater sensitivity and spatial resolution than earlier missions such as SAS 3 (Marshall & Clark 1984). The high resolution of the grating spectrometers onboard the modern X-ray

observatories *Chandra* and *XMM-Newton* have enabled new characterisations of absorption lines and edges imprinted on the spectra of bright, background sources by the intervening ISM (e.g. Paerels et al. 2001, Pinto et al. 2013).

2.2.1 Reddening by dust

The optical and ultraviolet bands are affected by dust, which preferentially scatters away shorter (bluer) wavelengths. The observed spectrum is therefore said to be *reddened*. Reddening is commonly quantified via a colour excess, $E(B-V) = A_B - A_V$, where A_B and A_V are the magnitude extinctions in the B band ($\lambda \approx 4300$ Å) and V band ($\lambda \approx 5500$ Å). The extinction at a given wavelength, A_λ, is often characterised by a reddening curve, dependent on the composition of the scattering medium. For example, Figure 2.3 shows that the Milky Way reddening curve has a strong 'bump' around 2175 Å which is not present in that of the Small Magellanic Cloud; the origin of this 2175 Å feature is not well understood, but it may be caused by graphite grains (Draine 1989). The ratio of total to selective absorption at V,

$$R_V = \frac{A_V}{E(B-V)}, \tag{2.2.1}$$

typically has the value 3.14 ± 0.01 in the Milky Way (Schultz & Wiemer 1975). For a measured $E(B-V)$, A_V can be determined using Equation (2.2.1) and a reddening curve (often normalised to $A_\lambda/A_V = 1$) can be renormalised appropriately. Then the extinction at the wavelength of interest, A_λ, can be computed. The reddening-corrected flux $F_{\rm cor}$ is related to the observed flux $F_{\rm obs}$ by

$$F_{\rm cor} = F_{\rm obs} \times 10^{A_\lambda/2.5}. \tag{2.2.2}$$

In this thesis, the Milky Way curve of Cardelli et al. (1989) is applied to correct for the effects of reddening.

X-ray emission can penetrate dust but is subject to photoelecrtic absorption by gas (see below). The amount of gas is commonly quantified in terms of its neutral

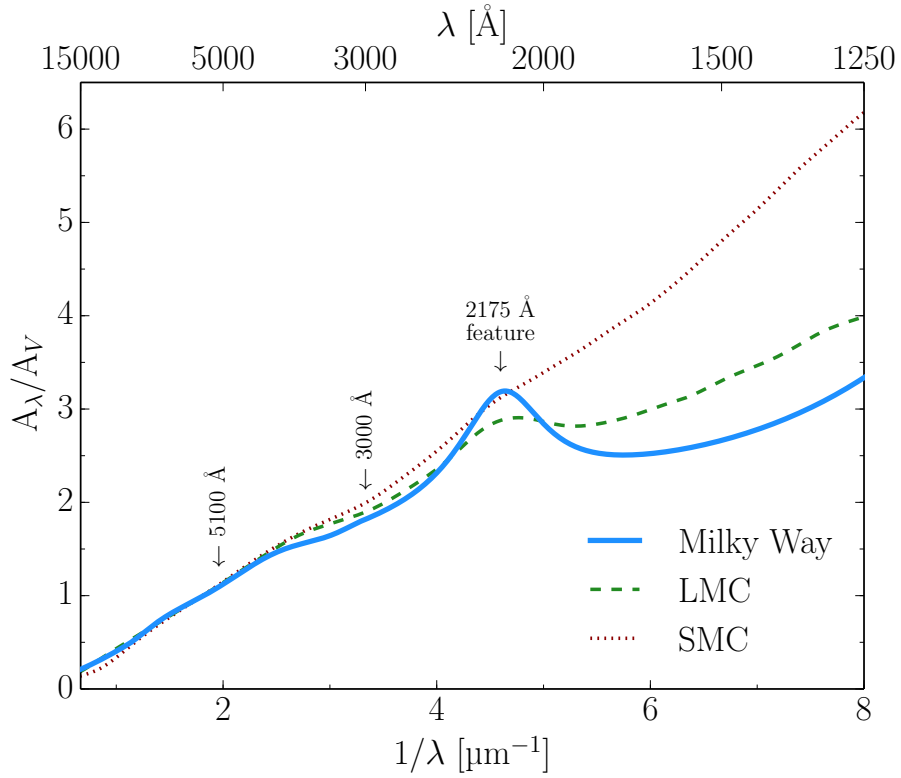

Figure 2.3: A comparison of the Cardelli et al. (1989) Milky Way reddening curve with those of the Large and Small Magellanic Clouds (LMC and SMC), determined by Gordon et al. (2003).

Hydrogen column density $N_{\rm H}$, measured in cm^{-2}, i.e. the surface density of Hydrogen atoms in the column of the line of sight. By studying absorption in the Lyα line along lines of sight to 100 stars, Bohlin et al. (1978) determined the relation

$$\left\langle \frac{N_{\rm H}}{E(B-V)} \right\rangle = 5.8 \times 10^{21} \ \ \text{atoms cm}^{-2}\ \text{mag}^{-1}.$$

Since AGN lie in the centres of other (sometimes very distant) galaxies, the AGN emission may be subject to attenuation in their host galaxy, or intervening galaxies or clouds in the intergalactic medium[3]. Such attenuation can be difficult to correct for, without the detailed mapping and analysis that has been undertaken for the Milky Way.

[3]For example the light from the AGN PKS J1222+0413 studied in Chapter 5 is absorbed by at least two Lyman limit systems on its way to us.

2.2.2 Photoelectric absorption by the interstellar medium

As described above, optical and ultraviolet photons are subject to scattering by dust grains, resulting in a reddening of the transmitted spectrum. Higher-energy X-ray photons ($E \sim 0.1$–10 keV) are not strongly scattered by dust, but may be absorbed by neutral or partially-ionised gas. The photoelectric absorption cross-section scales with the atomic number Z and photon energy E as $\sigma \sim (Z/E)^3$, so absorption is greater for low-energy photons and high-Z elements. Figure 2.4 shows how X-ray transmission increases with energy. Imprinted on the smooth curves are sharp absorption edges, where the photon energy becomes great enough to liberate an electron, leading to an increase in absorption. At very high column densities, Compton scattering becomes important. AGN obscured by a column density $N_{\rm H} \gtrsim 10^{24}$ cm^{-2} are said to be Compton-thick.

The neutral hydrogen column density along the line of sight to the γ-NLS1 1H 0323+342 is relatively high ($N_{\rm H} = 1.46 \times 10^{21}$ cm^{-2}, Dickey & Lockman 1990), which complicates the parameterisation of its soft X-ray spectrum, as I discuss in Chapter 4 and Appendix A.

In this thesis, I use the XSPEC model PHABS to account for the photoelectric absorption of X-rays. The elemental and molecular abundances of the ISM are always set to those determined by Wilms et al. (2000).

2.3 Modelling the accretion flow emission

As discussed in Section 2.2 above, far-ultraviolet and soft X-ray emission from AGN is attenuated by the interstellar medium of the Milky Way. As a result, we are often unable to observe the peak of the AGN SED (see lower panel of Figure 2.5). However, we can place constraints on the amount of unobserved FUV flux by applying an energy-conserving accretion flow model to data sampling either side of the peak of the accretion disc emission (i.e. optical/UV and X-ray data).

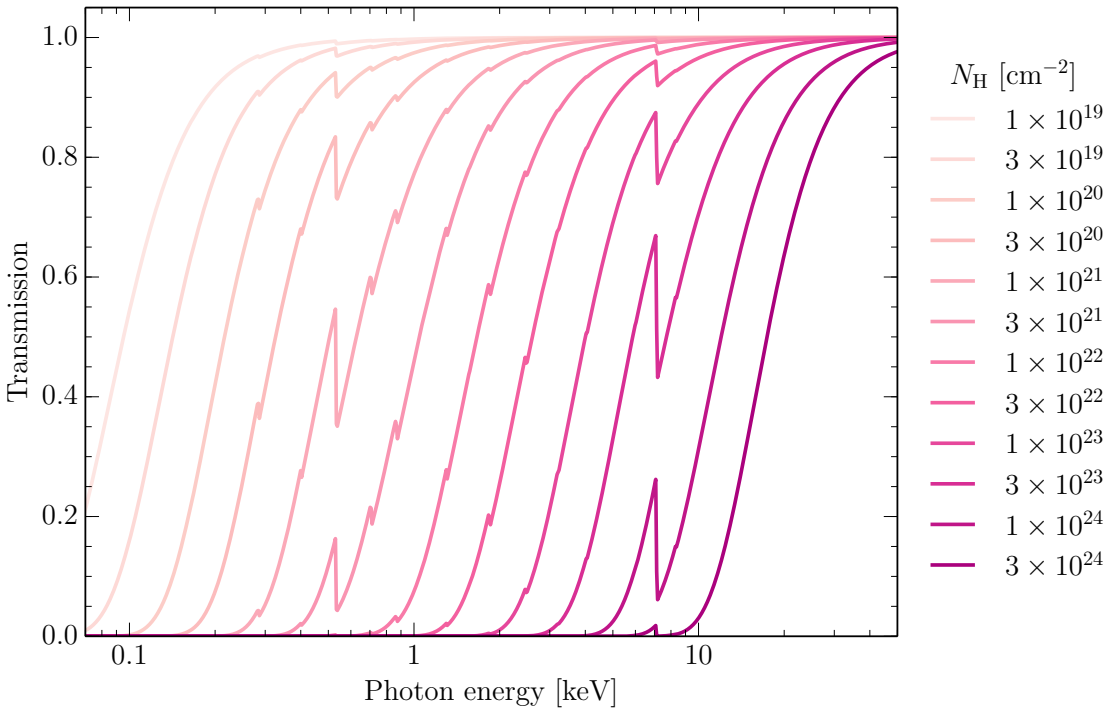

Figure 2.4: The transmission of X-rays as a function of photon energy. The transmission is plotted for various column densities of interstellar gas, ranging from $N_{\rm H} = 1 \times 10^{19}$ to 3×10^{24} cm^{-2}. K-shell absorption edges of O and Fe can be seen at 0.5 and 7.1 keV, respectively. The transmitted fraction of photons is nearly 1 at high energies for the full range of column densities shown. For $N_{\rm H} \gtrsim 1 \times 10^{24}$ cm^{-2} the effects of Compton scattering become important.

Throughout this thesis, I make use of the OPTXCONV model (Done et al. 2013), an extension of the OPTXAGNF model presented by Done et al. (2012). It includes the three principal accretion flow components I described earlier in Sections 1.1.3 and 1.1.4: the accretion disc, X-ray corona and soft X-ray excess. These are illustrated in the cartoon the top panel of Figure 2.5 and an example SED is shown below.

For a given SMBH mass, the accretion rate through the outer disc is determined by the observed near-infrared/optical emission. Assuming energy conservation, this fixes the power output of the inner UV and X-ray emission regions. An accretion disc spectrum is produced by radii between $R_{\rm out}$ and $R_{\rm cor} < R_{\rm out}$, which are free parameters in the model[4]. For radii interior to $R_{\rm cor}$ the remaining accretion power is divided between warm and hot Comptonisation regions. A fraction $f_{\rm pl}$ of this power

[4]Alternatively, it is possible to set the $R_{\rm out}$ disc self-gravity radius, which is recalculated as $\dot{m}$ changes during the fitting procedure.

goes into the corona, producing the power-law X-ray emission and the remainder is available to the warm Comptonisation region which produces the soft X-ray excess. Photons from the accretion disc emitted at $R_{\rm cor}$ provide a source of seed photons which are upscattered in energy in the warm Comptonisation region. This results in a emission hump peaking in the far-UV to soft X-ray band, the spectrum of which is determined by the electron temperature $kT_{\rm e}$ and optical depth τ. In turn, the photons from the warm Comptonisation region are Compton scattered by hot electrons in the corona, producing the X-ray power-law emission of index Γ. In both models, the inner flow radius $R_{\rm in} \equiv R_{\rm isco}$ is set by the free parameter $a_\star$, the dimensionless SMBH spin. However, for high SMBH spins, relativistic effects modify the spectrum and these effects are incorporated into OPTXCONV but not OPTXAGNF. The relativistic effects are inclination-dependent, so OPTXCONV additionally includes the inclination angle of the disc as a free parameter.

For low-mass AGN and high accretion rate systems the inner disc is very hot. As the disc temperature approaches, and exceeds, the hydrogen ionisation energy of 13.7 eV ($\approx 10^5$ K) the abundance of free electrons means that electron scattering processes will dominate over absorption and the disc will not fully thermalise. Both OPTXAGNF and OPTXCONV include a colour-temperature correction, which modifies the output disc spectrum to account for this. These codes therefore have relevance in the modelling of NLS1 spectra, since these sources are low-mass, high accretion rate systems and exhibit prominent soft X-ray excesses. In the case of γ-NLS1s, which possibly have spin-powered jets, the relativistic treatment of OPTXCONV is also relevant.

These models have been tested on small and moderate-sized samples of AGN by Collinson et al. (2015), Collinson et al. (2017) and Jin et al. (2012a).

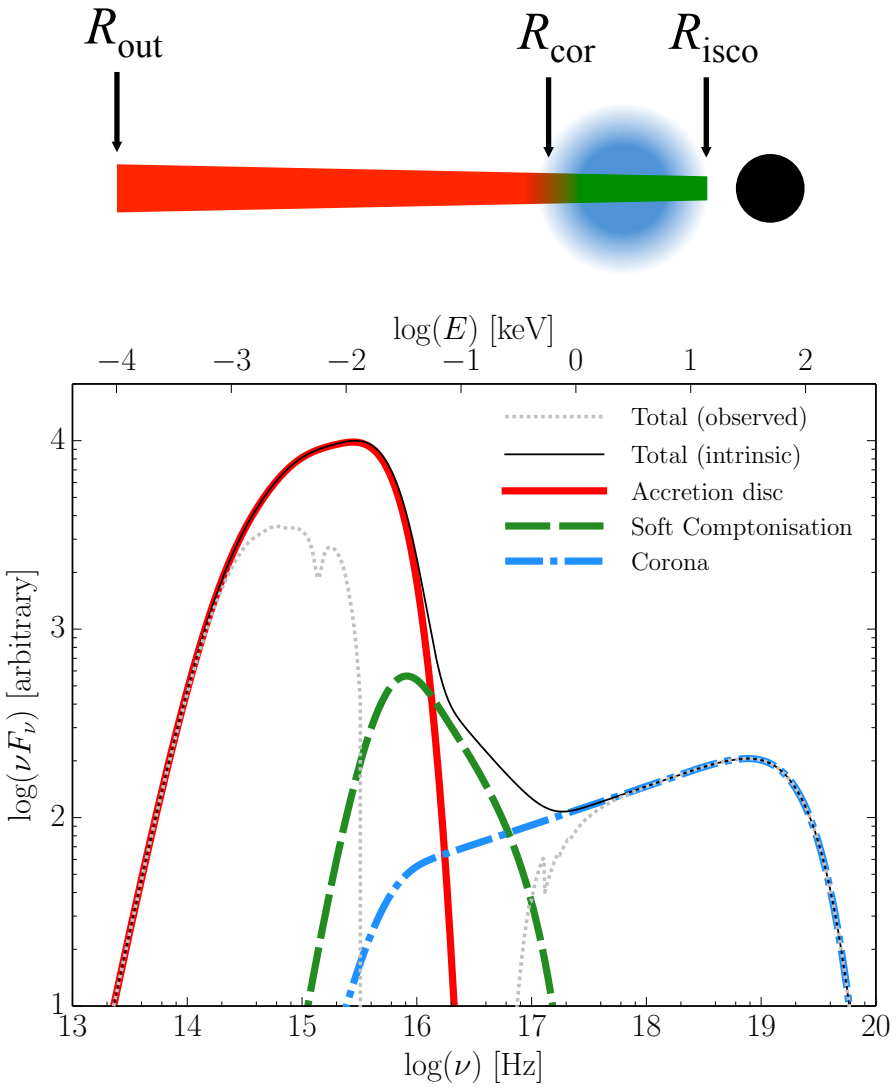

Figure 2.5: The OPTXCONV/OPTXAGNF accretion flow model of Done et al. (2012, 2013). *Top:* Cartoon illustrating the model geometry. A standard accretion disc (red) extends from its outer radius $R_{\rm out}$ down to $R_{\rm cor}$. Interior to $R_{\rm cor}$, the accretion power is divided between a hot, optically thin Comptonising corona (blue) and a cooler, optically thick Comptonising region (green). The accretion flow terminates at $R_{\rm isco}$. *Bottom:* A model SED illustrating the emission from the above components. The grey dotted line shows the flux observed, which is attenuated in the UV/soft X-ray bands by the interstellar medium of the Milky Way.

2.4 Modelling the jet emission

JET is a single-zone leptonic jet emission code and based on the model presented by G&T09 and coded by Gardner & Done (2018). The jet is modelled as a cone with a half opening angle ϕ originating at the SMBH. The jet is viewed by the observer at some angle of inclination i. The model assumes that the jet emission is dominated by radiation from a single spherical 'blob' of radius $R_{\rm diss} = \phi Z_{\rm diss}$ where $Z_{\rm diss}$ is its distance from the SMBH. The jet blob moves with a constant bulk Lorentz factor $\Gamma_{\rm BLF}$. Some fraction

$$P_{\rm rel} = \frac{4\pi}{3} R_{\rm diss}^3 m_{\rm e} c^2 \int_{\gamma_{\rm min}}^{\gamma_{\rm max}} \gamma Q(\gamma)\ {\rm d}\gamma \tag{2.4.1}$$

of the total jet power $P_{\rm j}$ is used to accelerate electrons within the emission region. The accelerated electrons have Lorentz factors between $\gamma_{\rm min}$ and $\gamma_{\rm max}$ and the injected electron population, $Q(\gamma)$, is parameterised as

$$Q(\gamma) = Q_0 \left(\frac{\gamma}{\gamma_{\rm brk}}\right)^{-s_1} \left[1 + \left(\frac{\gamma}{\gamma_{\rm brk}}\right)^{s_2 - s_1}\right]^{-1}, \tag{2.4.2}$$

where s_1 and s_2 are the slopes of the distribution below and above the break Lorentz factor $\gamma_{\rm brk}$, respectively. These electrons then cool by both 'internal' and 'external' mechanisms. The internal processes are the electrons' synchrotron emission (through interaction with the jet's magnetic field) and the Compton upscattering of these synchrotron photons by the electron population which produced them: the sychrotron self-Compton (SSC) process. The 'external Compton' (EC) process cools electrons by the Compton upscattering of photons from the seed photon field external to the jet. External seed photons from regions in front of the jet blob will be Doppler boosted in the jet frame. Equivalently, any seed photons originating behind the jet will be strongly de-boosted. The location of the jet emission region therefore plays an important role in determining the relative energy densities (as seen by the jet) of the different components of the external seed photon field (e.g. the emission from the disc, BLR and torus). The code runs through multiple cooling cycles until the

system reaches a steady state. The highest-energy electrons cool fastest and the steady-state distribution is found by calculating the Lorentz factor $\gamma_{\rm cool}$ of electrons that can just cool in the light-crossing time of the emission region and requiring this match the injected distribution below $\gamma_{\rm cool}$.

Finally, the code calculates the observed frame emission which is boosted and blue-shifted relative to the jet frame emission due to the bulk motion of the emitting plasma within the jet flow. The observed emission from a region moving with velocity $\beta = v/c$ is a factor δ^3 greater than the intrinsic emission where the Doppler factor $\delta = (\Gamma_{\rm BLF}[1 - \beta \cos i])^{-1}$. The code also outputs the calculated total jet power $P_{\rm j} = P_{\rm rad} + P_{\rm e} + P_B + P_{\rm p}$ which is the sum of the radiative power ($P_{\rm rad}$), the power in the bulk motions of electrons ($P_{\rm e}$) and protons ($P_{\rm p}$) and the Poynting power (P_B).

Chapter 3

Astronomical facilities and surveys

This thesis makes use of multiwavelength data from many different facilities and surveys operating in diverse wavebands across the full electromagnetic spectrum. This chapter presents a brief historical and technical overview of some of the key facilities used.

3.1 Radio to sub-mm

Quasars were first discovered as a result of their detection in the first radio sky surveys in the 1950s (e.g. the third Cambridge radio survey, '3C' Edge et al. 1959). Although all AGN are radio emitters, high radio-loudness is an indicator of the presence of a powerful jet in a fraction of AGN (but see Padovani 2017).

3.1.1 NVSS

NVSS (Condon et al. 1998) is the NRAO (National Radio Astronomy Observatory) VLA (Very Large Array) Sky Survey. Between 1993 and 1997 NVSS mapped the entire sky North of $\delta = -10^{\circ}$ at 20 cm (1.4 GHz) using the VLA, which is situated in New Mexico, USA.

3.1.2 FIRST

FIRST (Becker et al. 1995) captured Faint Images of the Radio Sky at Twenty-cm, also using the VLA, between 1993 and 2011. FIRST had far superior spatial resolution to NVSS (it had a beam size of 5.4 arcseconds compared with the 45 arcsecond beam used by NVSS); it therefore resolved small-scale structures and had much better astrometric accuracy. However, its fluxes for extended sources may be underestimated. FIRST was designed to overlap in sky coverage with the Sloan Digital Sky Survey (which conducts photometric and spectroscoptic observations in the optical band - see Section 3.3.1), and covered $\sim$ 1/4 of the sky around the North Galactic cap. Whilst early radio observations of Palomar Green (PG) quasars indicated an apparent bimodality in AGN radio-loudness (Kellermann et al. 1989), studies of the FIRST data suggest instead that AGN have a continuous distribution of radio-loudness (White et al. 2000).

3.1.3 Effelsberg

The Effelsberg 100 m Radio Telescope is located in Bad Münstereifel, Germany and is operated by the Max Planck Institute for Radio Astronomy. Observations began 1972 and for many years Effelsberg was the largest steerable radio telescope on Earth. This posed significant technical challenges because the dish would deform under its own weight when rotated. Effelsberg has a complex computer-controlled mirror support system to deform the dish into the correct parabolic shape to focus radio waves. The telescope operates at frequencies 0.395–95.5 GHz and has a 1.15 arcminute beam size at 10 GHz.

3.1.4 Planck

Planck was an ESA satellite mission which operated between 2009 and 2013 (Planck Collaboration et al. 2011). The main objective of the mission was to map and measure

the spatial anisotropies in the temperature of the Cosmic Microwave Background (CMB). It produced a high-resolution image of the entire microwave sky. A key result was the precise determination of the Hubble constant, $H_0 = 67.9 \pm 0.9$ km s^{-1} Mpc^{-1} (Planck Collaboration et al. 2016a).

The satellite carried two scientific instruments: a Low Frequency Instrument (covering the bands 30, 44 and 70 GHz) and a High Frequency Instrument (covering six bands between 100 and 857 GHz).

3.2 Infrared

Most infrared emission is absorbed by molecules in the Earth's atmosphere although there are some limited bands of high transmission between absorption features (mostly due to H_2O, CO_2 and CH_4 molecules). The near-infrared J, H and K bands are designed to avoid these absorption features. One of the challenges of infrared astronomy is to limit noise resulting from the thermal emission of the detectors. To avoid this noise, the detectors must be cooled to low temperatures using cryogens. For space-based infrared observatories, finite supplies of onboard coolant limit the useful lifetime of some instruments.

3.2.1 WISE

The *Wide-field Infrared Survey Explorer* (*WISE*; Wright et al. 2010) space telescope was launched in December 2009 with the aim of conducting an all-sky survey in the infrared. It observes in four photometric bands simultaneously: W1 (3.4 µm), W2 (4.6 µm), W3 (12 µm) and W4 (22 µm). Its hydrogen coolant was depleted in October 2010, so observations in the W3 and W4 bands became impossible. *WISE* operations were extended for four months to look for near-Earth objects such as asteroids as part of the Near-Earth Object *WISE* (*NEOWISE*) mission. Following its brief extension, *WISE* was placed into hibernation in February 2011. NASA

decided to reactive *WISE* in late 2013 to continue with *NEOWISE*, which is ongoing. *WISE*'s 22-month hibernation explains the gap in the infrared lightcurve of the 'Big Dipper' shown in Figure 6.1.

3.2.2 2MASS

The Two-micron All Sky Survey (2MASS: Skrutskie et al. 2006) was a ground-based infrared survey conducted between 1997–2001, using two 1.3 m telescopes. In the Northern Hemisphere, observations were made with the Fred Lawrence Whipple Observatory on Mount Hopkins, Arizona in the United States and in the Southern Hermisphere, the Cerro Tololo Inter-American Observatory in Chile was used. 2MASS made observations in the near-infrared J (1.2 µm), H (1.6 µm) and K (2.2 µm) bands (see Figure 3.2).

3.2.3 UKIDDS

The UKIRT (United Kingdom Infrared Telescope) Infrared Deep Sky Survey (UKIDDS: Lawrence et al. 2007) began in 2005 as a successor to 2MASS, surveying the sky in the near-infrared. UKIRT is a 3.8 m telescope situated on Mauna Kea in Hawaii.

3.2.4 Gemini

The Gemini observatory consists of two optical/infrared 8.1 m telescopes. Gemini North is located on Mauna Kea in Hawaii and Gemini South is located on Cerro Pachón in Chile. In Chapter 4 I use the infrared spectrum of the source 1H 0323+342 obtained using the Gemini North InfraRed Spectrograph (GNIRS, Elias et al. 2006). GNIRS was used in cross-dispersing mode, which gave wide wavelength coverage (0.9–2.5 µm), but which necessitated the use of a short slit to prevent inter-order contamination.

3.2.5 Spitzer

The *Spitzer Space Telescope* (Werner et al. 2004) launched in August 2003 and is still operational at the time of writing. *Spitzer* carries three scientific instruments. Its Infrared Array Camera (IRAC) images simultaneously at the wavelengths 3.6, 4.5, 5.8 and 8 µm; the Infrared Spectrograph (IRS) covers the wavelength range between ≈ 5–40 µm; the Multiband Imaging Photometer (MIPS) contains three arrays operating at 24 µm, 70 µm and 160 µm. *Spitzer*'s cryogen ran out in 2009 and since then it has been conducting its 'warm mission' using only the IRAC 3.6 and 4.5 µm bands. Science with the telescope is due to end on 30 January 2020.

3.3 Optical and ultraviolet

Astronomy in the optical band is the oldest form of astronomy, arguably beginning when the first humans looked up at the night sky. The Italian Galileo Galilei (1564–1642) is often cited as the father of observational astronomy; being the first person to use a telescope for astronomical purposes. The small, early telescopes used by Galileo used glass lenses to focus light. Large telescopes must make use of focussing mirrors in order to avoid the effects of chromatic aberration. The largest single-aperture telescope is currently the Gran Telescopio Canarias ('GranTeCan') on La Palma in the Canary Islands, which has a 10.4 m diameter mirror. This will be surpassed by the next generation of facilities such as the 39.3 m Extremely Large Telescope, now under construction in Chile, with first light expected in 2025. The optical band extends from ≈ 4000–7000 Å and some ground-based telescopes are capable of observing beyond this, into the infrared and near-ultraviolet. The Earth's atmosphere becomes opaque in the ultraviolet band so observations at short ultraviolet wavelengths must made from space with satellites such as *GALEX*.

Table 3.1: SDSS spectrograph parameters

	SDSS	BOSS
Fibres per plate	640	1000
Fibres diameter	3 arcsec	2 arcsec
Wavelength coverage	3800–9200 Å	3630–10400 Å
Spectral resolution	1500 at 3800 Å, 2500 at 9000 Å	

3.3.1 Sloan Digital Sky Survey

The Sloan Digital Sky Survey (SDSS: York et al. 2000) is an ambitious project to map one quarter of the Northern sky. It uses a 2.5 m optical telescope at Apache Point Observatory in the state of New Mexico in the United States. It was the first large survey to use digital detectors (charge-coupled devices: CCDs); earlier surveys relied on photographic plates.

Multicolour images of the sky were made as part of the first phase of SDSS (2000–2005). The photometric filters used for SDSS imaging are illustrated in Figure 3.2. From these images, and other multifrequency catalogues, interesting targets were chosen for spectroscopic follow-up. SDSS can record the spectra of multiple sources in a single pointing of the telescope. The positions of targets of interest are drilled into aluminium plates, which have a 3° diameter on the sky. The plate is then plugged with optical fibres. When observing, light is directed through the fibres, separated by dichroics into red and blue bands, and directed to the spectrograph CCD cameras. The SDSS can therefore obtain the spectra of hundreds of sources in a ≈ 45 minute observation. The parameters of the original SDSS spectrograph, and that of the current Baryon Oscillation Spectroscopic Survey (BOSS) spectrograph are listed in Table 3.1.

3.3.2 Pan-STARRS

Pan-STARRS is the Panoramic Survey Telescope and Rapid Response System (Chambers et al. 2016, Flewelling et al. 2016). The PanSTARRS-1 (PS1) 3π Survey

was conducted between 2009 and 2014, observing the ¾ of the sky north of $\delta = -30°$ multiple times per year in each of five filters (see Magnier et al. 2013 and Chambers et al. 2016).

3.3.3 William Herschel Telescope

The William Herschel Telescope (WHT) is a 4.2 m optical/near-infrared telescope, part of the Isaac Newton Group of Telescopes located at the Observatorio del Roque de los Muchachos on the island of La Palma in the Canary Islands. The telescope was built by Grubb Parsons, Newcastle-upon-Tyne, with construction beginning in 1983. The WHT was the last telescope to be built by Grubb Parsons, which ceased trading in 1985, 150 years after its founding. The company's contribution to astronomy is honoured to this day in the form of an annual lecture series on astronomical instruments at Durham University. Assembly of the WHT on La Palma was completed in early 1987 and it has been operational since June of that year.

In the summer of 2016 I spent two nights observing at the WHT, obtaining spectra of variable AGN using the Intermediate-dispersion Spectrograph and Imaging System (ISIS). ISIS is a medium-resolution double spectrograph used for long slit spectroscopy. Its dichroic filters permit simultaneous observations in the blue and red arms, each optimised for their particular wavelength range. In Chapter 6, I analyse eleven spectra of the AGN SDSS J2232−0806 which were recorded at the WHT over several years.

3.3.4 Liverpool Telescope

The Liverpool Telescope (LT: Steele et al. 2004) is a fully-robotic 2 m optical telescope owned by Liverpool John Moores University and situated at the Roque de los Muchachos Observatory on La Palma, where its operations began in 2004. As well as imaging cameras, the LT instrument suite also contains spectrographs and a

Figure 3.1: The Milky Way behind the William Herschel Telescope, 31 May 2016.

polarimeter. From a bank of approved targets, the telescope's robotic control system autonomously decides its observing strategy, based on the current target visibility and local weather conditions. In Chapter 6, I use photometric data recorded with the LT's RATCam and IO:O (Infared-Optical:Optical) cameras. The filter wheel for these cameras includes five filters matching the SDSS photometric bands (u, g, r, i, z).

3.3.5 MMT

The MMT Observatory is a single-mirror 6.5 m optical telescope situated on Mount Hopkins, Arizona in the United States. The current telescope replaced the original Multiple Mirror Telescope (MMT, which consisted of six smaller mirrors) in 1998.

3.3.6 Keck

The Keck Observatory consists of two 10 m optical telescopes situated near the summit of Mauna Kea in Hawaii. Science observations with Keck I began in 1993, and Keck II came online in 1996. Each of the two 10 m mirrors are composed of

36 hexagonal segments working in tandem. In Chapter 4 I make use of an optical spectrum obtained using the Low Resolution Imaging Spectrometer (LIRS; Oke et al. 1995), which operates at the focus of Keck I. As with the WHT, the spectrograph uses dichroic beamsplitters to direct light into blue and red arms of the detector.

3.3.7 Very Large Telescope

The Very Large Telescope (VLT, Enard 1989) is an ESO facility situated on Cerro Paranal in Chile. The VLT comprises four 8.2 m Unit Telescopes (UTs) which generally operate independently. Alternatively, the Very Large Telescope Interferometer (VLTI) can use the four UTs together (complemented by four, movable, 1.8 m Auxilliary Telescopes) to study bright objects with very high spatial resolution (∼milli-arcsecond). UT1 achieved first light in May 1998 and the completed telescope became fully operational in 2000.

Using the VLT, Gravity Collaboration et al. (2018) tracked the motion of the star S2 as it orbited the supermassive black hole at the centre of the Milky Way. They were able to detect the effects of Special and General Relativity due to the extreme gravity of the black hole.

I have obtained several spectra of five γ-ray emitting narrow-line Seyfert 1 galaxies using the X-shooter spectrograph on UT2. X-shooter is a multi-wavelength, medium resolution spectrograph which contains three arms (near-infrared, optical and ultraviolet) each with its own bespoke slits, optics and detectors. Each of the three arms is an independent cross-disperesed éschelle spectrograph; these operate simultaneously give very wide-range spectral coverage (300-2500 nm) of individual sources. I present the X-shooter spectrum of the γ-ray emitting narrow-line Seyfert 1 PKS J1222+0413 in Chapter 5.

3.3.8 Hubble Space Telescope

The *Hubble Space Telescope* (*HST*) is the world-famous NASA space-based telescope, launched in 1990 and still operational. It has observing capabilities in the near-infrared, optical and ultraviolet. Because the telescope is in low-Earth orbit, it is possible to service, and replace retired instruments with new ones. Infamously, an error made manufacturing *Hubble*'s mirror meant the telescope had to be fitted with 'spectacles' in 1993. In 2009, astronauts flew to *Hubble* on the space shuttle *Atlantis* and installed two new instruments, the Cosmic Origins Spectrograph (COS, Sahnow et al. 2010) and the third Wide Field Camera (WFC3, MacKenty et al. 2008), both of which are still in use. The COS has moderate spectral resolution at near- and far-ultraviolet wavelengths ≈ 90–320 nm and WFC3 is *Hubble*'s current primary imaging instrument.

Construction of the successor to *Hubble*, the *James Webb Space Telescope*, was completed in 2016 and the telescope is currently undergoing extensive testing with launch scheduled for 2021, following many delays. The *JWST* will observe at longer wavelengths than *Hubble* (≈ 0.6–27 µm), allowing it to study faint sources at higher redshift.

3.3.9 GALEX

NASA's *Galaxy Evolution Explorer* (*GALEX*; Martin et al. 2005) was a dedicated UV space telescope which launched in April 2003 and operated for ten years. Its telescope had a 50 cm-diameter and a field of view of 1.2°. It observed in two broad bands: the far-ultraviolet (FUV) ≈ 134–180 nm and near-ultraviolet (NUV) ≈ 169–300 nm. The filters are illustrated in Figure 3.2.

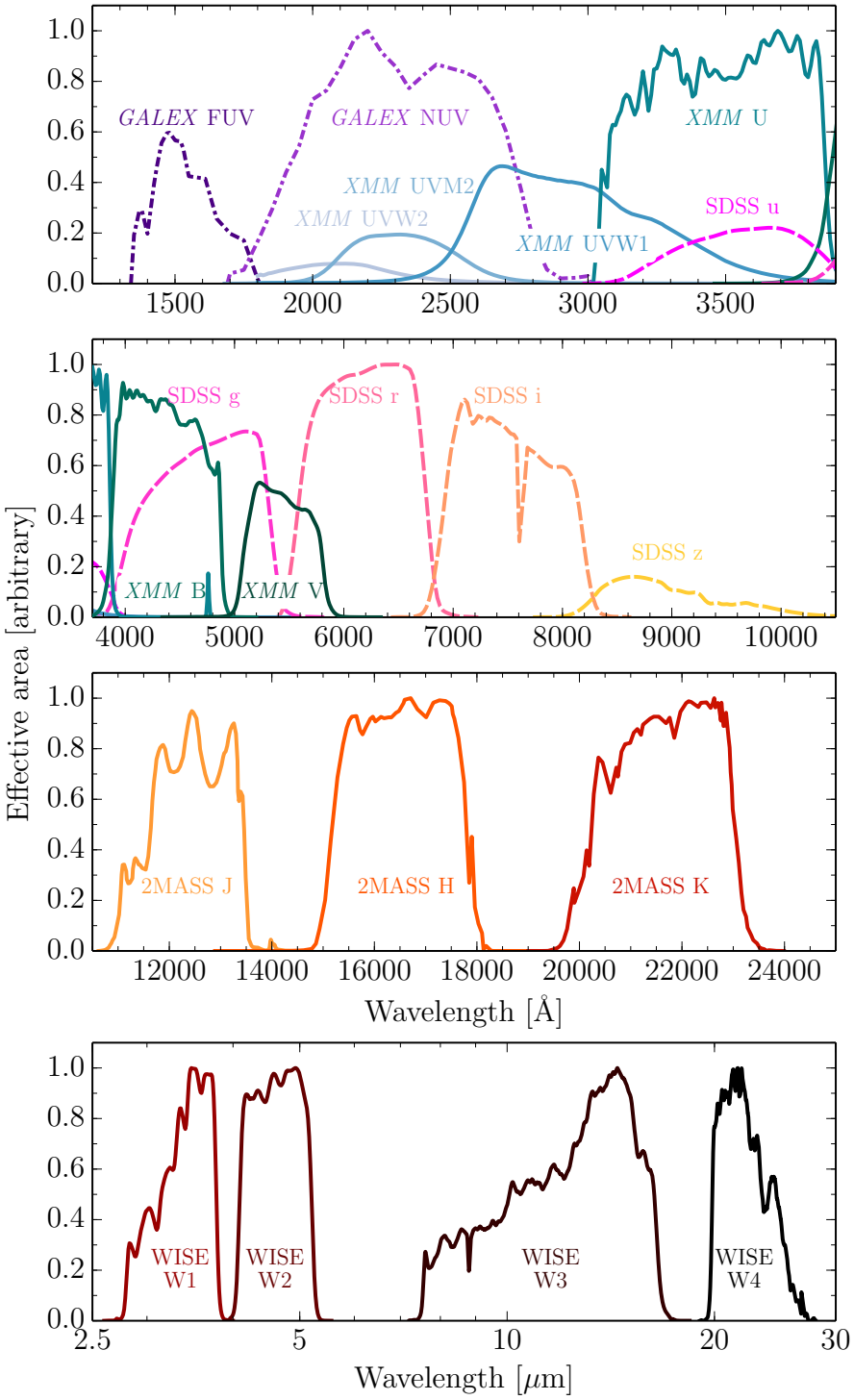

Figure 3.2: Normalised effective areas of key ultraviolet to mid-infrared instruments in the photometric bands used in this thesis. This plot illustrates the breadth of the wavelength coverage of each band and the relative sensitivity of instruments to different wavelengths.

Figure 3.3: High-energy observatories. *Clockwise from top left: XMM-Newton*, *NuSTAR*, *Fermi*, *Swift*.

3.4 X-ray

The Earth's atmosphere is largely opaque to X-rays, therefore telescopes observing in this waveband must be put into space. Early astronomical X-ray observations were made with detectors borne by rockets (e.g. Giacconi et al. 1962) and balloons (e.g. Clark 1965). Intending to study the X-ray flux from the Moon, Giacconi et al. (1962) instead discovered a bright, point-like source of X-rays likely situated outside of the Solar System. We now know this source to be the low-mass X-ray binary Scorpius X1. The discovery of extrasolar X-ray sources invigorated interest in the field. Modern X-ray astronomy utilises detectors onboard orbiting observatories, the first of which was the *Uhuru* satellite, launched on 12 December 1970 (Jagoda et al. 1972).

3.4.1 ROSAT

The *Röntgensatellit* (*ROSAT*) was a German-led X-ray mission, operated in partnership with NASA and was launched on 1 June 1990. It had a large field of view (2°) and conducted an all-sky survey during its first six months of operation (Voges

et al. 1999). The mission ended on 12 February 1999 and the satellite was destroyed on 23 October 2011 when it re-entered the Earth's atmosphere. *ROSAT* was designed for high sensitivity at low photon energies. Its X-ray detectors were position-sensitive proportional counters (PSPCs, Briel & Pfeffermann 1986) with which *ROSAT* conducted its all-sky survey. A proportional counter contains gas which reacts with X-rays. X-ray photons ionise atoms in the gas and the liberated electrons are driven towards the detector by an electric field applied across the ionisation chamber. The electronics in the detector are tuned to a region in which the response of the detector is proportional to the energy of the ionising photon. In addition to the PSPCs, the satellite also carried a High Resolution Imager (HRI) and extreme-UV Wide Field Camera (WFC). Among the successes of the *ROSAT* mission were the parameterisation of the 'soft X-ray excess' in active galactic nuclei (e.g. Boller et al. 1997).

3.4.2 XMM-Newton

The European Space Agency's X-ray Multi-Mirror Mission, *XMM-Newton* (Jansen et al. 2001), launched on 10 December 1999. The satellite was placed on a highly eccentric orbit ($e \approx 0.8$), with a perigee and apogee of 7000 and 114000 km, respectively in December 1999. This orbit has a long period of approximately 48 hours. The eccentricity of the orbit means that the satellite spends most of its time outside of the Van Allen radiation belts (which could damage the equipment) and allows for long, continuous observations. Science operations with *XMM-Newton* began on 1 June 2000, and are ongoing at the time of writing (spring 2019).

The satellite carries three European Photon Imaging Camera (EPIC) detectors (Turner et al. 2001, Strüder et al. 2001) and two reflection grating spectrometer (RGS: den Herder et al. 2001) modules which simultaneously conduct X-ray imaging and spectroscopy. *XMM-Newton* was designed for high-throughput X-ray spectroscopy and has three large X-ray telescopes to maximise photon collection. The X-ray

telescopes consist of a set of 58 nested mirrors with a large total collecting area. One of the telescopes is dedicated to the EPIC-pn detector; light from the other two telescopes is split between EPIC-MOS and RGS detectors. The EPIC detectors have moderate spatial (PSF FWHM $\approx$ 6 arcsec) and spectral ($E/\Delta E \approx$ 20–50) resolution, primarily in the energy range 0.1–10 keV. The RGS is capable of high-resolution spectroscopy ($E/\Delta E \approx$ 200–800), but limited to the soft X-ray band 0.35–2.5 keV (5–35 Å) and small field of view $\approx$ 5 arcminutes.

Modern X-ray observatories such as *XMM-Newton*, *Swift* and *NuSTAR* all use CCDs rather than PCs to detect X-rays. CCDs are able to make more accurate determinations of photon energies than PCs, but because CCD chips are small compared to the ionisation chambers of PCs, they have a smaller collecting area and field of view. CCDs are composed of silicon semiconductors; the energies of X-ray photons are sufficiently high to promote many electrons across the silicon band gap. The charge created is stored in capacitive bins until the frame is read out to the detector. The charge in each row of pixels is shuffled along to the read-out node on one side of the CCD chip. The detector then records the energy (from the charge), position (from the pixel number) and arrival time of the X-ray photons in the frame, assuming that only one (or zero) photons struck each pixel. If the time between read outs is too long compared with the arrival rate of X-ray photons, then two or more photons may 'pile-up' in a single pixel in that frame. If pile-up is not recognised and addressed in the data analysis then the resulting energy spectrum will be distorted. Another problem caused by bright sources is the arrival of photons during readout, which can create streaks across the X-ray image. Because the detectors are sensitive to infrared, optical and ultraviolet light as well as X-rays, blocking filters must be used if a very bright optical source is in the same field of view as the X-ray source of interest.

Because CCD X-ray detectors record the energy, position and arrival time of incoming X-ray photons, the subsequent analysis can be very versatile. Time-resolved, spatially-resolved, or energy-resolved analyses are all possible. I conduct a spectral-

timing analysis of X-ray data from the source 1H 0323+342 in Chapter 4.

The EPIC detectors have a relatively large field of view of ≈ 30 arcminutes. Consequently, for each pointing, as well as the proposed science target XMM-Newton typically detects around 70 other X-ray sources in the field serendipitously. I make use of the Serendipitous Source Catalogue in Chapter C.

XMM-Newton also carries a small (30 cm) optical/ultraviolet telescope: the Optical Monitor (OM, Mason et al. 2001). The OM has a smaller field of view than the X-ray telescopes (17 arcminutes) but better spatial resolution (≈ 1 arcsecond). The OM operates concurrently with the X-ray detectors and can cycle through six filters covering optical/UV wavelengths. The wavelength coverage of the filters and the normalised effective areas in these photometric bands are illustrated in Figure 3.2.

3.4.3 Neil Gehrels Swift Observatory

The *Swift* Gamma-Ray Burst Mission (Gehrels et al. 2004) was declared operational on 1 February 2005, following the satellite's launch on 20 November 2004. It was designed as a rapid-slewing observatory able to record the afterglow of highly energetic transient events such as gamma-ray bursts (GRBs), which last only fractions of a second to a few hours. After Principal Investigator Neil Gehrels' death in 2017, on 10 January 2018 the satellite was renamed the *Neil Gehrels Swift Observatory* in his honour.

The X-ray Telescope (XRT; Burrows et al. 2000) and Ultraviolet Optical Telescope (UVOT; Roming et al. 2005) were made from *XMM-Newton* flight spares. Improvements in technology and experience from the in-flight operation of *XMM-Newton* allowed for some upgrades to be made to the UVOT. A new mirror coating and improved anti-contamination controls give the UVOT superior sensitivity over the OM, particularly in the ultraviolet. The XRT uses a set of 12 nested mirrors to focus X-rays onto an EPIC-MOS detector. Although the XRT uses a similar detector to *XMM-Newton* it is much less sensitive, as a result of its much smaller effective area.

The Burst Alert Telescope (BAT; Barthelmy et al. 2005) is a hard X-ray instrument, purpose-built for the *Swift* mission. It is capable of recording high-energy photons in the range 15–150 keV. It has a very large field of view of 1.4 str (≈ 10 per cent of the sky), minimising the risk that it misses a high-energy transient.

3.4.4 NuSTAR

NuSTAR is the *Nuclear Spectroscopic Telescope Array* (Harrison et al. 2010) which was launched on 13 June 2012. Unlike *XMM-Newton*, *NuSTAR* is in low-Earth orbit, with a period of approximately 97 minutes. Consequently, long observations of sources are broken up into smaller exposures because of Earth occultations.

NuSTAR has two focal-plane X-ray detectors (Focal Plane Modules A and B) which have sensitivity over the 3–79 keV energy range. Its field of view is ≈ 12 arcminutes, reducing to 6 arcminutes at 68 keV. *NuSTAR*'s angular resolution is not as good as *XMM-Newton* and *Swift*, its PSF FWHM being ≈ 18 arcsec. The X-ray instruments have a long focal length of 10 m, so *NuSTAR* was built with a long, deployable mast to achieve this (see Figure 3.3).

The *Swift* telescope performs a short, 'snapshot' observation (≈ 2 ks) to complement pointed *NuSTAR* observations with soft X-ray and UV data.

3.5 Gamma-ray

3.5.1 Fermi

The *Fermi Gamma-Ray Space Telescope* (*Fermi*) is capable of detecting γ-rays in the energy range 20 MeV to 300 GeV. The satellite was launched on 2008 June 11 and was placed in low-Earth orbit. Its primary instrument is the Large Area Telescope (LAT, Atwood et al. 2009). The LAT has a very large field of view - 2.4 str (≈ 20 per cent of the sky). It is therefore very efficient in making maps of

the γ-ray sky. *Fermi* usually operates in sky survey mode and sweeps the entire sky once every three hours. However, in the event of of an exciting astrophysical event (such as a γ-ray burst or blazar flare), it can be quickly repointed to record the phenomenon of interest. Co-ordinated observations with other satellites (e.g. *Swift*) and ground-based facilities can provide a wealth of multiwavelength information on high-energy transient events.

The LAT is a pair-conversion device which, unlike most other telescopes, does not attempt to focus light onto a detector, but rather measures the paths and energies of particles produced by high-energy photons. When incoming γ-ray interacts with a tungsten atom in a thin foil within the detector it is converted into an electron-positron pair. The motion of these charged particles through the detector is tracked by layers of silicon strips. The direction of the γ-ray can be determined by extrapolating back from the paths of the electron and positron through the tracker. Eventually, the electron and positron strike the calorimeter at the bottom of the LAT, allowing the energy of the initial γ-ray photon to be inferred. An anticoincidence detector on the outside of the LAT enables a rejection of any signals from cosmic ray hits, since charged particles in cosmic rays trigger the anticoincidence detector and photons do not.

The *Fermi* source list from the first eight years of operation contains 5524 γ-ray sources, of which 3091 have been classified. Of the classified sources, 1030 (33%) are BL Lacs, 660 (21%) are FSRQs and 9 are narrow-line Seyfert 1s. A further 1234 (40%) are blazar candidates of uncertain type. *Fermi* has shown that the γ-ray sky is dominated by the emission from blazars.

3.5.2 Cherenkov Telescope Array

When γ-rays strike the Earth's atmosphere they cause a cascade of subatomic particles. Some of these particles travel faster than the speed of light in air and consequently emit Cherenkov radiation (analogous to the 'sonic boom' of objects

travelling faster than the speed of sound). It is these faint flashes of blue light which are detected by Cherenkov telescopes and used to determine the energy and direction of the incident γ-ray.

The Cherenkov Telescope Array (CTA) comprises two ground-based telescope arrays capable of detecting very high energy γ-rays (20 GeV to 300 TeV). The Northern hemisphere site is at the Roque de los Muchachos Observatory in La Palma and the Southern hemisphere site is at the European Southern Observatory (ESO) on Cerro Paranal in Chile. The arrays consist of three different sizes of telescope which give sensitivity in different energy bands. 4 large telescopes (23 m diameter) at each site provide sensitivity in the low energy range, 20 GeV–150 GeV. 40 medium-sized telescopes (12 m) shared between the two sites will provide coverage in the core energy range of 150 GeV–5 TeV. The array of 70 small-sized telescopes (4 m) will be installed at the Southern Site only and give sensitivity to the highest energies (5–300 TeV). Construction is currently planned to be completed in 2025, although preliminary science may be conducted as early as 2023, using only part of the array (CTA Consortium & Ong 2019).

Chapter 4

The γ-ray emitting narrow-line Seyfert 1 1H 0323+342

γ-ray emitting narrow-line Seyfert 1 galaxies (γ-NLS1s) are a very rare class of blazar-like AGN with powerful relativistic jets. Unlike the vast majority of blazars (BL Lacertae objects: 'BL Lacs' and flat spectrum radio quasars: 'FSRQs'), γ-NLS1s have been found to have low supermassive black hole (SMBH) masses and high accretion rates. It has been shown that blazar jet and accretion flow powers are well-correlated, so there must be some connection between the accretion and ejection process within blazars. The γ-NLS1s therefore provide us with the opportunity to investigate this connection at much lower SMBH masses and higher accretion rates than the general blazar population. This is important because it is still poorly understood how jets are launched and powered and why some AGN have powerful jets whereas the majority do not.

In this chapter, I present a case study of the source 1H 0323+342 which is currently the nearest γ-NLS1. This source a superb laboratory in which to explore the disc-jet connection. It has been extensively studied in the literature and has an extremely well-sampled multiwavelength data set which I exploit to model the ambient photon field produced by the accretion flow. I self-consistently apply this within a jet emission model to fit the entire broadband spectrum. I explore its mutliwavelength

properties and discuss the nature of the source as both a NLS1 and a blazar. I test simple scaling relations to examine whether this source can be interpreted as a 'mini-FSRQ': a typical blazar, but with much lower SMBH mass.

4.1 Introduction

The detection of several radio-loud narrow-line Seyfert 1 (NLS1) galaxies by the *Fermi Gamma-Ray Space Telescope* hints at the existence of a rare, new class of γ-ray emitting active galactic nuclei with low SMBH masses. Like FSRQs, their γ-ray emission is thought to be produced via the external Compton mechanism whereby relativistic jet electrons upscatter a photon field external to the jet, e.g. from the accretion disc, broad line region (BLR) and dusty torus, to higher energies. Unlike FSRQs, which have high-mass SMBHs with $\log(M_{\rm BH}/{\rm M}_\odot) \approx 8$–10, NLS1s are powered by accretion onto a SMBH of much lower mass (Abdo et al. 2009b; Foschini 2011).

The mechanisms by which relativisitic jets are launched and accelerated remain poorly understood. However, these γ-NLS1s can provide new insights on how these processes might scale with BH mass. In terms of AGN unification schemes it is insightful to investigate whether γ-NLS1s represent the low-mass, low-power tail of FSRQs in this sequence, or whether they constitute a genuinely new class of their own.

In this chapter I present a detailed study of the nearest γ-NLS1, 1H 0323+342[1] (RA: 03 24 41.16, Dec: +34 10 45.8), at a redshift of $z = 0.0625$ (Landt et al. 2017). High-energy γ-ray emission has been associated with its radio counterpart with high significance, and was first reported by Abdo et al. (2009b).

I assemble an unprecedentedly well-sampled SED containing several relatively high S/N spectra as well as complementary photometry. SEDs for this object have

[1]The J2000 name of this source, J0324+3410, is used in some papers.

previously been presented in e.g. Abdo et al. (2009b), Paliya et al. (2014) and Yao et al. (2015a), but here I include much more spectral and photometric data to assemble a more detailed and quasi-simultaneous SED.

I take a new approach to investigating the disc-jet connection. I observationally constrain the external photon field using quasi-simultaneous near-IR, optical and X-ray spectroscopy. Applying a one-zone leptonic jet model, I simulate the range of jet parameters for which this photon field, when Compton scattered to higher energies, can explain the γ-ray emission. I find that the site of the γ-ray emission lies well within the BLR and that the seed photons mainly originate from the accretion disc. The jet power that we determine, 1.0×10^{45} erg s^{-1}, is approximately half the accretion disc luminosity. I show that this object is not simply a low-mass FSRQ, its jet is intrinsically less powerful than predicted by scaling a typical FSRQ jet by SMBH mass and accretion rate. That γ-ray emitting NLS1s appear to host underpowered jets may go some way to explaining why so few have been detected to date.

This chapter is organised as follows: in Section 4.2 I present the multiwavelength data set I have assembled for this source. The mass of the source is determined from NIR and optical spectroscopic data in Section 4.3. In Section 4.4 I provide a detailed analysis of the *XMM-Newton* X-ray spectrum. I describe how I use the multiwavelength data to determine the ambient photon field contributions from the accretion disc, X-ray corona, BLR and torus in Section 4.5.1. In Section 4.5.2 I self-consistently apply this ambient photon field within a jet model to reproduce the entire broadband SED from radio to γ-rays. I test simple scaling relations for the jet with the SMBH mass and accretion rate and I determine the power in the jet and compare this to the accretion power and the jet power of other blazars. The discussion and conclusions are presented in Section 4.6 and Section 4.7. In particular, I investigate the nature of this source as both a NLS1 and a blazar.

For my adopted cosmological parameters, the redshift $z = 0.0625$ implies a luminosity distance of 280 Mpc and a flux-to-luminosity conversion factor of 9.41×10^{54} cm^2.

4.2 The multiwavelength data set

Below I present the multiwavelength data set I have assembled for 1H 0323+342. As a whole this data set is non-simultaneous, however parts of it are quasi-simultaneous. In particular, the observations which I use to calculate the external photon field (including near infrared, optical and X-ray spectroscopy: see Section 4.5.1) were all obtained in a time span of less than six months. The issue of variability is addressed in Section 4.4.1 and Section 4.6.4. The data set spans an exceptionally wide range of frequencies, from $\sim 10^9$ Hz in the radio up to $\sim 10^{24}$ Hz in γ-rays. In addition the SED is also well-sampled, with data in the radio, infrared, optical, ultraviolet, X-rays and γ-rays. Because it is a bright source, much of these data are high S/N and includes spectra in the infrared, optical and X-ray as well as photometry. Here, I present my new reductions / extractions of data from the *Spitzer Space Telescope* (Section 4.2.2.1); *XMM-Newton* (Section 4.2.1.3) and *Fermi* (Section 4.2.3.3). I also summarise the data which was used previously by Landt et al. (2017). These data sets are supplemented by archival data from other facilities in the radio / sub-mm, infrared, ultraviolet and X-ray bands. The complete data set and its reference sources are listed in Table 4.1. The multiwavelength SED is shown in Figure 4.1.

4.2.1 Quasi-simultaneous data sampling the external photon field

Although not strictly simultaneous, I have used three spectra (in the infrared, optical and X-ray bands) and optical/UV photometry sampling the accretion flow which were taken over a period of less than six months. In Section 4.5.1.1 I use these quasi-simultaneous data to parameterise the size scales and luminosities of the accretion disc, its X-ray corona and the hot dust emission from the torus, which (along with the BLR) contribute to the external photon field which is Compton upscattered by particles in the relativistic jet. In Section 4.2.3.3 a *Fermi* γ-ray spectrum is

Table 4.1: The multiwavelength data set

Q	Band	Instrument (Survey)	Observation date (D/M/Y or M/Y)	$\log(\nu_{\rm obs})$ [Hz]	Flux [10^{-14} erg/s/cm^2]	Luminosity [10^{41} erg/s]	Ref.
	Radio	Effelsberg	07/10–03/14	9.422	1.22 ± 0.16	1.15 ± 0.15	[1]
	Radio	Effelsberg	07/10–03/14	9.686	1.94 ± 0.31	1.82 ± 0.29	[1]
	Radio	Effelsberg	07/10–03/14	9.922	3.17 ± 0.64	2.98 ± 0.60	[1]
	Radio	Effelsberg	07/10–03/14	10.02	3.94 ± 0.87	3.71 ± 0.82	[1]
	Radio	Effelsberg	07/10–03/14	10.16	5.5 ± 1.7	5.2 ± 1.5	[1]
	Radio	Effelsberg	07/10–03/14	10.36	11.5 ± 5.3	10.8 ± 5.0	[1]
	Radio	Effelsberg	07/10–03/14	10.51	13.8 ± 8.7	13.0 ± 8.2	[1]
	Radio	Effelsberg	07/10–03/14	10.63	15.2 ± 5.0	14.3 ± 4.7	[1]
	Radio	IRAM	07/10–03/14	10.94	47 ± 1.5	43.9 ± 1.4	[1]
	Radio	*Planck*	08/09–11/10	11.00	56.4 ± 5.2	53.1 ± 4.9	[2]
	Radio	IRAM	07/10–03/14	11.15	73.7 ± 2.3	69.3 ± 2.2	[1]
	Radio	*Planck*	08/09–11/10	11.16	93.8 ± 5.7	88.2 ± 5.4	[2]
	Radio	*Planck*	08/09–11/10	11.34	89.3 ± 9.4	84.0 ± 0.9	[2]
	Far-IR	*Spitzer* MIPS	27/09/08	12.63	869 ± 8	817 ± 8	[3]
	Far-IR	*WISE*	10–11/02/10	13.13	1400 ± 70	1320 ± 70	[4]
	Far-IR	*Spitzer* IRS*	27/09/08	13.30	1130 ± 140	1060 ± 130	[3]
	Mid-IR	*WISE*	10–11/02/10	13.41	1360 ± 70	1280 ± 70	[4]
	Mid-IR	*Spitzer* IRAC	27/09/08	13.58	1390 ± 70	1310 ± 70	[3]
	Mid-IR	*Spitzer* IRAC	27/09/08	13.72	1230 ± 60	1160 ± 60	[3]
	Mid-IR	*WISE*	10/02/10–20/08/10	13.81	1150 ± 50	1080 ± 50	[4]
	Mid-IR	*Spitzer* IRAC	27/09/08	13.82	1230 ± 60	1150 ± 60	[3]
	Mid-IR	*Spitzer* IRAC	27/09/08	13.92	1260 ± 60	1180 ± 60	[3]
	Mid-IR	*WISE*	10/02/10–20/08/10	13.95	1310 ± 80	1230 ± 80	[4]
	Near-IR	(2MASS)	20/01/98	14.14	1170 ± 30	1100 ± 30	[5]
✓	Near-IR	GNIRS*	16/09/15	14.25	1030 ± 50	970 ± 50	[6]
	Near-IR	(2MASS)	20/01/98	14.26	1100 ± 40	1030 ± 40	[5]
	Near-IR	(2MASS)	20/01/98	14.39	1040 ± 30	980 ± 30	[5]
✓	Optical	Keck*	14/02/16	14.65	950 ± 50	890 ± 50	[6]
✓	Optical	*XMM-Newton* OM	23/08/15	14.74	1990 ± 10	1872 ± 9	[3]
✓	Optical	*XMM-Newton* OM	23/08/15	14.82	1856 ± 8	1746 ± 8	[3]
✓	UV	*XMM-Newton* OM	23/08/15	14.94	1963 ± 8	1847 ± 8	[3]
✓	UV	*XMM-Newton* OM	23/08/15	15.01	2600 ± 10	2446 ± 9	[3]
	UV	*GALEX*	27/12/11	15.11	2800 ± 1000	2600 ± 900	[7]
✓	UV	*XMM-Newton* OM	23/08/15	15.11	3010 ± 30	2830 ± 30	[3]
✓	UV	*XMM-Newton* OM	23/08/15	15.15	3190 ± 50	3000 ± 50	[3]
✓	X-ray	*XMM-Newton* EPIC*	23/08/15	17.68	430 ± 10	400 ± 10	[3]
	X-ray	*NuSTAR**	15–18/03/14	18.67	720 ± 20	680 ± 20	[6]
	X-ray	*Swift* BAT*	12/04–09/10	19.18	995 ± 200	940 ± 200	[8]
	γ-ray	*Fermi* LAT	01/08/15–30/09/15	22.39	1500 ± 450	1400 ± 420	[3]
	γ-ray	*Fermi* LAT	01/08/15–30/09/15	23.00	370 ± 130	345 ± 120	[3]
	γ-ray	*Fermi* LAT	01/08/15–30/09/15	23.74	70 ± 50	65 ± 50	[3]

*For spectra, I quote the flux at the indicated frequency at approximately the midpoint of each spectrum. The 'Q' flag indicates the quasi-simultaneous data from which I determine the external seed photon field, as described in Section 4.5.1 in the text. References: [1] Angelakis et al. (2015); [2] *Planck* Second Point Source Catalog, Planck Collaboration et al. (2016b); [3] this work; [4] *WISE* AllWISE Source Catalog, Wright et al. (2010); [5] Two Micron All-Sky Survey, Skrutskie et al. (2006); [6] Landt et al. (2017); [7] *GALEX* Data Release GR6, Martin et al. 2005; [8] *Swift* BAT 70-month All-Sky Hard X-ray Survey, Baumgartner et al. (2013).

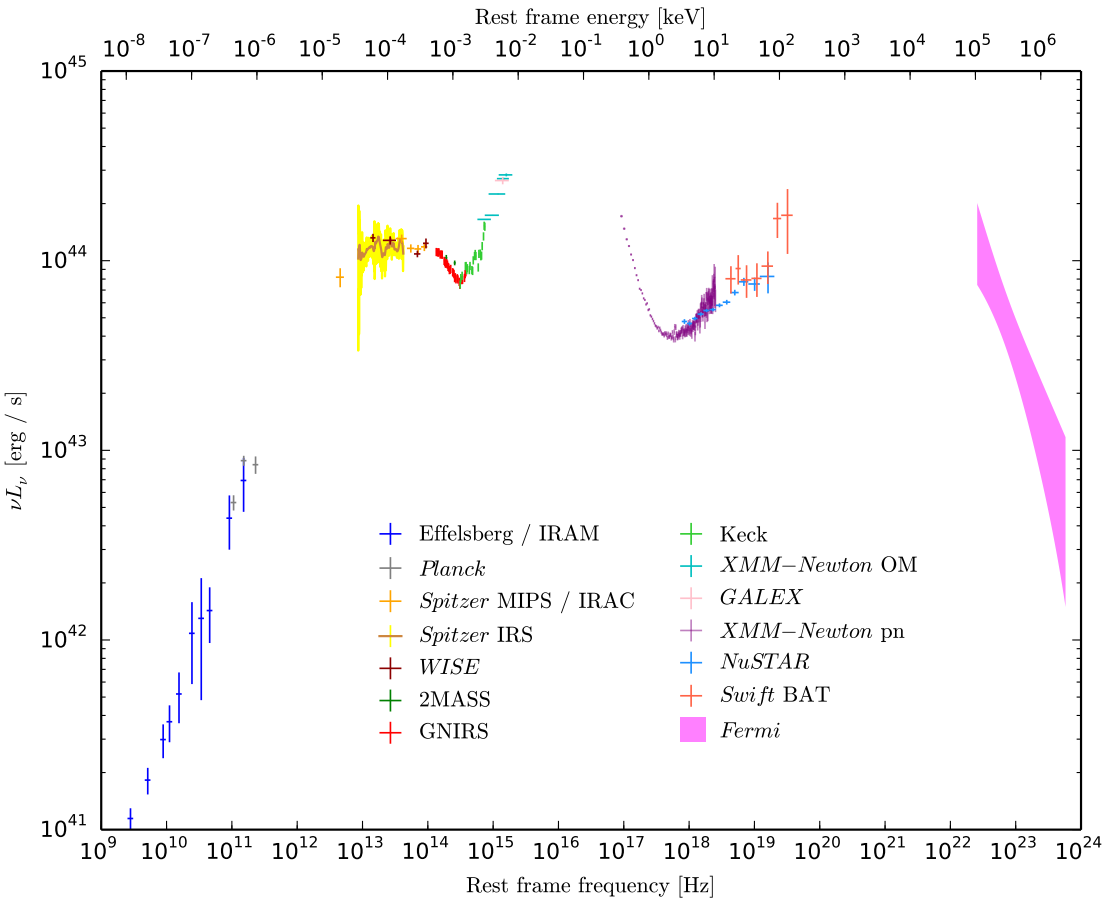

Figure 4.1: The multiwavelength spectral energy distribution of the γ-NLS1 1H 0323+342. The *XMM-Newton* X-ray spectrum has been deabsorbed using a Galactic column $N_{\rm H}^{\rm Gal} = 2.3 \times 10^{21}$ cm^{-2}. The optical / UV data have been dereddened using an $A_V = 0.71$. For details of the original sources of these multiwavelength data, see Table 4.1.

extracted, spanning a period from approximately a month either side of the *XMM-Newton* observation.

4.2.1.1 Gemini North

The near-infrared spectrum, obtained in September 2015 using the Gemini Near-Infrared Spectrograph (GNIRS) on the Gemini North 8 m telescope, was presented in Landt et al. (2017). The average continuum S/N obtained in the J, H and K bands were $\sim$ 40, 70 and 90, respectively. The spectrum was dereddened using the calculated extinction value $A_V = 0.71$ from the Galactic neutral hydrogen column density $N_{\rm H} = 1.46 \times 10^{21}$ cm^{-2} given by Dickey & Lockman (1990) (hereafter D&L90).

4.2.1.2 Keck

The optical spectrum was obtained using the Low Resolution Imaging Spectrometer mounted on the Keck 10 m telescope in February 2016. As described in Landt et al. (2017), the average continuum S/N was $\sim$ 60 and I scaled up this spectrum in flux by $\approx$ 40 % to match the near-IR spectrum.

4.2.1.3 *XMM-Newton*

The large effective area of the *XMM-Newton* X-ray observatory (Jansen et al. 2001) makes it an excellent telescope with which to obtain high S/N X-ray spectra. 1H 0323+342 was observed by *XMM-Newton* for 81 ks on 23-24 August 2015. The three EPIC X-ray detectors (pn, MOS1 and MOS2) were operating in Large Window mode with the Medium filter in place. Data from the observation (ID 0764670101; PI: D'Ammando) were obtained from the *XMM-Newton* Science Archive and the reduction was performed using the Science Analysis System (SAS, v15.0.0).

I extracted *XMM-Newton* OM photometry taken through all six filters using the SAS omichain and omsource tasks and standard procedures. Fluxes were calculated

from the count rates in each filter and dereddened using my derived $A_V = 0.71$ and adopting $R_V = 3.1$ and the reddening correction curves of Cardelli et al. (1989). Data and response files for use in the spectral fitting package XSPEC (Arnaud 1996) were generated using the flx2xsp tool. Photometry from the V filter was excluded from my later analysis because it contains a strong emission line.

After filtering the EPIC event lists for flaring particle background I was left with good exposure times of 60, 72 and 70 ks for the pn, MOS1 and MOS2 detectors, respectively. Source spectra from all three detectors were extracted from a 20″-radius circular region centred on the source. Background spectra were extracted from circular regions (60″ radius for pn and 40″ for MOS) on an offset blank patch of sky on the same chip as the source. Source count rates were 3.6, 0.94 and 1.0 counts s^{-1} in the pn, MOS1 and MOS2 detectors, respectively. The rate in pn exceeds the maximum rate of 1.5 counts s^{-1} for the avoidance of pile-up suggested in the Users Handbook. A test for pile-up was performed using the SAS epatplot task and no evidence for pile-up was found. The extracted spectra were rebinned using the specgroup tool to achieve a minimum S/N of 5 in each channel and to not oversample the intrinsic instrumental energy resolution by a factor greater than 3. Because of the large number of counts in the spectra, this easily satisfied the requirement for a minimum of 20 counts per bin needed for χ^2 analysis. My detailed X-ray spectral and temporal analyses are presented in Section 4.4.

I also obtained the Pipeline Processing System (PPS) products from the two RGS instruments aboard *XMM-Newton*. These instruments cover the 0.33–2.5 keV range at a much higher spectral resolution than the EPIC CCDs. In my analysis I used only the first spectral orders (containing $\sim$ 20000 counts in total, see Table 4.2).

4.2.2 Additional data sampling the external photon field

I supplement the data above with an infrared spectrum and photometry from *Spitzer* which I attribute primarily to emission from the dusty torus (see Section 4.2.2.1 and

Table 4.2: Summary of *XMM-Newton* exposures

Detector	Energy [keV]	Live time [ks]	Counts
EPIC-pn	0.3–10	60	217650
	0.33–2.5		182664
EPIC-MOS1	0.3–10	72	68017
	0.33–2.5		54272
EPIC-MOS2	0.3–10	70	73838
	0.33–2.5		58693
RGS1	0.33–2.5	80	8912
RGS2	0.33–2.5	80	10563

Section 4.6). Additionally, I have photometry from *WISE*, the 2MASS survey and *GALEX* in the same frequency ranges as the *Spitzer*, GNIRS and *XMM-Newton* OM data, respectively.

4.2.2.1 *Spitzer*

To obtain photometry from IRAC, I analysed the post-BCD (Basic Calibrated Data) images of 1H 0323+342 taken on the 27 September 2008 observation, available from the *Spitzer* archive. Using a 10″ aperture I determined fluxes at each of the four operating wavelengths with uncertainties ≈ 5 %.

The source was observed with IRS using the low spectral resolution (R∼60–130) modules between 7.6 and 37.9 µm in the spectral mapping mode. This IRS mapping observation was reduced using the standard pipeline (version C18.18). First, the background emission was subtracted and rogue pixels were removed using IRSCLEAN. Then, the single IRS pointings were projected into a grid similar to CUBISM (Smith et al. 2007). From the data cube, the spectra were extracted using a 7.7″ × 7.7″ and a 17.8″ × 17.8″ square aperture centred at the nuclei in the short-low (SL; 7.6–14 µm) and long-low (LL; 14–36 µm) cubes, respectively. A point-source aperture correction was applied based on the IRS mapping observations of stars. There is a good agreement between the continuum levels at the overlapping spectral ranges of the different modules (SL and LL). This suggests, that the mid-IR emission is dominated by a point-like source at the spatial resolution of IRS (∼2–9″, depending

on the wavelength). The IRS spectrum is shown in Figure 4.2 along with the MIPS and IRAC photometry.

I measured the possible [O IV] λ25.89 µm emission line in the IRS spectrum. To do so, I fit the 20–32 µm region with a Gaussian profile and the underlying continuum as a power-law of the form $F_\lambda = a(\lambda/b)^{-c}$ where the constants a, b and c are free parameters in the fit. I find the Gaussian line has a central, rest-frame wavelength of $25.92^{+0.03}_{-0.04}$ µm, consistent with the [O IV] line. From the fitted Gaussian, which has a FWHM $= 0.26 \pm 0.04$ µm, I calculate an integrated luminosity in the line $\log(L_{[\mathrm{OIV}]}) = 41.3$ erg s^{-1}.

1H 0323+342 was detected at 70 µm using MIPS. The data reduction was performed using the MOPEX analysis tool. Following the prescription in the MIPS instrument handbook v3.0, source counts were extracted from a circular region of radius 35″ and the background counts were taken from an annulus with inner and outer radii of 39″ and 65″, respectively. The photometric uncertainty was calculated using Eqn. (1) in Carpenter et al. (2008). The source was found to have a flux density 207 ± 2 mJy, equivalent to a flux of $(8.69 \pm 0.08) \times 10^{-12}$ erg s^{-1} cm^{-2}.

4.2.2.2 WISE

Photometry for the source 1H 0323+342 was obtained in each of these bands from the AllWISE Source Catalog[2]. The photometric magnitudes were calculated from multiple observations (24 for W1 and W2, 12 for W3 and W4) recorded during the survey. The observation start and end dates correspond to those listed in the online long form catalogue.

4.2.2.3 2MASS

1H 0323+342 was observed as part of the Two Micron All-Sky Survey (2MASS) which was conducted between 1997 and 2001. I obtained measurements in the J,

[2] http://irsa.ipac.caltech.edu/

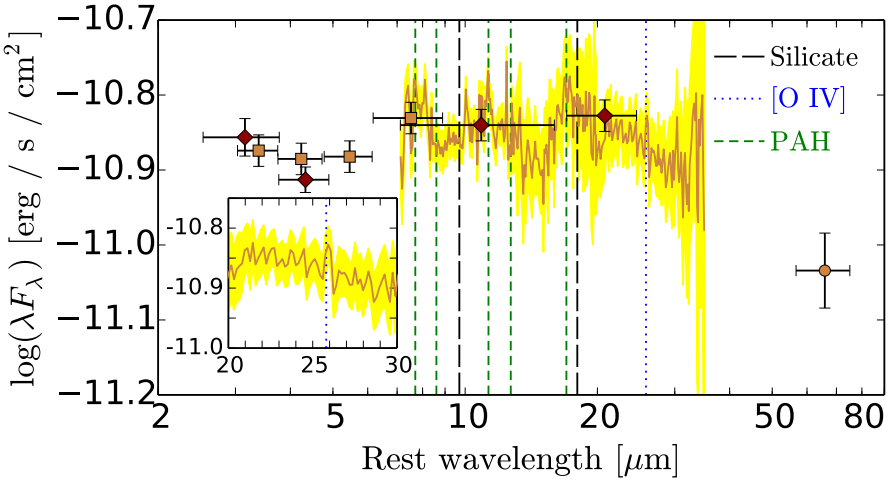

Figure 4.2: *Spitzer* spectroscopy and photometry of 1H 0323+342 taken in September 2008. The IRS spectrum is shown in ochre with its error region in yellow. Simultaneous photometry from IRAC and MIPS are shown with squares and a circle, respectively. For comparison, later *WISE* photometry points are shown with red diamonds. The wavelengths of the broad 9.7 and 18 µm silicate features are marked with black long dashed lines; the wavelengths of PAH features are marked with green short dashed lines and that of the [O IV] λ25.8 µm forbidden emission line is marked with a blue dotted line (this is also shown in the inset plot).

H and K_S bands from the 2MASS All-Sky Point Source Catalog[3] (Skrutskie et al. 2006). The S/N in these bands were 99.9, 95.3 and 131.0, respectively.

4.2.2.4 *GALEX*

1H 0323+342 was detected in the near-UV by *GALEX* during a 96 s exposure on 27 December 2011. Data were extracted from the sixth *GALEX* data release, GR6[4]. The flux was dereddened using the same procedure as for the *XMM-Newton* OM fluxes.

4.2.3 Data sampling the jet emission

At both the very low and very high frequency ends of the SED, I have data which sample the emission from the relatvistic jet.

[3] Also available from the Infrared Science Archive, see note 2.
[4] http://galex.stsci.edu/GR6/

4.2.3.1 Effelsberg and IRAM

Radio light curves and SEDs of 1H 0323+342 were produced as part of the *Fermi*-GST Multiwavelength Monitoring Alliance (F-GAMMA, Fuhrmann et al. 2016b) monitoring programme. The observations were conducted between 31 July 2010 and 11 March 2014. Flux densites at 2.64, 4.85, 8.35, 10.45, 14.60, 23.05, 32.00 and 43.05 GHz were obtained at the 100 m Effelsberg telescope. 86.24 and 142.33 GHz readings were made at the 30 m IRAM telescope. For my SED, I have taken the mean flux densities and their standard deviations as reported in Table 8 of Angelakis et al. (2015)[5]; I refer the reader to this paper for further details.

4.2.3.2 *Planck*

I complemented the low-frequency data with non-simultaneous Planck observations taken from the latest version of the *Planck* Catalog of Compact Sources[6] (PCCS2, Planck Collaboration et al. 2016b) that compiles all sources, both Galactic and extragalactic, detected with high confidence over the full sky during the period between August 2009 and August 2013. This catalogue contains average intensity information for the sources which may have been observed more than once.

Using a cone search of $1'$, clear association with 1H 0323+342 was found at 100 and 143 GHz in the good-quality PCCS2 catalogues, and in addition at 217 GHz, taken from the PCCS2E catalogue. The catalogue gives multiple flux density estimates, the source associated to 1H 0323+342 being clearly identified on the cutout images; the photometry reported in Table 4.1 are from Gaussian fitting method.

4.2.3.3 *Fermi*

The Large Area Telescope (LAT, Atwood et al. 2009) onboard the *Fermi* satellite detects γ-ray photons with energies between 20 MeV and above 300 GeV. The source

[5]In this paper the source is named J0324+3410.
[6]http://irsa.ipac.caltech.edu/data/Planck/release_2/catalogs/

1H 0323+342 is listed in the second catalogue of flaring γ-ray sources detected with the Fermi All-sky Variability Analysis[7] (FAVA), a tool that blindly searches for transients over the entire sky observed by the LAT (Abdollahi et al. 2017). The subset of those data over the period 1 August to 30 September 2015, covering the date of the *XMM-Newton* observation, were analysed using the publicly available Science Tools v10r0p53 . It appears that the source was in a low state.

Photons in a circular region of interest (RoI) of radius 10°, centred on the position of 1H 0323+342, were considered. The PASS 8 instrument response functions (event class 128 and event type 3) corresponding to the P8R2_SOURCE_V6 response were used together with a zenith-angle cut of 90°. The Galactic diffuse emission has been modelled using the file gll_iem_v06.fits (Acero et al. 2016) and the isotropic background using iso_P8R2_SOURCE_V6_v06.txt. Assuming a power-law spectral shape for 1H 0323+342, a binned likelihood analysis yields a detection with a Test Statistic TS = 11.26 ($\approx 3.4\sigma$) with a flux of $F_{0.1-100\ \mathrm{GeV}} = (4.65 \pm 1.68) \times 10^{-8}\ \mathrm{cm}^{-2}\ \mathrm{s}^{-1}$ and a photon index of $\Gamma = 2.98 \pm 0.33$.

To do this the fit was performed iteratively, with all the sources from the 3FGL catalogue within 14° around 1H 0323+342 included, with fixed parameters for those more than 10° away to account for event leakage in the RoI due to the large PSF at low energies. In a second step, the sources contributing to less than a TS of 9 and to less than 5 % of the total number of counts in the RoI have their parameters frozen. The only free parameters in the end are those of sources less than 3° away from 1H 0323+342, if not frozen in the previous step and the normalisations of the Galactic and isotropic diffuse emissions.

4.2.4 Supplementary X-ray data

I present *Swift* X-ray telescope (XRT) monitoring data covering the same frequency and time period as the *XMM-Newton* observation. Finally, hard X-ray spectra from

[7] https://fermi.gsfc.nasa.gov/ssc/data/access/lat/FAVA/

both *NuSTAR* and *Swift* burst alert telescope (BAT) bridge the frequency range between the *XMM-Newton* X-ray spectra and the γ-ray emission recorded by *Fermi*.

4.2.4.1 *Swift* XRT

Swift monitoring of the source was conducted from 2 August to 24 December 2015, with snapshot observations of approximately 2 ks durations taken with an average ≈ 6 day cadence. I reduced the data from the twelve observations taken between 2 August to 29 September 2015, around the time of the 81 ks *XMM-Newton* observation (see Section 4.2.1.3) and covering the period of the *Fermi* observations I use in this chapter (see Section 4.2.3.3). The XRT products were created using xrtpipeline v0.13.2. The source extraction regions were a 47″-radius circle centred on the source (corresponding to the 90 % encircled energy radius at 1.5 keV) and the background regions were 141″ circular regions offset from the source, in an area free of field sources. The spectra were extracted using xselect and ancilliary response files were created with xrtmkarf. The observations of 11 August and 29–30 September (OBS IDs 00036533056 and 00036533066) both had count rates slightly exceeding 0.5 counts s^{-1} and were investigated for pile up. The wings of the PSF beyond 15″ from the centre were fitted with a King function with the parameters $r_c = 5.8$ and $\beta = 1.55$ fixed (see Moretti et al. 2005 for further details). This function was then extrapolated into the inner regions. The deviation of the data from the model King function in the centre of the PSF was very marginal, so for my purposes it was unnecessary to extract the spectra from an annular region. Using GRPPHA, I rebinned each spectrum to contain a minimum of 20 counts per bin such that they were suitable for a χ^2 analysis.

4.2.4.2 *NuSTAR*

A 200 ks exposure of the source was taken using *NuSTAR* in March 2014. The data reduction is detailed in Landt et al. (2017). Here I use the co-added, time-averaged spectra from both focal plane modules FPMA and FPMB.

4.2.4.3 *Swift* BAT

I include catalogue data from the *Swift* BAT seventy-month all-sky survey. The survey includes all sources detected in the hard X-ray energy range $14 - 195$ keV in the period December 2004 and September 2010 (Baumgartner et al. 2013). The 14–195 keV photon index and flux were reported to be $\Gamma = 1.73$ and 2.993×10^{-11} erg s^{-1} cm^{-2}, respectively.

4.3 The black hole mass

In this section, the SMBH mass of the source 1H 0323+342 is estimated using the virial product between the width of a broad emission line and the continuum luminosity, which serves as a proxy for the BLR radius. The SMBH mass is first estimated using the near-IR relationship presented by Landt et al. (2013). This relationship is based on the virial product between the 1 µm continuum luminosity and the width (FWHM or line dispersion) of the strongest Paschen broad emission lines, Paα or Paβ. As detailed by these authors, the main advantage of the near-IR virial product over the optical one is the reliable measurement of its quantities; both Paα and Paβ are observed to be unblended and the continuum around 1 µm is free of major contaminating components. Host galaxy starlight has its emission maximum at ∼1 µm, but its contribution is usually negligible in luminous AGN if the near-IR spectrum was obtained through a small slit. In this case, the host galaxy flux at 1 µm enclosed by the spectral aperture can be estimated using the imaging results of León Tavares et al. (2014). These authors give surface brightness estimates in the R band for both a bulge and a bulge plus disc model of the host galaxy, which we use to scale the S0 galaxy template of Polletta et al. (2007). In this way, the luminosity of the host galaxy at 1 µm in the near-IR spectrum is estimated to lie a factor of 70 below the total luminosity. The Gemini GNIRS near-IR spectrum covers simultaneously both the Paα and Paβ emission lines as well as the rest-frame 1 µm wavelength region.

However, the Paβ emission line is strongly affected by atmospheric absorption since it lies at the end of the atmospheric window. Therefore, in the following, SMBH mass is estimated using only the Paα broad emission line, for which the linewidth is measured as the FWHM, i.e. equation 2 in Landt et al. (2013) is used. The measurement of the 1 µm continuum luminosity is straightforward the value of $\log(L_{1\mu m}) = 43.92$ erg s^{-1} is determined. However, in order to correctly measure the width of the Paα broad component, it is necessary to first separate it from the narrow component. Based on absent narrow components observed for the higher order Paschen emission lines, Landt et al. (2014) have suggested that the correct approach to this is to subtract the largest possible flux contribution from the narrow emission-line region. This contribution is obtained by first estimating the FWHM of a strong forbidden narrow emission line and then fitting a Gaussian of this width to the top part of the total emission line profile. This method is applied here and the result is shown in Figure 4.3. In the source 1H 0323+342, the Paϵ emission line, which is blended with the strong forbidden narrow emission line [S III]λ9531, has no narrow component (thick green line in Figure 4.3, upper left panel). A Gaussian fit to the [O III]λ5007 emission line observed in the optical spectrum gives an FWHM = 294 km s^{-1}.

Subtracting a Gaussian with this width from the top part of the total Paα emission line (thin black lines) leaves a broad component with a similar profile to that observed for the Paϵ emission line (Figure 4.3, upper right panel). A FWHM = 1120 km s^{-1} is measured for the Paα broad component, which results in a SMBH mass of $\left(2.0^{+0.8}_{-0.6}\right) \times 10^7$ M$_\odot$ (see also Table 4.3).

Next, the SMBH mass is estimated using the latest scaling relations based on the optical virial product between the ionizing 5100 Å continuum luminosity and the width of the strongest Balmer broad emission lines Hα and Hβ. All these three quantities are covered simultaneously in the Keck LRIS optical spectrum. The measurement of the 5100 Å continuum luminosity is straightforward and a value of $\log(L_{5100\text{Å}}) = 44.05$ erg s^{-1} is determined (in the scaled-up spectrum as described

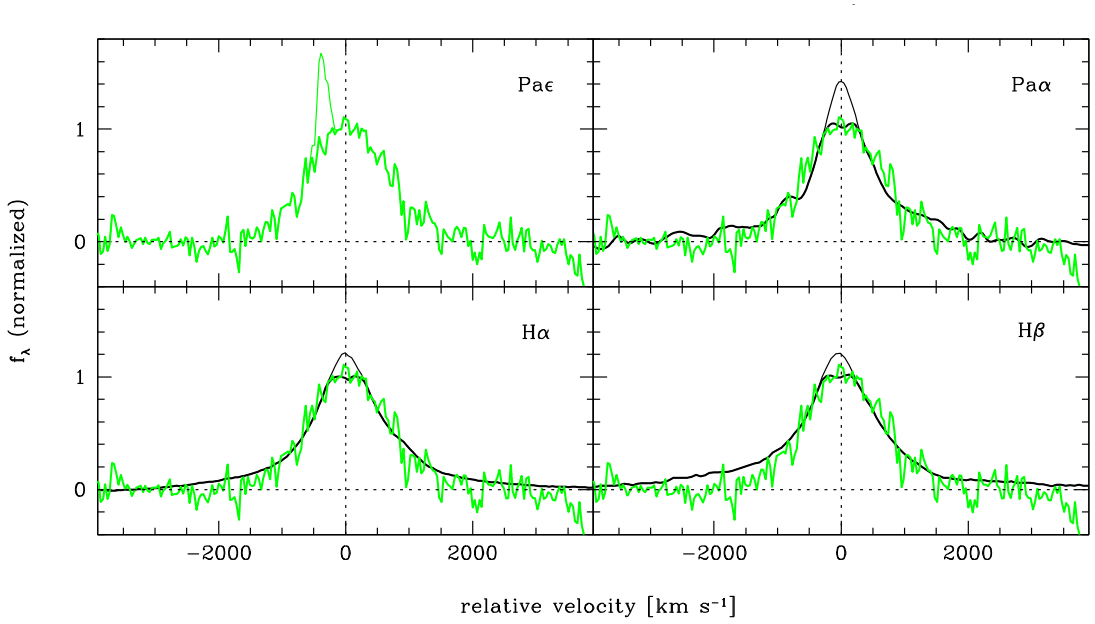

Figure 4.3: The profile of the Paϵ emission line (thick green lines in upper left panel; here taken from the Keck LRIS optical spectrum) is blended with the forbidden narrow emission line [S III]λ9531 (thin green lines) but its narrow component is absent. After removing the largest possible flux contribution from the narrow emission-line region (thin black lines), the resulting profile of the broad component of the Paα, Hα and Hβ emission lines (thick black lines in upper right, lower left and lower right panels, respectively) is similar to that of the Paϵ emission line (thick green lines).

in Section 2.2 of Landt et al. 2017). After subtracting the narrow component of the Hα emission line following the same method adopted for the Paα emission line (Figure 4.3, lower left panel), a FWHM = 1412 km s^{-1} is measured for the Hα broad component. Using the recently recalibrated SMBH mass relationship of Mejía-Restrepo et al. (2016), specifically the calibration for the local continuum fit corrected for small systematic offsets (see their table 7), the SMBH mass is estimated to be $\left(1.5^{+0.7}_{-0.5}\right) \times 10^7$ M$_\odot$ (see also Table 4.3). As is typical for narrow-line Seyfert 1 galaxies, the emission from permitted Fe II transitions is very strong in the source 1H 0323+342. This emission needs to be modelled and subtracted in order to reliably measure the width of the Hβ emission line, since the numerous optical Fe II multiplets form a pseudo-continuum around the line and blend in with its red wing. The template based on the optical spectrum of I Zw 1 published by Véron-Cetty et al. 2004 was used to model and subtract the Fe II emission. The

method generally used to subtract the Fe II emission from optical spectra was first introduced by Boroson & Green (1992). It consists of creating a spectral sequence by broadening (by convolution with Gaussians) and scaling of the Fe II template, which is subsequently packed together into a three-dimensional cube. This cube is then subtracted from a cube consisting in all three dimensions of the object's spectrum. But, as noted by Landt et al. (2008) and Vestergaard & Peterson (2005), it can be rather difficult to decide by eye unambiguously which pair of width and strength of the Fe II template gives the cleanest subtraction, and so it is necessary to constrain a priori the width of the Fe II template. Following Landt et al. (2008), this was done by using the width of the unblended near-IR iron emission line Fe II 1.0502 µm. For this, a value of FWHM = 1034 km s^{-1} was measured, which is similar to the linewidth of FWHM = 1100 km s^{-1} used for the Fe II template. Therefore, in this case it was not necessary to broaden the Fe II template but only to scale it. In this way, a satisfactory Fe II subtraction around the Hα line was achieved. After subtracting its narrow component in a similar way as was done for the Hα and Paα emission lines (Figure 4.3, lower right panel), a FWHM = 1437 km s^{-1} for the Hβ broad component was measured. Using the radius-luminosity relationship for the Hβ line of Bentz et al. (2013) derived from optical reverberation mapping results, specifically their calibration 'Clean2+ExtCorr' cleaned for bad time lags and corrected for internal extinction (see their table 14), and assuming a geometrical scaling factor of $f = 1.4$ appropriate for FWHM measures (Onken et al. 2004), a SMBH mass of $\left(2.2^{+0.8}_{-0.6}\right) \times 10^7$ $M_\odot$ was derived (see also Table 4.3).

Table 4.3: Estimates of the black hole mass of 1H 0323+342

Measurements	$M_{\rm BH}$ (10^7 $M_\odot$)	Reference
$\log \nu L_{1\mu m} = 43.92$ erg s^{-1} FWHM(Paα) = 1120 km s^{-1}	$2.0^{+0.8}_{-0.6}$	Equation 2 of Landt et al. (2013)
$\log \nu L_{1\mu m} = 43.92$ erg s^{-1} σ(Paα) = 875 km s^{-1}	$1.8^{+1.3}_{-0.7}$	Equation 3 of Landt et al. (2013)
$\log L_{Pa\alpha} = 41.46$ erg s^{-1} FWHM(Paα) = 1120 km s^{-1}	1.0±0.2	Equation 9 of Kim et al. (2010)
$\log \nu L_{5100Å} = 44.05$ erg s^{-1} FWHM(Hα) = 1412 km s^{-1}	$1.5^{+0.7\dagger}_{-0.5}$	Table 7 of Mejía-Restrepo et al. (2016)
$\log L_{H\alpha} = 42.44$ erg s^{-1} FWHM(Hα) = 1412 km s^{-1}	$0.6^{+0.4\dagger}_{-0.2}$	Table 7 of Mejía-Restrepo et al. (2016)
$\log \nu L_{5100Å} = 44.05$ erg s^{-1} FWHM(Hβ) = 1437 km s^{-1}	$2.2^{+0.8\dagger}_{-0.6}$	Table 14 of Bentz et al. (2013)
$\log L_{H\alpha} = 43.65$ erg s^{-1} FWHM(Hβ) = 1437 km s^{-1}	$1.2^{+0.8\dagger}_{-0.5}$	Table 2 of Greene et al. (2010b)
$\log L_{2-10keV} = 43.97$ erg s^{-1} FWHM(Hβ) = 1437 km s^{-1}	$2.2^{+1.8\dagger}_{-1.0}$	Table 2 of Greene et al. (2010b)

Notes: †The 1σ error is derived from the instrinsic scatter rather than the errors on the best-fit parameter values.

4.4 X-ray analysis

4.4.1 Variability

4.4.1.1 Short-term variability

I produced an RMS spectrum by creating lightcurves with 500 s time bins in fifteen energy bands between 0.2 and 10.0 keV. The excess RMS variability and its error were calculated for each lightcurve using the HEASARC ftool lcstats; these are plotted in Figure 4.4. The spectrum clearly shows a break around 1 keV with the soft and hard spectral components exhibiting different variability behaviour.

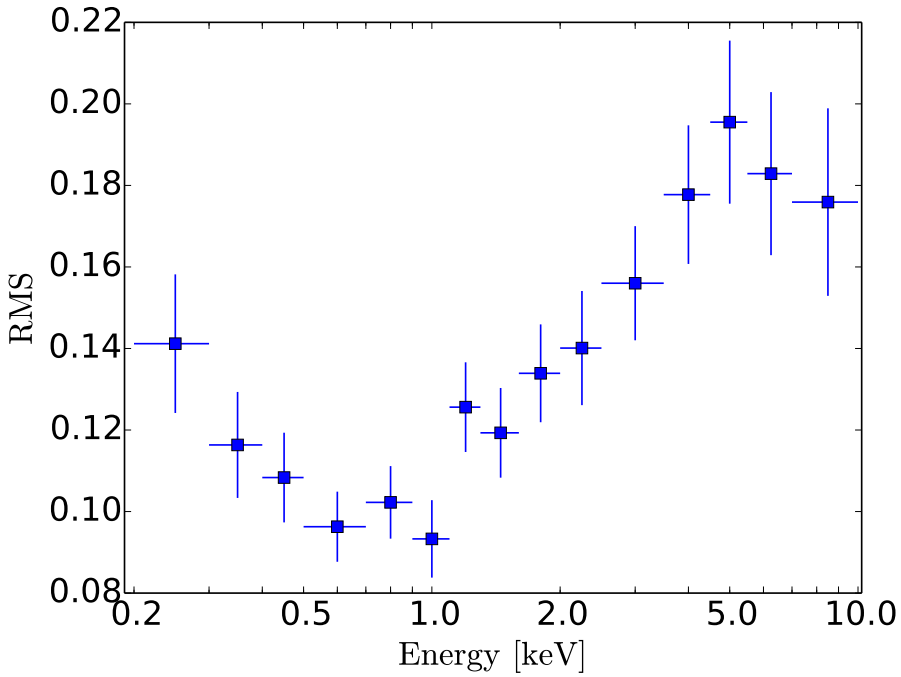

Figure 4.4: The X-ray RMS fractional variability spectrum of 1H 0323+342. Fifteen lightcurves spanning the 0.2–10.0 keV energy range were created from the *XMM-Newton* EPIC pn event file with time bins of 500 s.

4.4.1.2 Medium-term variability

Each of the twelve *Swift* spectra taken between 2 August and 30 September 2015 were fitted with a simple absorbed power-law model in XSPEC. To construct the lightcurve shown in Figure 4.5 I report the 0.3–10.0 keV count rates and also the best-fit X-ray photon indices. The count rates vary by a factor of four over this two-month period and the *XMM-Newton* observation was taken during a period of particularly low activity. The photon indices are poorly determined because of the limited S/N spectra, but by comparing the count rates and photon indices it can be seen that the source does not follow a simple 'softer-when-brighter' pattern of behaviour.

4.4.1.3 Longer-term variability

The *Swift* count rates in the main time interval of interest are ≈ 0.3 counts s^{-1} which are around the lowest values recorded in the five-and-a-half year lightcurve shown

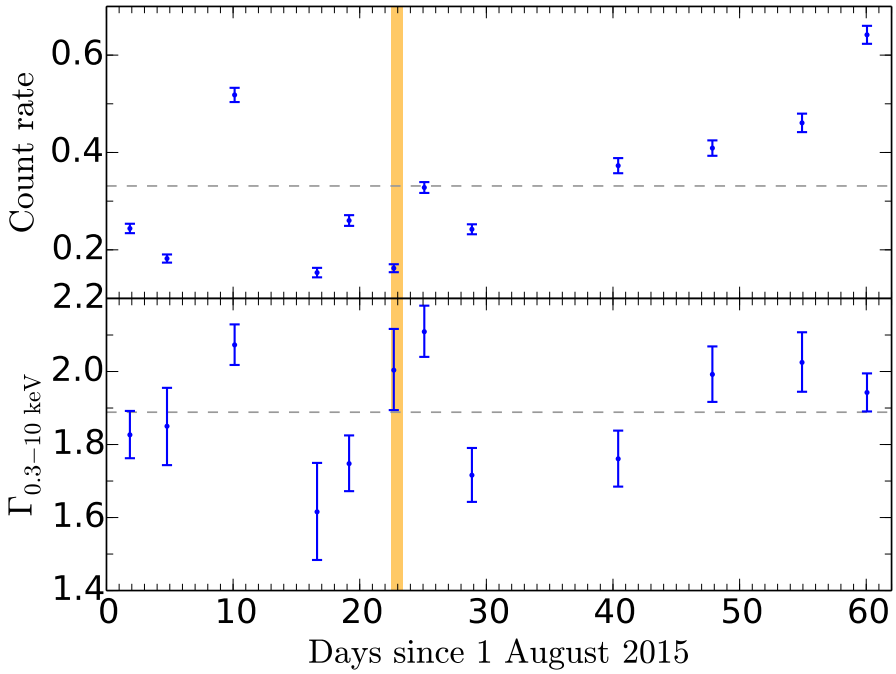

Figure 4.5: Upper panel: *Swift* XRT 0.3–10.0 keV count rates in counts s^{-1}. Lower panel: The X-ray photon index Γ of the best-fitting absorbed power-law model fit to the *Swift* spectrum. The mean values of both count rate and Γ are shown as grey dashed lines. The time span of the *XMM-Newton* observation is highlighted in orange.

in Paliya et al. (2014) (their Figure 1). As noted in Landt et al. (2017), I observed only a ~ 30 % variation in $2-10$ keV flux between the three epochs of *Swift* data (August 2013, December 2014 and September 2015) taken around the same time as my IR and optical spectra. In the corresponding *Swift* UVOT data, some variability in the B, U, UVW1 and UVW2 filters was observed, but only $\sim 20-30$ % at the $2-3\sigma$ level.

4.4.2 X-ray spectral analysis

The X-ray spectral fitting of the *XMM-Newton* data was performed in XSPEC v12.9.0n (Arnaud 1996). In all models I included a Galactic absorbing column (PHABS), initially adopting the D&L90 value $N_{\rm H}^{\rm Gal} = 1.46 \times 10^{21}$ cm^{-2}. Cross-normalisation factors were included to account for differences in calibration between the three EPIC detectors; these did not vary by more than 5 %.

4.4.2.1 The shape of the X-ray spectra

A single power-law (with $\Gamma_{2-10\ \rm keV} \approx 1.7$) fit to the 2–10 keV data shows an excess of soft emission below ≈ 2 keV (see Figure 4.6(a)). Consequently, a single power-law (with $\Gamma \approx 2.1$) to the whole 0.3–10 keV range results in a very poor fit to the data with a reduced chi-squared $\chi^2_\nu = 9.69$. These fits, and the shape of the RMS spectrum shown in Fig 4.4, clearly indicate that a continuum model with at least two components is required to fit the data.

A double power-law model (the first model in Table 4.4) is not a very good fit to the data. In the course of my modelling, I noticed that my models overpredict the data at energies below ≈ 0.5 keV. Additionally, the deabsorbed spectra do not rise towards lower energies to connect smoothly to the contemporaneous optical/UV photometry. These issues could be resolved by including some additional absorption in my models. Allowing $N_{\rm H}^{\rm Gal}$ to be a free parameter I consistently find it rises to a value $\approx 2.2 \times 10^{21}$ cm^{-2}, approximately 50 % greater than the D&L90 value,

Table 4.4: Results of X-ray spectral fits

Model	Parameter	Value
PHABS ×	$N_{\rm H}^{\rm Gal}$ [cm^{-2}]	$(1.46) \times 10^{21}$ [f]
(POWERLAW +	Γ_1	2.54 ± 0.02
	norm.	$\left(2.47^{+0.04}_{-0.05}\right) \times 10^{-3}$
POWERLAW)	Γ_2	1.06 ± 0.04
	norm.	$(4.7 \pm 0.4) \times 10^{-4}$
	χ^2/d.o.f.	$731/496 = 1.47$
PHABS ×	$N_{\rm H}^{\rm Gal}$ [cm^{-2}]	$(2.31 \pm 0.08) \times 10^{21}$
(POWERLAW +	Γ_1	3.54 ± 0.09
	norm.	$(2.10 \pm 0.04) \times 10^{-3}$
POWERLAW)	Γ_2	$1.49^{+0.02}_{-0.03}$
	norm.	$(1.34 \pm 0.06) \times 10^{-3}$
	χ^2/d.o.f.	$569/495 = 1.15$
PHABS ×	$N_{\rm H}^{\rm Gal}$ [cm^{-2}]	$(2.33 \pm 0.08) \times 10^{21}$
(POWERLAW +	Γ_1	3.59 ± 0.09
	norm.	$(2.06 \pm 0.04) \times 10^{-3}$
POWERLAW +	Γ_2	1.52 ± 0.02
	norm.	$\left(1.39^{+0.06}_{-0.07}\right) \times 10$
ZGAUSS +	E [keV]	$6.43^{+0.03}_{-0.02}$
	norm.	$(3.4 \pm 0.8) \times 10^{-6}$
	EW [eV]	34 ± 8
ZGAUSS)	E [keV]	6.95 ± 0.04
	norm.	$(2.4 \pm 0.8) \times 10^{-6}$
	EW [eV]	28 ± 9
	χ^2/d.o.f.	$540/491 = 1.10$

[f]Parameter was frozen during the fitting procedure. Errors are quoted at the 1σ level. The best-fit model is plotted in Figure 4.6.

and then gives a statistically significant improvement in the fits. I note that these values are similar to the total (H I plus H_2) Galactic column of 2.17×10^{21} cm^{-2} found by Willingale et al. (2013). A double power-law model with free $N_{\rm H}^{\rm Gal}$ is a significant improvement with $\Delta\chi^2 = 162$ and an F-test probability > 99.99 %. The implications of deabsorbing the EPIC X-ray spectrum with this higher $N_{\rm H}^{\rm Gal}$ are discussed further in Section 4.6. The fit can be further improved by the inclusion of two narrow emission lines, as is described in the next section.

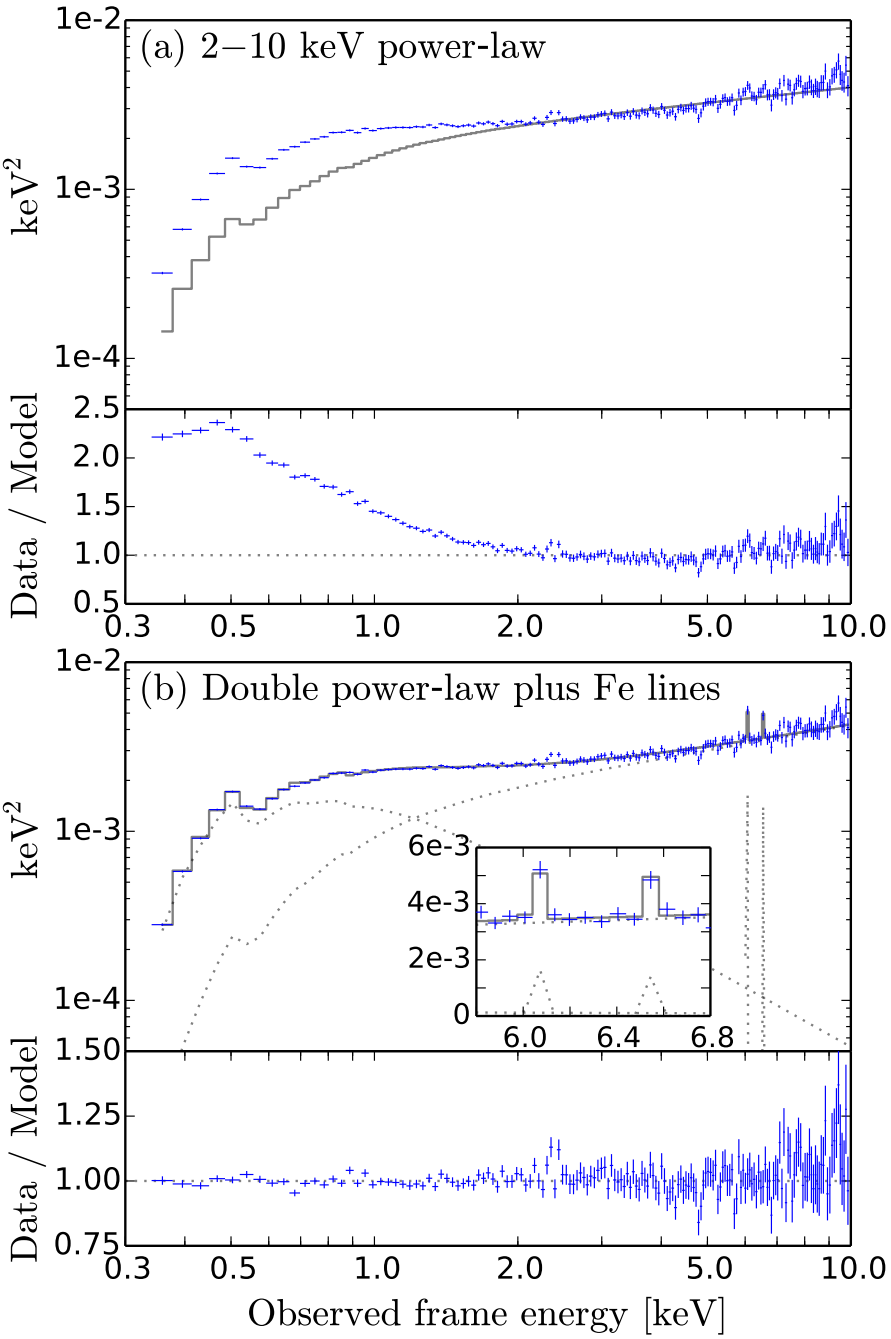

Figure 4.6: Fits to the *XMM-Newton* EPIC-pn X-ray spectrum of 1H 0323+342 taken during the 23–24 August 2015 observation. Fits were performed to all three spectra (pn, MOS1 and MOS2) simultaneously; for clarity I show only the pn data here. Upper panels show the data (crosses) with the total model (histograms) and the individual model components (dotted lines) for each of the three detectors in units of photons cm^{-2} s^{-1} keV^{-1}; lower panels show the data / model ratios. The model shown in (a) includes fixed $N_{\rm H}^{\rm Gal} = 1.46 \times 10^{21}$ cm^{-2}; the model shown in (b) has free $N_{\rm H}^{\rm Gal} = 2.33 \times 10^{21}$ cm^{-2}.

4.4.2.2 Iron line emission features in the X-ray spectra

Figure 4.7 shows that the fit statistic can be further improved by the addition of narrow emission lines at $\approx$ 6.4 and $\approx$ 6.9 keV. I first added a broad line at $\approx$ 6.4 keV, but the fitting procedure reduced the width of the line to below the detector resolution, which is unphysical, and so instead I fit a narrow line of fixed width $\sigma = 10$ eV. I find that its rest-frame energy is $6.43^{+0.03}_{-0.02}$ keV, consistent with neutral Fe Kα emission, and inconsistent with the 6.7 keV energy of Fe XXV. The fit is improved by a $\Delta\chi^2 = 19$ for three additional free parameters to $\chi^2_\nu = 550/493 = 1.12$, giving an F-test probability of 99.97 % compared to the model with no emission line. The line flux is $\left(3.1^{+0.7}_{-0.4}\right) \times 10^{-14}$ erg s^{-1} cm^{-2} and its equivalent width (EW) is low at 34 ± 8 eV, which I discuss in Section 4.6.

The fit is improved by a further $\Delta\chi^2 = 10$ with the inclusion of a second narrow Gaussian at 6.95 ± 0.04 keV, consistent with Fe XXVI. Clearly this is a weaker line than the neutral Fe Kα and I estimate its EW to be 28 ± 9 eV. My final X-ray spectral fit has a $\chi^2_\nu = 1.10$, its parameters are given in Table 4.4 and it is shown in Figure 4.6(b).

4.5 The origin of the γ-ray emission

The γ-ray emission from high accretion-rate blazars such as FSRQs and γ-NLS1s is thought to be produced by the external Compton (EC) mechanism whereby an ambient field of soft seed photons external to the jet is Compton upscattered by relativistic leptons within the jet. Emission from the accretion disc and its X-ray corona, the BLR and dusty torus can all potentially contribute to this external seed photon field. My new approach here is to determine the external photon field from my quasi-simultaneous IR-to-X-ray data which also samples the accretion flow. My parameterisation of the external photon field is presented below in Section 4.5.1. In Section 4.5.2 I then use a jet emission code to upscatter the external photon field and

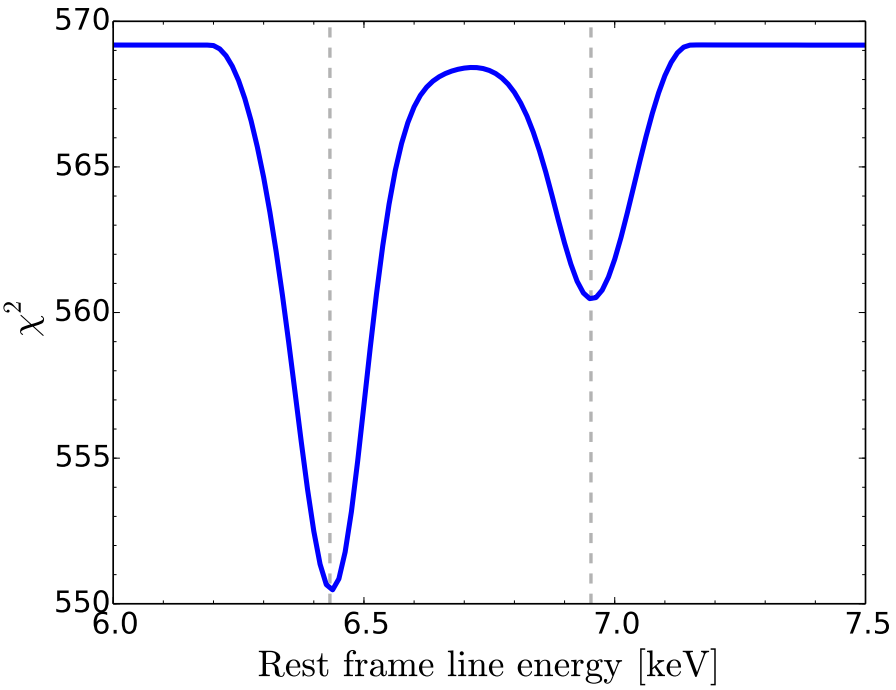

Figure 4.7: Variation in the χ^2 fit statistic with the rest frame line energy of a narrow (fixed width $\sigma = 10$ eV) Gaussian emission line. Best-fit line energies of 6.43 and 6.95 keV are indicated with dashed lines.

fit this to the full multiwavelength SED, determining the site of the γ-ray emission and the dominant source of seed photons.

4.5.1 Determining the external photon field

It is common in modelling EC emission to assume a standard external seed photon field which is upscattered by particles in the relativistic jet. Instead, I determine the external photon field of this particular source from my data. In Table 4.6 I summarise my findings and compare these to the standard assumptions made in the modelling of the photon field by Ghisellini & Tavecchio (2009) (hereafter G&T09), on which the jet emission code is based.

4.5.1.1 The accretion flow emission

The accretion flow emission is dominated by radiation from a disc of material accreting onto the SMBH. For low-mass and high accretion-rate SMBHs, the Wien tail of the accretion disc emission can extend into the soft X-ray bandpass. The disc itself not generally expected to emit much X-radiation. Most of the observed X-ray emission results from the Compton upscattering of photons by populations of hot electrons near to the SMBH. One such region is the optically thin corona of the accretion disc, which produces X-ray emission well-represented as a power-law extending up to ≈ 150 keV. As well as this power-law, many AGN also show evidence of a second Comptonisation region which is cooler and optically thicker than the corona. The emission from this region is observed as an excess of soft X-ray emission above the coronal power-law, so it is often dubbed the 'soft excess'. When modelled as a thermal component, the soft excess has a remarkably constant temperature (0.1–0.2 keV) across sources covering a wide range of SMBH masses and Eddington ratios (e.g. Gierliński & Done 2004; Porquet et al. 2004).

The continuum emission from the accretion flow of many AGN can therefore be represented by three components: the accretion disc emitting mostly in the optical/UV, plus a two Comptonisation regions producing soft excess and coronal X-rays. An energy-conserving version of this simple concept (OPTXAGNF, is included in the current version of XSPEC). Here I use the XSPEC local model OPTXCONV (Done et al. 2013), an extension of OPTXAGNF that approximates relativistic corrections to the spectrum, which are particularly pronounced at low inclinations and high spins. These models are described in Section 2.3.

At wavelengths longer than 1 µm, the Wien tail of blackbody emission from hot dust in the torus is dominant over the accretion disc emission. The 1 µm region is covered by both the GNIRS (near-infrared) and Keck (optical) spectra; I extracted from these spectra data points sampling the emission line free continuum so that I can also parameterise the hot dust emission.

I include the *NuSTAR* spectrum, taken 17 months prior to the *XMM-Newton* observation, thereby extending my SED up to 79 keV. I note that although similar in levels of flux, the photon index of the *NuSTAR* spectrum ($\Gamma = 1.80 \pm 0.01$) is softer than the index I determine in the overlapping energy range of *XMM-Newton* spectrum ($\Gamma_{3-10\ \mathrm{keV}} = 1.59 \pm 0.02$). It is known that a calibration issue with *XMM-Newton* results in harder spectral indices above ≈ 3 keV than those determined from other X-ray telescopes. For example, Ingram et al. (2017) found the spectral index of their *XMM-Newton* spectrum was harder than that of their *NuSTAR* spectrum taken simultaneously (with $\Delta\Gamma = 0.22$); the discrepancy I see here is very similar ($\Delta\Gamma \approx 0.21$, with the *XMM-Newton* spectrum appearing harder). In my non-simultaneous data the difference in spectral shape could be due to this miscalibration, but may of course result from a genuine spectral evolution between the two observations.

The mass accretion rate $\dot{M}$ through the outer accretion disc is constrained by the observed optical continuum emission. I set the outer accretion disc radius to be equal to the self-gravity radius R_{sg}, beyond which the disc fragments. The X-rays are emitted from a region between R_{cor} (a model parameter which I fit) and R_{isco}, the latter being determined by $a_\star$. Since I have no prior input on $a_\star$ (from e.g. broad Fe Kα) I test both zero- and high-spin cases with $a_\star$ fixed to 0.0 or 0.8. As well as fitting a model in which all of the hard X-ray emission originates from the corona, I also fit models which include a hard X-ray contrbiution from the jet. I model the jet as a broken power-law to allow for some curvature in its shape over the broad energy range. In all models I fix f_{pl} to 0.3 (Done et al. 2012; Jin et al. 2012a). From my models I are able to determine several parameters which I will use to set the external photon field; namely: the size scales and luminosities of the accretion disc, its corona, and the hot torus dust, as well as the temperature of the dust (see Section 4.5.1.3).

The results are presented in Table 4.5 and plotted in Figure 4.8. Both zero spin models represent the data reasonably well, and the accretion disc and hot dust parameters are very similar. The soft excess temperature $kT_{\mathrm{e}} = 0.30$ keV of the zero

spin, no jet model is slightly higher than is typically observed ($\langle kT_{\rm e} \rangle = 0.12 \pm 0.02$ keV, Gierliński & Done 2004). The zero spin plus jet model shows that if the harder X-rays originate from the relativistic jet then it is possible to describe the rest of the optical-to-X-ray SED with a very typical NLS1 model.

All three models imply a relatively high Eddington ratio $L/L_{\rm Edd} \approx 0.6$–$0.8$ but not super-Eddington accretion. I estimate the accretion disc luminosity at $L_{\rm AD} = 2.1 \times 10^{45}$ erg s^{-1} for the zero SMBH spin cases or ≈ 80 % greater in the high-spin case. However, the high spin model is a poorer fit to the data and cannot accommodate a soft excess component in the *XMM-Newton* bandpass. The fitting procedure lowers $kT_{\rm e}$ and raises τ to its maximum permitted value to force the soft excess emission out of the *XMM-Newton* bandpass so as to minimise the soft X-ray power. The soft excess thus appears to have a lower temperature than the inner accretion disc, which is unphysical in this model since the soft Comptonisation region is at smaller radii than the disc, implying that it should be hotter. If I remove this (unseen) soft excess component by setting $f_{\rm pl} = 1$, then I must lower $R_{\rm cor}$ to reduce the power in the coronal component. Consequently, the inner radius of the accretion disc is lower and the accretion disc emission appears in the soft part of the X-ray spectrum, overpredicting the data. In summary, an energy-conserving, high-spin model produces more soft X-ray power than is seen in the data.

With the available data I am unable to rule out the case that the corona produces all of the 2–10 keV X-ray emission. However, I prefer the zero spin model that includes a contribution from the jet for the following reasons. Firstly, it gives a statistically significant improvement in the fit compared to the no jet model with $\Delta\chi^2 = 112$ for four additional free parameters. Secondly, if I allow for jet emission at the hard energies, I recover parameters which are typical for a NLS1, showing a soft excess of temperature $kT_{\rm e} = 0.22$ keV and a soft-spectrum X-ray corona. Thirdly, the similarity of the hard X-ray photon indices (*XMM-Newton*: $\Gamma_{3-10\ \rm keV} = 1.59 \pm 0.02$, *NuSTAR*: $\Gamma_{3-79\ \rm keV} = 1.80 \pm 0.01$ and *Swift* BAT: $\Gamma_{14-195\ \rm keV} = 1.73 \pm 0.02$) are suggestive of a single spectral component, given that the discrepancy between *XMM-*

Newton and *NuSTAR* spectral shapes may be the result of a cross-calibration problem, as noted in Section 4.5.1.1. Taken together with the *Fermi* data, the hard X-rays appear to be the low-energy side of the Compton hump, as I will subsequently show in my jet models. In the following sections I proceed with the parameters determined from the model with zero SMBH spin plus a jet.

Table 4.5: Results from spectral fits to the deabsorbed IR to hard X-ray SED

	$a_\star$	$L/L_{\rm Edd}$	$\dot{M}$ [$M_\odot$/yr]	$R_{\rm cor}$ [$R_{\rm g}$]	$R_{\rm out}$ [$R_{\rm g}$]	$\log(L_{\rm AD})$ [erg/s]	$kT_{\rm e}$ [keV]	τ	$f_{\rm pl}$	$\Gamma_{\rm cor}$	$\log(L_{\rm cor})$ [erg/s]	$T_{\rm tor}$ [K]	$\log(L_{\rm tor})$ [erg/s]	$R_{\rm tor}$ [ld]	χ^2/dof
	(1)	(2)	(3)	(4)	(5)	(6)	(7)	(8)	(9)	(10)	(11)	(12)	(13)	(14)	(15)
(a)	0.0$^{\rm f}$	0.60	0.44	27.2	2450	45.27	0.30	11	0.3$^{\rm f}$	1.76	44.53	1720	44.10	292	799/236
(b)	0.0$^{\rm f}$	0.60	0.44	24.3	2440	45.30	0.22	12	0.3$^{\rm f}$	2.70	44.54	1730	44.10	297	687/232
(c)	0.8$^{\rm f}$	0.81	0.30	13.5	3380	45.55	0.03	100†	0.3$^{\rm f}$	3.25	44.83	1610	44.10	485	916/232

The columns are: (1) dimensionless SMBH spin; (2) Eddington ratio; (3) mass accretion rate; (4) outer coronal radius in gravitational radii, $R_{\rm g} = 2.95 \times 10^{10}$ m $= 1.14 \times 10^{-3}$ light days; (5) outer accretion disc radius which was set to $R_{\rm sg}$; (6) luminosity of the accretion disc; (7) electron temperature of the soft Comptonisation region; (8) optical depth of the soft Comptonisation region; (9) fraction of the disc power below $R_{\rm cor}$ emitted in the power-law tail; (10) photon index of the power-law tail; (11) luminosity of the power-law tail; (12) temperature of the dusty torus; (13) luminosity of the IR radiation from the torus; (14) the dusty torus inner radius in light days, see Section 4.5.1.3 in the text for details; (15) the χ^2 statistic over the number of degrees of freedom (dof) in the model. $^{\rm f}$Parameter was frozen during the fitting procedure. †Parameter has reached the limit of the allowed range. $\dot{M}$ and $R_{\rm tor}$ are not model parameters but have been derived from my results. These models are plotted in Figure 4.8.

4.5.1.2 The BLR luminosity and radius

The emission from the broad line region is another important component of the external photon field which can be Compton-scattered to higher energies by the particles in the relativistic jet. This emission region is located beyond the accretion disc, on a typical scale of several light-weeks. The two relevant measures for my jet modelling are then the luminosity and radius of the broad line region. I have estimated the broad line region luminosity following Celotti et al. (1997) as:

$$L_{\rm BLR} = \Sigma_i L_{i,\rm obs} \frac{\langle L^*_{\rm BLR} \rangle}{\Sigma_i L^*_{i,\rm est}}, \tag{4.5.1}$$

where $\Sigma_i L_{i,\rm obs}$ is the sum of the measured luminosities of the observed broad lines, scaled by the ratio of the estimated total broad line region luminosity $L^*_{i,\rm est}$ to the estimated luminosities of the observed broad lines. Both estimates were taken from the results of Francis et al. (1991) and, in the case of Hα, from Gaskell et al. (1981). The BLR luminosity is determined most accurately based on the actual measurement of the strongest emission lines, e.g. Lyα, C IV, Hα, etc. The optical spectrum covers two of the relevant broad emission lines, namely Hβ and Hα. For their broad components I get a luminosity of $\log L_{\rm H\beta} = 42.02$ erg s^{-1} and $\log L_{\rm H\alpha} = 42.44$ erg s^{-1}, respectively (Landt et al. 2017), which results in a total BLR luminosity of $\log L_{\rm BLR} = 43.33$ erg s^{-1}.

I have estimated the BLR radius in two ways, using both the near-IR and optical radius-luminosity relationships. The near-IR radius-luminosity relationship presented by Landt et al. (2011a, 2013) is based on the rest-frame 1 µm continuum luminosity, which, as these authors show, is still dominated by the ionising accretion disc luminosity. Landt et al. (2017) measured this quantity in the near-IR spectrum to be $\log \nu L_{1\mu\rm m} = 43.92$ erg s^{-1}. The derived BLR radius is then 23 light-days. The optical radius-luminosity relationship, which was most recently calibrated by Bentz et al. (2013), using the rest-frame 5100 Å continuum luminosity. From their optical spectrum Landt et al. (2017) measured this quantity to be $\log \nu L_{5100\ \text{Å}} = 44.05$ erg s^{-1};

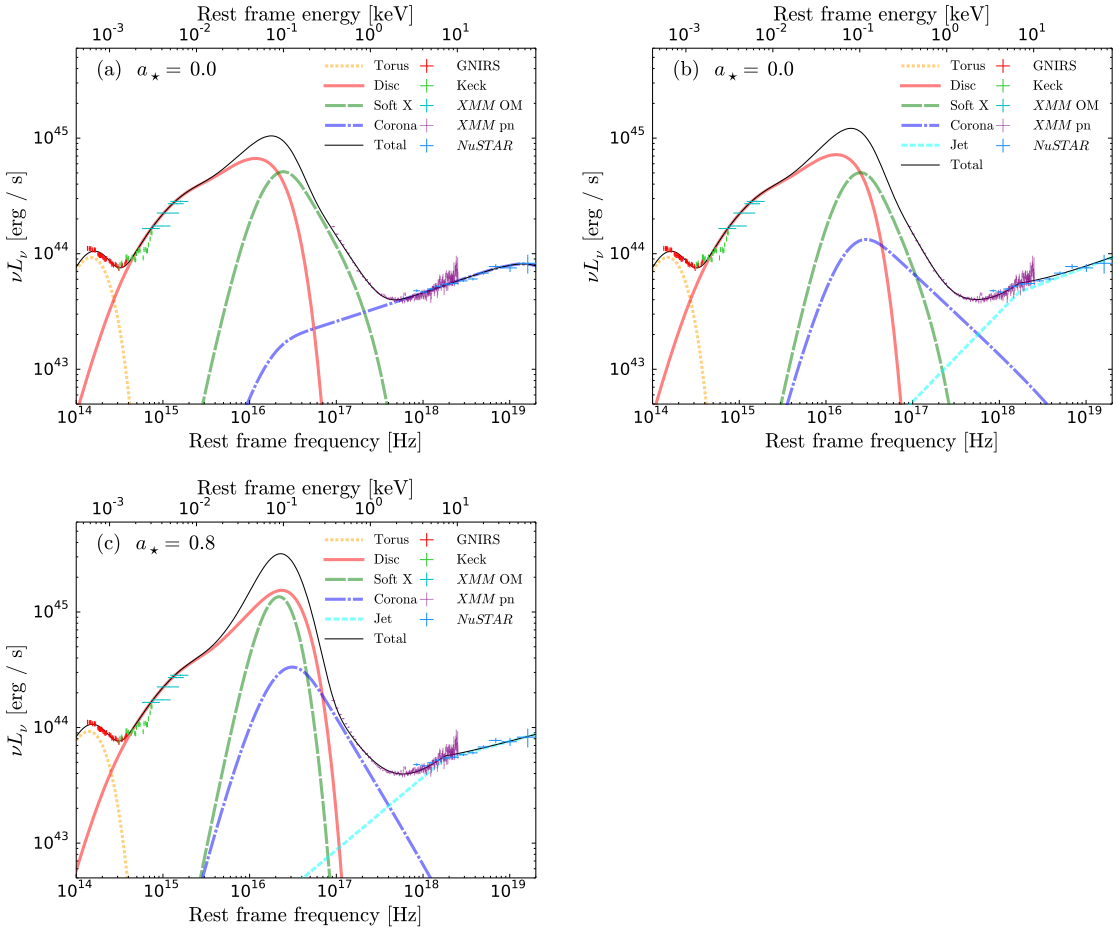

Figure 4.8: IR to hard X-ray SEDs of 1H 0323+342. The data are modelled by the energy-conserving accretion model OPTXCONV which calculates the emission from the accretion disc, corona and soft Comptonisation region ('Soft X'). In addition, I have added a blackbody modelling hot dust emission in the IR and, in models (b) and (c), a broken power-law to model hard X-ray emission from the jet. See Table 4.5 in the text for the model parameters.

the derived BLR radius is then 39 light-days. The two values resulting from the near-IR and optical radius-luminosity relationships are similar within the errors, which, when taken from the scatter in the relations, are $\sim 40 - 50$ %. In the following jet modelling, I have used the average between the two values of 31 light-days.

I note that Wang et al. (2016) calculated a BLR radius of $14.6^{+7.8}_{-2.9}$ light-days from the measurement of the lag in the response of Hβ to changes in the continuum flux. Whilst their estimate of the BLR radius is smaller than my two values it has a large positive error and is discrepant with my average value by only $\approx 2\sigma$.

4.5.1.3 The dusty torus luminosity and radius

The dusty torus is the most extended AGN component which contributes to the external photon field that is upscattered by the jet. This region is located further away from the SMBH than the BLR; indeed its hottest, innermost part may be the outermost boundary of the BLR, on scales of light-months. The relevant measures for my jet modelling are the luminosity, radius and temperature of the hot dust in the torus. The luminosity and temperature of the hot dust result directly from the blackbody fit to the near-IR continuum and are listed in Table 4.5. I have then estimated the hot dust radius using the theoretical relationship between bolometric luminosity and dust sublimation radius for grains with an average size given by Mor & Netzer (2012). I have assumed that the dust sublimation temperature corresponds to the hot dust temperature and since I find this value to be $T_{\rm tor} \sim 1700$ K, which is much higher than the sublimation temperature of ~ 1400 K for a silicate dust composition, I have used their Eqn. (2) for pure graphite dust[8]. The bolometric luminosity results directly from my accretion disc fits and is listed in Table 4.5. The resulting hot dust radius is then ≈ 300 light-days.

[8]In the case of silicate dust the radius increases by a factor of ≈ 1.6 compared with the value I quote here for graphite dust.

Table 4.6: Differences between the external photon field parameters I determined and those calculated from standard assumptions

Parameter		[units]	Standard scaling	Standard value	My value
Eddington ratio	$L/L_{\rm Edd}$		Davis & Laor (2011) Eqn. (7)*	0.66	0.60
Outer corona radius	$R_{\rm cor}$	$[R_{\rm g}]$		60	24
Outer disc radius	$R_{\rm out}$	$[R_{\rm g}]$		1000	2440
Disc luminosity	$\log(L_{\rm AD})$	[erg/s]		45.26	45.30
Corona luminosity	$\log(L_{\rm cor})$	[erg/s]	$= 0.1\ L_{\rm AD}$	44.26	44.54
BLR luminosity	$\log(L_{\rm BLR})$	[erg/s]	$= 0.1\ L_{\rm AD}$	44.26	43.33
BLR radius	$R_{\rm BLR}$	$[R_{\rm g}]$ (ld)	$= 5.29\ R_0\ \left(\frac{L_{\rm AD}}{10^{45}\ {\rm erg\ s^{-1}}}\right)^{1/2}$	4.58×10^4 (52)	2.72×10^4 (30)
Dusty torus luminosity	$\log(L_{\rm tor})$	[erg/s]	$= 0.3\ L_{\rm AD}$	44.74	44.10
Dusty torus radius	$R_{\rm tor}$	$[R_{\rm g}]$ (ld)	$= 132\ R_0\ \left(\frac{L_{\rm AD}}{10^{45}\ {\rm erg\ s^{-1}}}\right)^{1/2}$	1.20×10^6 (1400)	2.63×10^5 (300)
Dust temperature	$T_{\rm tor}$	[K]		370	1730

The scaling parameter $R_0 = 1.89 \times 10^{16}$ cm. See Gardner & Done (2018) for further details. *Here I make another measure of the Eddington ratio, scaled from the optical luminosity determined by Landt et al. (2017) and assuming a radiative efficiency $\eta = 6$ % in the calculation of the bolometric luminosity $L = \eta \dot{M} c^2$.

4.5.2 Determining the jet parameters

4.5.2.1 Calculating the observed jet emission

I use the single-zone leptonic jet model JET of Gardner & Done (2018) to model the full, broadband SED. This model is described in Section 2.4. JET can be used additively with the OPTXCONV code by linking together the parameters $M_{\rm BH}$, $L/L_{\rm Edd}$, i, the comoving distance $D_{\rm c}$ and z. I note that this single-zone model does not calculate all of the radio jet emission. Single-zone models calculate the emission from the base of the jet but most of the radio emission is produced further out. Synchrotron emission in the modelled zone is strongly self-absorbed below the synchrotron self-absorption frequency, $\nu_{\rm ssa}$, with the spectrum below this falling off in intensity as $I \propto \nu^{5/2}$. The observed radio slope in the SED results from the sum of emission from successive regions further along the jet with lower synchrotron self-absorption frequencies. The JET code does not calculate any emission below $\nu_{\rm ssa}$ but in the plots shown in Figure 4.9 I have subsequently added on a ν^0 slope illustrating the emission from multiple zones and I quote $\nu_{\rm ssa}$ in Table 4.8.

4.5.2.2 The site of the γ-ray emission

The location of the energy dissipation region $Z_{\rm diss}$ is an important but unknown factor in the determination of the jet SED. It governs the relative importance of the disc, BLR and torus seed photons in the EC process. Disc photons always arrive from behind the jet and so are de-boosted in the jet frame. However, because the disc is much more luminous than the BLR and torus, disc seed photons may dominate the seed photon energy density seen by the jet if the emission region is very near to the SMBH. When $Z_{\rm diss} < R_{\rm BLR}$, the BLR photons are boosted in the jet frame, so the BLR component will dominate the EC seed photon energy density further from the disc where $R_{\rm out} < Z_{\rm diss} \lesssim R_{\rm BLR}$. The structure and geometry of the BLR is unknown but it is modelled as a thin spherical shell. Following G&T09, the energy density of

BLR seed photons is calculated in three distance ranges: interior to $R_{\rm BLR}$ $U'_{\rm BLR}$ is constant (Eqn. 19 of G&T09); beyond $3R_{\rm BLR}$ it depends on both $Z_{\rm diss}$ and the bulk speed of the jet (Eqn. 20 of G&T09); between $R_{\rm BLR}$ and $3R_{\rm BLR}$ it is calculated as a power-law interpolation. For a $\Gamma_{\rm BLF} = 13$ jet, $U'_{\rm BLR}$ decreases by more than four orders of magnitude between $R_{\rm BLR}$ and $3R_{\rm BLR}$. When $R_{\rm BLR} < Z_{\rm diss} \lesssim R_{\rm tor}$ both the disc and BLR photons are de-boosted in the jet frame and the torus seed photons dominate the energy density.

The issue of whether $Z_{\rm diss}$ is near to, or far from, the SMBH is contentious and has been much discussed in the literature (see Madejski & Sikora 2016 for a recent overview). The rapid variability of jet emission suggests a compact dissipation region. Under the assumptions of a conical jet that radiates across its entire cross-section, this in turn implies a dissipation region relatively near to the central engine. On the other hand, the high energy density of UV photons near to the SMBH is a source of opacity to γ-rays and suggests a more distant dissipation region, particularly for objects which exhibit very high-energy (TeV) γ-ray emission. Ghisellini & Tavecchio (2015) showed that the dissipation regions of 191 FSRQs were almost always within the BLR radius. Sikora et al. (1994) suggested that it may be Lyα emission from the BLR which provides the dominant source of seed photons encountered by the jet. Conversely, in a study of 36 FSRQ-type blazars, Zheng et al. (2017) found that the dissipation regions were all outside of the BLR, and many were within the region in which the seed photon field is dominated by IR radiation from the torus. Since I have determined the external photon field of 1H 0323+342, I can use this to predict the jet SED for a range of $Z_{\rm diss}$ over three orders of magnitude. I consider the three possibilities that the seed photon field is dominated by: the accretion disc ($Z_{\rm diss} = 1280\ R_{\rm g}$: the mean $Z_{\rm diss}$ of FSRQs determined by Ghisellini et al. 2010, hereafter G10); the BLR ($Z_{\rm diss} \approx R_{\rm BLR} = 2.72 \times 10^4\ R_{\rm g}$) or the torus ($Z_{\rm diss} \approx R_{\rm tor} = 2.63 \times 10^5\ R_{\rm g}$). By comparing the predicted SED at each of these energy dissipation sites to the observed SED I can provide an observational constraint on $Z_{\rm diss}$.

4.5.2.3 Constraints on input jet model parameters

Whilst $Z_{\rm diss}$ is *a priori* unknown, I am able to fix or limit the range of several model parameters on observational or physical grounds; these are listed in Table 4.7.

The external photon field: The parameters of the external photon field are fixed to those I measured or derived from my zero spin plus jet model in Section 4.5.1.

The jet parameters: The jet viewing angle towards 1H 0323+342 was recently determined from VLBA monitoring by Fuhrmann et al. (2016a). They analysed Very Long Baseline Array (VLBA) radio images taken on several occasions between October 2010 and July 2013. Several components in the jet had apparent velocities up to $\beta \sim 7$. Using this information the authors estimated that the jet is aligned at an angle $i \leqslant 4$–13° to the line of sight. If I make the reasonable assumption of $i = 1/\Gamma_{\rm BLF}$, this also gives a bulk Lorentz factor $\Gamma_{\rm BLF} \geqslant 4.4$–$14.3$ which is consistent with the $\langle\Gamma_{\rm BLF}\rangle = 13$ for FSRQs determined by G10.

To produce the observed SED slope at radio frequencies, I require the sychrotron self-absorption frequency $\nu_{\rm ssa} \gtrsim 10^{11}$ Hz. For $R_{\rm diss} = \phi Z_{\rm diss}$, the synchrotron self-absorption frequency

$$\nu_{\rm ssa} = \left(4.62 \times 10^{14} K B^{5/2} \frac{\phi Z_{\rm diss}}{0.7}\right)^{2/7} \tag{4.5.2}$$

where K is the normalisation of the particle distribution. So the dominant factor governing $\nu_{\rm ssa}$ is the magnetic field B, with $\nu_{\rm ssa} \propto B^{5/7}$. The luminosity of the synchrotron peak depends on the magnetic field as $L_{\rm synch} \propto B^2$. I require that the synchrotron emission does not contribute substantially to the IR part of the SED as defined by the *Spitzer* and the *WISE* data, which I attribute to thermal emission from the extended dusty torus. The magnetic field must therefore be strong enough to result in a suitably high $\nu_{\rm ssa}$, but not so strong that the synchrotron emission dominates in the IR.

The position and shape of the two jet emission peaks are influenced by the shape of the accelerated electron distribution. I adopt as initial values the mean FSRQ

Table 4.7: Constraints on jet model parameters

Param.	Value	Constraint	Ref.
$M_{\rm BH}$	$= 2 \times 10^7$ M$_\odot$	My mass estimate	[1]
z	$= 0.0625$	NIR / opt. narrow lines	[1]
$R_{\rm in,cor}$	$= 24.3\ R_{\rm g}$	Accretion disc fitting	[Section 4.5.1.1]
$R_{\rm out}$	$= 2440\ R_{\rm g}$	Accretion disc fitting	[Section 4.5.1.1]
$\log(L_{\rm cor})$	$= 44.54$ erg/s	Accretion disc fitting	[Section 4.5.1.1]
$\Gamma_{\rm cor}$	$= 2.70$	Accretion disc fitting	[Section 4.5.1.1]
$E_{\rm cor}^{\rm cut}$	$= 150$ keV	Power-law cut-off	[2]
$\log(L_{\rm BLR})$	$= 43.33$ erg/s	Scaled from $L_{\rm H\alpha,H\beta}$	[Section 4.5.1.2]
$R_{\rm BLR}$	$= 2.72 \times 10^4\ R_{\rm g}$	Scaled from $L_{\rm 1\mu m,5100\AA}$	[Section 4.5.1.2]
$\log(L_{\rm tor})$	$= 44.10$ erg/s	Accretion disc fitting	[Section 4.5.1.3]
$R_{\rm tor}$	$= 2.63 \times 10^5\ R_{\rm g}$	Dust sublimation radius	[Section 4.5.1.3]
$T_{\rm tor}$	$= 1730$ K	Accretion disc fitting	[Section 4.5.1.3]
i	$\leqslant$ 4–13°	Radio jet kinematics	[3]
$\Gamma_{\rm BLF}$	$\geqslant$ 4.4–14.3	$i = 1/\Gamma_{\rm BLF}$	[3]
ϕ	$= 0.1$ radians	Jet opening angle	[2]
B	≈ 2.6	$\langle$FSRQ$\rangle$ value	[2]
$\gamma_{\rm min}$	$= 1$	$\langle$FSRQ$\rangle$ value	[2]
$\gamma_{\rm brk}$	≈ 300	$\langle$FSRQ$\rangle$ value	[2]
$\gamma_{\rm max}$	≈ 3000	$\langle$FSRQ$\rangle$ value	[2]
s_1	≈ 1	$\langle$FSRQ$\rangle$ value	[2]
s_2	≈ 2.7	$\langle$FSRQ$\rangle$ value	[2]
$P_{\rm j}$	$\lesssim 10\ L_{\rm AD}$	Typical jet power	[4]
$U_{\rm e}/U_B$	≈ 1	Equipartition	[5]

References: [1] Landt et al. (2017); [2] G10; [3] Fuhrmann et al. (2016a); [4] Ghisellini et al. (2014); [5] Dermer et al. (2014). $E_{\rm cor}^{\rm cut}$ is the high-energy cut-off of the coronal power-law; other parameters are described in Section 4.5.2 and Section 4.5.1.1 of the text.

values of Lorentz factors γ and slopes s from G10. I leave $\gamma_{\rm min}$ fixed to 1 and note that the value of $\gamma_{\rm max}$ does not generally affect the shape of my SED substantially.

The principle of energy equipartition: The lowest-energy solution to jet emission requires that the electron and magnetic field energy densities are approximately equal, i.e. $U_{\rm e}/U_B \approx 1$, (see e.g. Dermer et al. 2014). These quantities are not input parameters to the code, but they are calculated as outputs which can then be used as a check of how physically reasonable my models are. This ratio of energy densities can be tuned if necessary by adjusting the parameters $P_{\rm rel}$, B and $\Gamma_{\rm BLF}$.

4.5.3 Jet emission models

The full SED includes low-energy data from Effeleberg / IRAM and *Planck* and high-energy data from *Swift* BAT and *Fermi*, in addition to the mid-energy data I modelled in detail in Section 4.5.1. I then fit a FSRQ-like jet to my data and determine if the jet parameters I obtain are within the range found for the modelled EC emission of other blazars. My approach to this question is different from previous work. Whilst other studies of 1H 0323+342 have fit its SED including a jet (Paliya et al. 2014; Yao et al. 2015a), they made a number of assumptions about the external photon field. I apply the model BBODY+OPTXCONV+JET, tying together the parameters $M_{\rm BH}$, $L/L_{\rm Edd}$, i, the comoving distance $D_{\rm c}$ and z between OPTXCONV and JET. Unlike Section 4.5.1.1, i is not fixed to zero, but is set to be the inverse of the bulk Lorentz factor.

The jet power $P_{\rm j}$ may be expected to scale with the SMBH mass and mass accretion rate such that $P_{\rm j} \propto \dot{m} M_{\rm BH}$, where $\dot{m} = \dot{M}/\dot{M}_{\rm Edd}$. Lengths will scale linearly with the SMBH mass, so $Z_{\rm diss} \propto M_{\rm BH}$. Under the assumption that the jet power is a constant fraction of the accretion power, the power injected into the relativistic electrons ($P_{\rm rel}$), the normalised accretion rate ($\dot{m}$) and SMBH mass are related so that $P_{\rm j} \propto P_{\rm acc} \rightarrow P_{\rm rel} \propto \dot{m} M_{\rm BH}$. The power in the magnetic field is also a constant fraction of the accretion power. In the rest frame $P_B \propto R_{\rm diss}^2 U_B$, where the magnetic field energy density $U_B \propto B^2$; it follows that $B \propto \sqrt{\dot{m}/M_{\rm BH}}$. (See Gardner & Done 2014 for a more detailed discussion on the scaling relations.)[9] Following Gardner & Done (2018), I can determine $Z_{\rm diss}$, $P_{\rm rel}$ and B by appropriately scaling the mean FSRQ values presented by G10. For the other jet parameters, I adopt the mean value $\Gamma_{\rm BLF} = 13$ and $\langle$FSRQ$\rangle$ values for the electron distribution given in Table 4.7. Applying this appropriately-scaled FSRQ jet to my external photon field gives the

[9] Heinz & Sunyaev (2003) present a non-linear scaling of core radio flux with SMBH mass: $F_\nu \propto M_{\rm BH}^{1.4}$. This scaling relates to the radio synchrotron emission from the core of the jet and accounts for the fact that larger jets from AGN with more massive SMBHs are less self-absorbed and therefore more radiatively efficient for a given $\dot{m}$ at a particular radio frequency. Rather than applying their non-linear scaling (based on a single emission band), I follow the scalings of Gardner & Done (2014) as described above to model the full, multiwavelength SED.

scaled FSRQ model, shown as the blue line in the top-left panel of Figure 4.9 and the parameters of which are given in Table 4.8. This predicted SED is very flat because $B \propto \sqrt{\dot{m}/M_{\rm BH}}$ so the magnetic field for a low-mass, high accretion rate object is very high (here $B = 38$ G) and synchrotron cooling is highly efficient, resulting in an SED with low Compton dominance.

The product of $\dot{m}$ and $M_{\rm BH}$ I determine for 1H 0323+342 is a factor of ten lower than that for the average $M_{\rm BH} = 10^9$, $\dot{m} = 0.1$ FSRQ presented in G10. Simply scaling down the average FSRQ SED by a factor of ten produces the pink line shown in the same plot. It is immediately apparent that whilst the product $\dot{m}M_{\rm BH}$ for 1H 0323+342 is an order of magnitude lower than that of a standard FSRQ, its jet luminosity is at least *another* order of magnitude lower than these scalings predict.

In the EC-disc model I keep $Z_{\rm diss} = 1280\ R_{\rm g}$ (the same value as in the standard scaled models); as can be seen in Figure 4.9, at this location it is the disc photons which are upscattered into the Compton hump. However, I adjust the other parameters so as to produce the best fit to the observed SED. It is clear that it has been necessary to reduce B and $P_{\rm rel}$ dramatically compared with the scaled FSRQ model. As a result the total jet power $P_{\rm j}$ is approximately an order of magnitude lower than predicted by the scaling and in this model it is approximately half the accretion disc luminosity. To find a near-equipartion solution it has been necessary to reduce the $\Gamma_{\rm BLF}$ slightly to 12, but in doing so I can achieve $U_{\rm e}/U_B = 1.1$. The slope s_1 has been increased slightly to better match the shape of the SED but the other parameters defining the accelerated electron distribution are the same. In this model the γ-rays are produced by the upscattering of accretion disc photons, with a minor contribution from BLR photons at the hardest γ-ray energies. The model reproduces the observed jet emission at both low and high frequencies reasonably well.

In the EC-BLR model the dissipation region has been set to $Z_{\rm diss} = 2.7 \times 10^4\ R_{\rm g}$, just inside of the BLR radius where seed photons from the BLR are responsible for the majority of the γ-ray emission. The parameters of the accelerated electron distribution have been changed more significantly than in the EC-disc model to

match the shape of the high-energy part of the SED. However, the synchrotron component of this model now vastly overpredicts the observed radio emission. This is partly a consequence of increasing $Z_{\rm diss}$ which increases the size of the dissipation region and thus reduces the energy density and lowers $\nu_{\rm ssa}$. If I wish to match the high-frequency radio data in flux, I overpredict that at lower frequencies.

The dissipation region in the EC-tor model is set to $Z_{\rm diss} = 2.6 \times 10^5\ R_{\rm g}$, just inside of the hot dust radius. The BLR emission seen by the jet is now strongly de-boosted and the distance from the SMBH is so great that the energy density of disc and corona seed photons is also very low. At this distance the seed photons from the torus are, in effect, solely responsible for the observed γ-ray and hard X-ray emission. In the EC-tor model even with a relatively low B and high $P_{\rm rel}$, the ratio of $U_{\rm e}/U_B = 0.26$. Because the jet is upscattering low-frequency photons from the torus it is necessary to increase $\gamma_{\rm max}$ to produce the observed γ-rays. This EC-tor model also overpredicts the observed radio emission.

In summary, I conclude that the dissipation region must be located well within $R_{\rm BLR}$.

4.6 Discussion

4.6.1 Is 1H 0323+342 a typical NLS1?

The 2–10 keV photon indices of NLS1s are generally soft ($\langle\Gamma\rangle_{\rm NLS1} = 2.19 \pm 0.10$, Leighly 1999), whereas that of 1H 0323+342 is much harder ($\Gamma_{2-10\ \rm keV} = 1.7$). The X-ray RMS spectrum of the fast variability shows a clear break at ≈ 1 keV. At least two spectral components are therefore required to fit the *XMM-Newton* EPIC spectra. Landt et al. (2017) did not find such clear evidence for multiple spectral components in their analysis of *Swift* XRT data. Curvature in the X-ray spectrum was only apparent in the co-added spectrum of three *Swift* observations. Here, the higher quality of X-ray data obtained from a long *XMM-Newton* observation affords a better opportunity for a more detailed spectral decomposition. However, some

Table 4.8: Jet parameters obtained from spectral fits to the full multiwavelength SED with BBODY+OPTXCONV+JET models

Parameter	Units	Model value			
		Scaled	EC-disc	EC-BLR	EC-tor
$Z_{\rm diss}$	$[R_{\rm g}]$	1280	1280	2.7×10^4	2.6×10^5
$Z_{\rm diss}$	[ld]	1.5	1.5	30	300
$a_\star$		0.0	0.0	0.0	0.0
i	[deg]	4.41	4.77	4.98	4.98
$\Gamma_{\rm BLF}$		13.0	12.0	11.5	11.5
δ		13.0	12.0	11.5	11.5
B	[G]	38.0	8.00	0.75	0.15
$\gamma_{\rm min}$		1.00	1.00	1.00	1.00
$\gamma_{\rm brk}$		300	300	150	300
$\gamma_{\rm max}$		3000	3000	3000	30000
$\gamma_{\rm cool}$		19	47	58	163
s_1		1.00	1.50	2.00	1.50
s_2		2.70	2.70	4.25	3.20
$\log(\nu_{\rm ssa})$	[Hz]	11.6	10.6	9.67	8.76
$\log\left(\nu^{\rm sync}_{\rm peak}\right)$	[Hz]	13.8	12.5	11.0	11.2
$\log\left(\nu L^{\rm sync}_{\nu_{\rm peak}}\right)$	[erg/s]	45.56	43.12	42.96	42.92
$\log(P_{\rm rel})$	[erg/s]	42.24	41.00	41.80	41.50
$\log(P_{\rm rad})$	[erg/s]	43.95	42.51	42.76	42.74
$\log(P_{\rm e})$	[erg/s]	43.76	42.74	43.53	43.23
$\log(P_B)$	[erg/s]	44.12	42.70	43.25	43.82
$\log(P_{\rm p})$	[erg/s]	45.91	45.01	46.14	45.32
$\log(P_{\rm j})$	[erg/s]	45.93	45.01	46.14	45.34
$P_{\rm j}/L_{\rm AD}$		4.3	0.52	6.9	1.1
$U_{\rm e}/U_B$		0.44	1.1	1.9	0.26

Parameters are described in Section 4.5.2.1 and Section 4.5.3 of the text.

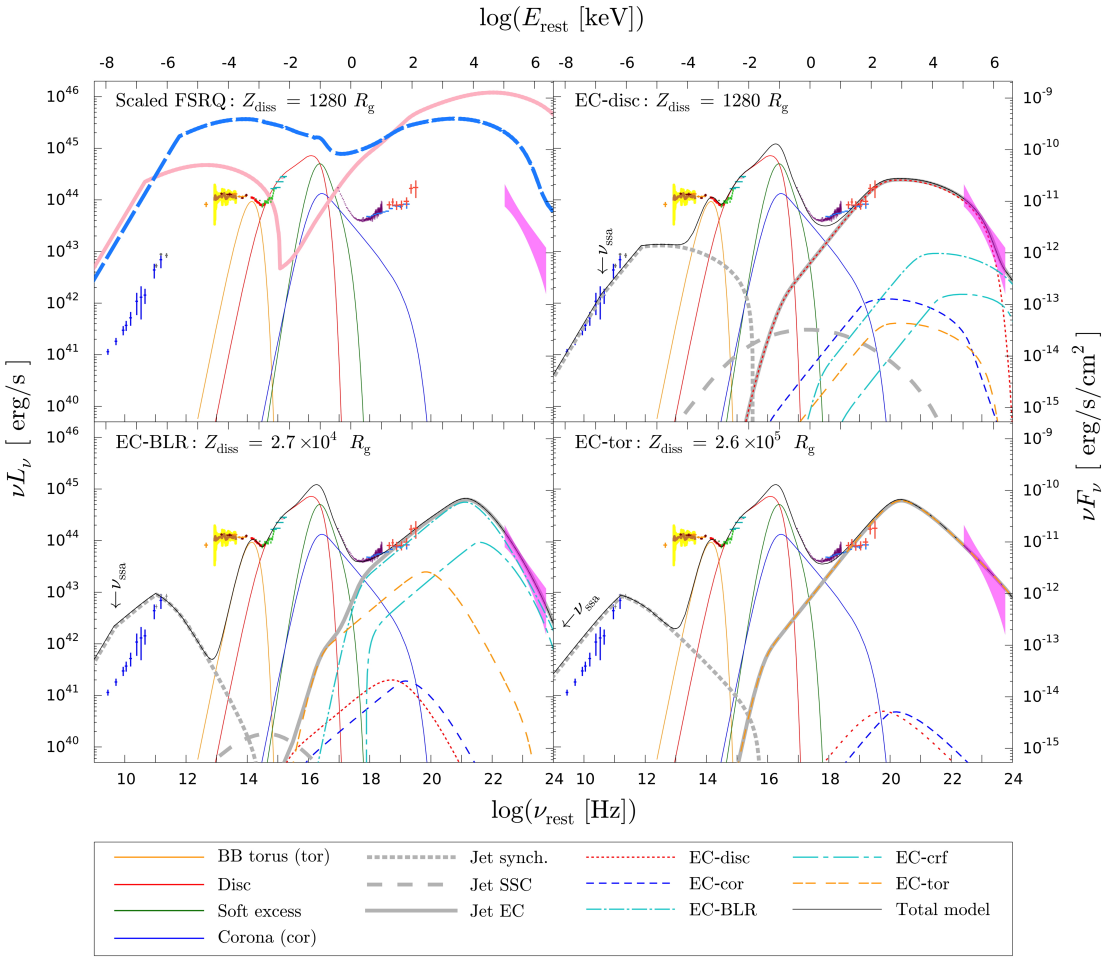

Figure 4.9: SED fits to radio to γ-ray data with the jet dissipation region at increasing distance $Z_{\rm diss}$ from the SMBH. The model parameters are given in Table 4.8. In the top left panel the blue dashed line shows the total jet plus accretion flow emission corresponding to the scaled FSRQ model; the pink solid line shows a typical high-mass FSRQ jet scaled down in luminosity by a factor of ten. I show the three components of the jet emission (synchrotron, synchrotron self-Compton 'SSC' and external Compton 'EC') as grey lines. The individual EC components (from the disc, corona, BLR, reflection of the corona off the BLR 'crf' and torus) are shown as coloured dotted and dashed lines. Note that the jet emission code does not calculate the radio spectrum below the synchrotron self-absorption frequency $\nu_{\rm ssa}$ indicated; here I have extended the radio emission to lower frequencies for illustrative purposes. I do not model the far- or mid-IR data since I attribute this emission to the cool dusty torus; my model here includes emission from the hot dust only. The data are colour-coded the same as in Figure 4.1; see Section 4.2 in the text for a description of the data.

degeneracy between spectral models still remains, as was discussed in Section 4.5.1.1 where I presented energy-conserving, physical models of the X-ray spectra.

Previous studies have attempted to determine the SMBH spin of 1H 0323+342 by fitting a blurred reflection model to X-ray spectral data, but the results are not conclusive. Paliya et al. (2014) found a high spin with $a_\star = 0.96 \pm 0.14$ by modelling *Swift* XRT and BAT data whereas Yao et al. (2015a) found an upper limit of $a_\star < 0.13$ using *Suzaku* data of a more limited energy range. I explored models which included the effects of SMBH spin in Section 4.5.1.1. Both zero spin models provide reasonably good fits to the data, but the high spin model overpredicted the soft X-ray power. My modelling is therefore suggestive of a low SMBH spin scenario for 1H 0323+342. However, my model makes a number of assumptions which, if relaxed, could in principle allow for a higher SMBH spin. The model is energy-conserving and assumes that the accretion power passing through the outer and inner disc is equal. This would not be the case if some power were lost as e.g. as disc wind or transported up the jet itself (Blandford & Payne 1982). A recent well-studied example where this may be the case is the super-Eddington AGN RX J0439.6-5311 (Jin et al. 2017b,a). A larger SMBH mass could also allow for a higher spin. Here, I fixed the mass to the value $M_{\rm BH} = 2 \times 10^7$ M$_\odot$ determined by Landt et al. (2017) from measurements of the hydrogen Balmer and Paschen lines. However, there is emerging evidence (from e.g. accretion disc peak fitting, Calderone et al. 2013; spectropolarimetry, Baldi et al. 2016 and the $M_{\rm BH}$-$L_{\rm bulge}$ relation, D'Ammando et al. 2017) that the SMBH masses of NLS1s are underestimated when using the standard single-epoch virial methods. These studies have found NLS1 SMBH masses more in line with the rest of the RL-AGN population with $M_{\rm BH} \geqslant 10^8$ M$_\odot$. In the case of this source, the two-month reverberation mapping study of 1H 0323+342 by Wang et al. (2016) also found a similarly low SMBH mass of $\left(3.4^{+0.9}_{-0.6}\right) \times 10^7$ M$_\odot$, so at present there is no strong evidence that the SMBH mass of 1H 0323+342 is substantially greater than the value I have used. My model also assumes that the accretion flow is not disrupted by the launching and presence of the powerful relativistic jet.

When modelling the *XMM-Newton* X-ray spectra, I allowed the Galactic column to be a free parameter and found the best fits required an excess of Galactic column density of about 50 % above the D&L90 value. Whilst the modelled value is more similar to the total column quoted by Willingale et al. (2013), I consider that it is unlikely that the Galactic column is in fact as high as my models determine since I found no evidence for the additional absorption in the *XMM-Newton* RGS spectrum or my optical and UV data (see the Appendix for further details). However, it is well established that NLS1s commonly exhibit complex intrinsic absorption (e.g. Komossa 2000) and emission (e.g. Smith et al. 2008) features. I tested several possibilities including neutral or ionised intrinsic absorption, and *ad hoc* absorption and emission features following Gallo et al. (2004) but these did not make as great an improvement in the fit as the increased neutral Galactic column or 'correct' the shape of the deabsorbed spectrum. I have adopted the increased Galactic column as the simplest solution in my models which corrects the spectral shape and gives the greatest improvement in the fit statistic. Doing so does not substantially change the main conclusions from my subsequent SED modelling. However, if I do not allow for this additional absorbing column, then I am unable to include a soft Comptonisation region in the models presented in Section 4.5.1.1. Consequently the corona photon index is slightly harder and the accretion disc emission increases by a factor ≈ 1.4 compared with my zero spin plus jet model. Nevertheless, these changes are not significant enough to basically alter my jet modelling or conclusions.

Apart from its jet, there is nothing I have found here that sets 1H 0323+342 apart from other NLS1s; its mass and Eddington ratio are both only slightly higher than the average values reported by Rakshit et al. (2017). My extensive exploration of the modelling parameter space shows that the IR-to-X-ray SED of 1H 0323+342 is within the range observed for NLS1s, but with the addition of a jet component. Why this particular NLS1 possesses a relativistic jet when the vast majority of others do not therefore remains an open question.

In relation to the overall AGN population, 1H 0323+342 has:

- a SMBH mass $M_{\rm BH} = 2 \times 10^7$ $M_\odot$ which is lower than than both the mean SMBH mass of broad-line Seyfert 1s (BLS1s), 10^8 $M_\odot$ (Rakshit et al. 2017) and typical blazars which have even higher masses (10^8–10^9 $M_\odot$: Ghisellini et al. 2010);

- a higher accretion rate than BLS1s ($L/L_{\rm Edd} \approx 0.6$ compared with the BLS1 mean ≈ 0.1: Rakshit et al. 2017) and typical blazars which have $\langle L/L_{\rm Edd} \rangle_{\rm FSRQ} = 0.1$ and $\langle L/L_{\rm Edd} \rangle_{\rm BL\,Lac} < 10^{-3}$ (Ghisellini et al. 2010);

- a prominent soft X-ray excess: whereas the X-ray emission from many AGN is well-represented by a power-law of index $\Gamma \approx 2$, 1H 0323+342 has an excess of soft emission below ≈ 2 keV with index $\Gamma = 3.59$;

- a higher radio loudness parameter than the majority of AGN: for 1H 0323+342, $R_{\rm 1.4GHz} = 318$ (Foschini 2011) whereas the majority of AGN (≈ 90 %) are radio-quiet with $R < 10$;

- a particularly high radio loudness parameter for a NLS1: the radio-loud fraction of NLS1s is very low, Komossa et al. (2006) determined that only ≈ 7 % (≈ 2.5 %) have $R > 10$ ($R > 100$);

- clear evidence for a powerful, relativistic jet: currently only 23 other NLS1s have been detected in γ-rays by *Fermi*.

1H 0323+342 is therefore an unusual source in these respects.

4.6.2 Contribution of the jet to the IR and X-ray emission

Turning to a much lower-frequency part of the SED, my *Spitzer* IRS spectrum is shown in Figure 4.2. It can been seen in the figure that the *WISE* photometry agrees well with my *Spitzer* data despite the former being taken approximately eighteen months later, indicating very little, if any, variability over a timescale of years. In the *Spitzer* IRS spectrum two strong, broad humps can be seen at ≈ 11 and 18 µm

which I attribute to the 9.7 and 18 µm silicate features commonly seen in emission in type 1 AGN spectra. The 9.7 µm feature is often not observed at the rest-frame wavelength 9.7 µm, but redward of this position. The apparent redshift of this feature was seen in all of the *Spitzer* spectra of a sample of 12 RL-AGN studied by Landt et al. (2010), and had previously been seen in a few other sources (e.g. Schweitzer et al. 2008; Sturm et al. 2005; Siebenmorgen et al. 2005) but its cause is currently unknown. Some weak polycyclic aromatic hydrocarbon (PAH) features may also be present in the spectrum. Since I do not see a featureless continuum or flux variability which would be expected from synchrotron emission, these features suggest that most of this mid/far-IR emission originates from the torus rather than from the jet. This interpretation is contrary to that of others (Abdo et al. 2009b; Paliya et al. 2014; Yao et al. 2015a) who have studied this object and attributed the IR emission to the jet synchrotron component. As a consequence my jet models have a lower-luminosity synchrotron peak and higher Compton dominance in the SED.

In Section 4.2.2.1 I measured the flux and hence the luminosity of the mid-IR emission line [O IV] λ25.89 µm. I compared the luminosity of the line to the X-ray luminosities in the *XMM-Newton* and *Swift* BAT bands. Using the derived luminosity of [O IV], $\log(L_{[\mathrm{OIV}]}) = 41.3$, and the 2–10 keV X-ray luminosity, $\log(L_{2-10\ \mathrm{keV}}) = 43.9$, I can compare these values with those of the sample of AGN studied by Diamond-Stanic et al. (2009); it can be seen that 1H 0323+342 is broadly consistent with other Seyfert 1s shown in their Figure 4. However, looking at the corresponding relation between the hard X-rays and [O IV] (e.g. LaMassa et al. 2010, their Figure 8) it can be seen that 1H 0323+342, having $\log(L_{14-195\ \mathrm{keV}}) = 44.45 \pm 0.05$, lies above the correlation, suggesting it is more luminous in hard X-rays by a factor of about five with respect to the other Seyfert 1 AGN in their sample. The detection of the [O IV] line is clearly of limited significance, given the S/N of the *Spitzer* IRS spectrum. If instead I treat the measured flux as an upper limit, then 1H 0323+342 must be even more overluminous in 14–195 keV X-rays, in terms of the correlation found for other

AGN. This excess of hard X-ray luminosity supports my preference for a model in which emission from the relativistic jet makes a contribution to the hard X-rays.

In Section 4.4.2.2 I show that the continuum fit to the X-ray spectrum is improved if I add a narrow line feature at 6.43 keV with EW $= 36 \pm 8$ eV which I associate with neutral Fe Kα. For comparison, Shu et al. (2010) measured the EWs of the narrow cores of Fe Kα in a sample of Seyfert AGN observed by *Chandra*, finding $\langle \mathrm{EW} \rangle = 53 \pm 3$ eV. In RL AGN, the contribution to the X-ray continuum of Doppler-boosted emission from the jet will result in a relative weakness (of the EW, by dilution from the additional continuum flux) of the fluorescent Fe Kα emission line. Bianchi et al. (2007) derived a relationship between the EW of the narrow Fe Kα and the 2–10 keV luminosity based on RQ type 1 AGN (Eqn. (1) in their paper). From this relation, I can estimate that the narrow Fe Kα EW should be ≈ 56 eV if 1H 0323+342 were RQ and the jet made no contribution to the 2–10 keV continuum. The lower EW I have determined tentatively suggests some jet emission may be present in the *XMM-Newton* bandpass.

4.6.3 The external photon field

My new approach here was to use the wealth of quasi-simultaneous spectroscopy and photometry to derive the seed photons for the external Compton components input into the jet code. This is clearly a better approach than assuming a given SED shape, especially given my well-sampled SED.

The accretion disc luminosity (consequently the Eddington ratio) I determine from my zero spin plus jet model actually agrees very well with the values I would obtain from estimating the mass accretion rate $\dot{M}$ from the optical luminosity (Davis & Laor 2011) and assuming $\eta = 6$ % to calculate the bolometric luminosity from $L = \eta \dot{M} c^2$. The agreement of these values with my zero spin plus jet SED model lends some support to this model over the high-spin case model where the Eddington ratio and disc luminosity were both higher. In the G&T09 model, the corona extends out

to 60 R_g and has one tenth of the accretion disc luminosity. As can be seen from Table 4.6, my corona is more luminous but more compact than this, extending to 24 R_g. The corona photon index in the G&T09 model is assumed to be 2 whereas the values I determined are much softer at 3.59 in Section 4.4.2.1 and 2.7 in the zero spin plus jet model. Despite being more luminous than the standard model assumes, the EC-corona emission is not a very strong component in any of my models. The JET model is insensitive to subtle changes in the spectral shape and geometry of the corona so the difference in photon indices and radii also have very little impact on my results. G&T09 scale the BLR luminosity and radius from the accretion disc luminosity. Table 4.6 shows that their standard assumptions predict a larger and much more luminous BLR than I determined in Section 4.5.1.2. The smaller radius I determine is in better agreement with the value obtained from the reverberation mapping study of Wang et al. (2016). Interestingly, my value for the BLR luminosity is a factor of ten lower than the G&T09 model assumption that it is one tenth of the accretion disc luminosity. The BLR radius that I determine is just over half of the value calculated in the standard model. However, the energy density of BLR seed photons is $U'_{\rm BLR} \propto L_{\rm AD}$ and $U'_{\rm BLR} \propto R_{\rm BLR}^{-2}$, so the overall difference in $U'_{\rm BLR}$ is a factor ≈ 3 which does not substantially change my conclusions.

The torus I adopt is smaller and less bright than the standard model assumes. My infrared spectrum only samples emission from the hottest dust on the inner edge of the torus, so the temperature I determine from my models is much greater than that in the G&T09 prescription which characterises the dust as much cooler and more extended. Of course, both are simplifications of the actual torus temperature-radius and luminosity-radius profiles. Had I used the standard assumptions with an energy density $U'_{\rm tor}$ smaller by a factor ≈ 5, the torus component in the EC-BLR model would be weaker. The dissipation region in my EC-tor model would have been placed even further out, so $\upsilon_{\rm ssa}$ would be smaller and the model would still overpredict the radio emission.

4.6.4 The impact of variability

I have reason to claim that the non-simultaneity of my broadband data does not strongly affect my results and conclusions. The *XMM-Newton* optical/UV photometry and X-ray spectra are truly simultaneous and sample the outer and inner accretion flows, respectively. The high-frequency end of the *XMM-Newton* spectra and low-frequency end of the *NuSTAR* spectra are of very similar flux levels despite the seventeen-month gap between observations. As noted in Section 4.5.1.1, the apparent discrepancy in spectral shape may be due to a calibration issue. Considering the higher frequencies, the flux levels of the *NuSTAR* and *Swift* BAT X-ray spectra are consistent in their region of overlap and the *Fermi* γ-ray data was chosen to sample the period covering the *XMM-Newton* observation. Turning to lower frequencies, the *XMM-Newton* optical photometry (simultaneous with the X-rays) are consistent with points sampling the continuum determined from the Keck optical spectrum. The GNIRS spectrum was flux-scaled to match the Keck data, because I suspect that the apparent difference in flux is due to a shift resulting from the uncertain absolute flux calibration of the near-IR spectrum rather than genuine source variability (as described in Landt et al. 2017). After this correction has been applied, the near-IR data then appears to connect with the mid- and far-IR bands sampled by *Spitzer* and *WISE*. As I commented in Section 4.6.2, the *WISE* photometry agrees very well with the *Spitzer* data even though the observations were separated by more than a year.

With regards to the Effelsberg and IRAM radio data, Angelakis et al. (2015) reported flux density variability magnitudes on average ≈ 30 % and up to 63 %, with the variability being more pronounced at higher frequencies. Whilst the flux densities at lower frequencies were generally stable, frequencies 14.6 GHz and above exhibited occasional flaring. However, the mean values from which I used in my analysis are not strongly affected by the flaring episodes and are broadly consistent with the stable, baseline level.

I noted in Section 4.4.1.2 and Section 4.2.3.3 that the X-ray and γ-ray data were obtained during periods of low activity. Given the constancy in flux betweeen neighbouring frequency bands, it is therefore reasonable to conclude that all of my multiwavelength data is appropriate to describe this source in a low state. Although my data are mostly not simultaneous, for the reasons given above I do not expect that this impairs my overall conclusions.

4.6.5 The origin of the γ-ray emission

It is generally accepted that in the case of a high-accretion rate blazar, such as 1H 0323+342, the γ-ray emission results from the EC process. Here I compare my general findings with those from other similar studies. Both Abdo et al. (2009b) and Paliya et al. (2014) (for the quiescent state) found that the dissipation region must be relatively near to the SMBH, with $Z_{\rm diss} \approx 1300\ R_{\rm g}$, very similar to the value I used in the EC-disc model here, which adopts the mean FSRQ $Z_{\rm diss}$ of G10. Yao et al. (2015a) were unable to constrain the location so well, since models with a dissipation region located inside or outside of the BLR both reasonably reproduced their broadband SED. In my preferred EC-disc model, the jet emission region appears to be relatively near the accretion disc, with EC-disc photons producing the hard X-rays and the γ-rays. This is different to the findings of Paliya et al. (2014) where EC-BLR photons were dominant in all states (both quiescent and flaring). This is also different to Yao et al. (2015a) who considered only EC-BLR and EC-torus situations. Here, both the EC-BLR and EC-tor models are shown to overpredict the observed radio emission.

In many jet models, such as mine, it is assumed that $R_{\rm diss} = \phi Z_{\rm diss}$, therefore a compact emission region (with small $R_{\rm diss}$) must be relatively near to the core of the AGN. However, other geometries have been proposed such as the 'spine-sheath' (e.g. Sol et al. 1989, Ghisellini et al. 2005, Sikora et al. 2016) or 'turbulent cell' (e.g. Marscher & Jorstad 2010) models. In these cases, the jet does not radiate across

its entire cross-section so a compact emission region does not necessarily imply one that is close to the SMBH. For simplicity, and for the ease of comparison with the work of other authors, I have not considered alternative jet geometries here.

Overall, my EC-disc model has a set of parameters that best match the broadband SED, across an exceptionally wide range of frequencies, from the radio to γ-rays. This model has the added attraction that is very close to an energy equipartition solution with $U_e/U_B = 1.1$. The parameters of the accelerated electron distribution for this model are the same as those for the scaled-down FSRQ model, with the exception of the slope s_1 which is 1.5 in the former and 1.0 in the latter. It differs from the scaled FSRQ model mainly in that its magnetic field and power injected into the electrons are much lower than predicted.

The jet parameters determined from the fit to the SED are model-dependent. The parameter space is large and complex, so it cannot be claimed that one set of parameters represents a unique solution. I have attempted to restrict the various parameters through observational or theoretical considerations, using the modelling of G&T09 and G10 as a framework; Table 4.7 lists these parameters and their determined values or ranges. The external photon field parameters are very well determined from the multiwavelength data. Jet parameters such as the inclination angle are determined observationally and (under the assumption $\Gamma_{\rm BLF} \approx 1/i$) this sets a reasonable range for $\Gamma_{\rm BLF}$. The parameters of the accelerated electron distribution are also likely to be relatively well determined; Table 4.8 shows that I do not have to alter these greatly from the mean FSRQ values to achieve a reasonable fit to the data. It was necessary to adjust the slope s_1 of the distribution. Since the shape of the electron distribution is directly related to the (observed) shape of the synchrotron and EC humps, this minor alteration is justified by the data. The similarity of the injected electron distribution parameters to the mean FSRQ values implies that the electron acceleration mechanism in 1H 0323+342 is very similar to that in a typical FSRQ. Less well-determined quantities include the precise values of B and $P_{\rm rel}$ which in turn influence the jet power. However, as described in Section 4.5.3 it is possible

to tune B and $P_{\rm rel}$ and $\Gamma_{\rm BLF}$ together to find a near-equipartition solution.

4.6.6 Where does 1H 0323+342 lie in the blazar sequence?

My interpretation of mid-IR emission as being torus-dominated limits the peak luminosity of the synchrotron component and increases the dominance of the EC peak in the SED. I therefore arrive at an SED shape typical of a FSRQ but at a luminosity more like that of a BL Lac. It has been predicted that low-mass, lower-luminosity FSRQs would be detected by *Fermi*, which has a greater sensitivity than its predecessor *EGRET*. However, the blue line in the top-left panel of Figure 4.9 shows that a scaled-down FSRQ SED is both more luminous and has a flatter shape more like a BL Lac than is observed. If I simply scale down a typical FSRQ SED by a factor of ten (the pink line in the top-left panel of Figure 4.9), it is also much more luminous than the data although the shape is more similar to the one I fit in the EC-disc model. In both cases the synchrotron and Compton humps in the SED are at frequencies more typical of FSRQs than the 'bluer' SEDs of BL Lacs. The accelerated electron distribution in my EC-disc model has parameters very similar to that of a typical FSRQ; the higher-frequency peaked BL Lacs have much greater $\gamma_{\rm brk}$ and $\gamma_{\rm max}$. Additionally, the bulk Lorentz factor of this model is more similar to that of an FSRQ than a BL Lac (which have $\langle\Gamma_{\rm BLF}\rangle = 15$, G10). 1H 0323+342 lies in the low-luminosity region of the blazar sequence shown on the left of Figure 1.8: its luminosity is similar to the BL Lacs, but its SED shape is very similar to the higher-luminosity FSRQs.

Ghisellini et al. (2014) found a clear positive correlation between the jet and disc powers in a sample of over 200 blazars. As well as this relation, they also found that the jet powers exceeded the accretion disc luminosities typically by a factor ~ 10. Clearly, this is not the case for 1H 0323+342 where the jet power in my EC-disc model is approximately half the disc luminosity. Zero SMBH spin implies a low radiative efficiency, $\eta = 0.06$, and I can determine that $\log\left(\dot{M}c^2\right) = 46.5$, so 1H 0323+342 lies

well outside of the 3σ dispersion of $P_{\rm j}$-$\dot{M}c^2$ determined by Ghisellini et al. (2014). Even if I allow for a high spin (which my energy-conserving models disfavoured) I calculate $\log\left(\dot{M}c^2\right) = 45.8$ and 1H 0323+342 is then only just inside of the 3σ region. In this sequence of blazar jet power versus accretion power, 1H 0323+342 lies below the main track populated by BL Lacs and FSRQs (see Figure 5.11 in the next chapter and compare with the right-hand panel of Figure 1.8). I showed in my EC-disc jet model that in order to match the observed SED it is necessary to reduce both $P_{\rm rel}$ and B from the values predicted by the scaled FSRQ model. As well as having a very low jet power for a FSRQ, 1H 0323+342 has a low jet power compared with the prototypical γ-NLS1 PMN J0948+0022, as was noted by both Abdo et al. (2009b) and Paliya et al. (2014). Since the strength of the magnetic field determines how efficiently the jet can extract the rotational energy of the SMBH, it is possible that the (relatively) weak magnetic field of 1H 0323+342 is less well able to extract spin power and inject it into the jet. My findings also indicate that it is plausible that 1H 0323+342 has a lower SMBH spin than other blazars, and consequently is unable to host as powerful a jet.

4.6.7 A comparison of jet powers

I claim that 1H 0323+342 hosts an underpowered jet for a FSRQ, compared with those presented by G10 and Ghisellini et al. (2014). The determined jet power is strongly dependent on the assumptions made in the modelling. It can be seen from Tables 4.8 and 4.9 that the total jet power is usually dominated by the kinetic power (i.e. the bulk motion of protons carried in the jet). The value of the total jet power calculated therefore hinges on the assumption of one cold proton per radiating electron. This is somewhat controversial, since it is possible that the jet emission is due to an electron-positron plasma containing no protons; however, G10 justify this assumption in FSRQ-type jets. Additionally, this simple assumption is commonly adopted by other authors so this issue does not prevent a comparison of jet powers between works. Other authors have determined the jet power of 1H 0323+342 by

Table 4.9: Comparison of 1H 0323+342 jet powers

Jet model	$\log(P_{\rm rad})$ (1)	$\log(P_{\rm e})$ (2)	$\log(P_B)$ (3)	$\log(P_{\rm p})$ (4)	$\log(P_{\rm j})$ (5)
EC-disc (5°)	42.51	42.74	42.70	45.01	45.01
EC-disc (3°)	42.18	42.15	42.58	44.44	44.45
Abdo[a]	42.8	42.7	43.3	44.3	44.4
Paliya[b]	41.29			44.06	
Paliya[c]	43.94	43.34	43.42	45.82	45.82
Yao[d]	43.9	43.4	42.6	43.7	44.2

Here I compare the jet powers calculated for my EC-disc model with those of: [a]Abdo et al. (2009b); the quiescent state model of [b]Paliya et al. (2014); the model of [c]Paliya et al. (2019) and the IC/BLR model of [d]Yao et al. (2015a). In the columns I quote the logarithms of: (1) the radiative power; (2) the power in the bulk motion of electrons; (3) the Poynting power; (4) the power in the bulk motion of protons and (5) the total jet power, in units erg s^{-1}.

fitting a single-zone leptonic jet model to its broadband SED; I tabulate the relevant values in Table 4.9. It can be seen that power that was calculated for my preferred model, 'EC-disc (5°)', is greater than those of these previous studies and here I discuss some of the differences.

The most straightforward comparison is to the model adopted by Abdo et al. (2009b) because they use the most similar modelling prescription to my own. However they have adopted a SMBH mass estimate half of my value, so whilst their $R_{\rm diss}$ is equal to mine in mass-scaled units, it is a factor of two smaller in absolute terms which affects the calculated energy densities. Another key difference is their use of a smaller inclination angle $i = 3°$ rather than my value of $i = 1/\Gamma_{\rm BLF} \approx 5°$, although they use the same $\Gamma_{\rm BLF} = 12$ as us. The Doppler boosting in their case is therefore greater by a factor of four and they can fit the observed γ-ray emission with a jet which is around five times less powerful than mine. I find that I can replicate the shape of my EC-disc SED model at a lower inclination angle of 3° by turning down B and $P_{\rm rel}$, but keeping $\Gamma_{\rm BLF} = 12$. In this case I obtain a jet power very similar to Abdo et al. (2009b), as shown in Table 4.9.

The quiescent state model of Paliya et al. (2014) has approximately an order of

magnitude lower kinetic power than my model. This difference is in part due to their choice of a much lower $\Gamma_{\rm BLF} = 7$; since $P_{\rm p} \propto \Gamma^2_{\rm BLF}$, for the same number of protons the kinetic power would be reduced by a factor ≈ 0.3.

The IC/BLR model of Yao et al. (2015a) has a very low $\Gamma_{\rm BLF} = 2.7$, therefore the bulk motion of particles is not the dominant factor in the jet power, and the radiative power contributes approximately half of the total jet power. Their injected electron distribution is skewed towards higher Lorentz factors, with $\gamma_{\rm brk} = 1073$ in their case compared with my value of $\gamma_{\rm brk} = 300$. As a result, the power in the bulk motion in protons is only approximately twice the power in the bulk motion in electrons. However, since they do not quote the injected power $P_{\rm rel}$ I am unable to make a more detailed comparison.

This diversity of jet powers illustrates the strong dependence on the modelling assumptions. Since I adopted the same approach as G10, the most appropriate comparison is to their large sample of FSRQs. The models of other authors can fit similar SEDs for this source and they have found even lower jet powers. Therefore, I am confident that my principal conclusion that 1H 0323+342 hosts a low-powered jet remains robust.

4.7 Summary and conclusions

I assembled a well-sampled and wide-ranging multiwavelength data set including my new infrared, optical and X-ray spectra and supplemented these with archival data including spectra and photometry in other wavebands from radio through to γ-rays. The observations, data reduction and reference sources were described in Section 4.2. In Section 4.4 I performed a temporal and spectral analysis of a long (80 ks) *XMM-Newton* observation. I found evidence for complexity in the low-energy range of the X-ray spectrum which is possibly due to absorption in addition to the Galactic column. The dereddened / deabsorbed IR, optical and X-ray spectra and optical/UV photometry were used to fit an energy-conserving accretion disc model to my data

in Section 4.5.1.1. The results from this modelling, along with measurements of emission lines observed in my optical spectrum, allowed me to define the photon field in the vicinity of the central engine of 1H 0323+342. In particular, I determined the size scales and luminosities of the accretion disc and its corona, the BLR and the dusty torus. I then introduced these parameters into a relativistic jet emission code to determine the jet parameters which best reproduce the observed SED. The results from my modelling of the jet are presented in Section 4.5.3.

My main conclusions are as follows:

(i) It is possible to fit an energy-conserving accretion flow model to the IR-to-X-ray SED in which the accretion flow has parameters typical of a NLS1 and where the jet makes a contribution to the hard X-rays. This is only possible if the SMBH spin is low or zero; a high SMBH spin model predicts more energy in soft X-rays than is seen in the data. I find the X-ray emission has contributions from a soft-spectrum corona and a soft Comptonisation region with temperature $kT_{\rm e} = 0.22$ keV, and determine a relatively high Eddington ratio of $L/L_{\rm Edd} = 0.6$.

(ii) I detect a weak iron line in the *XMM-Newton* EPIC spectra which has an energy consistent with neutral Fe Kα fluorescence.

(iii) I find that 1H 0323+342 has a broadband SED with a similar shape to an FSRQ (showing high Compton dominance) but with a similar luminosity to a BL Lac. I show that this source is *not* a consistent with being a mini FSRQ, since scaling down standard FSRQ jet parameters by SMBH mass and mass accretion rate produces an SED model which vastly overpredicts the observed emission. The jet in 1H 0323+342 appears to be underpowered by at least an order of magnitude compared with predictions made by scaling an average FSRQ jet. With respect to the accretion power, the source lies outside of the 3σ dispersion region of the $P_{\rm j}$-$\dot{M}c^2$ relation determined by Ghisellini et al. (2014).

(iv) I show that (within the assumptions of my jet model) the energy dissipation region of the jet must be located near to the SMBH and well within the BLR radius. In my preferred jet emission model, seed photons from the accretion disc are upscattered to produce the observed γ-ray emission.

My detailed study of 1H 0323+342 has shed new light on its accretion properties e.g. the Eddington ratio the nature of its outflow (jet), the interplay between the relativistic particles and the radiation field and its relation to other blazars. However, this is only one example of the small group of γ-NLS1s, and in-depth studies of a number of other examples need to be made to reveal whether they share similar characteristics, or are a heterogeneous sample.

Chapter 5

The γ-ray emitting narrow-line Seyfert 1 PKS J1222+0413

In this chapter I present a multi-frequency study of PKS J1222+0413 (4C +04.42), currently the second-highest redshift γ-ray emitting narrow-line Seyfert 1 (γ-NLS1). I present a determination of its supermassive black hole (SMBH) mass from new spectroscopic data in Section 5.1.2. PKS J1222+0413 is found to have a SMBH mass which is much greater than most other NLS1s, $M_{\rm BH} \approx 2 \times 10^8$ M$_\odot$, and similar to those found in flat spectrum radio quasars (FSRQs). This source therefore provides insight into how the jets of γ-NLS1s relate to those of FSRQs. As a result of its higher mass, its broad emission lines are on the borderline of the typical 2000 km s^{-1} limit which defines the NLS1 class. I examine whether this source may be considered a 'true' NLS1.

The accretion disc peak is a prominent feature in the spectral energy distribution (SED) of PKS J1222+0413 (unlike some other γ-NLS1s in which the disc emission is overwhelmed by the jet); PKS J1222+0413 is therefore another excellent source in which to explore the disc-jet connection. I assemble a broadband SED including several new datasets: X-ray data obtained with the *NuSTAR* and *Neil Gehrels Swift* observatories; near-infrared, optical and UV spectroscopy obtained with VLT X-shooter; and multiband radio data from the Effelsberg telescope. These new

observations are supplemented by archival data from the literature. Taking a similar approach to that taken with 1H 0323+342 in the previous chapter, I apply physical models to the broadband SED, parameterising the accretion flow and jet emission to investigate the disc-jet connection. The ambient photon field produced by the accretion flow is parameterised and self-consistently applied within a model of the relativistic jet. As with 1H 0323+342, I test simple scaling relations for the jet with the SMBH mass and accretion rate. I determine the power in the jet and compare this to the accretion power and the jet power of other blazars including the lower-mass 1H 0323+342. I discuss how these two γ-NLS1s relate to other radio-loud NLS1s and other blazars.

5.0.1 The source PKS J1222+0413

PKS J1222+0413 (RA: 12 22 22.548, Dec: +04 13 15.75) was identified as a γ-ray NLS1 candidate by Yao et al. (2015b) and, at redshift $z = 0.9662$, is currently the second most distant example of this class known. From its SDSS spectrum, they determined its mass to be $M_{\rm BH} = 1.8$–2.0×10^8 $M_\odot$. Its simultaneous and quasi-simultaneous SED was studied by Giommi et al. (2012), although at the time it was not known to be a NLS1. In this chapter I present new data for this source from VLT X-shooter (Section 5.1), *NuSTAR* (Section 5.2.1.1) and Effelsberg (Section 5.2.2.1). The X-shooter spectrum samples the accretion disc emission and several broad emission lines, from which the SMBH mass is estimated in Section 5.1.2. Because of its prominent accretion disc emission, PKS J1222+0413 is another ideal object in which to examine the disc-jet connection. The VLT X-shooter data enables me to investigate the NLS1 nature of the source and measure the AGN continuum emission from the accretion disc. In Section 5.3.1 I describe how I use the multiwavelength data to determine the ambient photon field contributions from the accretion disc, X-ray corona, BLR and torus.

The 0.3–10 keV X-ray band has been shown to contain contributions from both the

accretion flow and jet (e.g. Chapter 4, Larsson et al. 2018) whereas the higher-energy X-rays, sampled by *NuSTAR* and *Swift* BAT, are jet-dominated.

For my adopted cosmology, the redshift $z = 0.9662$ implies a luminosity distance of 6332.3 Mpc and a flux-to-luminosity conversion factor of 4.80×10^{57} cm^2. Length scales are often quoted in gravitational radii, $R_{\rm g} = GM_{\rm BH}/c^2 = 2.95 \times 10^{11}$ m $= 1.14 \times 10^{-2}$ light days for my derived mass.

5.1 X-Shooter spectroscopy

5.1.1 The observations and data reduction

I have obtained X-shooter (Vernet et al. 2011) observations of five γ-NLS1s (including PKS J1222+0413) in the Southern and equatorial sky, with the aim of characterising their accretion disc continuum and emission line properties. By operating three spectrographs simultaneously (in the near-infrared, optical and near-ultraviolet), X-shooter offers a very wide wavelength coverage from 300 to 2500 nm. The $0.9'' \times 11''$, $1.2'' \times 11''$, $1.3'' \times 11''$ slits were used, giving spectral resolutions $R \approx 5600$, 6700 and 4000 in the IR, optical and UV spectra, respectively. The observation was conducted on 3 April 2017 under favourable weather conditions with clear skies and seeing $\approx 1''$ at 500 nm. The on-source integration time was 1 hour and the mean S/N achieved in the IR, optical and UV spectra were 12, 16 and 23, respectively.

The data reduction was performed with the ESO REFLEX software which outputs wavelength- and flux-calibrated 1D spectra. Corrections for telluric absorption in the optical and UV spectra were performed with the xtellcor_general tool available as part of the SPEXTOOL IDL package (Vacca et al. 2003; Cushing et al. 2004). The final science spectrum is shown in Figure 5.1.

To sample the AGN continuum emission within the X-shooter spectral range, I averaged the flux in several emission line free windows of width 50 Å. These were (rest frame): 1660, 2000 and 2200 Å observed in the UV; 3050, 3930 and 4205 Å

observed in the optical; 5100, 6205, 8600 and 11020 Å observed in the IR. Five of these windows are those suggested by Capellupo et al. (2015) for the purpose of modelling accretion disc emission in SEDs.

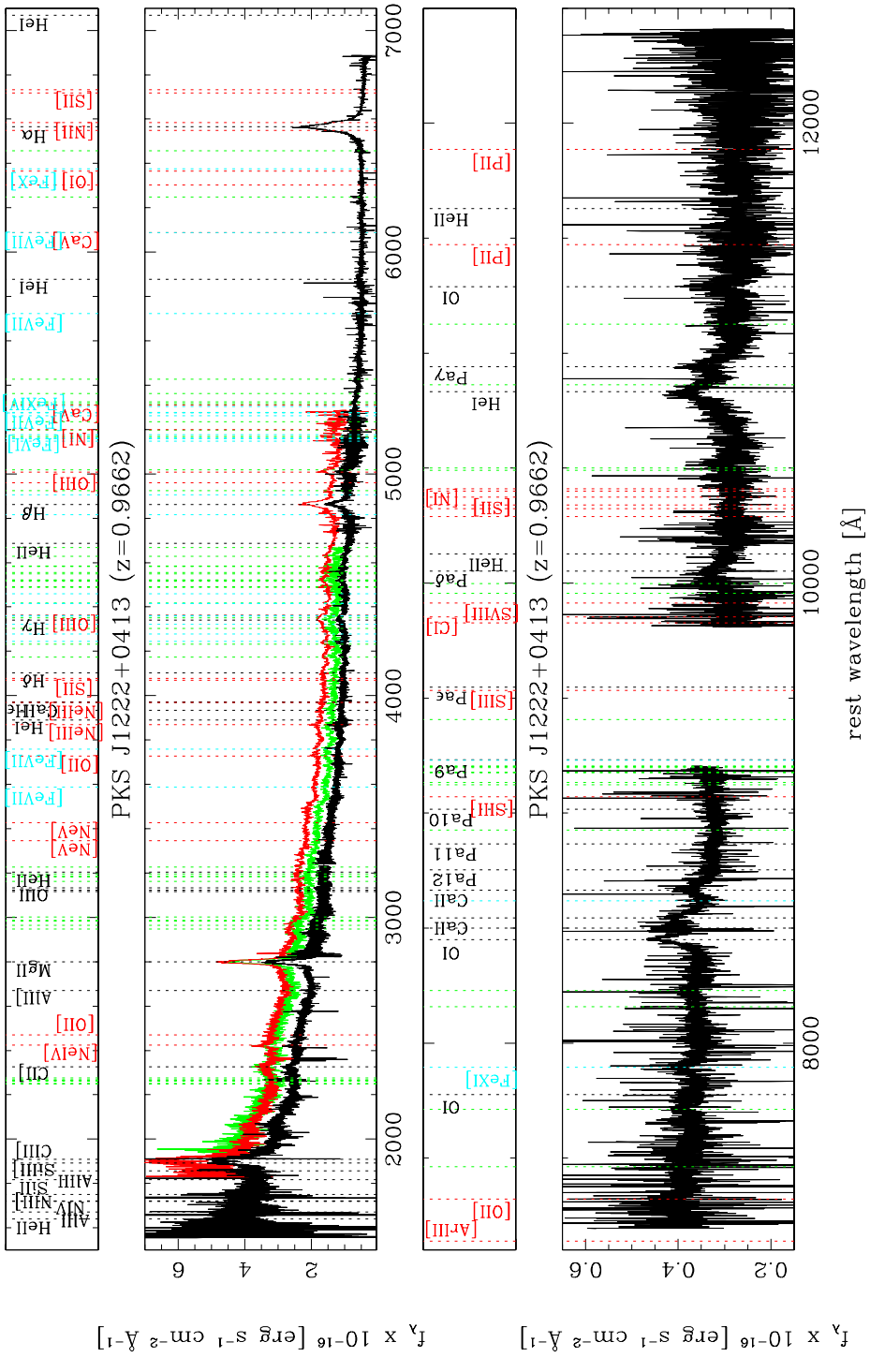

Figure 5.1: VLT X-shooter spectra (black) taken 3 April 2017. SDSS spectra taken 13 February 2008 and 26 March 2011 are overplotted in green and red, respectively.

5.1.2 Estimates of the black hole mass

I estimate the SMBH mass of PKS J1222+0413 using virial scaling relations employing the full widths at half-maximum (FWHMs) of the broad components of permitted emission lines (namely Hα, Hβ and Mg II) and the ionising continuum luminosities measured at 5100 and 3000 Å in the rest frame. All of these quantities are covered simultaneously by my X-shooter spectrum. The measurements of the 5100 Å and 3000 Å continuum luminosities are straightforward and I get values of $\log \nu L_{5100\text{Å}} = 45.56$ erg s^{-1} and $\log \nu L_{3000\text{Å}} = 45.66$ erg s^{-1}, respectively.

Before measuring the emission line widths and fluxes, Fe II emission complexes around Hβ and Mg II were subtracted following the method described in Section 4.3 of the previous chapter. The Mg II λ2008 emission line is a blended doublet of lines centred at 2795 and 2802 Å with an intensity ratio of approximately 1.2:1. To determine the widths of the individual broad lines I model the doublet as the sum of two broad Lorentzians with their intensities and wavelength separation fixed to the theoretical values. Additionally, I include two narrow Gaussian lines to account for any contribution from the narrow emission line region. The narrow lines are fixed to the same intensity ratio and separation, and their widths are limited to be in the range $300 \leqslant \text{FWHM} \leqslant 900$ km s^{-1}. The fitting is performed with a custom PYTHON script employing the LMFIT package, which uses the Levenberg-Marquardt method of least-squares fitting. I find that the inclusion of the narrow lines does not improve the fit therefore I model the doublet simply as the sum of two Lorentzians (see Figure 5.2). The FWHM of these lines is ≈ 1750 km s^{-1}. Using the recently-recalibrated SMBH mass relationship of Mejía-Restrepo et al. (2016)[1], I estimate the SMBH mass to be $\left(2.6^{+2.0}_{-1.2}\right) \times 10^8$ M$_\odot$.

In order to correctly measure the widths of the Balmer emission line broad components, I need to subtract any contribution from the narrow line region. Commonly,

[1]Specifically, I use the calibration for the local continuum fit corrected for small systematic offsets (see their Table 7).

the [O III]λ5007 forbidden emission line is taken as being representative of the narrow emission line profiles. A narrow line with the same profile as [O III]λ5007 is then subtracted from the (total) permitted line profiles, in principle leaving only their broad components. However, the [O III]λ5007 line is very weak so its profile is unsuitable for this purpose. Instead, I measure its total flux and use this to estimate the likely scaled flux of narrow Hβ in the following way. 'Normal' Seyferts have a typical [O III]λ5007 to narrow Hβ flux ratio of ≈ 10 (e.g. Cohen 1983) and analyses of large samples have found consistent narrow line ratios in NLS1s (e.g. Véron-Cetty et al. 2001; Zhou et al. 2006; Rakshit et al. 2017). I estimate the [O III]λ5007 line luminosity by integrating the observed flux density and I determine $\log L_{[\mathrm{OIII}]} = 42.3$ erg s^{-1}. Assuming the ratio $L_{[\mathrm{OIII}]}/L^{\mathrm{n}}_{\mathrm{H}\beta} = 10$ for this source, $\log L^{\mathrm{n}}_{\mathrm{H}\beta} = 41.3$ erg s^{-1}, which is negligible compared to the total line luminosity $\log L_{\mathrm{H}\beta} = 43.11$ erg s^{-1}. Clearly, if the contribution from the narrow line component is negligible then I can measure the FWHM of Hβ directly from its observed profile and I obtain FWHM(Hβ) ≈ 1760 km s^{-1}, which is extremely close to the FWHMs of the blended components of the Mg II doublet. Using the Bentz et al. (2013) radius-luminosity relationship for the Hβ line[2], derived from optical reverberation mapping results, I determine a BLR radius of 260^{+91}_{-67} light-days. Then, assuming a geometrical scaling factor of $f = 1.4$ appropriate for FWHM measures (Onken et al., 2004), I derive a SMBH mass of $\left(2.2^{+0.8}_{-0.5}\right) \times 10^8$ M$_\odot$. I measure a FWHM = 1850 km s^{-1} for Hα. Using the SMBH mass relationship of Mejía-Restrepo et al. (2016) I estimate the SMBH mass to be $\left(2.5^{+1.1}_{-0.8}\right) \times 10^8$ M$_\odot$. These mass estimates and the relations used to calculate them are tabulated in Table 5.1.

My estimates of the SMBH mass based on the ionising continuum luminosity and the width of the broad Balmer emission lines Hα and Hβ and the Mg II emission line give a very small range of values of $\approx 2.2 - 2.6 \times 10^8$ M$_\odot$, with an average value of $\approx 2.4 \times 10^8$ M$_\odot$.

Alternative methods to estimate the SMBH mass, which are based on the line

[2]Specifically, their 'Clean2+ExtCorr' calibration.

Table 5.1: Estimates of the black hole mass of PKS J1222+0413

Measurements	$M_{\rm BH}$ (10^8 $M_\odot$)	Reference
$\log \nu L_{3000\text{Å}} = 45.66$ erg s^{-1} FWHM(Mg II)=1750 km s^{-1}	$2.6^{+2.0}_{-1.2}$	Table 7 of Mejía-Restrepo et al. (2016)
$\log \nu L_{5100\text{Å}} = 45.56$ erg s^{-1} FWHM(Hα)=1850 km s^{-1}	$2.5^{+1.1}_{-0.8}$	Table 7 of Mejía-Restrepo et al. (2016)
$\log \nu L_{5100\text{Å}} = 45.56$ erg s^{-1} FWHM(Hβ)=1760 km s^{-1}	$2.2^{+0.8}_{-0.5}$	Table 14 of Bentz et al. (2013)
$\log L_{\rm H\alpha} = 43.65$ erg s^{-1} FWHM(Hα)=1850 km s^{-1}	$0.5^{+0.3}_{-0.2}$	Table 7 of Mejía-Restrepo et al. (2016)
$\log L_{\rm H\beta} = 43.11$ erg s^{-1} FWHM(Hβ)=1760 km s^{-1}	$0.8^{+0.5}_{-0.3}$	Table 2 of Greene et al. (2010b)

Note: The 1σ error is derived from the instrinsic scatter rather than the errors on the best-fit parameter values.

luminosity instead of the ionising continuum luminosity (e.g. Greene et al. 2010b; Mejía-Restrepo et al. 2016) are also considered and I quote the results in Table 5.1. These estimates are in the range of $\sim 0.5 - 0.8 \times 10^8$ $M_\odot$, which are a factor of ~ 4 smaller than found previously. Since I use the same broad line FWHMs in both estimates, the difference in the estimated masses is due to the different choice of proxy for the ionising luminosity (i.e. the monochromatic continuum luminosity or the broad line luminosity). I argue that it is unlikely that the difference in masses is due to an overestimation of the 3000 Å and 5100 Å luminosities because of unsubtracted emission from the host galaxy or the jet. Firstly, for a bright AGN such as this, I expect the host galaxy emission to be relatively weak, as was previously noted by Yao et al. (2015b). Certainly at 3000 Å in the rest frame the host galaxy emission will be negligible. Second, estimates of the mass depend approximately on the square root of the (continuum or line) luminosity. The two mass estimation methods would agree only if I have over-estimated the AGN contribution to $L_{5100\text{Å}}$ and $L_{3000\text{Å}}$ by a factor $\sim 4^2$, which is highly unlikely. If it is the case that $L_{5100\text{Å}}$ and $L_{3000\text{Å}}$ are contaminated, then since the mass estimates using both luminosities are similarly high, they must contain an approximately equal fraction of contaminating emission (i.e. the contaminating non-acrretion disc emission must have a spectral shape similar

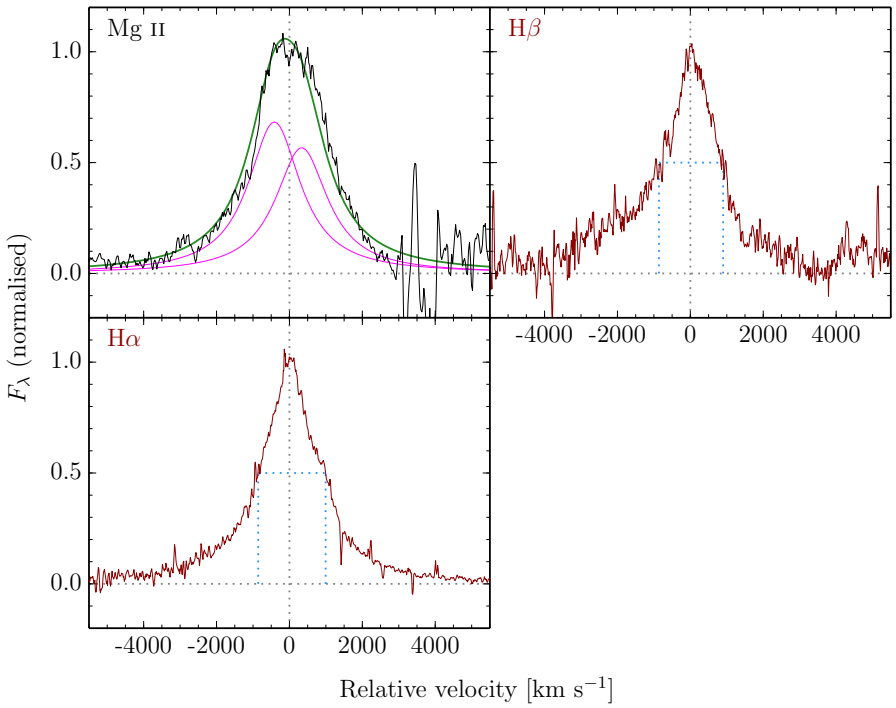

Figure 5.2: The profiles of the three broad emission lines Hα, Hβ and Mg II that I used to estimate the SMBH mass for PKS J1222+0413. The profiles are shown in velocity space relative to the expected rest-frame wavelength and have been Fe II- and continuum-subtracted and normalized to the same peak intensity. In the top left panel, the Mg II profile has been modelled as the sum of two Lorentzians (magenta) and the total modelled profile is shown in green. Since the narrow line region likely makes a negligible contribution to the Balmer line fluxes, the FWHM of the broad Hβ and Hα lines may be estimated directly from the observed line profiles, as shown.

to that of an accretion disc); again this seems contrived. My SED models in the following sections also demonstrate the accretion disc emission dominates at 5100 and 3000 Å (see Figures 5.9 and 5.10). In Chapter 2, Figure 2.1, I have compared the two methods of BLR radius and SMBH mass estimations using large samples of AGN. I find that values derived using the line luminosities are systematically smaller than those using the continuum luminosities. It can be seen that PKS J1222+0413 is within the scatter of other AGN.

The SMBH mass was previously estimated by Yao et al. (2015b). These authors used the width of the Hβ broad component (modelled with a broad Lorentzian profile) and the 5100 Å continuum luminosity and obtained a value of $\approx 2 \times 10^8$ M$_\odot$, which

is consistent with my estimates using the emission line FWHMs and continuum luminosities. I adopt the mass 2×10^8 $M_\odot$ in the following.

5.2 The multiwavelength data set

In the following section I describe the data used to assemble the broadband SED (Figure 5.3).

5.2.1 Data quasi-simultaneous with X-shooter

5.2.1.1 NuSTAR

I obtained an X-ray observation of PKS J1222+0413 with the *Nuclear Spectroscopic Telescope Array* (*NuSTAR* Harrison et al. 2013) on 2017 June 27–18 (OBS ID: 60301018002). The data reduction was performed following the method described in Landt et al. (2017) (see Section 2.3.1 in that paper) and employing the latest software available (NuSTARDAS version 1.7.1, HEASOFT version 6.21 and CALDB version 20170222). The sum of good-time intervals after event cleaning and filtering the event files is 24.5 ks for both FPMA and FPMB. The signal-to-noise ratio is 25.5 and 15.5 per module for the 3–10, and 10–79 keV bands, respectively. The PSF-corrected source count rate was stable around $0.10\,s^{-1}$ per module throughout the observation.

The *NuSTAR* spectra were analysed using XSPEC (Arnaud, 1996). FPMA and FPMB spectra were fitted simultaneously, without co-adding, with a cross-normalisation factor allowed to vary during the fit. Galactic absorption was assumed to be fixed at $1.64 \times 10^{20}\,cm^{-2}$, according to (Kalberla et al., 2005). A simple power-law model already fits the data very well, with $\chi^2 = 91.3$ for 89 degrees of freedom (d.o.f.). The best-fit photon index is 1.33 ± 0.06, where the uncertainty is given as the 68 % confidence interval. Replacing the power-law continuum with a more flexible

log-parabolic model ($F(E) \propto E - \alpha - \beta \log E$), it is found that the curvature parameter (β) is consistent with zero within uncertainties. Fluxes in the 3–10 keV and 10–79 keV bands are $1.26 \pm 0.05 \times 10^{-12}$ erg s^{-1} cm^{-2} and $6.8 \pm 0.5 \times 10^{-12}$ erg s^{-1} cm^{-2}, respectively.[3]

5.2.1.2 Swift

A 2 ks *Swift* snapshot was taken simultaneously with the *NuSTAR* observation. I created X-ray telescope (XRT) data products using the XRTPIPELINE v0.13.2. The source extraction region was a 47″-radius circle centred on the source (corresponding to the 90% encircled energy radius at 1.5 keV) and the background region was a 141″-radius circular region offset from the source, in an area free of field sources. The spectra were extracted using XSELECT and ancilliary response files were created with XRTMKARF. The source count rate was 0.003 counts s^{-1}.

The snapshot included a UV observation with the 2600 Å UVW1 filter. Circular source and background regions of 5″ and 30″ radius, respectively, were analysed. Inspecting the data with the UVOTSOURCE tool, the Vega magnitude was determined to be 16.76 ± 0.04 mag. The tool UVOT2PHA was used to create XSPEC-ready files.

5.2.1.3 XMM-Newton

A short observation (12 ks) of PKS J1222+0413 was made by *XMM-Newton* on 2006 July 12. I obtained the observation data files (OBS ID: 0401790601) from the *XMM-Newton* Science Archive and reduced them using the Science Analysis System (SAS, v16.0.0). The observation was strongly affected by background flaring, so after filtering the EPIC event files the good exposure times were 1.8, 3.8 and 3.6 ks for the pn, MOS1 and MOS2 detectors, respectively. Circular regions of radius 40″ and 120″ were used to extract the source and background spectra, respectively. The source

[3] For comparison with previous observations, the 2–10 keV flux is $1.53 \pm 0.06 \times 10^{-12}$ erg s^{-1} cm^{-2}.

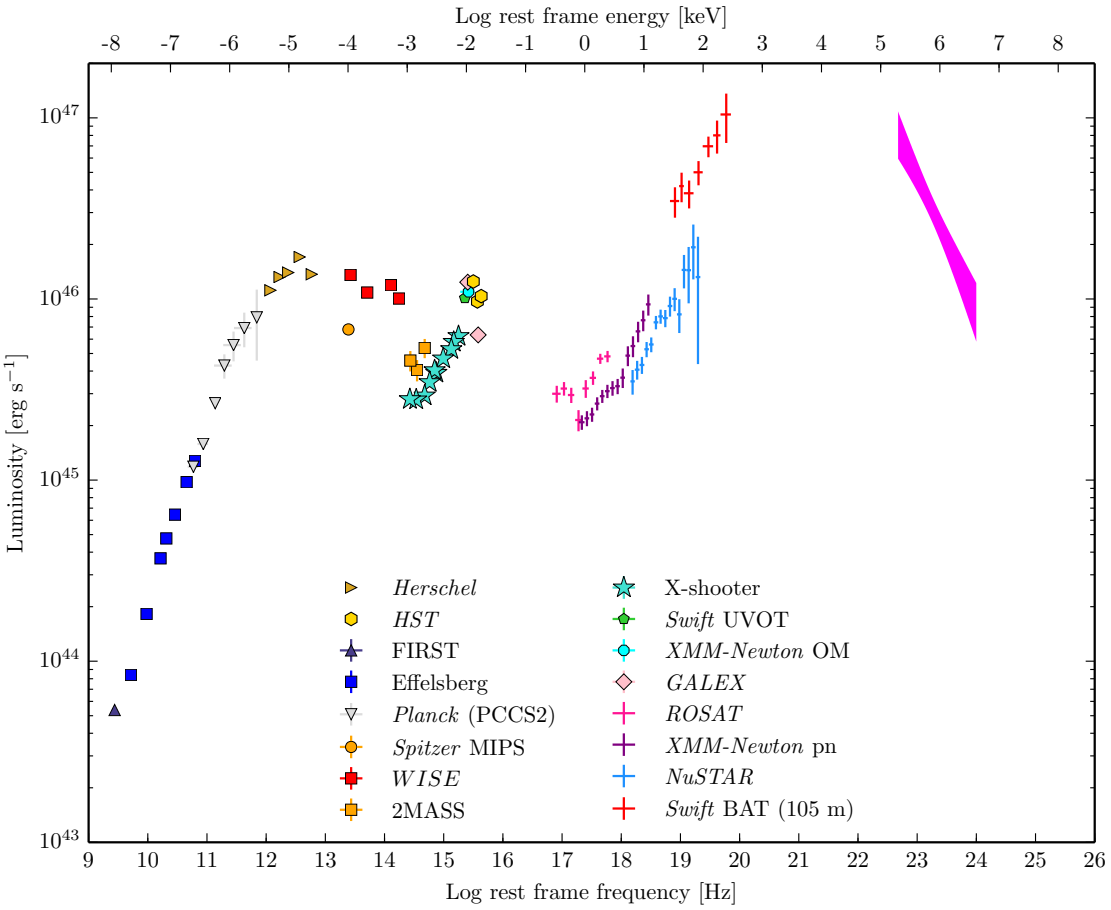

Figure 5.3: The multiwavelength SED of PKS J1222+0413. The data from Effelsberg (recorded between 2011 May and 2012 February), VLT X-shooter (recorded on 2017 April 3), *NuSTAR* and *Swift* (recorded on 2017 June 27) are shown with a *Fermi* γ-ray spectrum covering the same period as my new NIR/optical/UV/X-ray data (2017 March – July). I also show archival data from other facilities.

extraction regions were centred on the source whereas the background extraction regions were placed on a blank patch of sky on the same chip as the source.

The *XMM-Newton* optical monitor (OM) observed PKS J1222+0413 using only the UVM2 filter. I extracted photometry for this filter using the SAS OMICHAIN and OMSOURCE tasks and standard procedures.

Data analysis was performed with the X-ray spectral fitting package XSPEC v12.9.0n (Arnaud 1996). I fitted all three EPIC (pn, MOS1 and MOS2) spectra simultaneously, allowing for a cross-normalisation factor between them; these did not vary by more than $\approx 6\%$. In all models I include a photoelectric absorption model (PHABS) with the Galactic neutral hydrogen absorbing column set to the value $N_{\rm H} = 1.66 \times 10^{20}$ cm^{-2} reported by Dickey & Lockman (1990) and adopting the elemental abundances of Wilms et al. (2000). The inclusion of an intrinsic absorber (ZPHABS) at the redshift of the source did not improve any of the fits. A broken power-law model is a statistically significant improvement over a single power-law, with an F-test probability greater than 99.99%. A more physical model including two Comptonisation regions, COMPTT (Titarchuk 1994) plus NTHCOMP (Życki et al. 1999) was no improvement over the simpler broken power-law. For the broken power-law model I determine an intrinsic flux of $(3.4 \pm 0.1) \times 10^{-12}$ erg s^{-1} cm^{-2}. The model parameters and fit results are summarised in Table 5.2 and the modelled spectra are shown in Figure 5.4.

5.2.1.4 Lyα contamination of photometry

The strong Lyα ($\lambda_{\rm rest} = 1216$ Å) line emission from the source appears at 2390 Å in the observed frame; it therefore contaminates the *Swift* UVOT UVW1, *XMM-Newton* OM UVM2 and *GALEX* NUV photometry. Precisely correcting for this contamination in this case is difficult since I have no measurement of the Lyα EW and, as noted by Elvis et al. (2012), there is no (or weak) correlation between it and the EWs of either the Balmer lines or Mg II. However, if I assume a typical Lyα EW of 60 Å (in the rest frame), I can determine from the equations of Elvis et al. (2012)

Table 5.2: Results of *XMM-Newton* X-ray spectral fits

Model	Parameter	Value
POWERLAW	Γ	1.49 ± 0.03
	norm.	$(3.6 \pm 0.1) \times 10^{-4}$
	χ^2/d.o.f.	179 / 134 = 1.34
BKNPOWER	Γ_1	1.65 ± 0.04
	$E_{\rm break}$ [keV]	2.4 ± 0.3
	Γ_2	1.1 ± 0.1
	norm.	$(3.5 \pm 0.1) \times 10^{-4}$
	χ^2/d.o.f.	151 / 132 = 1.15
COMPTT +	$kT_{\rm e}$ [keV]	$0.7^{+0.2}_{-0.1}$
	τ	11^{+2}_{-1}
	norm.	$\left(1.5^{+0.5}_{-0.3}\right) \times 10^{-2}$
NTHCOMP	Γ	1.2 ± 0.1
	norm.	$(1.5 \pm 0.4) \times 10^{-4}$
	χ^2/d.o.f.	151 / 131 = 1.16

Errors are quoted at the 1σ level. All of the above models included a Galactic absorption component (PHABS) with $N_{\rm H} = 1.66 \times 10^{20}$ cm^{-2}. The best-fit (broken power-law) model is plotted in Figure 5.4.

(their section 4.1.3) that Lyα contributes approximately 20 % of the photometric flux.

5.2.1.5 Fermi

The *Fermi* γ-ray source 3FGL J1222.4+0414 is associated with PKS J1222+0413. In the *Fermi* LAT 4-year source catalogue (3FGL, Acero et al. 2015) the γ-ray source detection significance, derived from the test statistic (TS), is 30.01σ. In the updated *Fermi*-LAT 8yr1 (FL8Y) description of the γ-ray sky with respect to 3FGL, the source significance improved slightly (30.77σ), and the spectral shape is described as a soft power-law with an index of $\Gamma = 2.87 \pm 0.04$, in the 100 MeV to 30 GeV energy range.

To construct a contemporaneous SED of PKS J1222+0413, γ-ray data were extracted from the period 2017 March 20–July 11 (to include my VLT X-shooter and *NuSTAR* observations) and from the period 2011 March–April (covering the *HST* COS UV

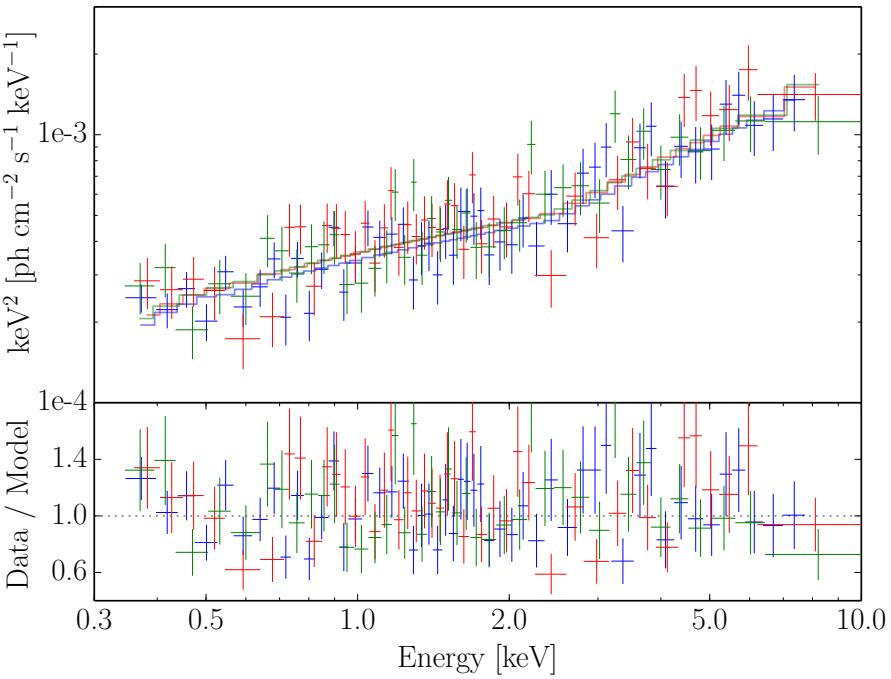

Figure 5.4: *XMM-Newton* EPIC X-ray spectra modelled with a broken power-law. Data from the pn, MOS1 and MOS2 detectors are shown in blue, red and green, respectively. The upper panel shows the data model with the detector responses folded out; the lower panel the data/model ratios.

spectrum of March 22 and SDSS optical spectrum of March 26). Photons in a circular region of interest (RoI) of radius 10°, centred on the position of PKS J1222+0413, were considered. A zenith-angle cut of 90° was applied. The analysis was done using the *Fermi* Science Tools software package version v10r0p5, in combination with the PASS 8 instrument response functions (event class 128 and event type 3) corresponding to the P8R2_SOURCE_V6 response and the gll_iem_v06.fits and iso_P8R2_SOURCE_V6_v06 models for the Galactic and isotropic diffuse background, respectively. The spectral model of the region included all sources located within the RoI with spectral shapes and initial parameters as in the 3FGL catalogue (Acero et al. 2015).

The extraction of the *Fermi*-LAT data is complicated by the presence of two bright, nearby γ-ray sources in the RoI (see Figure 5.5). The prototypical quasar 3C 273 has an angular separation $\approx 2.7°$ from PKS J1222+0413, comparable to the *Fermi* point spread function (PSF) at 1 GeV. Another quasar, PKS 1237+049, is $\approx 4.3°$ from

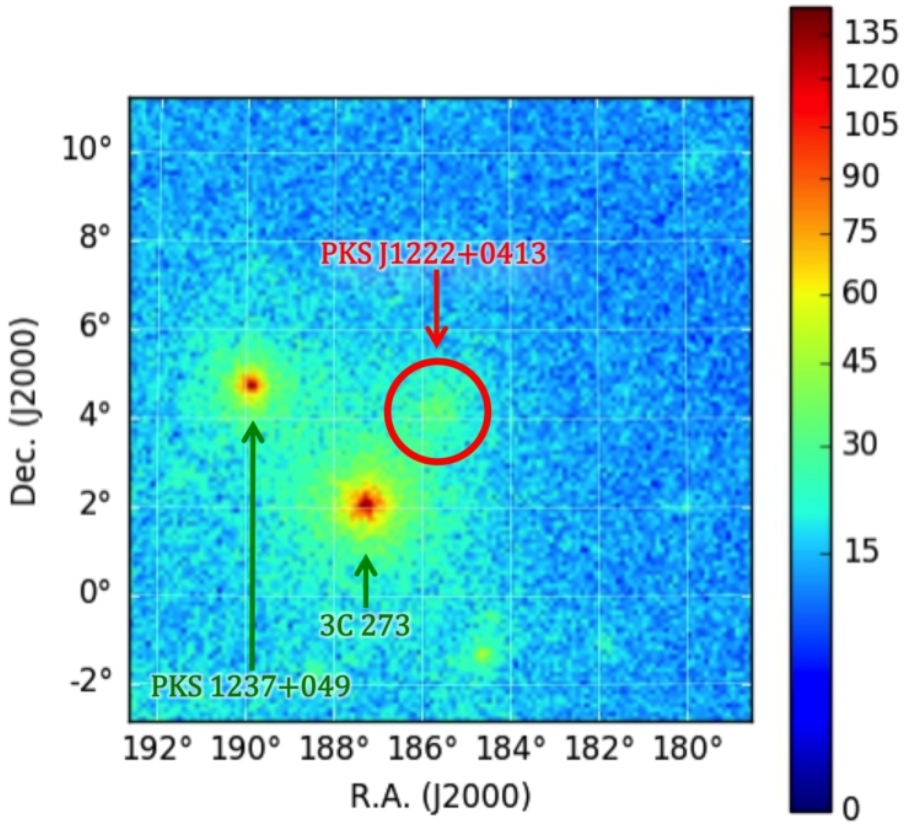

Figure 5.5: *Fermi* count map for the period beginning at the mission start and ending 2017 July 31. PKS J1222+0413 is in the centre of the field (indicated by the red circle). The nearby γ-ray bright AGN 3C 273 and PKS 1237+049 (3FGL J1239.5+0443) are also shown.

PKS J1222+0413. The *Fermi* PSF is larger at lower energies: the 95 % containment radius at 100 MeV is $\geqslant 10°$.

In the earlier time period (2011), PKS J1222+0413 is detected with a TS of 29.02 ($\approx 5.4\sigma$), the photon index being $\Gamma = 2.72 \pm 0.25$. The *Fermi*-LAT flux points at two bins/decade and the model spectrum up to the highest energy photon from the source in that period are shown in Figure 5.6, although a flux detection is obtained in one low-energy bin only. Note that γ-ray flux upper limits at the 95 % confidence level are computed for bins were TS < 9. In the 2017 time window, PKS J1222+0413 is detected with a TS of 56.68 ($\approx 7.5\sigma$), with a photon index of $\Gamma = 2.74 \pm 0.18$. The last significant energy bin is 1–3.16 GeV. Therefore no attempt to study the γ-ray variability was made. Note that in the *Fermi* All-Sky Variability Analysis (FAVA2) flare map of the region (generated in 2019 January using all available data from the

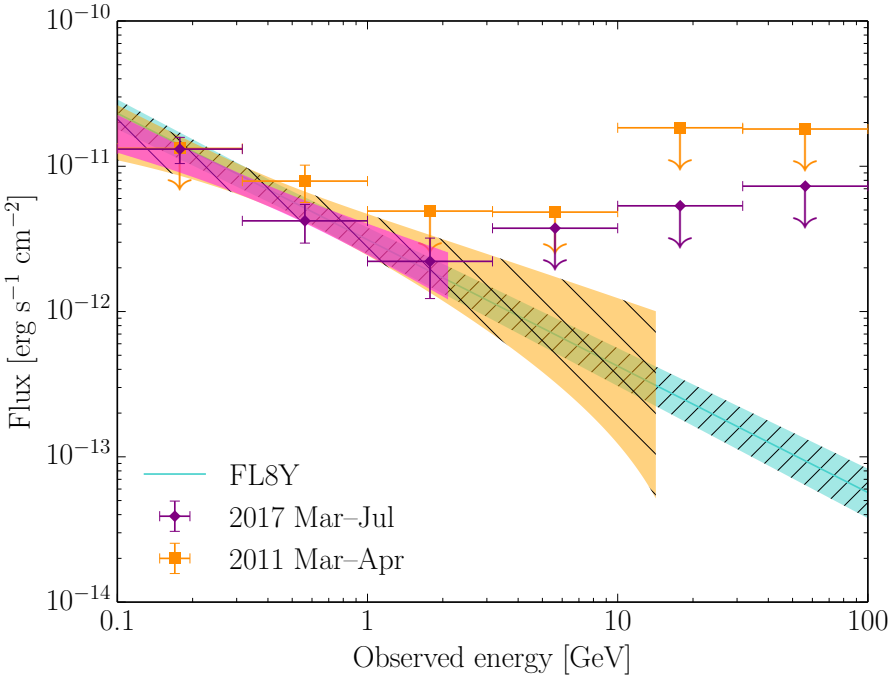

Figure 5.6: *Fermi* γ-ray spectra of PKS J1222+0413. The spectrum extracted from the period 2017 March 20 to July 11 is shown in fuchsia; the corresponding model is shown as the short (0.1–2 GeV) bow-tie. The spectrum extracted from the period 2011 March 1 to April 30 is shown in orange; the corresponding model is shown as the medium-length (0.1–14 GeV) bow-tie. For comparison, the model spectrum taken from the *Fermi*-LAT 8-year Source List (FL8Y) is shown as the long, turquoise bow-tie.

mission start) that all of the flare activity is associated with other sources in the field (particularly 3C 273) and there are no recorded flare events in the vicinity of PKS J1222+0413. The spectral index found in both periods is fully compatible with the entire data set (FL8Y) within statistical errors (see Figure 5.6).

5.2.2 Radio monitoring data

5.2.2.1 Effelsberg

Observations were conducted with the 100 m Effelsberg telescope in Germany, with the secondary focus receivers at 2.64, 4.85, 8.35, 10.45, 14.6, 23.05 and 32 GHz. For the multiple-feed systems at 4.85, 10.45 and 32 GHz the measurements were conducted differentially thus removing most of the linear tropospheric effects. To

Table 5.3: Radio monitoring data from Effelsberg

Freq. (GHz)	$\langle S \rangle$ (mJy)	σ_S (mJy)	N	Start	Rate (days)
2.64	663	3	9	2011-06-06	32.0
4.85	779	3	9	2011-05-19	34.3
8.35	923	5	10	2011-05-19	30.5
10.45	950	6	10	2011-05-19	30.5
14.60	920	10	10	2011-05-19	30.5
23.05	880	20	7	2011-05-19	45.7
32.00	830	20	6	2011-05-19	54.9

This table quotes the error-weighted mean radio flux densities and their 1σ errors, the number of detections N in the observation period starting on the given date and ending on 2012-02-18.

correct for potential pointing offsets a cross-scan technique was adopted; that is, the telescope response was registered while slewing its main beam over the expected source position. With this setup a complete radio SED needs roughly 40–45 minutes. It is therefore reasonable to assume that the observations are free of variability. Each pointing has been subjected to a pipeline of post-measurement corrections accounting for power losses caused by: (a) potential pointing offsets, (b) atmospheric absorption, and (c) deformations of the main telescope reflector. The fractional effect of each of these operations is given in Table 3 of Angelakis et al. (2019). The observed dataset has been finally calibrated with reference to standard sources listed in Table 3 of Angelakis et al. (2015). Table 5.3 in this chapter summarises the flux densities at all observing frequencies weighted averaged over a period roughly from 2011 May 19 to 2012 February 18. The uncertainty in the average flux densities is limited to less that a couple of per cent.

5.2.3 Additional archival data

5.2.3.1 FIRST

Querying the FIRST source catalogue, I find a radio source 0.5″ from the optical coordinates of PKS J1222+0413, which is the only radio source within a search radius

of 30″. The integrated flux density was reported to be 800.63 mJy and I adopt an error of 5 %, representative of the systematic uncertaintiy for bright sources (White et al. 1997). The catalogue fluxes are measured in coadded images from multiple observations; the mean observation date is given as 2001 March 14 with an RMS of ≈ 4 days.

5.2.3.2 Planck

I perform a cone search of the *Planck* Compact Source Catalog using the default radius equal to the beam FWHM at each frequency (see Planck Collaboration et al. 2016b). In Table 5.4 I give the fluxes derived from the quoted catalogue flux densities which were calculated using the Gaussian fitting method. The source is not detected at 545 or 857 GHz either in the PCCS2 catalogue or the lower-reliability PCCS2E catalogue.

5.2.3.3 Herschel

The *Herschel Space Observatory* (Pilbratt et al. 2010) operated contemporaneously with *Planck*, from 2009 July to 2013 April. *Herschel* carried three science instruments: the Photodetecting Array Camera and Spectrometer (PACS, covering 55–220 µm), the Spectral and Photometric Imaging Receiver (SPIRE, containing a low-resolution spectrometer covering 194–672 µm and a photometer with three bands centred on 250, 350 and 500 µm) and the Heterodyne Instrument for the Far Infrared (HIFI, covering 157–210 and 236–615 µm). I searched the PACS and SPIRE point source catalogues (Marton et al. 2016; Marton et al. 2017) and obtained the data listed in Table 5.4.

5.2.3.4 Spitzer

PKS J1222+0413 has been observed by the *Spitzer Space Telescope* (Werner et al. 2004). The source was detected by the 24 µm array of the the Multiband Imaging

Photometer for *Spitzer* (MIPS) during an observation made on 28 January 2005. The source flux density is taken from the Spitzer Enhanced Imaging Products[4] (SEIP) source list.

5.2.3.5 WISE

The *Wide-field Infrared Survey Explorer* (*WISE*; Wright et al. 2010) made photometric observations in four bands: W1 (3.4 µm), W2 (4.6 µm), W3 (12 µm) and W4 (22 µm). For each band I have calculated the flux from the instrumental profile-fit photometry magnitude listed in the AllWISE catalogue[5]. The magnitudes recorded for the bands were W1: 12.802 ± 0.023; W2: 11.634 ± 0.023; W3: 8.901 ± 0.034 and W4: 6.513 ± 0.080; the photometric quality of each band was reported to be of the highest quality.

Infrared photometry spanning several years is available for the W1 and W2 filters, recorded since 2013 September during *NEOWISE* mission (Mainzer et al. 2014). In PKS J1222+0413, these filters sample the hot dust emission. In Figure 5.7 I show the infrared lightcurves. Several exposures were taken on each pass of the telescope (with a cadence of roughly six months), which I have binned into the ten single-epoch measurements shown. For each epoch I have calculated the mean magnitude and its standard error from the individual exposures, after applying a 3σ clipping algorithm to remove anomalous data. The peak-to-peak magnitude change (from the first *WISE* observation in mid-2010 to the latest *NEOWISE* observation in mid-2017) is ≈ 1.2 mag, and ≈ 0.6 mag changes are seen in the *NEOWISE* period.

5.2.3.6 2MASS

PKS J1222+0413 was detected as part of the Two Micron All Sky Survey (2MASS, Skrutskie et al. 2006). The J, H and K_s profile-fit instrumental magnitudes recorded

[4] http://irsa.ipac.caltech.edu/data/SPITZER/Enhanced/SEIP/
[5] http://irsa.ipac.caltech.edu/

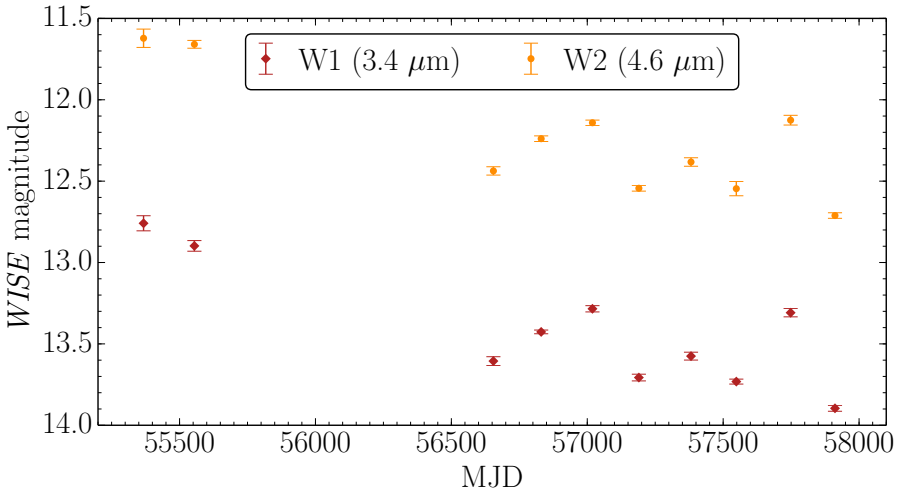

Figure 5.7: The *WISE* and *NEOWISE* infrared lightcurve of PKS J1222+0413, showing observations made between 2010 June and 2017 June.

in the 2MASS All-Sky Point Source Catalog (PSC) were 16.348±0.133, 15.849±0.146 and 14.969 ± 0.140, respectively.

5.2.3.7 Sloan

Two optical spectra of the source have been recorded as part of the Sloan Digital Sky Survey (SDSS). The first was taken on 12 February 2008 with the original SDSS spectrograph; the second was taken on 26 March 2011 with the Baryon Oscillation Spectroscopic Survey (BOSS) spectrograph, allowing a greater wavelength coverage. The two spectra are compared with my recent X-shooter spectrum in Figure 5.1. It can be seen that the 2011 spectrum is redder than that of 2008. Margala et al. (2016) noted that in the spectra of BOSS quasars, the flux densities were overestimated by ∼ 19 per cent at 3300 Å and underestimated it by ∼ 24 per cent at 1 µm. Given the ∼ 1″ seeing at 500 nm during the X-shooter observation, slit losses are likely minimal in the optical and UV, for which the 1.2″ and 1.3″ width slits, respectively, were used.

In the observed frame, the flux density at 4000 Å (7000 Å) is approximately 30 (25) % greater in the 2008 SDDS spectrum than in the 2017 X-shooter spectrum, and the flux densities of the two SDSS spectra are similar at 4000 Å.

5.2.3.8 GALEX

The *Galaxy Evolution Explorer* (*GALEX*; Martin et al. 2005) detected the source in both its near-ultraviolet (NUV) and far-ultraviolet (FUV) bands. The FUV flux is severely absorbed because the filter (1340–1806 Å) covers a spectral region blueward of the Lyman break of a Lyman limit system at 1793 Å (observed).

5.2.3.9 Hubble Space Telescope

Wotta et al. (2016) studied absorbing systems on sight lines towards 61 AGN, including PKS J1222+0413. As part of this study they obtained a short (900 s) exposure of the UV spectrum of the source using the G140L (900–2150 Å) filter of the *HST* Cosmic Origins Spectrograph (COS). This snapshot spectrum was recorded on 2011 March 22. They identified a Lyman limit system (LLS) with $\log(N_{\rm H}) = 17.55 \pm 0.10$ cm^{-2} at redshift $z_{\rm LLS} = 0.6547$. The $N_{\rm H}$ was determined by assessing the suppression of continuum flux density relative to the composite quasar template of Telfer et al. (2002)[6], scaled to match the unabsorbed region of the spectrum. I correct the observed spectrum for the Lyman continuum absorption by multiplying the fluxes by a factor e^{τ_λ} where the optical depth

$$\tau_\lambda = \sigma_0 \left(\frac{\lambda}{\lambda_{\rm LLS}} \right)^3 N_{\rm H} \quad \text{for} \quad \lambda \leqslant \lambda_{\rm LLS}, \tag{5.2.1}$$

the absorption cross-section at the Lyman limit $\sigma_0 = 6.3 \times 10^{-18}$ cm^2 and $\lambda_{\rm LLS} = (1 + z_{\rm LLS}) \times 912$ Å (Shull et al. 2017; Paresce 1984). The observed and corrected spectra are shown in Figure 5.8.

To estimate the AGN continuum, I select several regions free from narrow absorption lines and calculate the mean flux density in each of these and then bin into three wider regions, shown in Figure 5.8. It should be noted that the estimate of the column density of the LLS is dependent on the shape of the composite template

[6]The template shown in Figure 5.8 is the composite of the radio loud subset of sources. It is constructed from 205 spectra of 107 objects, all with $z > 0.33$ and with $\langle z \rangle = 1.00$.

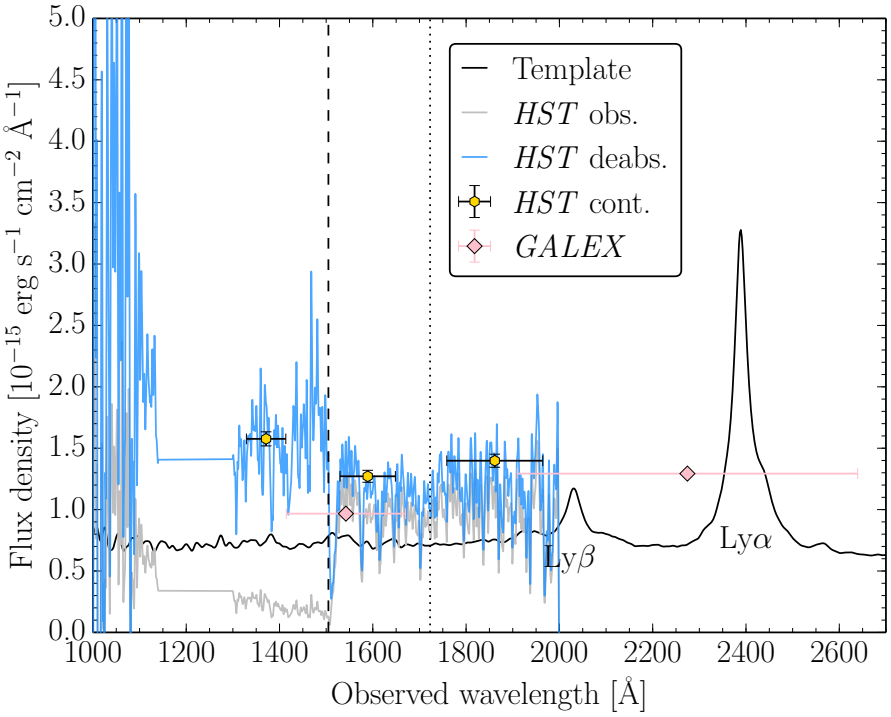

Figure 5.8: The *HST* COS spectrum of PKS J1222+0413. The observed spectrum is shown in grey. Overplotted in blue is the spectrum corrected for Galactic reddening and the Lyman continuum absorption of a Lyman limit system (LLS) at $z_{\rm LLS} = 0.65$. The dashed vertical line indicates the Lyman break of the LLS; the dotted vertical line indicates the Lyman break of an intervening partial LLS at $z_{\rm pLLS} = 0.89$. *GALEX* NUV and FUV photometry (corrected for Galactic reddening) are shown as pink diamonds. For reference, the composite spectrum of Telfer et al. (2002) is shown in black. This template has been scaled to approximately match the continuum flux level of the 2011 SDSS spectrum.

used to approximate the intrinsic continuum. Without an independent measure of the column density, my 'recovery' of the PKS J1222+0413 AGN continuum is therefore also dependent on the shape of the template, so the flux density determined at 1370 Å should be treated with some caution. The continuum flux density at 1590 Å is perhaps slightly underestimated because of the intervening partial LLS at $z_{\rm pLLS} = 0.89$, the column density of which is undetermined. The continuum flux density at 1860 Å is more reliable although all three estimates are hampered by the limited signal-to-noise of the spectrum. The spectrum blueward of ≈ 1100 Å is too noisy to be of use.

5.2.3.10 ROSAT

An 8 ks pointed observation of PKS J1222+0413 was made by the *Röntgensatellit* (*ROSAT*; Voges et al. 1999) on 24 December 1992. I reduced the archival data using HEAsoft XSELECT v2.4d. The source extraction region was chosen to be a 120″-radius circle centred on the source. The background region was a 360″-radius circle offset on a blank patch of sky, on the same chip as the source. The 0.1–2.0 keV source count rate was ≈ 0.15 counts s^{-1}. The source spectrum was rebinned using the GRPPHA tool to contain a minimum of 20 counts per bin.

The best fitting model was a simple power-law with $\Gamma = 1.72 \pm 0.04$ and normalisation $(5.2 \pm 0.2) \times 10^{-4}$, giving $\chi^2_\nu = 90/57 = 1.58$. The best fit $N_{\rm H} = (7 \pm 2) \times 10^{-3}$, lower than the Dickey & Lockman (1990) value but improving the fit by only $\Delta\chi^2 = 9$ for one additional free parameter.

5.2.3.11 Swift BAT

In the broad-band SED I also include data from the *Swift* Burst Alert Telescope (BAT) 105-month all-sky hard X-Ray survey (Oh et al. 2018) spanning the period 2004 December – 2013 August. The time-averaged spectrum and response file were obtained from the online archive. The spectrum was well-fit in XSPEC with a single power-law of index $\Gamma = 1.5 \pm 0.1$ and normalisation $\left(9^{+5}_{-3}\right) \times 10^{-4}$, giving $\chi^2_\nu = 0.32$.

Table 5.4: The multiwavelength data set

Q	Band	Instrument (Survey)	Observation date (D/M/Y or M/Y)	$\log(\nu_{\rm obs})$ [Hz]	Flux [10^{-14} erg/s/cm^2]	Luminosity [10^{43} erg/s]	Ref.
	Radio	(FIRST)	03/01	9.15	1.12 ± 0.06	5.4 ± 0.3	[1]
	Radio	Effelsberg	06/11–02/12	9.42	1.750 ± 0.0008	8.40 ± 0.04	[7]
	Radio	Effelsberg	05/11–02/12	9.69	3.80 ± 0.01	18.3 ± 0.07	[7]
	Radio	Effelsberg	05/11–02/12	9.92	7.71 ± 0.04	37.0 ± 0.2	[7]
	Radio	Effelsberg	05/11–02/12	10.02	9.93 ± 0.06	47.7 ± 0.3	[7]
	Radio	Effelsberg	05/11–02/12	10.16	13.4 ± 0.2	64.5 ± 0.7	[7]
	Radio	Effelsberg	05/11–02/12	10.36	20.3 ± 0.5	97 ± 2	[7]
	Radio	*Planck*	08/09–08/13	10.48	25 ± 2	119 ± 9	[2]
	Radio	Effelsberg	05/11–02/12	10.51	26.6 ± 0.6	128 ± 3	[7]
	Radio	*Planck*	08/09–08/13	10.64	33 ± 2	158 ± 11	[2]
	Radio	*Planck*	08/09–01/12	10.85	55 ± 3	266 ± 16	[2]
	Radio	*Planck*	08/09–01/12	11.00	89 ± 14	429 ± 66	[2]
	Radio	*Planck*	08/09–01/12	11.16	116 ± 22	560 ± 100	[2]
	Radio	*Planck*	08/09–01/12	11.34	144 ± 31	690 ± 150	[2]
	Radio	*Planck*	08/09–01/12	11.55	165 ± 70	790 ± 340	[2]

References: [1] FIRST catalogue, Helfand et al. (2015); [2] *Planck* Second Point Source Catalog, Planck Collaboration et al. (2016b); [3] *Herschel* point source catalogues, Marton et al. (2016); [4] *Spitzer* SEIP Source List, Werner et al. (2004); [5] *WISE* AllWISE Source Catalog, Wright et al. (2010); [6] Two Micron All-Sky Survey, Skrutskie et al. (2006); [7] this work; [8] Sloan Digital Sky Survey DR7, Abazajian et al. (2009); [9] Sloan Digital Sky Survey DR9, Ahn et al. (2012); [10] *GALEX* Data Release GR6, Martin et al. (2005); [11] *Swift* BAT 105-month all-sky hard X-Ray survey, Oh et al. (2018). The 'Q' flag indicates my quasi-simultaneous data (✓ for data used in my SED fitting of Section 5.3.1.1 and † for optical/UV data used in Section 5.2.3.9).

Table 5.4: The multiwavelength data set (continued)

Q	Band	Instrument (Survey)	Observation date (D/M/Y or M/Y)	$\log(\nu_{\rm obs})$ [Hz]	Flux [10^{-14} erg/s/cm^2]	Luminosity [10^{43} erg/s]	Ref.
	Far-IR	*Herschel*	03/07/10	11.78	233 ± 13	1117 ± 60	[3]
	Far-IR	*Herschel*	03/07/10	11.93	276 ± 14	1322 ± 67	[3]
	Far-IR	*Herschel*	03/07/10	12.08	292 ± 17	1399 ± 81	[3]
	Far-IR	*Herschel*	03/07/10	12.27	356 ± 41	1706 ± 200	[3]
	Far-IR	*Herschel*	03/07/10	12.48	285 ± 21	1369 ± 100	[3]
	Far-IR	*Spitzer* MIPS	28/01/05	13.11	142 ± 1	679 ± 6	[4]
	Mid-IR	*WISE*	18–22/06/10	13.13	283 ± 21	1358 ± 100	[5]
	Mid-IR	*WISE*	18–22/06/10	13.41	226 ± 7	1085 ± 34	[5]
	Mid-IR	*WISE*	06/10–12/10	13.81	248 ± 5	1191 ± 25	[5]
	Mid-IR	*WISE*	06/10–12/10	13.95	210 ± 4	1005 ± 21	[5]
	Near-IR	(2MASS)	25/02/00	14.14	95 ± 12	457 ± 59	[6]
	Near-IR	(2MASS)	25/02/00	14.26	84 ± 11	405 ± 55	[6]
✓	Near-IR	VLT X-shooter	03/04/17	14.27	57.3 ± 0.5	275 ± 2	[7]
	Near-IR	(2MASS)	25/02/00	14.39	112 ± 14	536 ± 65	[6]
✓	Optical	VLT X-shooter	03/04/17	14.48	74.2 ± 1.1	363 ± 5	[7]
	Optical	(SDSS)	12/02/08	14.48	124 ± 8	621 ± 40	[8]
†	Optical	(SDSS)	26/03/11	14.48	122 ± 2	596 ± 10	[9]
†	UV	(SDSS)	26/03/11	14.71	140 ± 7	699 ± 35	[9]
✓	UV	VLT X-shooter	03/04/17	14.71	91.2 ± 0.6	513 ± 3	[7]
✓	UV	*Swift* UVOT	27/06/17	15.06	211 ± 8	1011 ± 37	[7]
	UV	*XMM-Newton* OM	12/07/06	15.13	228 ± 4	1094 ± 19	[7]
	UV	*GALEX*	31/03/04	15.12	250 ± 8	1199 ± 38	[10]
†	UV	*HST* COS	22/03/11	15.21	220 ± 20	1240 ± 90	[7]
†	UV	*HST* COS	22/03/11	15.27	180 ± 20	1000 ± 100	[7]
	UV	*GALEX*	31/03/04	15.29	135 ± 16	649 ± 77	[10]

Table 5.4: The multiwavelength data set (continued)

Q	Band	Instrument (Survey)	Observation date (D/M/Y or M/Y)	$\log(\nu_{\rm obs})$ [Hz]	Flux [10^{-14} erg/s/cm^2]	Luminosity [10^{43} erg/s]	Ref.
†	UV	*HST* COS	22/03/11	15.35	30 ± 3	1040 ± 20	[7]
	X-ray	*ROSAT*	24/12/92	17.35	100 ± 9	500 ± 40	[7]
✓	X-ray	*Swift* XRT	27/06/17	17.37	46 ± 12	230 ± 60	[7]
	X-ray	*XMM-Newton* EPIC	12/07/06	18.08	150 ± 8	720 ± 40	[7]
✓	X-ray	*NuSTAR*	27/06/17	18.86	220 ± 10	1060 ± 50	[7]
	X-ray	*Swift* BAT	12/04–09/10	19.18	1450 ± 200	6960 ± 960	[11]
✓	γ-ray	*Fermi* LAT	03/17–06/17	22.63	1300 ± 270	6300 ± 1300	[7]
✓	γ-ray	*Fermi* LAT	03/17–06/17	23.13	420 ± 120	2020 ± 600	[7]
✓	γ-ray	*Fermi* LAT	03/17–06/17	23.63	220 ± 100	1100 ± 470	[7]
✓	γ-ray	*Fermi* LAT	03/17–06/17	24.13	< 370	< 1800	[7]
✓	γ-ray	*Fermi* LAT	03/17–06/17	24.63	< 530	< 2600	[7]
✓	γ-ray	*Fermi* LAT	03/17–06/17	25.13	< 730	< 3500	[7]

5.3 The origin of the γ-ray emission

5.3.1 Determining the external photon field

Here, I determine the parameters of the ambient photon field with which the jet interacts to produce the observed high-energy emission. In the following I use my multiwavelength data to determine the size scales and luminosities of the accretion disc and its corona, the broad emission line region and the hot dusty torus. These are applied in the jet model which is described in Section 2.4 and Gardner & Done (2018).

5.3.1.1 The accretion flow

To model the infrared-to-X-ray SED I have scaled up the X-shooter fluxes by a factor 1.3 to match the level of the SDSS spectra in the UV (see § 5.2.3.7 and Figure 5.9). The *Swift* UVOT, *XMM* OM and *GALEX* NUV photometry have been scaled by a factor 0.8 to account for Lyα contamination (see § 5.2.1.4). The *XMM* pn and *ROSAT* X-ray spectra have been scaled by factors 0.8 and 0.5, respectively, to match the flux level of my joint *NuSTAR-Swift* XRT observation. Note that the 2011 SDSS spectrum and *HST* COS spectrum (shown in lime green in Figure 5.9) were recorded three days apart.

I employ the energy-conserving accretion flow model, OPTXCONV, of Done et al. (2013) and perform a simple test to determine whether the spin of the SMBH can be constrained by our the data. A brief description of the model is given in Seection 2.3. In this test I fix several parameters to those typical of a NLS1; namely, the warm Comptonisation region electron temperature $kT_{\rm e}$= 0.2 keV and optical depth τ= 15, the photon index of the power-law tail $\Gamma_{\rm PL}$ = 2.4 and the ratio of power-law to soft excess power $f_{\rm PL}$= 0.3. The outer accretion disc radius is fixed at 1000 $R_{\rm g}$.

As well as the accretion flow, I model the hot dust emission as simple blackbody, a

scaled host galaxy template[7] and add a power-law with $\Gamma = 1.4$ to model the putative jet emission at hard X-ray energies. The hot dust temperature and luminosity is well determined by the *WISE* W1 and W2 points. The hot dust temperature is well-determined from the *WISE* W1 and W2 points and changes little between fits. As can be seen in Figure 5.9, the data do not strongly discriminate between zero- and high-spin models. However, the high-spin model slightly overpredicts the soft X-ray flux (although the modelled *ROSAT* spectrum has been scaled down by 20 % to match the flux level of the *Swift* XRT data) and cannot accommodate soft Comptonisation or coronal components. I note that this model conserves energy between the outer and inner accretion flow, producing the optical and UV/X-ray emission, respectively. The UV/X-ray flux would be lower if power were lost between outer and inner radii as the result of an accretion disc wind which could be present if the accretion rate were super-Eddington as in the high-spin model. I cannot therefore rule out a high SMBH spin. Overall, the zero-spin model is a better representation of the data and the parameters of the accretion flow components are then typical of a NLS1.

[7] I use the 5 Gyr-old elliptical galaxy template of Polletta et al. 2007, scaled so that the total model fits the data at ≈ 1 µm.

Table 5.5: Results from spectral fits to the deabsorbed IR to hard X-ray SED

	$a_\star$	$L/L_{\rm Edd}$	$\dot{M}$ [$M_\odot$/yr]	$R_{\rm cor}$ [$R_{\rm g}$]	$\log(L_{\rm AD})$ [erg/s]	$\log(L_{\rm SX})$ [erg/s]	$\log(L_{\rm PL})$ [erg/s]	$T_{\rm tor}$ [K]	$\log(L_{\rm tor})$ [erg/s]	$R_{\rm tor}$ [ld]	$\log(L_{\rm AGN})$ [erg/s]	χ^2/dof
	(1)	(2)	(3)	(4)	(5)	(6)	(7)	(8)	(9)	(10)	(11)	(12)
(a)	0.0	0.93	7.3	11.7	46.64	45.53	45.17	1430	46.19	4000	46.68	172/126
(b)	0.8	2.16	7.8	2.90	46.91	00.00	00.00	1350	46.21	4000	46.91	198/127

The columns are: (1) dimensionless SMBH spin: this was fixed at this value; (2) Eddington ratio; (3) mass accretion rate; (4) outer coronal radius in gravitational radii, $R_{\rm g} = 2.95 \times 10^{11}$ m $= 1.14 \times 10^{-2}$ light days; (5) luminosity of the accretion disc; (6) luminosity the soft Comptonisation region 'SX'; (7) luminosity of the power-law tail 'PL'; (8) temperature of the dusty torus; (9) luminosity of the IR radiation from the torus; (10) the dusty torus inner radius in light days; (11) the total AGN luminosity AD+SX+PL; (12) the χ^2 statistic over the number of degrees of freedom (dof) in the model. $\dot{M}$ and $R_{\rm tor}$ are not model parameters but have been derived from my results.

5.3.1.2 The broad line region luminosity and radius

Following the method described in Section 4.5.1.2 of the previous chapter, I estimate the luminosity and radius of the BLR, from which the energy density of BLR photons can be calculated. My X-shooter spectrum covers four of the prominent broad emission lines, (C III], Mg II, Hβ and Hα) from which I can estimate the BLR luminosity. The luminosities of the Hα and Hβ broad components are listed in Table 5.1 and for the Mg II line and C III] broad components I get a luminosity of $\log L_{\rm MgII} = 43.30$ erg s^{-1} and $\log L_{\rm CIII]} = 43.42$ erg s^{-1}, respectively. This results in a total BLR luminosity of $\log L_{\rm BLR} = 44.54$ erg s^{-1}. As noted in Section 5.1.2, I estimate the BLR radius to be 260^{+91}_{-67} light-days ($\approx 2.28 \times 10^4$ $R_{\rm g}$ for my adopted SMBH mass) from the Hβ radius-luminosity relationship of Bentz et al. (2013).

5.3.1.3 The dusty torus luminosity and radius

Photons from the extended (∼parsec-scale) dusty torus are also upscattered by interaction with the jet. I parameterise this source of seed photons by the torus luminosity and radius (the latter is dependent on the dust temperature). The hot dust luminosity and temperature are determined from the blackbody fit to the mid-IR photometry: the values are listed in Table 5.5. Then, for a silicate dust composition, I estimate the hot dust radius to be ~ 4000 light-days ($\approx 3.51 \times 10^5$ $R_{\rm g}$). Note that the torus hot dust radius may be smaller than this depending on the assumption of grain size.

5.3.2 The broadband SED

I use the Gardner & Done (2018) single-zone, leptonic jet code JET (based on the physics of Ghisellini & Tavecchio 2009), adapted so that the external photon field can be set via input parameters[8]. I first test the standard jet scalings against the data.

[8] A concise description of the model is given in Section 2.4 of this thesis; further details can be found in Gardner & Done (2018) and Ghisellini & Tavecchio 2009.

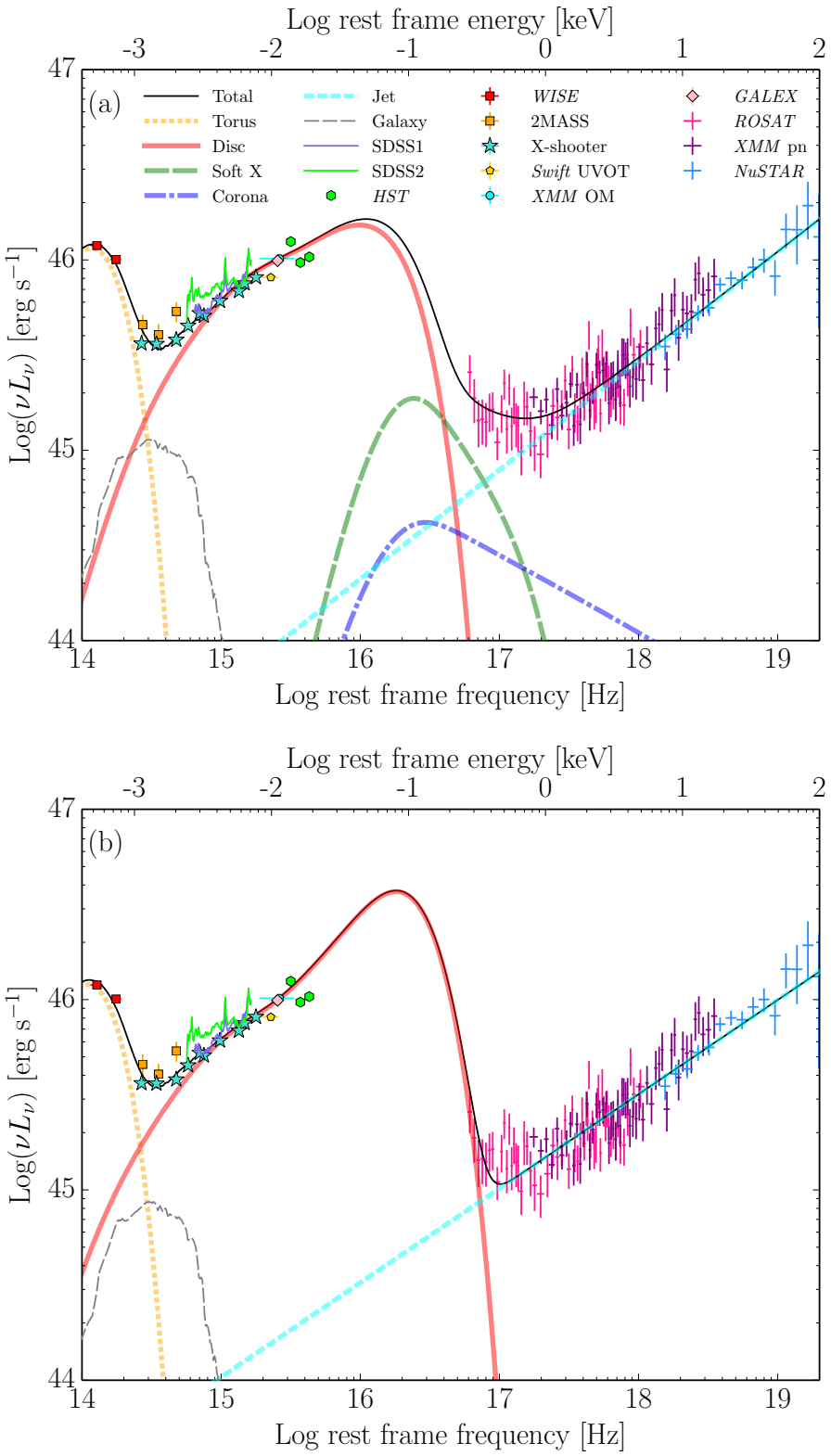

Figure 5.9: Accretion flow models applied to the NIR to X-ray SED, for different SMBH spins: (a) $a_\star = 0$; (b) $a_\star = 0.8$.

For a SMBH of mass $M_{\rm BH} = 2 \times 10^8$ M$_\odot$ with $L/L_{\rm Edd} = \dot{m} = 0.93$, the scalings of Gardner & Done (2018) predict a magnetic field strength of $B \propto \sqrt{\dot{m}/M_{\rm BH}} = 17.7$ G and power injected into relativistic electrons $P_{\rm rel} \propto \dot{m} M_{\rm BH} = 3.72 \times 10^{43}$ erg s^{-1}. Lengths scale linearly with mass, so in mass-normalised units the site of the jet emission region is equal to that of a typical Ghisellini et al. (2010) FSRQ, i.e. $Z_{\rm diss} = 1280\ R_{\rm g}$. For the jet geometry, I assume an opening angle $\phi = 0.1$ radians and inclination to the line of sight equal to the inverse of the bulk Lorentz factor $i = 1/\Gamma_{\rm BLF}$. I keep all other jet parameters equal to the mean FSRQ parameters of Ghisellini et al. (2010), listed under the "Scaled" model in Table 5.6, the resultant model is shown in Figure 5.10.

I find that the SED is not as discrepant as when performing the same test with 1H 0323+342 (see the top panels of Figure 5.10). The jet power $P_{\rm j}$ (relative to disc power) in this scaled model is comparable to other blazars but clearly the model needs some adjustment to fit the data.

I adjust the parameters of the scaled model to better fit the broadband SED. The Compton dominance (the ratio of peak Compton to synchrotron peak luminosities) of the scaled model is clearly too low; this can be increased by lowering B. The magnetic field is lowered approximately by a factor five in my fitted model compared to the scaled one. This is necessary in part to avoid the synchrotron self-Compton peak overpredicting the low-energy X-ray data. Increasing $P_{\rm rel}$ and $\Gamma_{\rm BLF}$ has the effect of increasing the jet SED in luminosity. A solution near equipartition (equal energy densities in electrons and the magnetic field) is found by adjusting B, $P_{\rm rel}$ and $\Gamma_{\rm BLF}$. By increasing $\Gamma_{\rm BLF}$, I can lower $P_{\rm rel}$ to reach approximate equipartition, having lowered B. Then, the shapes of the synchrotron and EC peaks are adjusted by tuning the parameters of the injected electron distribution (i.e. the low- and high-energy slopes s_1 and s_2 and the break Lorentz factor $\gamma_{\rm brk}$). It is necessary to lower $\gamma_{\rm brk}$ slightly to match the frequency peak of the synchrotron emission. The jet power in this fitted model is approximately half that of $L_{\rm AD}$.

It can be seen in Figure 5.10 that this fitted EC-disc model fits the broadband SED

well. In particular I am able to achieve good agreement with my optical/UV data from X-shooter and *Swift* UVOT, soft X-ray data from *NuSTAR* and the *Fermi* γ-ray spectrum, all of which were obtained within the ∼three-month period 2017 March–June. However, this model does not fit the high-energy *NuSTAR* specrtum as well, although it is likely that the spectral shape above ≈ 20 keV is not very well defined by the *NuSTAR* data. The harder jet X-ray spectrum in my model does match the *Swift* BAT spectrum taken from the 105-month monitoring campaign. The model also slightly overpredicts the mid-infrared data. This may be because I have not accounted for any synchrotron jet emission in the infrared in my modelling in Section 5.3.1.1. The mid-infrared variability seen in the *WISE* lightcurve (Figure 5.7) would suggest that the jet does make some contribution in this waveband. Any overestimation I may have made of the hot dust luminosity will have minimal impact on the models I have presented. This is because the jet emission region is closer to the accretion disc and BLR than the torus, therefore the energy density of infrared torus seed photons is relatively low.

5.4 Discussion

5.4.1 PKS J1222+0413 as a NLS1

In Section 5.1.2 I found that the FWHM of the Hα and Hβ Balmer lines and the individual lines of the Mg II doublet are each lower than 2000 km s^{-1}, the limiting line width that is usually used to separate NLS1s from broad-line Seyferts (see Table 5.1). If, however, I use Gaussian rather than Lorentzian profiles to model the Mg II lines, I determine FWHMs of 2240 km s^{-1}. Yao et al. (2015b) found a similar FWHM = 2264 km s^{-1} for Hβ when modelling its broad component with a Gaussian. Torrealba et al. (2012) modelled the total Mg II profile with two Gaussians (one broad and one narrow) centred at 2800 Å. For the broad component they determined a FWHM = 5268 km s^{-1}. Clearly, the determination of the emission line FWHMs

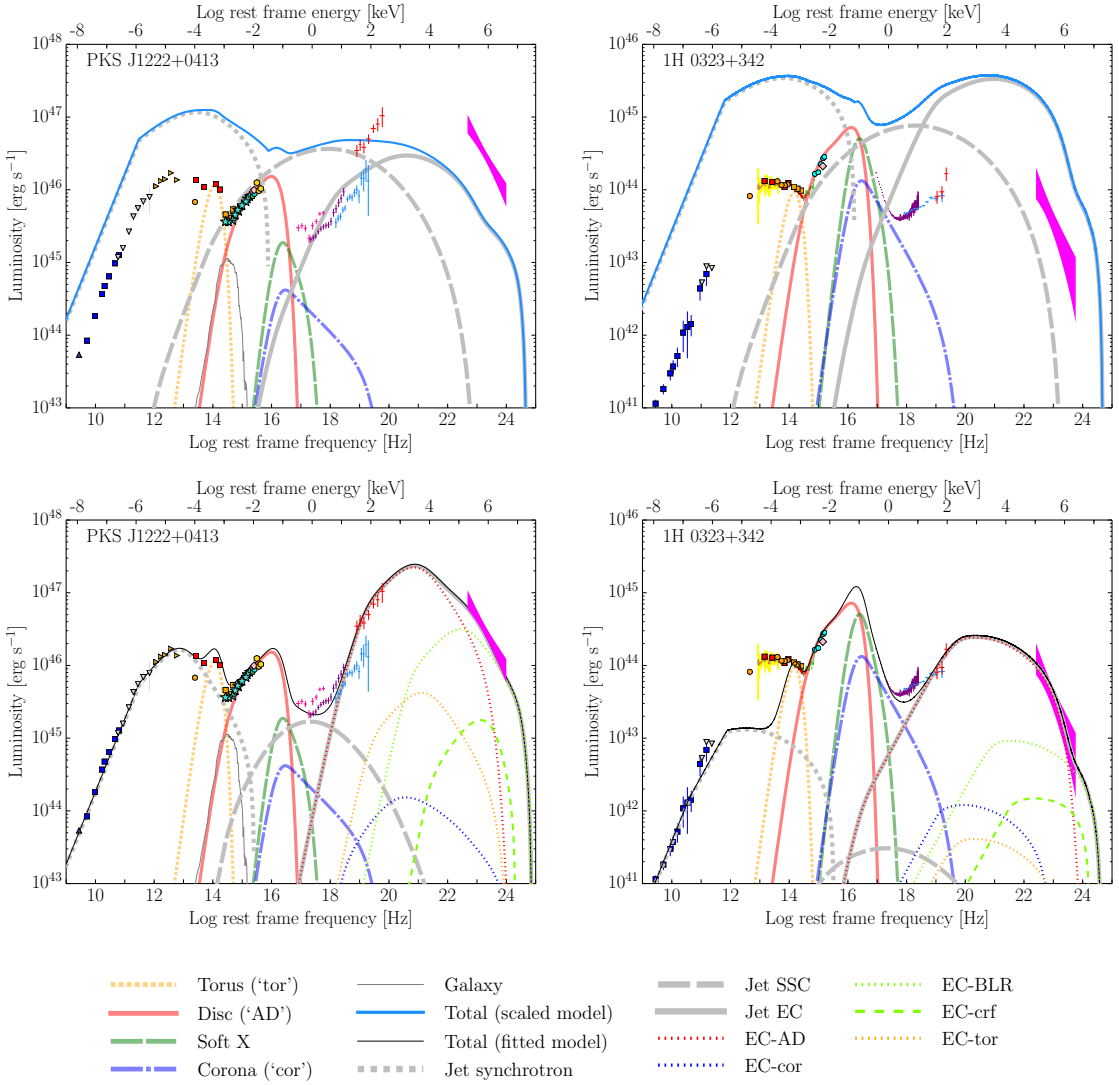

Figure 5.10: *Top:* Black hole mass and accretion rate scaled models of the jet emission from PKS J1222+0413 (left) and 1H 0323+342 (right). *Bottom:* Fitted EC-disc models for PKS J1222+0413 (left) and 1H 0323+342 (right). I show the three components of the jet emission (synchrotron, synchrotron self-Compton 'SSC' and external Compton 'EC') as grey lines. The individual EC components (from the disc, corona, BLR, reflection of the corona off the BLR 'crf' and torus) are shown as coloured dotted and dashed lines. The PKS J1222+0413 data are coded the same as Figure 5.3.

Table 5.6: Jet parameters obtained from spectral fits to the full multiwavelength SED with BBODY+OPTXCONV+JET models

Parameter	Units	Model value			
		PKS J1222+0413		1H 0323+342	
		Scaled with $M_{\rm BH}$ & $\dot{m}$	EC-disc	Scaled with $M_{\rm BH}$ & $\dot{m}$	EC-disc
Input parameters:					
$Z_{\rm diss}$	$[R_{\rm g}]$ (ld)	1280 (15)	1280 (15)	1280 (1.5)	1280 (1.5)
$a_\star$		0.0	0.0	0.0	0.0
i	[deg]	4.41	2.86	4.41	4.77
$\Gamma_{\rm BLF}$		13	20	13	12
δ		13	20	13	12
B	[G]	17.7	3.75	38	8
$\log(P_{\rm rel})$	$[\mathrm{erg\,s^{-1}}]$	43.6	42.9	42.24	41.0
$\gamma_{\rm min}$		1.00	1.00	1.00	1.00
$\gamma_{\rm brk}$		300	200	300	300
$\gamma_{\rm max}$		3000	3000	3000	3000
s_1		1.0	-1.0	1.0	1.5
s_2		2.7	3.2	2.7	2.7
Output / derived parameters:					
$\gamma_{\rm cool}$		12	23	19	47
$\log(\nu_{\rm ssa})$	[Hz]	11.5	11.5	11.6	10.6
$\log\left(\nu^{\rm sync}_{\rm peak}\right)$	[Hz]	13.5	12.9	13.8	12.5
$\log\left(\nu L^{\rm sync}_{\nu_{\rm peak}}\right)$	$[\mathrm{erg\,s^{-1}}]$	47.1	46.2	45.56	43.12
$\log(P_{\rm rad})$	$[\mathrm{erg\,s^{-1}}]$	45.32	44.94	43.95	42.51
$\log(P_{\rm e})$	$[\mathrm{erg\,s^{-1}}]$	45.01	44.69	43.76	42.74
$\log(P_B)$	$[\mathrm{erg\,s^{-1}}]$	45.45	44.48	44.12	42.70
$\log(P_{\rm p})$	$[\mathrm{erg\,s^{-1}}]$	47.28	46.31	45.91	45.01
$\log(P_{\rm j})$	$[\mathrm{erg\,s^{-1}}]$	47.30	46.35	45.93	45.01
$P_{\rm j}/L_{\rm AD}$		4.4	0.51	4.3	0.52
$U_{\rm e}/U_B$		0.37	1.6	0.44	1.1

Comparison of jet models for PKS J1222+0413 and the best fit model for 1H 0323+342 determined in Chapter 4. $P_{\rm rad}$, $P_{\rm e}$, P_B, $P_{\rm p}$ and $P_{\rm j}$ are the radiative, electron, magnetic field, kinetic and total jet powers, respectively. $U_{\rm e}/U_B$ is the ratio of relativistic electron to magnetic field energy densities. The corresponding models are shown in Figure 5.10.

(hence the classification of this source as either a narrow- or broad-line Seyfert 1) depends on the assumed line shape and the contribution of the narrow line component to the total line flux. Here, I have measured the Balmer line widths directly from their observed profiles, without assuming a particular line shape. In doing so, I have assumed that the flux contribution of the narrow line region is negligible, based on my estimation from a typical ratio of [O III]λ5007 to narrow Hβ luminosities. If the narrow Balmer lines are somewhat stronger than I have estimated (which is possible, given the range of values of $L_{[\mathrm{OIII}]}/L^{\mathrm{n}}_{\mathrm{H}\beta}$ determined from large AGN samples[9]) then the FWHMs of the broad Balmer would correspondingly increase to slightly above 2000 km s^{-1}. Alternative measures of the emission line FWHMs of this source may give values exceeding 2000 km s^{-1}, in which case PKS J1222+0413 is not strictly a NLS1. However, I point out that the 2000 km s^{-1} limit is arbitrary and other authors have used more relaxed definitions of NLS1s (e.g. Zhou et al. 2006, Rakshit et al. 2017, Lakićević et al. 2018).

Czerny et al. (2018) emphasise that the 2000 km s^{-1} division is a *phenomenological* one. The NLS1 definition of Osterbrock & Pogge (1985) was determined from low-mass objects in the local Universe. It has been proposed that NLS1s are objects that lie at the extreme of 'Eigenvector 1' (Boroson & Green 1992), with the sequence driven primarily by the accretion rate. A high accretion rate may be a better indicator of the high-mass, high-z analogues of local NLS1s than the emission line FWHMs given that linewidths will be greater for higher-mass sources. Czerny et al. (2018) calculate that the dividing FWHM between narrow- and broad-line AGN is a factor ≈ 2 greater in objects of a mass 3×10^8 M$_\odot$ than those of 10^7 M$_\odot$. Therefore for PKS J1222+0413, based on the SMBH mass the above scaling would imply a FWHM $\lesssim 4000$ km s^{-1}. Additionally, the strong Fe II and weak [O III] emission seen in the optical spectra are typical of NLS1s. I therefore confirm that PKS J1222+0413 is a NLS1, although one with a much greater than average mass.

[9]Note that Zhou et al. (2006) found that only ~ 15 % of NLS1s had a ratio $\lesssim 5$, and in most of the sources with low ratios a large fraction of the emission was from H II regions of the host galaxies. It is therefore very unlikely that $L^{\mathrm{n}}_{\mathrm{H}\beta}$ is much greater than I have estimated.

The apparent weakness of the NLR is consistent with the view of this object as a high-luminosity, highly-accreting quasar. Netzer et al. (2004) suggested that the NLRs of high-luminosity AGN may be different to those of lower-luminosity, nearby sources. The NLR of high-luminosity sources may be lost as a result of being dynamically unbound. Collinson et al. (2017) found an anti-correlation between [O III] λ5007 line strength and Eddington ratio in their sample of high-redshift AGN. Several of their highest accretion rate sources had very weak [O III] emission, similar to what is seen in PKS J1222+0413. Based on their study of the super-Eddington NLS1 RX J0439.6−5311, Jin et al. (2017b) present a picture of high accretion rate AGN which explains the weakness of the NLR as the result of it being (partly) shielded from the nuclear ionising flux by a 'puffed up' inner accretion disc or by a disc wind. Given the Eddington ratio determined for this source, it is unlikely that PKS J1222+0413 has a super-Eddington wind like RX J0439.6−5311. However, its SED peaks in the FUV and the accretion flow X-ray spectrum is very soft and would therefore not over-ionise material driven out in a UV line-driven wind. It may be that PKS J1222+0413 has a UV line-driven wind partly shielding the NLR. Although the narrow emission lines are weak, I find that the high-ionisation lines (emitted by gas between the BLR and NLR) are strong, e.g. Neon ([Ne IV]λ2423) and the Iron transitions (Fe XI).

In relation to the overall AGN population, PKS J1222+0413 has:

- a SMBH mass $M_{\rm BH} = 2 \times 10^8$ M$_\odot$ which is greater than than both the mean SMBH mass of broad-line Seyfert 1s (BLS1s), 10^8 M$_\odot$ (Rakshit et al. 2017) and more similar to typical blazars which have high SMBH masses (10^8–10^9 M$_\odot$: Ghisellini et al. 2010);
- a much higher accretion rate than BLS1s ($L/L_{\rm Edd} \sim 1$ compared with the BLS1 mean ≈ 0.1: Rakshit et al. 2017) and typical blazars which have $\langle L/L_{\rm Edd} \rangle = 0.1$ (FSRQs) and $\langle L/L_{\rm Edd} \rangle < 10^{-3}$ (BL Lacs: Ghisellini et al. 2010);
- particularly weak emission from the NLR (see Figure 5.1);

- a higher radio loudness parameter than the majority of AGN: for PKS J1222+0413, $R_{5\mathrm{GHz}} \sim 1700$ (Yao et al. 2015a) whereas the majority of AGN (≈ 90 %) are radio-quiet with $R < 10$;
- an exceptionally high radio loudness parameter for a NLS1: the radio-loud fraction of NLS1s is very low, Komossa et al. (2006) determined that only ≈ 7 % (≈ 2.5 %) have $R > 10$ ($R > 100$);
- clear evidence for a powerful, relativistic jet: currently only 23 other NLS1s have been detected in γ-rays by *Fermi*.

PKS J1222+0413 is therefore an unusual source in these respects.

5.4.2 The jet of PKS J1222+0413

It was challenging to extract the γ-ray spectrum of PKS J1222+0413 (Section 5.2.1.5). Because of the close proximity of the bright γ-ray sources 3C 273 and PKS 1237+049 it was found that very few photons in the field had a strong statistical association with PKS J1222+0413; most were more favourably associated with the other sources. Applying an 85 per cent confidence cut left very few photons and a limited γ-ray spectrum. As I noted earlier, there have been no γ-ray flares recorded by *Fermi* near the location of PKS J1222+0413. Rapid variability in the optical has not been recorded either, with Ojha et al. (2019) noting that the intra-night optical variability was remarkably low, and consistent with levels see in non-jetted (radio-quiet) sources. However, the *WISE* data (Figure 5.7) show variability which is likely from jet synchrotron emission.

Whereas the viewing angle to the jet (and hence the bulk Lorentz and Doppler factors, under the assumption $i = 1/\Gamma_{\mathrm{BLF}} \approx \delta$) was constrained by radio measurements (Fuhrmann et al. 2016a) in the case of 1H 0323+342 (previous chapter), I have no such observational constraint for the jet of PKS J1222+0413. Lister et al. (2016)[10]

[10]In this paper the source is named 4C +04.42.

investigated the radio jet of PKS J1222+0413 as part of the MOJAVE project and found that the jet is two-sided on kpc scales (but it is one-sided on pc scales). Lister (2018) notes that no measurable motion within the jet has been recorded in a 14-year monitoring period and that the maximum apparent jet speed is sub-luminal: $(0.9 \pm 0.3)c$. If the transverse speed of the jet $v_t = 0.9c$, this would imply a large viewing angle to the jet axis with $i \approx 50$–$90°$ and a low bulk Lorentz factor whereas high Lorentz factors are determined by SED modelling (e.g. Yao et al. 2015b). The viewing angle is likely to be small because of the one-sided pc-scale jet structure. Its long-term (2008 to date) 15 GHz radio lightcurve, recorded by the Owens Valley Radio Observatory (OVRO, Richards et al. 2011), shows variability which is also suggestive of a high Doppler factor and low viewing angle. It is likely that the apparent sub-luminal motion is due to a lack of traceable bright knots, rather than a low-speed jet.

Whilst it is difficult to extract a reliable γ-ray spectrum for PKS J1222+0413 because of its low γ-ray flux and the presence of bright nearby sources, I am confident of the γ-ray nature of the source. Other, well-defined properties such as the radio and infrared variability and high-resolution radio images of the jet are supportive of the presence of very high energy processes. Furthermore, the X-ray data from *NuSTAR* and *Swift* BAT are evidence of a high-energy Compton component, and the γ-ray spectrum appears to be consistent with the very high-energy tail of this feature.

5.4.3 Comparison with 1H 0323+342

I presented a similar analysis of the lowest-redshift γ-NLS1, 1H 0323+342, in Chapter 4. Here I make a comparison with my findings from PKS J1222+0413. Obviously, PKS J1222+0413 has a much greater SMBH mass than 1H 0323+342. Therefore it is expected that PKS J1222+0413 will be more similar to a standard (high-mass) blazar. Indeed, when I scale a standard FSRQ jet by mass and mass accretion rate I see that discrepancy between the predicted SED and the data is

much less than I found for 1H 0323+342 in the previous chapter. The high accretion rate of PKS J1222+0413 means that a high magnetic field is predicted from the scaling relations. As with 1H 0323+342, the resultant predicted SED has a low Compton dominance and a shape much more akin to a BL Lac, albeit at a much higher luminosity than BL Lacs. I can better fit the data by turning down the magnetic field strength. (With 1H 0323+342 it was necessary to turn down both the magnetic field strength and the power injected into the relativistic electrons.) As with 1H 0323+342, a typical NLS1 SED model fits the observed NIR–X-ray SED well, if a (jet) power-law is added to account for hard X-rays. in the previous chapter I found that for 1H 0323+342 that the X-ray photon index below $\approx$ 2 keV was $\Gamma \approx 3.59$, typical of (non-jetted) NLS1s which have very soft low-energy photon indices ($\Gamma_{0.1-2.4\mathrm{keV}} \gtrsim$ 2–5 Boller et al. 1996). Above 2 keV, the photon index was much harder ($\Gamma \approx 1.52$), typical of nonthermal jet emission. This was interpreted as a transition from accretion-flow-dominated to jet-dominated emission. I do not find such strong evidence of a soft, low-energy photon index in PKS J1222+0413 (Sections 5.2.1.3 and 5.3.1.1), likely because its higher mass and redshift mean that the accretion flow makes less of a contribution to the flux in the *XMM-Newton* bandpass.

In Chapter 4 I showed that 1H 0323+342 had a low jet power for its accretion power, compared to the *Fermi* blazars studied by Ghisellini et al. (2014). Here, I find that the jet of PKS J1222+0413 is similarly underpowered relative to its accretion power. However, since it has a SMBH mass similar to FSRQs, in terms of its *absolute* jet power it occupies the same region of the blazar sequence as the FSRQs, as one might expect. Foschini (2017) proposed that there are two branches on the blazar sequence. This can be seen if the jet power (calculated from the radio luminosity) is plotted against accretion power (see Figure 5.11). The track of the main branch, containing FSRQs and BL Lacs (which have similar SMBH masses), may be explained as a difference in the environment in which the relativistic electrons cool. The lower track, connecting radio-loud NLS1s to FSRQs (which have similar cooling environments),

must be driven by the difference in the SMBH masses. A small number of the sources shown in Figure 5.11 have jet powers estimated both from their radio luminosity and from SED modelling. I find that the jet power calculated via SED modelling is generally greater than that estimated from the radio luminosity. In Figure 5.11, the sources with jet power calculated from SED modelling are shown as solid stars, connected to the corresponding estimate from the radio luminosity shown as open stars. Recently however, Paliya et al. (2019) have modelled the broadband SEDs of sixteen γ-NLS1s to determine the jet powers, and have compared these to a sample of previously-modelled blazars. Their results suggest that γ-NLS1s form the low-jet-power tail of the FSRQ population, rather than forming a separate branch.

The SMBH masses and normalised accretion rates of the BL Lacs, FSRQs and RL-NLS1s plotted in Figure 5.11 are shown in Figure 5.12; the distinctions between the subsets are very clear in this plot.

Yao et al. (2015b) also modelled the SED of PKS J1222+0413 and presented both an EC-BLR and EC-torus case in which the γ-rays were predominantly upscattered seed photons from the BLR or torus, respectively. Here, I have demonstrated that an EC-disc model can also reproduce the observed SED. In my EC-disc model I determine a high bulk Lorentz factor $\Gamma_{\rm BLF} = 20$, which is substantially greater than the mean value 13 Ghisellini et al. (2010) found for FSRQs and the value 12 I previously found for 1H 0323+342. The factors determined by Yao et al. (2015b) from their jet models were even higher: $\Gamma_{\rm BLF} = 26, 35$ for the EC-BLR and EC-torus models, respectively. Unfortunately, Yao et al. (2015b) do not quote any jet powers determined from their models, or give sufficient details of their model parameters and so it is not possible to undertake a meaningful comparison. I emphasise that the jet power and parameters determined by SED fitting are still model-dependent. The results which are obtained will depend on the detailed assumptions made, and the approaches taken to compute the complex physical processes. Even within the same prescription, the complexity of jet models mean that it is difficult to converge on a unique solution. My approach has been to construct a quasi-simultaneous data set

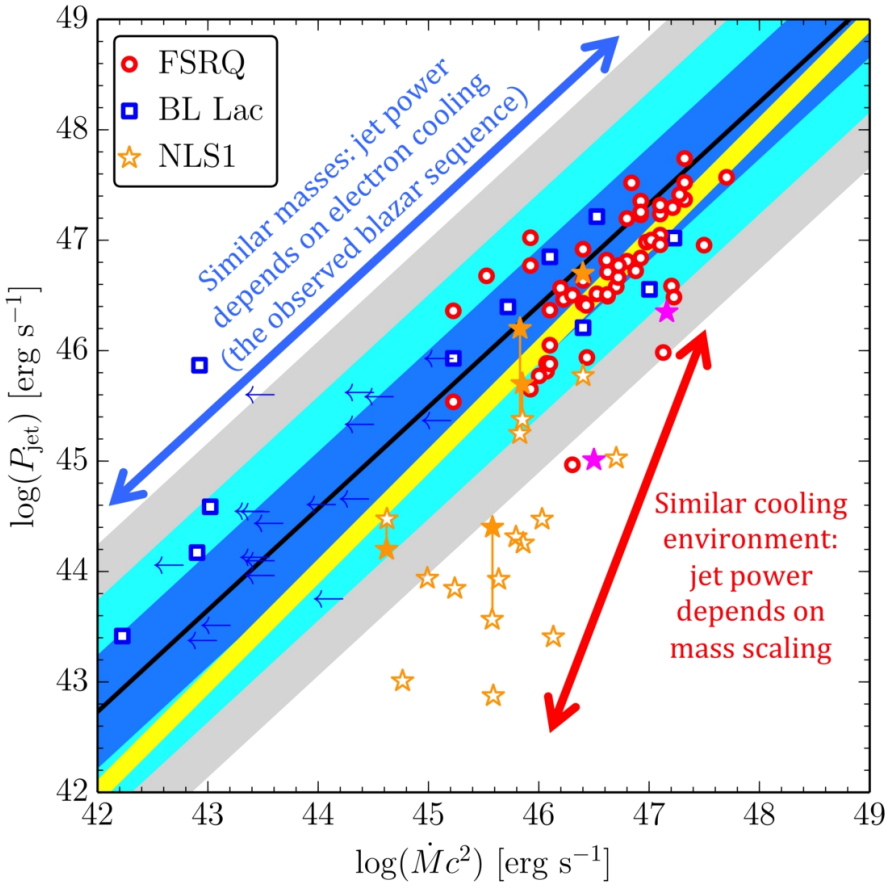

Figure 5.11: A comparison of jet and accretion powers for different types of RL-AGN. The solid yellow line shows the one-to-one relation. The solid black line and shaded regions are the best fit relation and 1, 2, and 3σ confidence regions, taken from Ghisellini et al. (2014) (c.f. Figure 1.8). The data points are taken from Foschini (2014), in which the jet power has been estimated from the radio luminosity. Jet powers of γ-NLS1s computed from SED modelling (in which $P_{\rm jet}$ is the total power calculated from the model, values taken from elsewhere in the literature) are shown as solid orange stars, and are connected to the corresponding estimate from the radio luminosity. The two γ-NLS1s represented by magenta stars are 1H 0323+342 and PKS J1222+0413, with values taken from this thesis. The accretion powers have been calculated from the disc luminosities assuming a radiative efficiency $\eta = 0.3$.

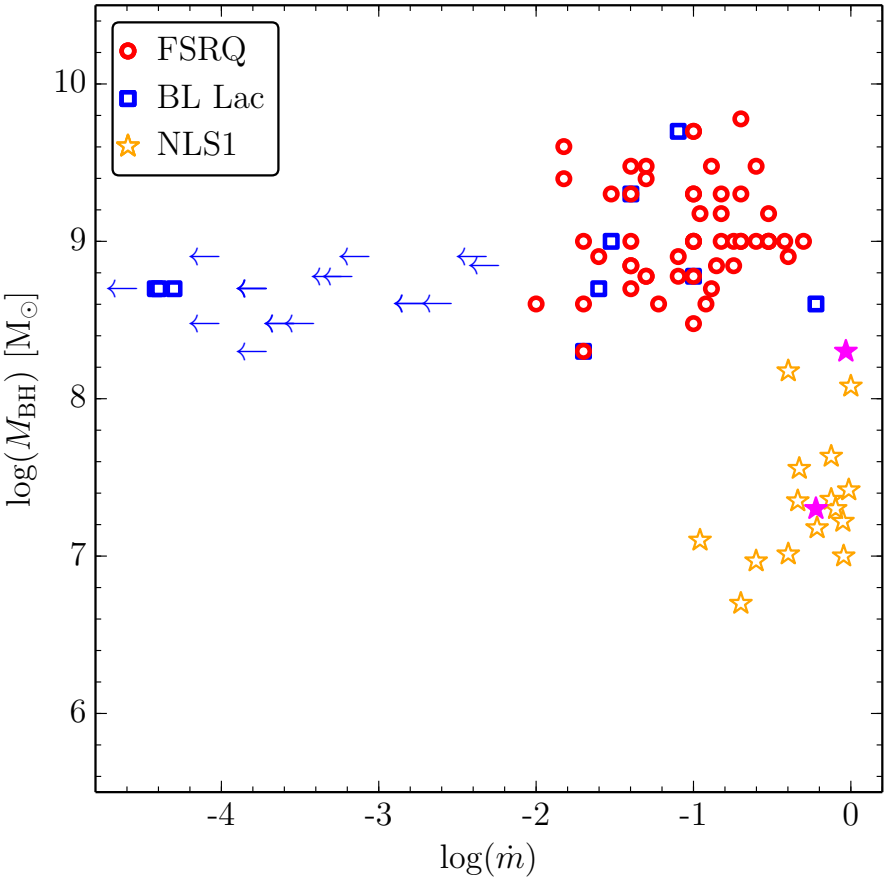

Figure 5.12: For the sources shown in Figure 5.11, this plot shows their SMBH masses ($M_{\rm BH}$) versus normalised accretion rates ($\dot{m}$). It is clear that BL Lacs and FSRQs have similar masses but different normalised accretion rates; FSRQs and NLS1s have similar normalised accretion rates but different masses. The γ-NLS1s studied in this thesis, 1H 0323+342 and PKS J1222+0413, are represented by magenta stars.

and to self-consistently model and apply the ambient photon field which is crucial in reproducing the observed external Compton (X-ray and γ-ray) emission. In future studies it would be useful if the results were presented in a more uniform way, with equivalent model parameters and basic assumptions stated.

As was discussed for 1H 0323+342 in the previous chapter, my approach of measuring and self-consistently applying the ambient photon field within the jet model removes some of the assumptions other authors make about the seed photon energy densities. As with 1H 0323+342, I do not have to greatly alter the parameters of the injected electron distribution from the mean FSRQ values of Ghisellini et al. (2010) in order to fit the data. The similarity implies that the electron acceleration mechanism in these two γ-NLS1s is the same as that of typical FSRQs. This aspect of the jet modelling is likely to be firmer than the determination of values for B, $P_{\rm rel}$ and $\Gamma_{\rm BLF}$, which influence the jet powers. However, my initial test (simply scaling these three parameters from the mean FSRQ values of Ghisellini et al. 2010) allows for a comparison of the predicted values with the fitted values. In this way, the parameter values obtained can be assessed in relative terms, even if the precise values are less certain.

5.5 Conclusions

My main results are summarised below:

- The SMBH mass $\approx 2 \times 10^8$ $M_\odot$ is very high for a NLS1, which typically have an order of magnitude smaller SMBH masses.

- I conclude that PKS J1222+0413 is a NLS1, based on my new data and analysis of its optical spectral properties and the accretion flow parameters obtained from modelling its broadband SED. This is in agreement with the NLS1 classification made by Yao et al. (2015b).

- The very weak [O III] is suggestive of a UV line-driven disc wind shielding the narrow-line region from ionising UV flux produced near to the SMBH.

- The jet power is approximately half of the accretion disc luminosity whereas for BL Lac and FSRQ-type blazars, the jet power typically exceeds the accretion power (Ghisellini et al. 2014). This finding is similar to the result for the γ-NLS1 1H 0323+342 (Chapter 4) which I also found to have an underpowered jet.

- Because of its high SMBH mass, similar to FSRQ-type blazars, PKS J1222+0413 lies in the region of the blazar sequence occupied by the FSRQs. Most other γ-ray detected NLS1s, like 1H 0323+342, have much lower absolute jet powers (similar to BL Lacs) but share many of the same jet properties as FSRQs. PKS J1222+0413 is therefore an ideal object in which to explore the relationship between γ-NLS1s and FSRQs.

Chapter 6

The 'Big Dipper': A study of a hypervariable AGN

All AGN are variable, but some are more variable than others. In the last few decades, an increasing number of extremely optically-variable AGN have been discovered. The optical continuum in these sources is observed to diminish or increase by factors of a few or more over several years. This variability is of greater amplitude than the ubiquitous ~ 10 % optical variability which likely results from the reprocessing of the central UV/X-ray flux that occurs on shorter timescales. Several lines of evidence point to a change in the accretion disc luminosity (rather than temporary obscuration of the nucleus) in many hypervariable sources. However, the extreme variability of these AGN on observable timescales poses a serious challenge to the current paradigm of thin, viscous, AGN accretion discs.

In newly-discovered hypervariables is therefore imperative to determine whether or not the optical continuum variations can be explained by extrinsic or intrinsic mechanisms. It is important to characterise the continuum and emission line changes in intrinsically hypervariable AGN as this can enable us to better understand the processes at work and improve our models of AGN accretion discs. A key question is whether hypervariable AGN are a distinct subset of the larger AGN population (i.e. the accretion process in hypervariables and less-variable AGN is different somehow)

or whether hypervariables are simply at the tail end of a broad distribution in AGN variability.

SDSS J2232−0806 (the 'Big Dipper') has been identified as a 'slow-blue nuclear hypervariable': a galaxy with no previously known active nucleus, blue colours and large-amplitude brightness evolution occurring on a timescale of years. Subsequent observations have shown that this source does indeed contain an active galactic nucleus (AGN). An optical photometric and spectroscopic monitoring campaign has been ongoing since 2012 and has has recorded one major dimming event (and subsequent rise) over a period of around four years; there is also evidence of previous events consistent with this in archival data recorded over the last twenty years. In this chapter I report an analysis of the eleven optical spectra obtained to date and I assemble a multiwavelength data set including infrared, ultraviolet and X-ray observations. I find that an intrinsic change in the luminosity is the most favoured explanation of the observations, based on a comparison of continuum and line variability and the apparent lagged response of the hot dust. This source, along with several other recently-discovered 'changing-look' objects, demonstrate that AGN can exhibit large-amplitude luminosity changes on timescales much shorter than those predicted by standard thin accretion disc models.

6.1 Introduction

Numerous AGN variability studies have been conducted, both on large samples (e.g. Stripe 82, MacLeod et al. 2012, Schmidt et al. 2012, and Zuo et al. 2012) and detailed studies of individual cases (e.g. NGC 4593 by McHardy et al. 2018 and NGC 5548 by Pei et al. 2017 and references therein). In addition to these studies some cases of extreme variability have been identified in the form of the so-called 'changing-look' quasars (CLQs: e.g. MacLeod et al. 2019, Yang et al. 2018b, Rumbaugh et al. 2018 and LaMassa et al. 2015) which are AGN with (dis)appearing broad emission lines as well as strong continuum changes. It is very probable that

more than one physical mechanism is responsible for the variations seen across all samples. Changes in the dust extinction in some AGN were proposed in early studies (e.g. Goodrich 1995), but this explanation is not generally preferred in the case of changing-look AGN. In recent studies, often the most favoured cause is a change in the emission from the accretion disc or its associated Comptonisation regions (e.g. Katebi et al. 2018, Noda & Done 2018, Stern et al. 2018, Ross et al. 2018, Wang et al. 2018, Sheng et al. 2017, Gezari et al. 2017, Parker et al. 2016, Ruan et al. 2016, MacLeod et al. 2016, Runnoe et al. 2016 and LaMassa et al. 2015). Other, rarer events, such as stellar tidal disruption, supernovae in the nuclear regions, and gravitational microlensing, have also been proposed (e.g. Lawrence et al. 2016, Bruce et al. 2017 and references therein). To make further progress it is important to better characterise the properties of variability to help distinguish between the various mechanisms responsible.

6.1.1 The source SDSS J2232−0806

SDSS J223210.51−080621.3 (hereafter SDSS J2232−0806) is an AGN at redshift $z = 0.276$ (Collinson et al. 2018). It was identified as a 'slow-blue nuclear hypervariable' object by Lawrence et al. (2016) on the basis that it showed large-amplitude optical brightness variability ($|\Delta g| \geqslant 1.5$) and the change was slow and blue (occurring over several years, in contrast to the fast and red transients which are likely associated with supernovae).

Photometric monitoring of this source with the Liverpool Telescope since 2013 has captured one substantial dimming event, and there is sparsely sampled archival photometry that is consistent with similar past events.

6.1.2 The aims of this study

I aim to investigate whether the variability behaviour of this source is best explained by either obscuration of the nucleus, or by some intrinsic change in the emission

from the central engine. The optical spectroscopic monitoring campaign conducted with the William Herschel Telescope allows an investigation of changes in both the AGN continuum and line emission from the broad line region (BLR).

For the redshift $z = 0.276$, my adopted cosmology implies a luminosity distance of 1410.8 Mpc and a flux-to-luminosity conversion factor of 2.38×10^{56} cm^2.

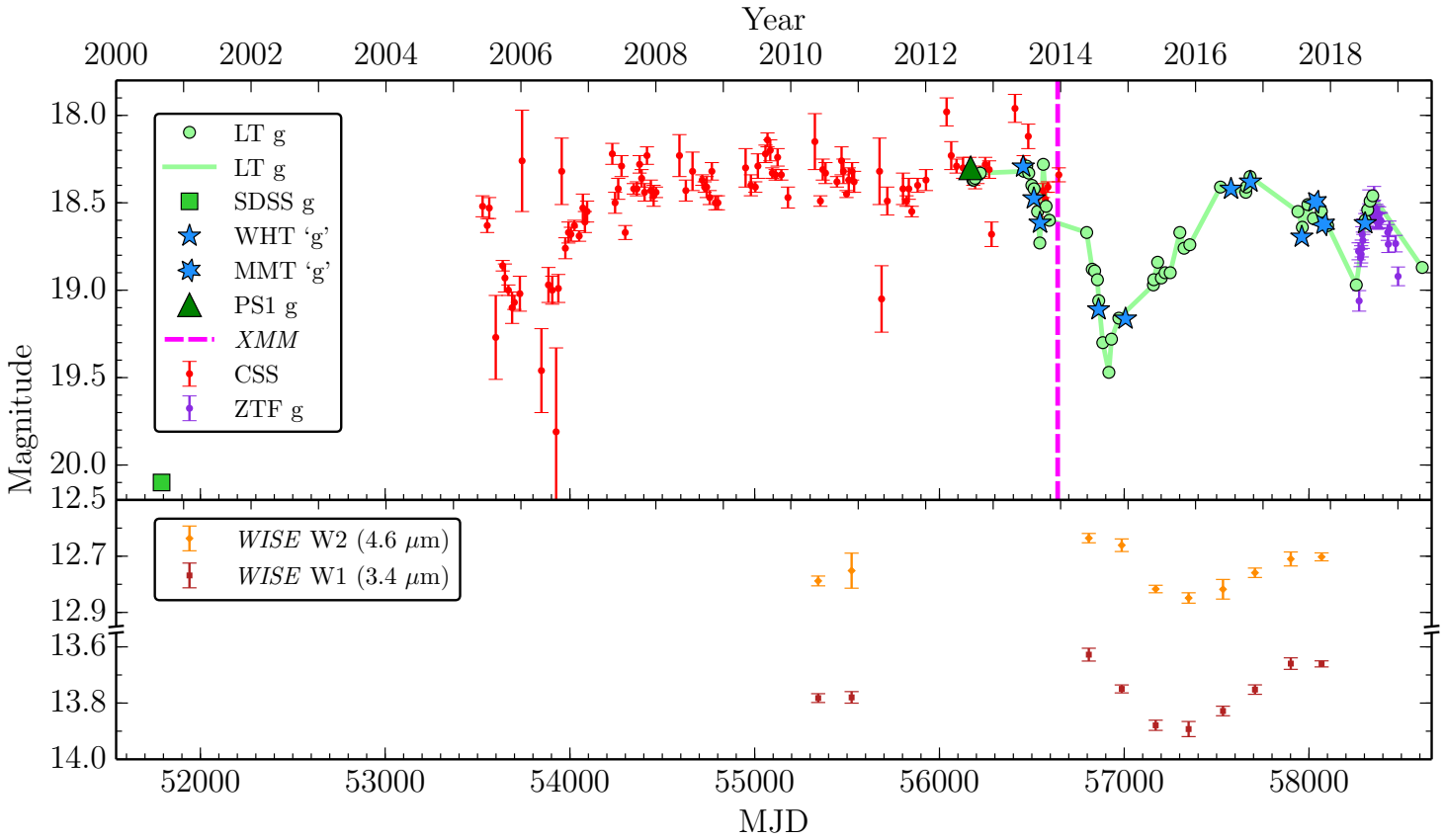

Figure 6.1: *Top*: the optical lightcurve of SDSS J2232−0806, showing g magnitudes from the Sloan Digital Sky Survey (SDSS), PanSTARRS-1 (PS1), the Liverpool Telescope (LT), the Catalina Sky Survey (CSS) and the Zwicky Transient Facility (ZTF). I also show the equivalent g magnitudes derived from spectroscopic observations made with the William Herschel Telescope (WHT) and the MMT. The date of the *XMM-Newton* X-ray and optical-UV observations is also indicated. *Bottom*: the *WISE* infrared lightcurves.

6.2 The optical monitoring campaign

Lawrence et al. (2016) found that in 2012 the PanSTARRS-1 (PS1) 3π Survey g band photometry of SDSS J2232−0806 was 1.8 magnitudes brighter than it was in a SDSS photometric observation made in 2000. To further investigate this interesting source, a photometric monitoring campaign began in 2012 using the Liverpool Telescope and is ongoing. Optical spectroscopic monitoring commenced in 2013, primarily using the William Herschel Telescope, with an additional two spectra taken in late 2017 with the MMT. The observing campaign has revealed a dip in brightness of around a factor three in flux and shows a recovery in the most recent observations. In this section I present my analysis of the optical data.

6.2.1 Observations and data reduction

6.2.1.1 Liverpool Telescope optical photometric monitoring

Photometric observations were taken with the Liverpool Telescope (LT) in the r, g and u bands. Forty-five independent photometric observations were obtained using the g filter ($\lambda_{\rm eff.} = 4696$ Å) between 2012 September and 2019 May are shown in Figure 6.1. The g and r bands are much more frequently sampled than the u band, for which I have only twenty-one photometry points. The observed variability amplitude in the g band ($\Delta g \approx 1.2$) is greater than that of r band ($\Delta r \approx 0.8$) although I note that the r band ($\lambda_{\rm eff} = 6111$ Å) is subject to increasing contamination from the host galaxy as the AGN contribution diminishes. In addition, the u band ($\lambda_{\rm eff} = 3499$ Å) covers the strong, broad Mg II emission line (observed at 3573 Å) and so it is not a clean measure of the AGN continuum. For these reasons, I use only photometry obtained in the g band.

6.2.1.2 William Herschel Telescope optical spectroscopic monitoring

SDSS J2232−0806 has been observed with the William Herschel Telescope (WHT) on nine occasions between 2013 June and 2018 July. The Intermediate dispersion Spectrograph and Imaging System (ISIS) long-slit, double spectrograph was used with the 5300 Å dichroic which directed the light into the red and blue arms containing the R158B and R300B gratings, respectively. Typically ×2 binning in the spatial direction was used to improve the signal-to-noise ratio (SNR). This set-up gave a spectral resolution of $R \approx 1000$ at 7200 Å in the red and $R \approx 1500$ at 5200 Å in the blue, for a slit width of 1 arcsecond. The total wavelength coverage was ≈ 3100–10600 Å, this window includes the principal emission lines Mg II λ2800, Hβ λ4861, [O III] $\lambda\lambda$4959, 5007 and Hα λ6563.

The data reduction was performed with a pipeline using custom PYRAF scripts and standard techniques. The pipeline is described in detail in Bruce et al. (2017) (Section 2.3.3 in that paper).

Unfortunately, I do not have a spectrum contemporaneous with the nadir of the LT lightcurve, which occurred around 2014 September 17. The spectra obtained on 2014 July 23 and December 16 were recorded 56 days before and 90 days after the photometric minimum and sample the falling and rising side of the dip in the lightcurve, respectively (see Figure 6.1).

6.2.1.3 MMT spectroscopic monitoring

Two optical spectra of SDSS J2232−0806 were obtained with the MMT in 2017 December. The observations were conducted during grey time; on both occasions the observing conditions were clear with sub-arcsecond seeing. The MMT Blue Channel spectrograph was used with the 300 g mm^{-1} grating and a 1 arcsecond slit. This set-up gives a spectral resolution of $R \approx 740$ at 4800 Å, lower than that which was obtained with the WHT. The target spectra used here are the co-added medians of three 10 minute exposures.

6.2.2 Optical spectral analysis

Optical and ultraviolet fluxes are affected by reddening caused by dust in the Milky Way. The Galactic neutral hydrogen column density towards SDSS J2232−0806, $N_{\rm H} = 4.52 \times 10^{20}$ cm^{-2} (Dickey & Lockman 1990), implies a colour excess $E(B-V) = 0.078$ mag based on the relation derived by Bohlin et al. (1978). Here, and in Section 6.3, I correct the data for Galactic reddening using this value of $E(B-V)$ and the Milky Way reddening curve of Cardelli et al. (1989).

6.2.2.1 Internal scaling of spectra

Before I perform the spectral analysis, I rescale the spectra to account for variations in the absolute flux calibration caused by effects such as seeing (slit losses) and thin cloud. Since the strong, narrow [O III] λ5007 forbidden emission line originates in a low-density, large-volume gas, it should not vary during the course of the monitoring period and is therefore a suitable line to use for internal cross-calibration (provided it it not spatially resolved). Rather than simply assuming the flux in the line remains constant (which depends upon an accurate determination of the underlying continuum flux level), I assume instead that the line profile is constant and determine the appropriate flux scaling factors using the PYTHON package MAPSPEC developed by Fausnaugh (2017). This package is an implementation of, and improvement on, the method of van Groningen & Wanders (1992). As noted by them this method should produce a more accurate internal flux scaling than the standard method of simply scaling each spectrum so that the integrated [O III] λ5007 line flux is equal to a chosen reference value.

6.2.2.2 Absolute flux scaling of spectra

From the internally-scaled optical spectra, I calculated the equivalent LT g magnitude. The LT optical CCD camera was changed from the RATcam to the IO:O at the end

of 2014 February, so in my calculations I use the filter specifications appropriate to the LT instruments in use at the time the spectrum was recorded, although the resultant difference in magnitude is very minor. For each spectrum I measured the mean flux $\langle \nu F_\nu, g \rangle$ in the LT g band (RATcam 3945–5532 Å, IO:O 3933–5630 Å) then calculated the g magnitude equivalent

$$g = -2.5 \log \left(\frac{\langle \nu F_\nu, g \rangle \times 10^{23}}{\nu_{\text{eff}}\ \text{ZP}} \right)\ \text{mag}, \tag{6.2.1}$$

where ZP is the zero point magnitude of the filter (RATcam 3940.5 Jy; IO:O 3936.7 Jy) and ν_{eff} is the frequency equivalent to the filter's effective wavelength λ_{eff} (RATcam 4730 Å; IO:O 4696 Å).

By comparison with the LT g magnitudes, I found that the equivalent magnitudes appeared systematically offset by ≈ 0.15 mag. This slight discrepancy is likely due to slit losses, resulting in a lower flux in our narrow-slit spectra compared with the large-aperture photometry. Adjusting the magnitudes by -0.15 mag (an increase of ≈ 15 per cent in flux) the equivalent magnitudes replicate both the shape and level of the LT lightcurve, as can be seen in Figure 6.1. In the following, all of the measurements that I make from the spectra include the internal and absolute flux scalings described here.

6.2.2.3 Comparison of the optical spectra

All eleven optical spectra are shown in the top panel of Figure 6.2. To highlight the spectral variability I have coloured the brightest and faintest spectra in blue and red, respectively, and plotted both their difference and ratio in green and purple, respectively, in the panels below. The ratio between the brightest and faintest spectrum shows the fractional variability at each wavelength. The fractional variability at longer wavelengths is diluted by emission from the host galaxy and it can be seen in the ratio spectrum that the fractional variability is greater in the blue end. Taking the difference removes the constant components including the host galaxy. In the difference spectrum it can be seen that the absolute flux variation in

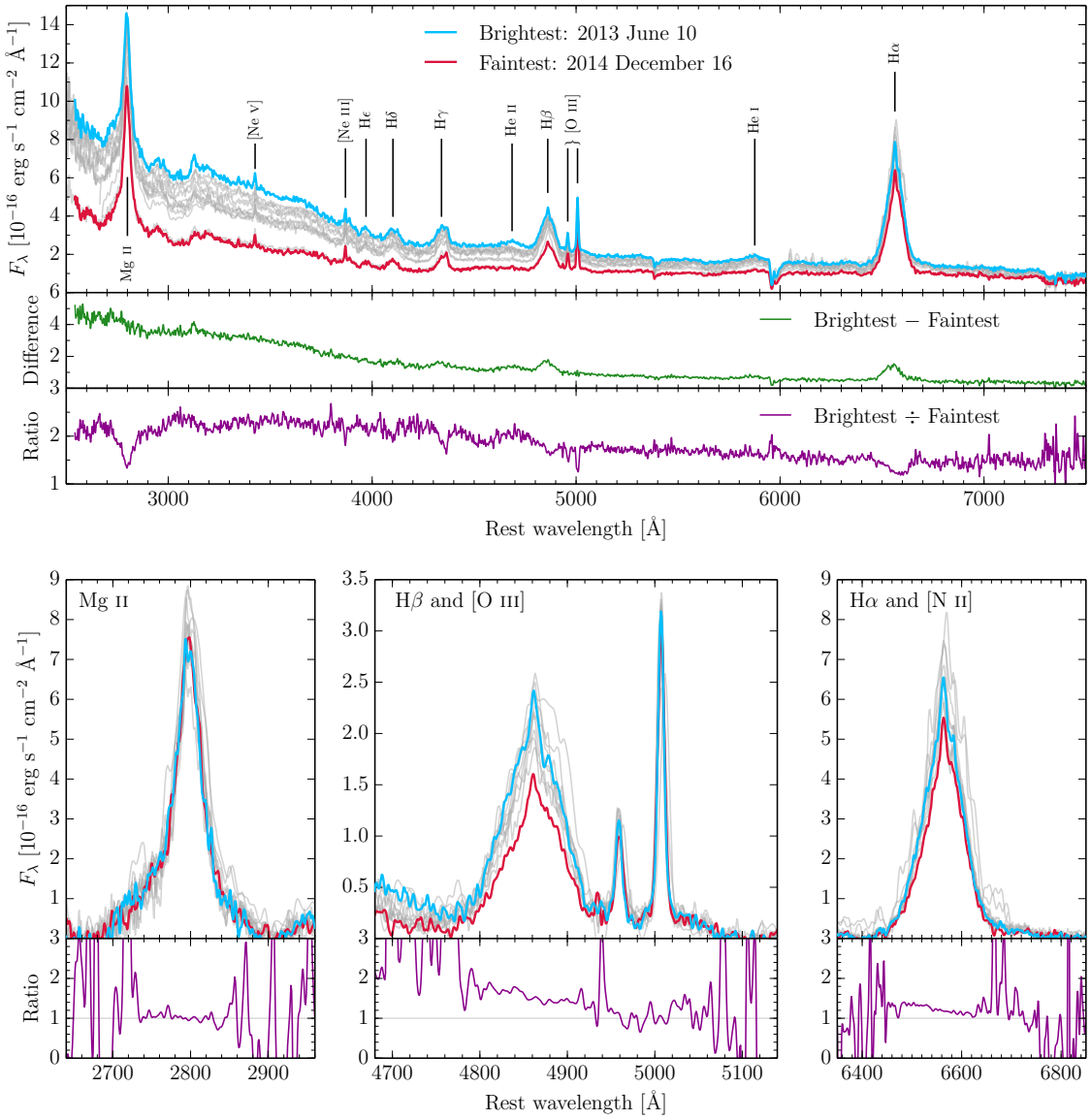

Figure 6.2: *Top*: All eleven optical spectra of SDSS J2232−0806, rescaled to the same [O III] λ5007 emission line profile and corrected for Galactic reddening ($A_V = 0.24$). The brightest spectrum (2013 June) is shown in blue and the faintest spectrum (2014 December) is shown in red; the other nine spectra are shown in grey. Prominent emission lines are labelled. In the lower panels the difference spectrum is shown in green and the ratio spectrum in purple. *Bottom*: Continuum-subtracted regions containing key emission lines. Spectra are colour-coded as in the top plot. In the lower panels, the ratios between the brightest and faintest spectra is shown in purple.

the blue continuum ($\lambda \lesssim 4200$ Å) is greater than in the red. The [O III] $\lambda\lambda 4959, 5007$ lines, which I assumed to be non-variable, are absent in the difference spectrum which gives me confidence that the flux scaling method I have adopted works well. Whereas differences in the Hα and Hβ lines between bright and faint spectra are clear, the Mg II line appears to be less variable. This is obvious in the ratios of the continuum-subtracted lines (shown in purple in the lower panels of the bottom three plots of Figure 6.2) where the core of Mg II changes very little and no substantial change is apparent in the broad wings. The change in the Balmer lines is most apparent on the blue side of the lines, which seem to have a slight 'red shoulder' in the fainter spectra. A similar skewness of the Hα profile in the faint state of the CLQ J0159+0033 was found by LaMassa et al. (2015).

I computed the mean and root-mean-square (RMS) spectra following the method of Peterson et al. (2004): the mean spectrum of a set of N spectra is simply

$$\langle F(\lambda) \rangle = \frac{1}{N} \sum_{i=1}^{N} F_i(\lambda) \tag{6.2.2}$$

and the RMS spectrum is defined as

$$S(\lambda) = \sqrt{\frac{1}{N-1} \sum_{i=1}^{N} [F_i(\lambda) - \langle F(\lambda) \rangle]^2}. \tag{6.2.3}$$

Before performing the calculations, the single-epoch spectra are first shifted in wavelength so that the centroids of the [O III] λ5007 lines (as determined from my model fits) are aligned. The two MMT spectra are noisier than the nine obtained at the WHT and have less wavelength coverage (particularly redward of Hα). I confirmed that the shapes and general features of the mean and RMS spectra are (broadly) unchanged if I exclude the MMT spectra. Having done so, I proceeded with the mean and RMS spectra determined from just the WHT observations, so as to extend the results into the red.

The resultant spectra are shown in Figure 6.3. As in the difference spectrum, the [O III] lines are removed in the RMS spectrum whereas the Balmer lines, Balmer continuum ($\approx$ 2000–4000 Å) and He II λ4685 are all visible. I also note that the Mg II

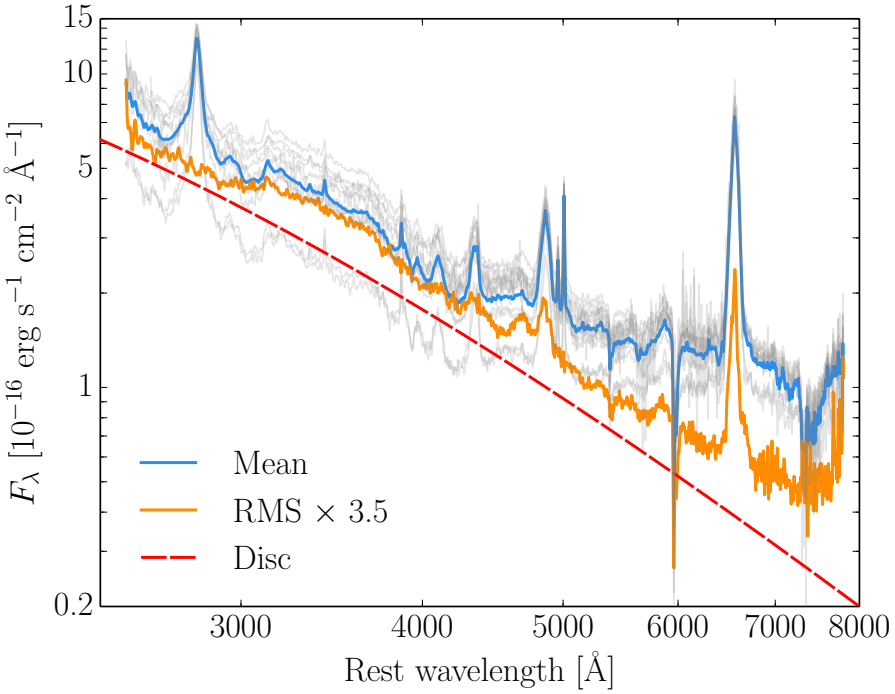

Figure 6.3: The mean spectrum of SDSS J2232−0806 is shown in blue and the root-mean-square (RMS) spectrum is shown in orange. The RMS spectrum has been scaled up by a factor 3.5 to ease the comparison with the mean. The eleven spectra from the monitoring campaign are underplotted in grey. The dashed red line shows the model spectrum of an AGN accretion disc with $L/L_{\rm Edd} = 3$ % and $R_{\rm out} = 100\ R_{\rm g}$.

emission line is absent from the RMS spectrum, which I discuss later. Comparing the shapes of the mean and RMS spectra, it can be seen that the RMS spectrum is bluer since the non-variable host galaxy component has been removed: I discuss this in Section 6.3.3.1. The shape of the RMS spectrum is very similar to that of an accretion disc; in Figure 6.3 I show a standard disc spectrum for comparison, calculated for a SMBH mass of 2×10^8 M$_\odot$, $L/L_{\rm Edd} = 0.03$ and outer radius of 100 gravitational radii (equal to that determined in my SED model in Section 6.3.3.2).

6.2.3 Measurement of the continuum and the emission lines

The continuum and emission line fitting was performed using a custom PYTHON script employing the LMFIT package[1] which employs a Levenberg-Marquardt algorithm for non-linear, least-squares minimisation. The fitting routine appeared to underestimate the errors on the returned parameters, so rather than quoting the error on a single fit, an iterative approach was taken. Each spectrum was fitted 100 times: on each iteration Gaussian noise was added to the flux density with the amplitude of the noise determined by the measurement error. The final model parameters and errors are the mean and standard deviation calculated from the 100 iterations. The standard deviation quantifies the spread of parameter values that can reasonably fit the data. The errors on the physical quantities derived from the model parameters (e.g. the line flux, equivalent width etc.) have been propagated using standard methods. The results of this iterative fitting procedure are tabulated in Tables B.1 and B.2.

6.2.3.1 Red continuum determination

For the WHT spectra, the (rest frame) 3900–7800 Å continuum is estimated from five emission line free windows of width 50 Å; these are centred on the wavelengths 4240, 5100, 6205, 7050 and 7700 Å. Because of the narrower wavelength coverage of the two spectra obtained using the MMT, only the first three of these windows are available. I fitted a power-law continuum of the form $F_\lambda = C\,(\lambda/5100\ \text{Å})^{-\alpha}$ through these points to determine the global continuum, allowing the slope α and normalisation C to be free parameters in the fit.

[1] https://lmfit.github.io/lmfit-py/

6.2.3.2 Modelling of the principal emission lines

To model the Balmer lines, the red continuum is subtracted from two wavelength windows containing the emission lines of interest (rest frame 4740–5100 Å for Hβ and [O III]; 6380–6800 Å for Hα and [N II]). The permitted lines were initially fit with a sum of two Gaussians (one broad and one narrow) with the same central wavelength. However, there were clearly substantial residuals in the line profiles, particularly prominent in the red wing of Hα. I therefore added a third Gaussian component to the Balmer lines, modelling a very broad base, and allowed this to be offset from the central wavelength of the narrower components. The two [N II] forbidden lines were each fit with a single, narrow Gaussian. As well as a strong, narrow Gaussian, a weak, broad Gaussian base was added to the [O III] λ4959 and λ5007 lines. In all fits I include the permitted Fe II emission line template of Bruhweiler & Verner (2008), with its normalisation left as a free parameter in the fits. The model was refined to include the following constraints:

i) all narrow, broad and very broad lines have the same velocity width (with the exception of the broad bases of the [O III] forbidden lines: these had equal width but this was not tied to the width of the broad permitted lines);

ii) the very broad lines in the Hα and Hβ profiles have the same velocity offset;

iii) it proved impossible to reliably fit both the width and offset of the very broad lines simultaneously so we fixed the velocity width of these components to ≈ 11500 km s^{-1} and placed the limit $\Delta v_{\rm vb} \lesssim +2500$ km s^{-1} on the offset[2];

iv) the [O III] λ4959 and λ5007 lines have a fixed flux ratio of 1:3;

v) the [N II] λ6548 and λ6583 lines have a fixed ratio of 1:3;

[2]The line width is approximately equal to the mean FWHM of the very broad Balmer line components of the broad line AGN modelled by Jin et al. (2012b). The offset was limited to keep the centre of the very broad component within the core of the line.

vi) the stronger [N II] λ6583 line has its amplitude fixed to the mean value determined in the WHT spectra;

vii) the narrow lines ought not to vary significantly over the monitoring period, therefore the Hα narrow line was fixed to 0.67 of the [O III] λ5007 flux, the error-weighted mean value determined from all of the WHT spectra;

viii) the Balmer decrement of the narrow lines was a challenge to determine so was fixed at 6.7, again the error-weighted mean value determined from the WHT spectra.

The narrow-line Balmer decrement adopted here is high, although it is within the range $\approx$ 1–12 found by Jin et al. (2012b) for a sample of fifty-one type 1 AGN and at the upper end of the range found by Lu et al. (2019) for 554 SDSS DR7 quasars. If the intrinsic narrow line region (NLR) Balmer decrement is 2.9 (Osterbrock & Ferland 2006) the measured value implies an NLR reddening of $A_V \approx 2.6$ mag. However, my aim is to investigate relative changes in the broad line decrement so as long as the subtraction of the narrow line components is consistent, its precise value will have little effect on my results.

In calculating the Balmer and [O III] emission line EWs I have subtracted the host galaxy contribution to the flux beneath the line (these are determined in § 6.3.3.1) so that the strength of the line is assessed relative to the AGN continuum emission alone[3]. The Balmer, [O III] and [N II] line properties derived from the best fit model parameters are quoted in Tables B.1 and B.1. The Balmer, [O III] and Mg II emission line fits are shown in Figure 6.4.

Since there are no emission line free regions in the vicinity of the Mg II line, I do not subtract the continuum before fitting the line. Instead I fit the line, Fe II template and a power-law continuum simultaneously in the wavelength window 2650–2950 Å. The Mg II $\lambda\lambda$2795, 2802 doublet was not resolved in the composite spectrum produced by

[3]The host galaxy makes a negligible contribution at the wavelength of Mg II.

stacking the WHT spectra; I therefore fit a single Mg II λ2800 profile. This emission line was fitted with two Gaussians, one broad and one very broad for the base. As well as measuring the FWHM of the two components separately, I also calculate the FWHM of the total line profile. The quantities derived from the best fit model parameters are quoted in Table B.2.

6.2.4 The black hole mass

To calculate the mass of the supermassive black hole (SMBH) from my emission line and continuum measurements I use the relation

$$M_{\rm BH} = K \times L^{\alpha} \times {\rm FWHM}^2 \tag{6.2.4}$$

of Mejía-Restrepo et al. (2016) with the appropriate values of K and α taken from their Table 7 (the local calibration corrected for small systematic offsets) for the relevant combinations of the emission line FWHM and continuum or line luminosity L. In Table 6.1 I quote the K and α values used for each relation along with the line and continuum parameters determined as the error-weighted means of values obtained in the four brightest spectra[4]. I find that the mass is in the range $M_{\rm BH} = 1.6$–3.5×10^8 M$_\odot$ (see Table 6.1), marginally greater than the 1.2–1.6×10^8 M$_\odot$ determined by Collinson et al. (2018). There are considerable uncertainties on the masses estimated by virial methods, which are due to the scatter on the scaling relations. For relations based on Hα and Hβ the 1σ scatter is in the range 0.13–0.18 dex; the Mg II relation has a greater scatter of 0.25 dex. I adopt a mass of 2×10^8 M$_\odot$ in the following.

[4]Those recorded on 2013 June 10 and August 7 and 2016 July 9 and October 22.

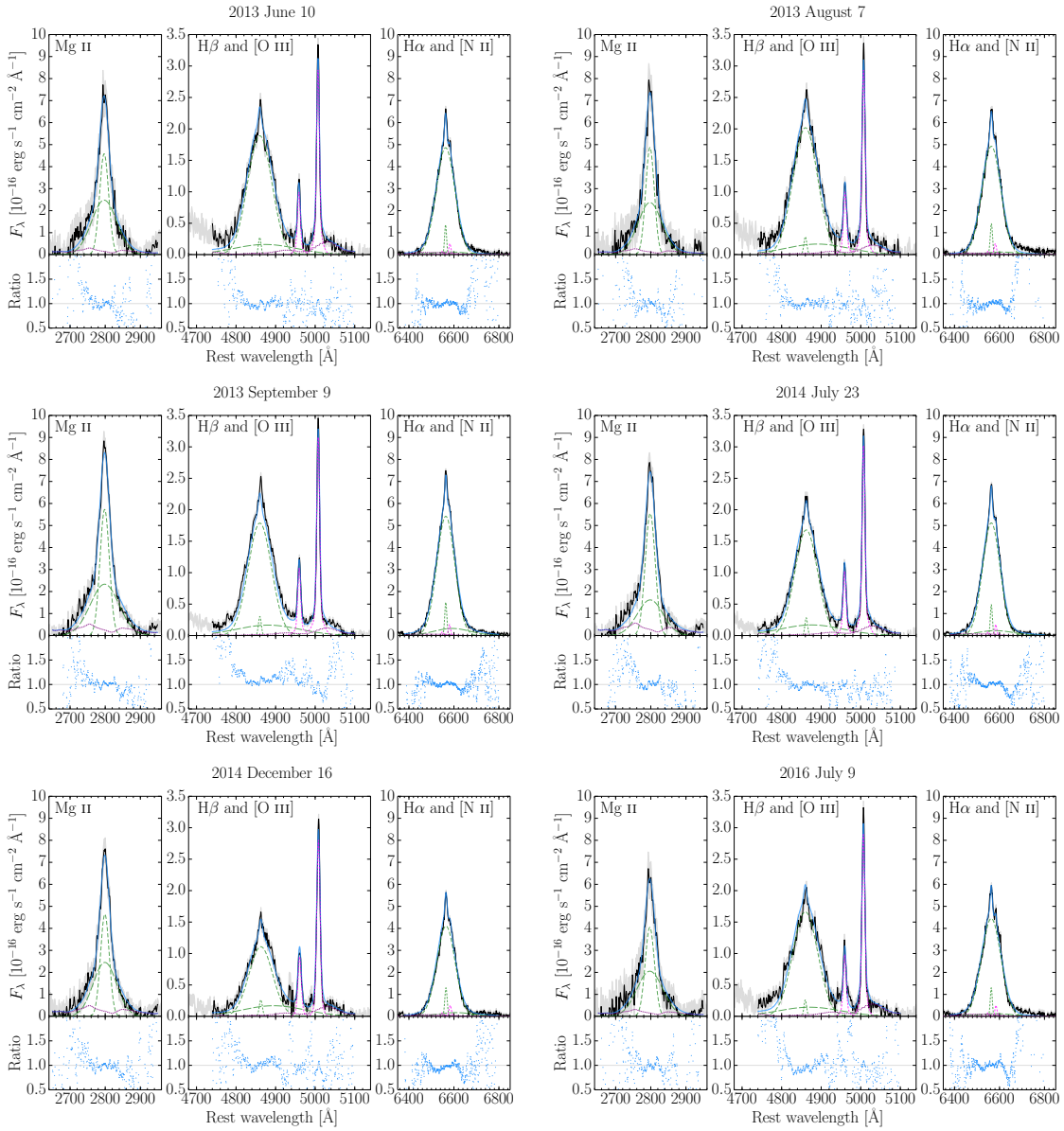

Figure 6.4: Emission line fits to continuum-subtracted spectral windows. In the upper panels, the solid black lines show the wavelength regions of the spectra that were fit, and the solid grey area indicates the error on the flux density; the green short-dashed, dashed and long-dashed lines show the modelled narrow, broad and very broad components of the permitted lines, respectively; the magenta short-dashed lines show the modelled [O III] and [N II] forbidden lines; an Fe II emission template is shown by the purple dotted line and the total model is shown by the solid blue line. The lower panels show the data / model ratios in the fitted regions.

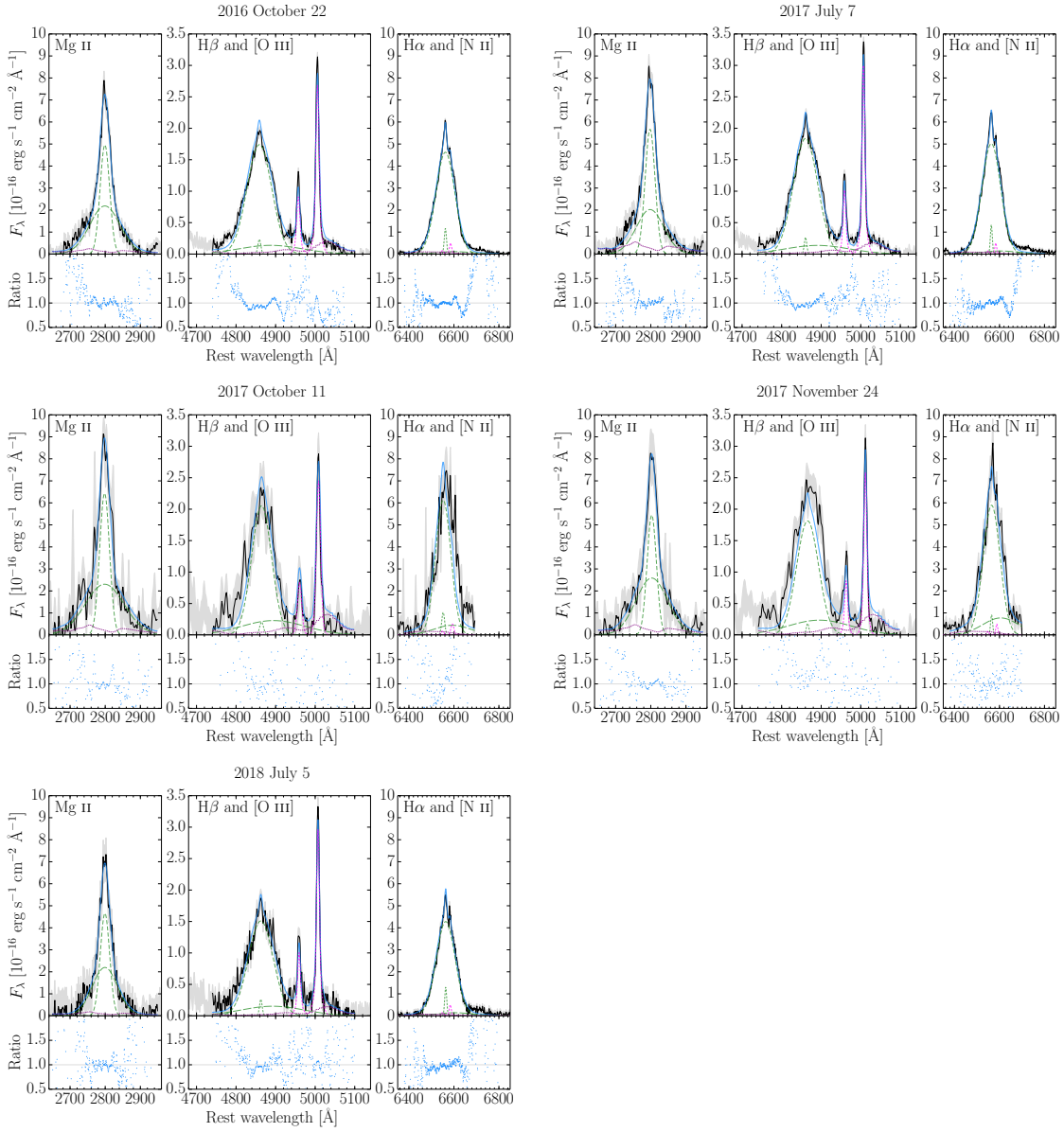

Figure 6.4: Continued.

Table 6.1: Black hole mass estimates from optical spectra

Relation	$\log(K)$	α	FWHM	L	$M_{\rm BH}$
FWHM(Hα), $\lambda L_{5100\,\text{Å}}$	6.845	0.650	4.51	1.66	2.0
FWHM(Hα), $L_{\rm H\alpha}$	7.389	0.563	4.51	0.13	1.6
FWHM(Hβ), $\lambda L_{5100\,\text{Å}}$	6.740	0.650	4.51	1.66	1.6
FWHM(Mg II), $\lambda L_{3000\,\text{Å}}$	6.925	0.609	4.19	4.21	3.5

The broad line FWHMs are in 10^3 km s^{-1}, the luminosities L in 10^{44} erg s^{-1} and the calculated SMBH masses $M_{\rm BH} = KL^\alpha \times \text{FWHM}^2$ in 10^8 M$_\odot$.

6.3 Multiwavelength data

6.3.1 X-ray and UV observation with *XMM-Newton*

A 30 ks *XMM-Newton* observation of SDSS J2232−0806 was made on 2013 December 14 (OBS ID: 0724441001; PI: Lawrence). At this time, the source was in a relatively high optical flux state (see Figure 6.1). The three EPIC X-ray detectors (pn, MOS1, and MOS2) were operating in a Full Frame mode with the Thin filter in place. Ultraviolet photometry was recorded by the onboard Optical Monitor (OM) which cycled through three of the six filters: U, UVW1 and UVM2.

The data were reduced using the *XMM* Science Analysis Software (SAS, v16.0.0) and the latest calibration files available at the time. The X-ray observation suffered from substantial particle background flaring such that, after filtering, the remaining good time intervals were 8.6, 8.5 and 8.2 ks for the pn, MOS1 and MOS2 detectors, respectively. The source spectra were extracted from 47 arcsec radius circular regions centred on the source. The background spectrum was extracted from larger 94 arcsec radius circular regions offset from the source on a blank area of sky. The spectra were regrouped so as not to oversample the detectors' intrinsic energy resolution by a factor of more than three and to contain at least 20 counts per energy bin, so that they are suitable for a χ^2 analysis.

The OM photometry in the three filters were extracted using the SAS tasks OMICHAIN and OMISOURCE, following the standard procedures. The OM filter bandpasses cover several emission lines and so do not accurately represent the continuum flux level. Following the method of Elvis et al. (2012), I can 'correct' the photometric fluxes to obtain an improved estimate of the continuum level by multiplying the measured fluxes by the photometric correction factor

$$P_{\rm c} = \frac{\rm BW}{\rm EW_{rest} \times (1+z) + BW} \tag{6.3.1}$$

where BW is the bandwidth of the photometric filter covering a line of rest-frame

equivalent width $\mathrm{EW_{rest}}$. The OM U filter (BW = 840 Å) covers the Mg II emission line, for which I estimate $\mathrm{EW_{rest}} \approx 60$ Å $\rightarrow P_\mathrm{c} = 0.92$. Assuming a C III] $\mathrm{EW_{rest}} \approx 24$ Å (Vanden Berk et al. 2001), the correction factor in the UVM2 filter is $P_\mathrm{c} = 0.95$. I conclude that the UVW1 filter is very weakly affected by line emission, since the C III] and Mg II lines only partially appear at the very ends of its bandpass where the sensitivities are lowest.

6.3.1.1 X-ray spectral analysis

Analysis of the X-ray spectra was performed in XSPEC (Arnaud 1996) v12.9.1e. The spectra from the three EPIC detectors were fitted simultaneously, allowing for cross-normalization factors to account for differences in calibration between the detectors; these did not vary by more than 5 %. All models included a Galactic absorption component (PHABS) with the column density fixed at $N_\mathrm{H}^\mathrm{Gal} = 4.52 \times 10^{20}$ cm^{-2}. A single power-law was an unsatisfactory fit to the data, giving a reduced χ^2 of 1.27. A broken power-law was a significant improvement, decreasing the χ^2 value by 48 for the introduction of two additional free parameters and I achieve an acceptable fit with a reduced χ^2 of 1.01. The F-test probability of this improved model was > 99.99 %. I then tested for an intrinsic absorber by the inclusion of a ZPHABS component with the redshift fixed to that of the source. This gave no significant improvement in the fit and I determined an upper limit on the intrinsic column density $N_\mathrm{H}^\mathrm{int} < 7 \times 10^{19}$ cm^{-2}. The results of the X-ray spectral fitting are given in Table 6.2.

6.3.2 Archival photometric data

6.3.2.1 *WISE*

The *Wide-field Infrared Survey Explorer* (*WISE*, Wright et al. 2010) telescope observed SDSS J2232−0806 twice in 2010. Data for this source was found in the All-

Table 6.2: X-ray spectral models

Model	Parameter	Value
POWERLAW	Γ	2.19 ± 0.02
	Norm.	$(2.83 \pm 0.04) \times 10^{-4}$
	χ^2/d.o.f.	$223/175 = 1.27$
BKNPOWER	Γ_1	$2.35^{+0.04}_{-0.05}$
	$E_{\rm brk}$ (keV)	$1.7^{+0.5}_{-0.2}$
	Γ_2	$1.79^{+0.07}_{-0.17}$
	Norm.	$\left(2.71^{+0.07}_{-0.05}\right) \times 10^{-4}$
	χ^2/d.o.f.	$175/173 = 1.01$
ZPHABS ×	$N_{\rm H}^{\rm int}$ (10^{19} cm^{-2})	< 7
BKNPOWER	Γ_1	$2.35^{+0.04}_{-0.02}$
	$E_{\rm brk}$ (keV)	$1.7^{+0.5}_{-0.2}$
	Γ_2	$1.79^{+0.07}_{-0.20}$
	Norm.	$\left(2.71^{+0.06}_{-0.05}\right) \times 10^{-4}$
	χ^2/d.o.f.	$175/172 = 1.01$

All models included a Galactic absorption component (PHABS) with the column density fixed at $N_{\rm H}^{\rm Gal} = 4.52 \times 10^{20}$ cm^{-2}.

WISE Source Catalog, hosted by the Infrared Science Archive (IRSA[5]); in Table 6.3 I quote the reported instrumental profile-fit magnitudes. The photometric quality of these detections were A (best) for the W1, W2 and W3 filters and B for the W4 filter.

As well as the catalogue magnitudes, I also obtained infrared lightcurves in the W1 and W2 filters from the *WISE* and *Near-Earth Object WISE Reactivation* (*NEOWISE*) archives. In addition to the two visits made during the *WISE* mission, SDSS J2232−0806 has been observed with roughly six-month cadence since the start of *NEOWISE* mission in December 2013. Typically a dozen exposures are made on each visit; to construct the lightcurves shown in Figure 6.1, I have calculated the mean and standard error on the magnitudes recorded on each visit. I exclude the seven exposures taken on MJD 57345, because there was a large scatter on these magnitudes and a set of eleven exposures was taken three days later. This visit on MJD 57348 (2015 November 19) corresponds to the minima of the infrared

[5] http://irsa.ipac.caltech.edu/

lightcurves and occurs 428 days later than the observed minimum in the LT optical lightcurve (see Section 6.2.1.1). There is a 0.26 mag peak-to-trough change in W1 and a 0.21 mag change in W2.

6.3.2.2 Two-Micron All Sky Survey

SDSS J2232−0806 was observed as part of the Two-Micron All Sky Survey (2MASS, Skrutskie et al. 2006). In Table 6.3 I quote the J, H and K_s profile-fit magnitudes reported in the 2MASS All-Sky Point Source Catalog (PSC)[6]. The photometric quality of these detections were C for all filters.

6.3.2.3 Sloan Digital Sky Survey

Although no Sloan Digital Sky Survey (SDSS) spectroscopic data exists for this source, photometry was obtained on 2000 March 9. As can been seen in Figure 6.1, the source was in a very low state at this time. The object was classified as a (passive) galaxy based on its photometric colours.

6.3.2.4 PanSTARRS-1 3π Survey

Originally searching for tidal disruption events, Lawrence et al. (2016) identified SDSS J2232−0806[7] as one of a number of 'slow blue nuclear hypervariables': objects with no previously known AGN, blue colours and evolution on timescales of years. This particular source was brighter by $\Delta g = 1.80 \pm 0.04$ in the PanSTARRS-1 (PS1) 3π Survey observation made in 2012, compared with the SDSS photometry of 2000.

6.3.2.5 UK Schmidt Telescope

I located a record for SDSS J2232−0806 in the SuperCOSMOS Science Archive (SSA[8]). The B_j band (λ = 3950 Å) observation was made using the UK Schmidt

[6] Also available from IRSA, see earlier note.
[7] The common name of the source in this paper is J223210.
[8] http://ssa.roe.ac.uk/.

Telescope (Cannon 1975) on Siding Spring Mountain, NSW, Australia, on 1986 August 1. Its sCorMag (stellar magnitude in the Vega system) is given in the SSA as $B_j = 19.02$ mag. Converting this to a g band AB magnitude, I estimate $g \approx 18.6 \pm 0.3$, where the uncertainty is the standard single-passband uncertainty on SuperCOSMOS magnitudes (Hambly et al. 2001).

6.3.2.6 Catalina Real-time Transient Survey

The Catalina Real-time Transient Survey (CRTS, Drake et al. 2009) makes use of data recorded for the Catalina Sky Survey (CSS). Catalina uses a very wide V photometric filter. To ease the comparison with the other data, the V magnitudes shown in Figure 6.1 have been scaled to approximately match the PS1 and LT g magnitudes.

6.3.2.7 Zwicky Transient Facility

The Zwicky Transient Facility (ZTF, Bellm et al. 2019, Graham et al. 2019) is the successor survey to the Palomar Transient Factory (PTF, Law et al. 2009). The survey began at the Palomar Observatory, California, USA, in 2017. With a very wide field of view and fast-readout electronics, it is able to survey more than ten times faster than PTF. The first public data were released on 2019 May 8. One of the ZTF g band magnitudes of SDSS J2232−0806 was recorded on 2018 July 5: the source was also observed with the LT and WHT on that day. The ZTF g magnitudes shown in Figure 6.2 are scaled down by 0.17 mag so that the three contemporaneous g magnitudes are consistent.

6.3.2.8 Hubble Space Telescope

Two short-exposure photometric observations were made with the Wide Field Camera 3 (WFC3) onboard the *Hubble Space Telescope* (*HST*) on 2015 September 18. The exposure times were 330 s in the wide IR F125W filter ($\lambda_{\rm eff} = 1.25$ μm, J band) and

Table 6.3: The multiwavelength photometric dataset

Date	Telescope or survey	Filter	Measurement	Unit	log(ν)[a]	Flux[b]	Luminosity[c]
2010/05/27–28	*WISE*	W4	7.536 ± 0.157	Vega mag	13.13	1.10 ± 0.16	2.62 ± 0.38
2010/05/27–28	*WISE*	W3	10.258 ± 0.073	Vega mag	13.41	6.48 ± 0.44	15.4 ± 1.0
2010/05/27–11/25	*WISE*	W2	12.783 ± 0.027	Vega mag	13.81	8.62 ± 0.21	20.5 ± 0.5
2010/05/27–11/25	*WISE*	W1	13.782 ± 0.027	Vega mag	13.95	8.50 ± 0.21	20.2 ± 0.5
1998/10/01	2MASS	K_s	15.419 ± 0.182	mag	14.14	6.29 ± 1.06	15.0 ± 2.5
1998/10/01	2MASS	H	16.166 ± 0.208	mag	14.26	6.31 ± 1.21	15.0 ± 2.9
1998/10/01	2MASS	J	17.124 ± 0.201	mag	14.39	5.47 ± 1.01	13.0 ± 2.4
2000/03/09	SDSS	z	18.33 ± 0.04	asinh mag	14.53	5.6 ± 0.2	14.8 ± 0.5
2000/03/09	SDSS	i	18.97 ± 0.02	asinh mag	14.61	3.78 ± 0.07	10.4 ± 0.2
2000/03/09	SDSS	r	19.20 ± 0.02	asinh mag	14.69	3.71 ± 0.07	10.8 ± 0.2
2000/03/09	SDSS	g	20.10 ± 0.03	asinh mag	14.81	2.14 ± 0.06	6.7 ± 0.2
2012/08/30	PanSTARRS-1 3π	g	18.30 ± 0.05	mag	14.80	11.0 ± 0.5	34 ± 2
2012/09/11	Liverpool	g	18.37 ± 0.02	AB mag	14.81	10.5 ± 0.2	33.0 ± 0.6
1988/06/01	Schmidt	g^*	18.6 ± 0.3	AB mag	14.81	9 ± 2	27 ± 6
1988/06/01	Schmidt	B_j	19.0 ± 0.3	Vega mag	14.88	10 ± 3	23 ± 7
2000/03/09	SDSS	u	19.79 ± 0.05	asinh mag	14.92	3.8 ± 0.2	12.7 ± 0.7
2013/12/14	*XMM-Newton* OM	U	2.219 ± 0.038	cts s^{-1}	14.94	14.8 ± 0.2	27.0 ± 0.4
2013/12/14	*XMM-Newton* OM	UVW1	1.154 ± 0.017	cts s^{-1}	15.01	16.2 ± 0.2	31.6 ± 0.4
2013/12/14	*XMM-Newton* OM	UVM2	0.390 ± 0.011	cts s^{-1}	15.11	19.9 ± 0.6	48 ± 1
2003/08/22	*GALEX*	NUV	20.67 ± 0.22	AB mag	15.12	2.6 ± 0.5	15 ± 3
2004/08/24	*GALEX*	NUV	19.81 ± 0.04	AB mag	15.12	6.8 ± 0.2	40 ± 1
2003/08/22	*GALEX*	FUV	21.10 ± 0.32	AB mag	15.29	2.6 ± 0.7	14 ± 4
2004/08/24	*GALEX*	FUV	19.62 ± 0.03	AB mag	15.29	8.4 ± 0.3	46 ± 2

Notes: [a]Logarithm of the observed frequency ν in Hz; [b]observed flux νF_ν in units of 10^{-13} erg s^{-1} cm^{-2}; [c]intrinsic luminosity νL_ν in units of 10^{43} erg s^{-1}, dereddened where appropriate. *Converted from the quoted B_j magnitude below.

1200 s in the extremely wide UVIS F475X filter ($\lambda_{\rm eff} \approx 4776$ Å, and including the g band).

6.3.2.9 *GALEX*

Two epochs of ultraviolet (UV) photometry were found by searching the *Galaxy Evolution Explorer* (*GALEX*, Martin et al. 2005) space telescope archive. In both records, the UV source is coincident with the optical coordinates of SDSS J2232−0806 within 1.3 arcsec. The UV flux increases by a factor ≈ 3 between the two epochs and there is also an apparent colour change, with SDSS J2232−0806 appearing bluer in the later observation.

6.3.3 The spectral energy distribution

6.3.3.1 Host galaxy contribution to the SED and spectra

Infrared and optical emission from the host galaxy bulge may make a non-negligible contribution to the spectra, particularly in the faint state. It can be seen in the SED (Figure 6.5) that the bulge component dominates over the AGN continuum redward of Hβ. However, this is not representative of the host galaxy flux in the spectra, since the narrow 1 arcsec wide slit excludes much of the extended host galaxy emission: a typical bulge diameter of 15 kpc would be ≈ 3.6 arcsecs across on the sky.

I examined the *HST* images of the source, taken in 2015 September (see Section 6.3.2.8). The high spatial resolution of the instrument in principle allows me to separate the point-like AGN emission from the more extended host galaxy. I made a visual inspection of the 1D brightness profiles of the source in the two filters. Whereas the source emission in the UVIS filter was PSF-like, the J band profile had a slightly more extended base than the PSF, suggesting the presence of some light from the host galaxy. Unfortunately, however, the snapshot *HST* exposures are not sufficiently deep to robustly assess the host galaxy emission.

Instead, I can estimate the host galaxy luminosity at 5100 Å in the spectral extraction aperture using the relation of Landt et al. (2011b). From a sample of low-redshift ($z \lesssim 0.3$), bright, broad emission line AGN, the authors determined the host galaxy luminosities enclosed in the apertures from stacked *HST* images (see their Section 3 and Figure 1). When extracting the WHT spectra, the integration was performed over 4.75 arcsec on average in the spatial direction; the 4.75 arcsec^2 aperture is therefore equivalent to a spatial size of 20 kpc^2 at the source. From the Landt et al. (2011b) relation I then estimate $F_{5100\text{Å}} \approx 4.2 \times 10^{-17}$ erg s^{-1} cm^{-2} Å^{-1}.

The RMS spectrum I constructed in Section 6.2.2.3 largely removes the non-variable host galaxy contribution, whereas the mean spectrum does not. Therefore, if I assume that the mean AGN emission has the same spectral shape as the variable component,

I can estimate the host galaxy contribution by the 'red excess' of the mean spectrum in comparison with the RMS. For the host galaxy component I used the 5 Gyr old elliptical galaxy template of Polletta et al. (2007). I add the RMS and host galaxy spectra, and rescale the two components until the sum satisfactorily matches the shape of the mean spectrum. From the appropriately-scaled galaxy template I determine the mean flux densities in several 150 Å wide windows. The flux densities at 4861, 5007, 5100 and 6563 Å are 4.9, 4.8, 4.6 and 4.8×10^{-17} erg s^{-1} cm^{-2} Å^{-1}, respectively; the value at 5100 Å is consistent with the Landt et al. (2011b) estimate calculated above, given the uncertainties. The host galaxy contribution to the fluxes at 2800 Å (under Mg II) and at 3000 Å is negligible. In the rest of this study I correct the AGN continuum fluxes (and hence the emission line EWs) using these values. The emission line EWs recorded in the Tables in the Appendix reflect this correction.

6.3.3.2 Accretion flow model

To model the multiwavelength SED, I use the energy-conserving accretion flow model OPTXAGNF of Done et al. (2012). The model is described in Section 2.3. In addition to the direct accretion flow emission, I include a redshifted blackbody (ZBBODY) modelling the hot dust which is sampled by the *WISE* W1 and W2 bands. In Figure 6.5 I show the W1 and W2 fluxes corresponding to the earliest *NEOWISE* observation (2014 May 31: the closest in time to the *XMM-Newton* pointing). The downward error bars show the extent of the flux diminution over the observing period. For completeness, the figure also shows the *WISE* W3 and W4 band fluxes, which sample cooler dust. I do not model these data points; the emission may be attributed to AGN- or starlight-heated dust (or some mixture of the two). I show my model SED in Figure 6.5, along with the modelled multiwavelength data. Archival data are also shown for illustrative purposes, including two epochs of *GALEX* UV photometry, 2MASS infrared photometry and the SDSS optical photometry from 2000 during which the AGN was in a deep flux minimum. In Figure 6.5 I also

show the Polletta et al. (2007) 5 Gyr old elliptical host galaxy template which is normalised to fit the SDSS photometry.

My SED model has a very prominent soft Comptonisation region that emits from the optical/UV into the soft X-ray band. The standard disc component is required only to provide a source of seed photons for the soft Comptonisation region in the model calculations and not to fit the shape of the SED itself. I note that Collinson et al. (2018) presented an alternative SED model which contained no soft Comptonisation region and in which the optical/UV emission was attributed to a standard accretion disc, with the X-ray spectrum modelled by a single power-law component. This model cannot replicate the curvature in the X-ray spectrum which I detected significantly in Section 6.3.1.1. Additionally, whilst the single power-law of Collinson et al. (2018) has a photon index of $\Gamma = 2.2$, a harder index (such as the $\Gamma = 1.85$ I determine here) would be expected for a system of this Eddington ratio (e.g. Kubota & Done 2018). However, the Eddington ratio determined in both models, $^{L}/_{L_{\rm Edd}} = 0.1$, is the same.

Table 6.4: Multiwavelength SED model parameters

Model	Parameter	Units	Description	Value
ZBBODY	$kT_{\rm dust}$	keV (K)	Hot dust temperature	9.30×10^{-5} (1140)
	B.body norm.		Hot dust blackbody normalisation	2.43×10^{-5}
HOSTPOL	Gal. norm.		Host galaxy template normalisation	2.71×10^{-7}
OPTXAGNF	$\log(L/L_{\rm Edd})$		Eddington ratio	-1.00
	$kT_{\rm e}$	keV	Electron temperature of soft Comptonisation region	0.20
	τ		Optical depth of soft Comptonisation region	17.3
	Γ		Photon index of power-law coronal emission	1.85
	$f_{\rm pl}$		Fraction of power below $R_{\rm cor}$ emitted in power-law	0.32
	$R_{\rm cor}$	$R_{\rm g}$	Inner (standard) accretion disc radius	80.0
	$\log(R_{\rm out})$	$R_{\rm g}$	Outer accretion disc radius	2.01
	$F_{\rm dust}$	erg s^{-1} cm^{-2}	Flux of hot dust blackbody	1.25×10^{-12}
	$F_{\rm disc}$	erg s^{-1} cm^{-2}	Flux of (standard) accretion disc	6.81×10^{-13}
	$F_{\rm SX}$	erg s^{-1} cm^{-2}	Flux of of soft Compton emission	8.03×10^{-12}
	$F_{\rm pl}$	erg s^{-1} cm^{-2}	Flux of coronal power-law emission	3.78×10^{-12}
	$F_{\rm UV}$	erg s^{-1} cm^{-2}	AGN flux between 100–4000 Å (rest-frame)	7.92×10^{-12}
	$F_{\rm AGN}$	erg s^{-1} cm^{-2}	Total AGN flux	1.25×10^{-11}

Note: Distances are measured in gravitational radii $R_{\rm g} = GM_{\rm BH}/c^2$.

6.4 The nature of the variability

I now bring together all of these data-sets, and use them to confront two generically distinct scenarios i.e. that the flux changes seen in Figure 6.2 are due to reddening by dust, or, that they are a result of an intrinsic variation in the continuum emission from the nuclear region, primarily powered by processes occurring within the accretion disc.

6.4.1 Obscuration interpretation

In Figure 6.6 I show the relative variations of the continuum fluxes and those of the Mg II and broad Balmer emission lines. The estimated host galaxy flux at 5100 Å has been subtracted from the red continuum flux (see Section 6.3.3.1). Shorter wavelengths are more sensitive to reddening than longer ones so, under the assumption that the observed changes are due to reddening, one would expect the 5100 Å flux to have a shallower fractional variability curve than at 3000 Å. Based on the Cardelli et al. (1989) Milky Way[9] reddening curve, I have calculated the extinction (A_V) required to cause the observed fractional changes in the blue continuum and then predict the fractional change in the red continuum for the same A_V. It can be seen that the observed AGN flux at 5100 Å shows a significantly greater fractional variability than this prediction, and is broadly consistent with the fractional variations at 3000 Å. There is considerable uncertainty in the AGN continuum 5100 Å fractional flux variations due to the uncertainty in the host galaxy flux subtraction. However, even in the very conservative case when I perform no host galaxy flux subtraction, the 5100 Å fractional flux variability is still inconsistent with that predicted from a reddening law (as indicated by the upper error bars in Figure 6.6).

Additionally, I find that the amplitude of line flux changes are somewhat lower than

[9]I note the reddening curves for the Small and Large Magellanic Clouds are very similar to the Milky Way curve for wavelengths $>$ 3000 Å which I consider here. See Figure 2.3.

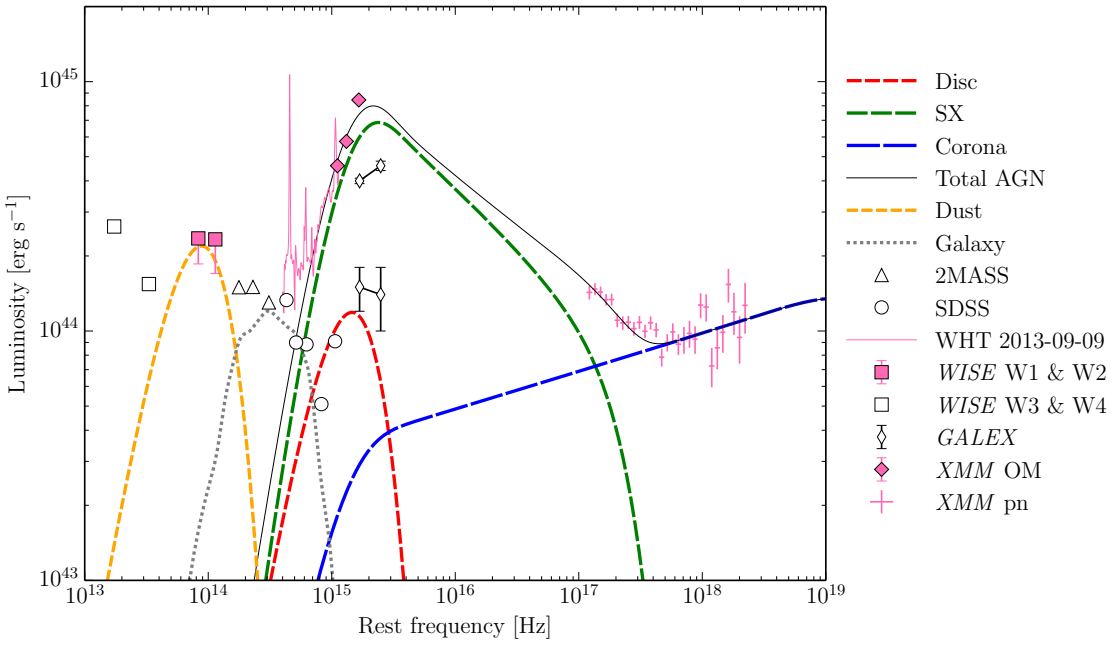

Figure 6.5: The multiwavelength spectral energy distribution of SDSS J2232−0806. Modelled data are shown in pink: the *XMM-Newton* OM and EPIC-pn data of 2013 December 14; WHT spectrum of 2013 September 9 and *WISE* W1 and W2 IR photometry. Additionally, I show other archival data in white: *WISE* W3 and W4 IR photometry from 2010; 2MASS IR photometry from 1998; SDSS photometry from 2000 and two epochs of *GALEX* UV photometry from 2003 (faint) and 2004 (bright).

those in the continuum. The 3000 Å flux exhibits variability of more than a factor two whereas the lines show only $\approx$ 40 % decrease. (Note that the spectroscopic observations did not cover the deep flux minimum seen in the photometric lightcurve.) There is a trend for the emission line EWs to be anticorrellated with the continuum fluxes: increasing when the continuum dims and vice versa. I find that the minimum (maximum) emission line EWs determined over the spectroscopic monitoring period are 570 (1200), 110 (250) and 50 (110) Å for Hα, Hβ and Mg II, respectively. In the case of a simple screen obscuring both the accretion disc (from which the continuum originates) and BLR (from which the broad lines originate), the equivalent widths of the lines ought not to change since both continuum and line flux at any given wavelength will be suppressed equally. However, if the absorber covers more of the very compact accretion disc than the larger BLR then the EW of the broad lines would be seen to increase.

In Figure 6.7 I show how the continuum colour (the ratio of red to blue fluxes) and Balmer decrement have varied together. In the simple scenario of a reddening screen of variable column density obscuring both the BLR and accretion disc, there would be a linear relationship between the Balmer decrement and red/blue continuum flux. I show a reddening vector describing the predicted relationship, again based on the Galactic reddening curve of Cardelli et al. (1989) and positioned so that the Balmer decrement in the case of zero reddening is 2.72 (Gaskell 2017). It can be seen that these data do not follow the trend of this reddening vector so reddening alone cannot explain the observed spectral changes.

6.4.1.1 Cloud crossing timescale

If the dimming of the AGN continuum and broad emission line fluxes is due to an obscurer moving across the line of sight, then I can predict the timescale on which such an occultation event would occur. I estimate the BLR size from Bentz et al.

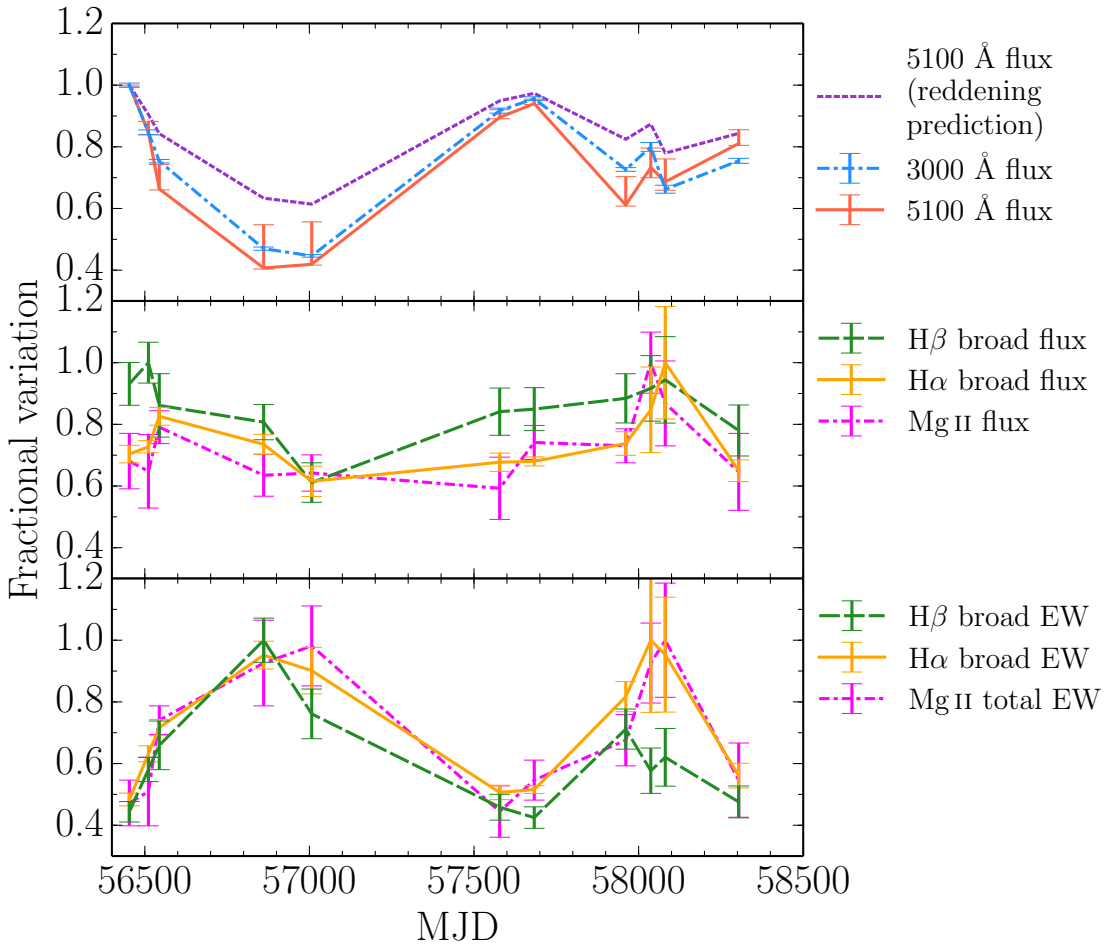

Figure 6.6: Fractional variations in the 3000 and 5100 Å continuum fluxes and emission line fluxes and equivalent widths (EWs) over the monitoring period. In the top panel, as well as the observed continuum variations I also show the predicted 5100 Å variations, calculated from the observed 3000 Å variations, on the assumption that these are caused by reddening (see text). The measured 5100 Å fluxes have been corrected for host galaxy contamination using the estimate determined in Section 6.3.3.1 in the text; the upper error bars indicate the fractional variations calculated with no host galaxy subtraction. For the Balmer lines, values are calculated from the sum of very broad and broad components; the Mg II values are calculated from the whole line profile.

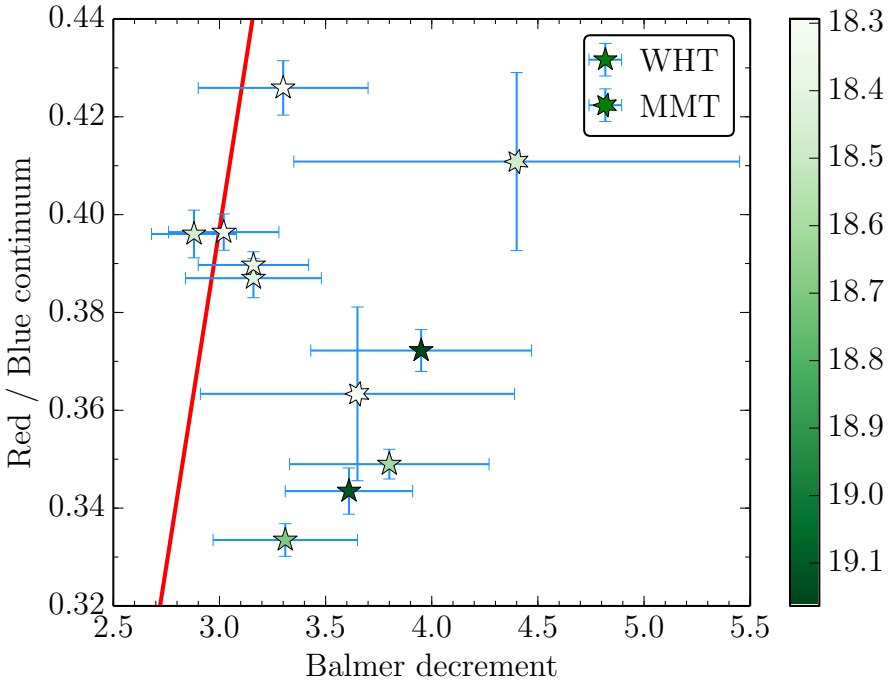

Figure 6.7: The Balmer decrement (the ratio of broad Hα to broad Hβ fluxes) versus continuum colour (the ratio of 5100 Å to 3000 Å monochromatic fluxes) as measured in each of the eleven optical spectra taken at the WHT and MMT. The colour of the points indicates the equivalent g band magnitude of the spectra calculated in Section 6.2.2.2: fainter spectra are a darker green. The red line shows the predicted relation for a Cardelli et al. (1989) Galactic reddening curve (assuming the intrinsic Balmer decrement in the case of zero reddening is 2.72).

(2013) using the equation

$$\log\left(\frac{R_{\rm BLR}}{1\ \text{light day}}\right) = K + \alpha \log\left(\frac{\lambda L_{5100\text{Å}}}{10^{44}\ \text{erg s}^{-1}}\right), \tag{6.4.1}$$

with values $K = 1.559$ and $\alpha = 0.549$ taken from their 'Clean2+ExtCor' calibration. For the range of $\lambda L_{5100\text{Å}}$ observed in the monitoring campaign, the BLR size is $\approx$ 40–60 light days.

Following LaMassa et al. (2015), I calculate the crossing time[10] $t_{\rm cross}$ of a cloud occulting the central regions as

$$t_{\rm cross} = 0.07 \left(\frac{R_{\rm orb}}{1\ \text{light day}}\right)^{3/2} \left(\frac{10^8\ \text{M}_\odot}{M_{\rm BH}}\right)^{1/2} \arcsin\left(\frac{R_{\rm src}}{R_{\rm orb}}\right)\ \text{years}, \tag{6.4.2}$$

where $R_{\rm orb}$ is the orbital radius of the cloud and $R_{\rm src}$ is the radius of the emission source being obscured (here the BLR). As a conservative estimate (minimising the crossing time), I calculate the crossing time for a cloud at the inner edge of the BLR, i.e. $R_{\rm src} = R_{\rm orb} = R_{\rm BLR} \approx 50$ light days. The cloud crossing time at this radius is $\approx$ 27 years, much longer than the dip-and-rise event in the observed lightcurve which takes $\approx$ 3 years in the rest frame.

Lamer et al. (2003) took a different approach to determining the physical parameters of the absorbing cloud responsible for an occultation event in NGC 3227. They were able to determine the column density of the cloud and its crossing time from the variable obscuration observed in X-rays (assuming the cloud is a uniform sphere). They related the obscuring cloud's size to its density via the ionisation parameter, using an estimate of the ionising continuum luminosity $L_{13.6\,\text{eV}-13.6\,\text{keV}}$. My data do not place strong constraints on either the column density of the obscurer or the ionising continuum, so I cannot adopt the same approach. However, if I assume the obscurer in SDSS J2232−0806 is the same size as the one in NGC 3227 ($\sim$ 1 light day), then it must be at a distance 50 $R_{\rm BLR}$ in order to occult the BLR, which is 50 times larger. A cloud of this size orbiting at $R_{\rm orb} = 50\ R_{\rm BLR}$ would have a crossing

[10] This is the time it takes a cloud at radius $R_{\rm orb}$ to traverse the arc corresponding to the projected size of the BLR, which has an inner radius $R_{\rm BLR}$. The velocity of the cloud is calculated assuming a circular, Keplerian orbit around the SMBH.

time of ≈ 124 years, very much longer than the observed ≈ 3 year event. Lamer et al. (2003) note that a cloud ~ 1 light day across is very much larger than the estimate of a typical BLR cloud size ($\sim 3 \times 10^8$ m $\approx 1 \times 10^{-5}$ light days; Peterson 1997). A much smaller cloud would have to be placed at a very large distance to effectively occult the BLR, increasing the crossing time dramatically.

6.4.2 Intrinsic change interpretation

6.4.2.1 Dust reverberation

As noted in Section 6.3.2.1, there is a dip in the infrared lightcurves, delayed with respect to the optical dip by around 400 days. It can be seen in Figure 6.5 that there is negligible host galaxy emission at the wavelengths of the *WISE* W1 and W2 bands (this is true even in the case of a starburst host galaxy, as the IR emission of starlight-heated dust peaks at longer wavelengths). The infrared lightcurves may therefore be evidence of AGN-heated dust reverberating with the variable intrinsic AGN continuum. However, whilst there is a large (factor ≈ 3) change in the optical flux, the change in the near-infrared is much more modest (≈ 30 %). The dust emission ought to be a good bolometer of the intrinsic AGN luminosity, so one might expect it to show variability of the same amplitude as seen in the optical. If I attribute the infrared variability to an echo response to variations in the central source, I must account for this discrepancy. Here, I assess whether the observed infrared lag and magnitude changes can be plausibly attributed to dust reverberation.

I can calculate the expected dust reverberation radius from the model SED parameters via

$$R_{\rm dust,rev} = \sqrt{\frac{L_{\rm UV}}{16\pi\sigma T^4}}, \tag{6.4.3}$$

where σ is the Stefan-Boltzmann constant and the T is the dust temperature $T = 1140$ K (from Table 6.4). Since the dust reverberates with the dip in the optical/UV continuum, I take the UV luminosity in the dip to be a factor 2.5 less than I

determined at the time of the *XMM-Newton* observation: $L_{\rm UV,dip} \approx 7.5 \times 10^{44}$ erg s^{-1}. I therefore calculate $R_{\rm dust,rev} \approx 150$ light days. The observed delay between the minimum of the infrared lightcurve with respect to the optical is ≈ 428 days, equivalent to ≈ 335 days in the rest frame, around a factor two greater than $R_{\rm dust,rev}$.

I employ the model tori of Almeyda et al. (2017) to simulate how the dust may respond to a variable, driving optical source. The authors consider the cases of a compact and extended torus, in which the ratio of outer to inner dust cloud radii are 2 and 10, respectively and the inner dust radius in their model is set by dust sublimation. They consider the effects of differing illumination of the torus dust clouds. In the case of isotropic illumination, dust sublimation surface is spherical. In the anisotropically-illuminated case, more ionising flux is emitted in polar directions than in the equatorial plane; the resultant dust sublimation surface is 'bowl-shaped' (see e.g. Kawaguchi & Mori 2010) and the dust near the equatorial plane can survive much closer to the central source than in the isotropic case. The inner dust radius is dependent on the AGN luminosity and the dust sublimation temperature, for which we adopt a value of 1500 K, close to the mean hot dust temperature found by Landt et al. (2011b). For SDSS J2232−0806, I calculate the AGN luminosity $L_{\rm AGN}$ from the bolometric flux of the model SED and assume that was 30 % greater in the bright state than observed at the time of the *XMM-Newton* observation. I therefore determine that $L_{\rm AGN} \approx 4 \times 10^{45}$ erg s^{-1}. For the isotropic case, $R_{\rm in} = R_{\rm sub} \approx 0.7$ pc (≈ 800 light days) whereas for the anisotropic case $R_{\rm in} = R_{\rm sub}(\theta = 90°) \approx 0.25$ pc (≈ 300 light days).

To construct the driving lightcurve, I interpolate between the LT optical photometry points to create a continuous lightcurve, which I then smooth to remove the short-term, stochastic variability and retain only the shape of the longer-term, systematic, large-amplitude changes. Almeyda et al. (2017) provide their impulse response functions at 3.6 μm for a torus viewed at a polar angle of $\theta_{\rm obs} = 45°$ (see their Figure 8). I convolve the optical lightcurve with four response functions (for compact/extended, isotropically-/anisotropically-illuminated tori) and compare

the simulated dust responses with the *WISE* W1 data. I find that the response functions for the isotropically-illuminated tori produce much longer lags than is observed. The lags for the anisotropically-illuminated tori are shorter because the of the closer proximity of the dust to the optical/UV source, and are in much better agreement with the data. The simulated responses for the compact tori are too deep, an extended distribution is required to smear out the response and reduce its amplitude. In Figure 6.8 I show the simulated dust response in the case of an extended, anisotropically-illuminated torus. In this figure I have slightly decreased $R_{\rm in}$ to 250 light days from the 300 light days calculated from $L_{\rm AGN}$, to better match the observed lightcurve.

6.4.2.2 Accretion disc variability timescales

I now assess the predicted timescales for the transmission of changes through a standard thin accretion disc. In Section 6.3.3.2 I determined the outer radius of the accretion disc to be $R \sim 100\ R_{\rm g}$. For a disc of this size, the dynamical timescale is

$$t_{\rm dyn} \approx \left(\frac{R^3}{GM_{\rm BH}}\right)^{1/2} \approx 10 \text{ days;} \tag{6.4.4}$$

the thermal timescale is

$$t_{\rm therm} \approx \frac{t_{\rm dyn}}{\alpha} \approx 3 \text{ months,} \tag{6.4.5}$$

where I assume the disc viscosity parameter $\alpha \approx 0.1$; the viscous timescale is

$$t_{\rm visc} \approx \frac{t_{\rm dyn}}{\alpha}\left(\frac{H}{R}\right)^{-2} \approx 1 \text{ Myr} \tag{6.4.6}$$

where H/R is the ratio of the disc's thickness to its radius. I have calculated H/R using Equations 1.1.7 and 1.1.15 and obtain a value 4×10^{-4}. I note that this calculation of the scale height assumes that the disc is gas-pressure dominated at this radius. If instead it is radiation-pressure dominated, a larger scale height of 0.02 is calculated and $t_{\rm visc} \sim 1000$ years (J. Goodman, private correspondence). In either case, the viscous timescale is much longer than the observed variability.

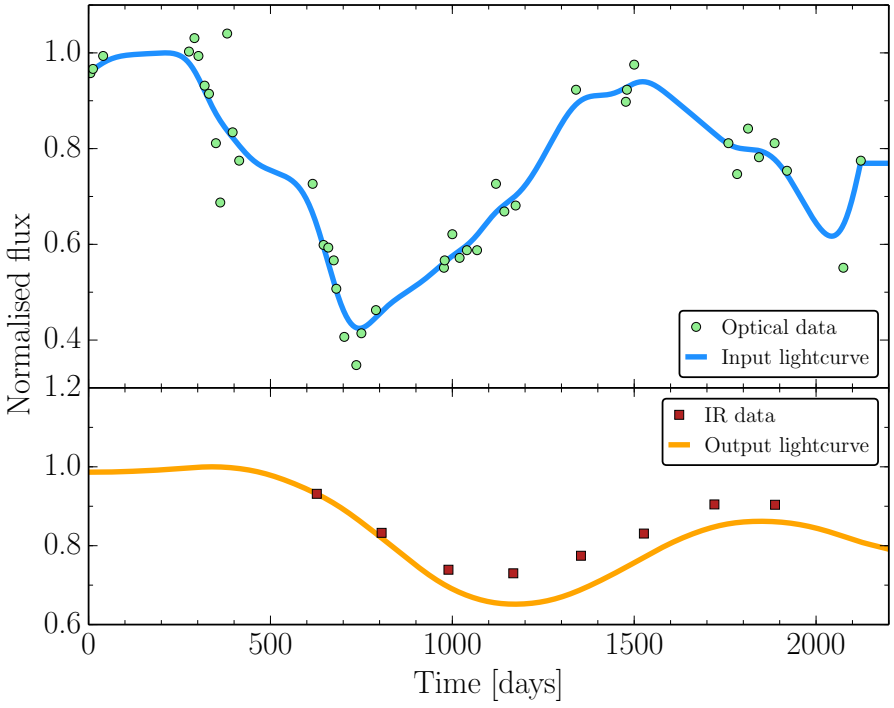

Figure 6.8: The simulated dust response to the variable optical source. *Top:* The optical data (LT g band photometry) are shown as green circles. I linearly interpolate between these and smooth the result to create an input optical lightcurve (the blue line). *Bottom:* I convolve the input lightcurve with an impulse response function to predict the infrared lightcurve (the orange line). The impulse response function was calculated by Almeyda et al. (2017) for an anisotropically-illuminated, radially extended ($R_{\rm out}/R_{\rm in} = 10$) distribution of dust clouds in a torus of angular width $\sigma = 45°$ with $R_{\rm dust} = 250$ light days and a viewed at a polar angle of $\theta_{\rm obs} = 45°$. The *WISE* W1 (3.4 μm) photometry are shown as red squares and the data is normalised such that the first point falls on the predicted lightcurve.

These findings are consistent with what Noda & Done (2018) found for Mrk 1018: the dynamical and thermal timescales are too short compared with the observed variability and the viscous timescale is far too long.

6.5 Discussion

6.5.1 An extrinsic cause of variability

The hypothesis of an extrinsic cause of the variability (i.e. variable obscuration) is inconsistent with the observations in several important respects:

- The continuum colour change is inconsistent with reddening since I see approximately equal fractional flux change in the red as in the blue (Figure 6.6). Even if I perform no subtraction of host galaxy flux at 5100 Å the source still exhibits significantly more variability in the red than would be inferred from the blue, assuming that reddening causes the variability. I note that the choice of reddening curve makes very little difference at the wavelengths studied.

- The Balmer decrements do not change consistently (Figure 6.7), although this test is less compelling given the substantial uncertainties in the measurements. However, since the emission line EWs change, the obscurer cannot be covering both the accretion disc and all of the BLR.

- Different variability behaviours of the broad emission lines are observed: the Balmer lines and He II all vary strongly, whereas Mg II does not.

- I was able to place an upper limit of 7×10^{19} cm^{-2} on the intrinsic column density from the *XMM-Newton* X-ray observation, although a column of $\approx 4 \times 10^{20}$ cm^{-2} would be required to produce the observed 30 % drop in the g band flux. Furthermore, Maiolino et al. (2001) reported that the dust reddening of AGN is generally much lower than one would calculate from the

gas column density probed by X-rays, assuming a Galactic dust-to-gas ratio and extinction curve, as I do here. If this were the case for SDSS J2232−0806, an even greater $N_{\rm H}^{\rm int}$ would be predicted, increasing the discrepancy with the X-ray observations.

- The timescale for obscuration is far too long. I calculate that the crossing time of an obscuring cloud at the inner BLR radius is ≈ 27 years, much longer than the 3 years observed. Furthermore, this scenario does not explain how a dust cloud could survive relatively near to the central ionising source.

- Variable obscuration fails to explain the observed variations in the infrared. Since mid-infrared wavelengths are less sensitive to reddening than the optical, a 0.26 mag change at 3.4 μm would imply a simultaneous 5.5 mag change in the g band which is clearly inconsistent with out data. If the obscurer were exterior to the torus, it would be at an extremely large orbital radius and the crossing time would be even longer than calculated above. If the obscurer were interior to the torus it would need to be implausibly close to the accretion disc (to explain the lag), and implausibly large (to obscure a sufficient fraction of the AGN flux as seen by the dust).

6.5.2 An intrinsic cause of variability

Having ruled out the possibility of an extrinsic change, I consider that the variability is due to an intrinsic change in the luminosity of the accreting matter. In Section 6.4.2.1 I simulated dust responses to a driving optical continuum. My intention with this test was not to infer the properties of the torus but to examine the plausibility that the infrared emission reverberates with the optical. Although I have tested only a few points in the dust response parameter space presented by Almeyda et al. (2017), the simulated IR lightcurve shown in Figure 6.8 captures both the lag and shape of the observed IR variability very well. It is therefore very plausible that the IR emission exhibits a genuine light echo of the optical variability.

Sheng et al. (2017) studied a sample of changing-look quasars that exhibited significant, large-amplitude ($|\Delta W1|$ or $|\Delta W2| > 0.4$ mag) mid-infrared variability. Since mid-infrared wavelengths are not strongly affected by dust extinction, the mid-infrared variability would imply much greater changes in the optical than observed if both were due to variable obscuration. They also found that the timescales for dust cloud obscuration of the torus were far too long whereas the observed lags between infrared and optical were consistent with those expected for hot dust reverberation. They concluded that in all of the ten objects they investigated that the variability was intrinsic in nature. I argue that SDSS J2232−0806 shows the same behaviour.

The RMS spectrum (Figure 6.3) indicates different variability behaviours of the observed emission lines. The broad Balmer emission lines appear as strong features in the RMS spectrum, highlighting their significant variability. The He II λ4686 and He I λ5876 emission lines are known to respond strongly and rapidly to changes in the continuum, and are also prominent. However, Mg II almost completely disappears in the RMS spectrum, indicating that it has varied very little over the monitoring campaign. Recently, Shen et al. (2016) have shown that Mg II varies similarly to Hβ in the SDSS reverberation mapped quasars, but numerous other studies have found Mg II to be less responsive. MacLeod et al. (2019) noted that whilst Hα and Hβ varied similarly in their sample, Mg II behaved differently, being less responsive to strong continuum changes. Both Zhu et al. (2017) and Sun et al. (2015) have studied the reverberation of Mg II in quasars observed multiple times as part of the SDSS. Zhu et al. (2017) noted that Mg II responds relatively weakly to changes in the 3000 Å continuum. Sun et al. (2015) compared the Mg II and Hβ emission line variability and found that Mg II is ≈ 1.5 times less responsive to changes in the continuum than Hβ. It is not currently known why this is the case. It may be that Mg II is emitted over a much larger range of radii than Hβ and so its response is more strongly diluted. Alternatively, differences in the excitation/de-excitation mechanisms or in the optical depths of the two lines are also possible explanations. A future paper based on the MacLeod et al. (2019) sample will investigate Mg II variability specifically (Homan

et al. 2019, in preparation). I note that the spectroscopic monitoring campaign of SDSS J2232−0806 made no observations in 2015, shortly after the photometric minimum. If Mg II has a longer response time than the Balmer lines, it is possible that its strongest response occurred in this window when no spectra were recorded. More frequent spectroscopic observations would have enabled a better characterisation and comparison of the emission line responses. High-cadence spectroscopic monitoring of AGN made by the SDSS Reverberation Mapping Project indicates that Mg II varies similarly to the Balmer lines (Shen et al. 2016). However, as discussed above, there is precedent for Mg II being found to be less responsive to continuum changes. It still remains the case that the RMS spectrum clearly shows that Mg II behaves differently to the Balmer lines in this source.

Whilst I favour an intrinsic cause of the variability over an extrinsic cause, the calculations in Section 6.4.2.2 show that the predicted timescales for such changes do not match the observations. It has been known for some time that large-amplitude variability of AGN occurs on timescales much shorter than predicted for thin, viscous accretion discs. Dexter & Begelman (2019) address this so-called 'quasar viscosity crisis' (Lawrence 2018) and propose that all AGN accretion discs may be 'magnetically elevated' and have a much greater scale height than is typically assumed, dramatically reducing the predicted variability timescales. Alternative models have recently been developed to explain the extreme variability seen in individual sources. Ross et al. (2018) presented a scenario for the CLQ SDSS J110057.70−005304.5 in which a dramatic change in magnetic torque at the innermost disc radii resulted in a collapse of the UV continuum and triggered a cooling/heating front propagating through the disc, out to $\sim 200\ R_{\rm g}$. Taking a different approach, Noda & Done (2018) determined that Mrk 1018 underwent a spectral state transition , similar to those seen in stellar-mass black hole binaries (BHBs). Whilst scaling up to AGN size-scales by BH mass predicts too long variability timescales in AGN, the authors discuss ways in which scalings between BHBs and AGN may break down.

6.5.3 SDSS J2232−0806 in the context of other hypervariable AGN

How extreme is the behaviour of SDSS J2232−0806? Recent, intensive studies of several sources with *Swift* have revealed strong, multiband variability (in X-rays, ultraviolet and optical) on timescales of months to years. NGC 5548, monitored by McHardy et al. (2014), varied by a factor ≈ 4 in the *Swift* UVOT ultraviolet UVW2 band over the course of two years. Edelson et al. (2019) additionally studied Mrk 509, NGC 4151 and NGC 4593 with *Swift* over $\approx$ 1–9 months, and all showed substantial ultraviolet variability (up to a factor ≈ 2.5 for Mrk 509) in UVW2. However, variability in the *Swift* UVOT B band ($\lambda_{\rm eff} = 4346$ Å) is the most appropriate comparison the the optical g band used in this study. The optical variability of these sources was much more modest than that seen in the ultraviolet. The B band variability of NGC 5548 was only $\approx 30\,\%$ in the McHardy et al. (2014) campaign and the Edelson et al. (2019) sources exhibited changes of a similar magnitude. During these campaigns, none of these sources have exhibited such strong, systematic, optical variability as seen in SDSS J2232−0806[11].

Obviously, extreme transient behaviour is more likely to be observed the longer sources are observed for. However, intensive monitoring campaigns such as those mentioned above are impractical over very long periods and for large AGN samples. Systematic searches for extreme variability over long timescales (several years to decades) can be made by from 'snapshots' of AGN lightcurves recorded by large sky surveys. Both MacLeod et al. (2019) and Rumbaugh et al. (2018) have recently presented the results of systematic searches for extremely variable quasars (EVQs: sources with $|\Delta g| > 1$ mag). Rumbaugh et al. (2018) compared photometric variability over a $\sim$ 15 year baseline using data from both SDSS and the Dark Energy Survey (DES). The distribution of maximum g band variability for

[11] I note, however, that NGC 4151 is an archetypal changing-look AGN and has undergone more dramatic events in its past (Lyutyj et al. 1984; Edelson et al. 2017).

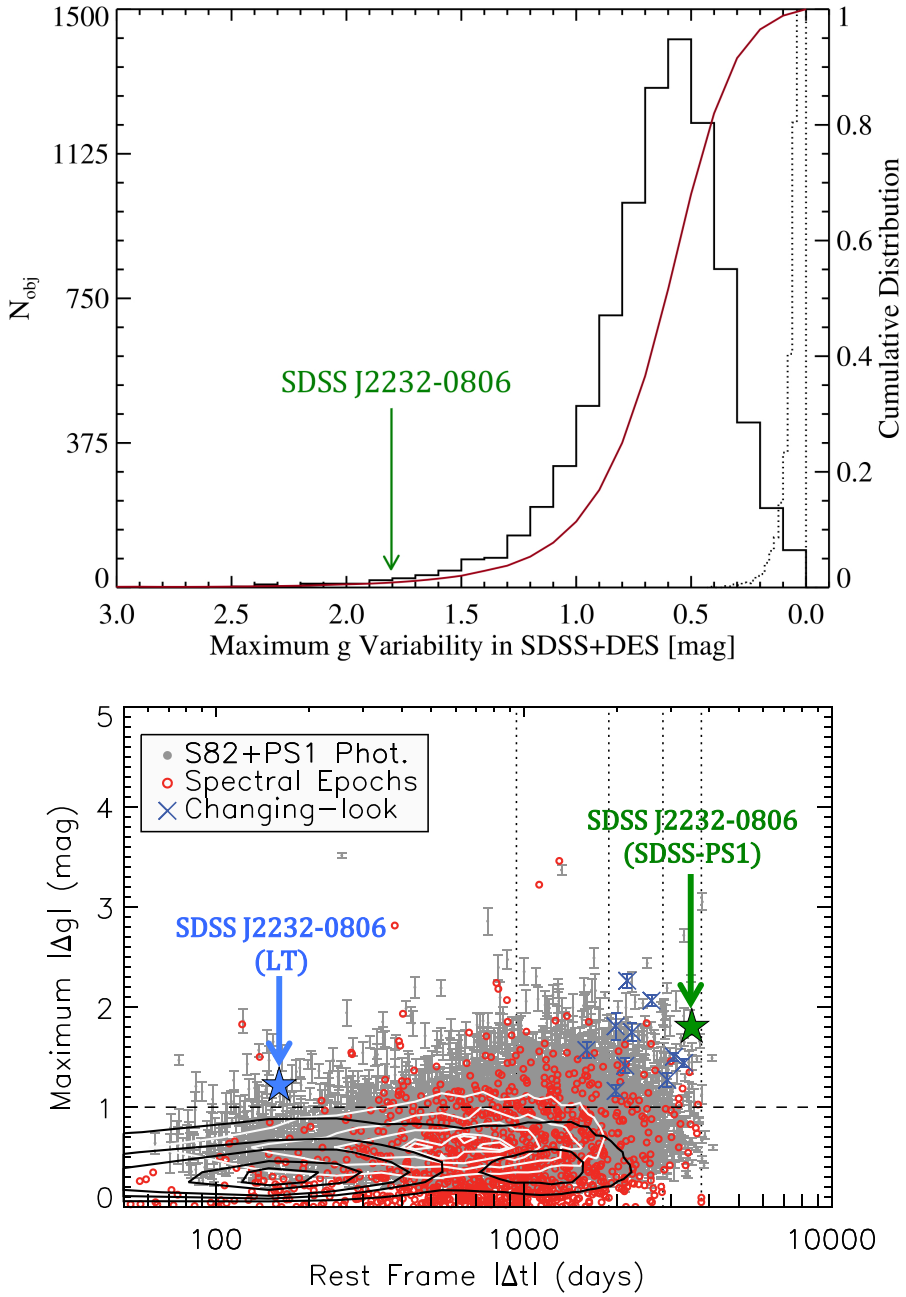

Figure 6.9: *Top:* Maximum $|\Delta g|$ recorded for quasars in both SDSS DR7 and the Dark Energy Survey (DES). The dotted line shows the expected distribution of zero variability convolved with photometric errors, demonstrating that the observed variability is intrinsic. SDSS J2232−0806 is in the very tail of this distribution, as indicated. Adapted from Rumbaugh et al. (2018). *Bottom:* Maximum $|\Delta g|$ recorded for SDSS, PS1 and Stripe 82 (S82) AGN as a function of the corresponding time difference. Black contours refer to the SDSS DR7 quasars, with values taken from SDSS and PS1; white contours are for the S82 subset. Each quasar in the S82 subset is shown by a grey point. Quasars with repeated SDSS spectra are shown with red open circles. Changing-look quasars are shown with dark blue crosses. Points for SDSS J2232−0806 indicating the maximum $|\Delta g|$ in the LT monitoring campaign (light blue) and between SDSS and PS1 (green) are shown as stars. Adapted from MacLeod et al. (2019).

their 8640 sources is shown in the top panel of Figure 6.9, in which the variability of SDSS J2232−0806 ($|\Delta g|_{\rm max} = 1.8$ mag) is also shown. It can be seen that the observed optical variability of SDSS J2232−0806 is extreme compared to most of the rest of this sample. Rumbaugh et al. (2018) calculate that 10 % (2 %) of their sample have $|\Delta g|_{\rm max} > 1$ mag ($|\Delta g|_{\rm max} > 1.5$ mag). Of course, searching for EVQs in this way is likely to miss a substantial fraction of highly-variable sources because of the relative sparseness of the lightcurve sampling. Accounting for the incompleteness of their selection, Rumbaugh et al. (2018) estimate that *intrinsically* EVQs account for ≈ 30–50 % of all quasars. In this sense, large-amplitude variability is not unique to rare and extreme sources, it is just that such variability is rarely *observed* because of its transient nature.

MacLeod et al. (2019) presented follow-up spectroscopic observations of a sample of EVQs and were able to confirm that ≈ 20 % of these were CLQs. SDSS J2232−0806 is shown among the distribution the MacLeod et al. (2019) EVQs, CLQs and their parent sample in the lower panel of Figure 6.9; again, SDSS J2232−0806 is one of the most optically-variable sources.

MacLeod et al. (2019) compared the CLQs with a luminosity- and redshift-matched, less-variable control sample and found that CLQs on average have lower $L/L_{\rm Edd}$ than their less-variable counterparts, as Rumbaugh et al. (2018) found for their sample. Both studies suggested that EVQs and CLQs represent the extremes of a tail of 'normal' quasar variability. At the far range of this tail, some sources exhibit nearly an order of magnitude change in optical flux over a baseline of ∼ 10 years. Compared to many of these changing-look AGN, the continuum flux change observed during the monitoring of SDSS J2232−0806 is modest. Its $\log(L/L_{\rm Edd}) = -1$ is slightly higher than the peaks of the distributions of CLQs and EVQs (which occur at $\log(L/L_{\rm Edd}) \approx -1.5$, see Figure 6 of MacLeod et al. 2019) although it is consistent with the range of values for all of the populations shown (CLQs, EVQs, the less-variable control sample and all 105783 of the SDSS DR7 quasars). Assuming the bolometric flux of the source decreases proportionally to the observed optical, I

can estimate that the accretion rate of SDSS J2232−0806 drops to ∼a few % of Eddington in the faint state.

Elitzur & Ho (2009) proposed a disc wind model of the BLR in which AGN with a very low $L/L_{\rm Edd}$ are unable to support a BLR. After studying a sample of low-luminosity AGN, they determined that the BLR disappears when the AGN luminosity drops below a critical value, $L_{\rm AGN} \lesssim 5 \times 10^{39} (M_{\rm BH}/10^7 {\rm M}_\odot)^{2/3}$ erg s^{-1}. MacLeod et al. (2019) found that their CLQs were distributed close to this critical value and likely dropped below it in their faint state, naturally explaining the disappearance of the broad emission lines. Whilst the broad Balmer emission lines in SDSS J2232−0806 do weaken in response to a dimming continuum, the source does not satisfy the criterion of a changing-look AGN because these lines have not been observed to disappear. The source was in a deep minimum in 2000, and it is likely that the host galaxy emission dominates all of the SDSS bands except u. Its UV flux in this epoch was ≈ 4 times fainter than when it was observed by *XMM-Newton*. Assuming the bolometric flux was also 4 times fainter, its luminosity in 2000 was $\approx 8 \times 10^{44}$ erg s^{-1}. For the SMBH mass of SDSS J2232−0806, the critical luminosity for a BLR in the disc-wind model is $\approx 4 \times 10^{40}$ erg s^{-1}, so the broad lines ought to have been visible even in this deep minimum. Therefore, I suggest that SDSS J2232−0806 lies on the sequence of quasar variability, being highly variable whilst its mass accretion rate is too high for it to undergo a changing-look transition. Figure 6.10 shows the position of SDSS J2232−0806 among the $L/M_{\rm BH}^{2/3}$ distributions of quasar samples considered by MacLeod et al. (2019). It can be seen that the $L/M_{\rm BH}^{2/3}$ value for SDSS J2232−0806 is greater than the peaks of the EVQ and CLQ distributions, but is consistent with the peak of the less-variable, non-EVQ control sample (which was matched with the EVQs in luminosity and redshift). This suggests that its Eddington ratio is somewhat higher than other hypervariable AGN, and more in line with their less-variable counterparts. I note however, that there is considerable overlap between the distributions and SDSS J2232−0806 is not 'unusual' for any of the samples.

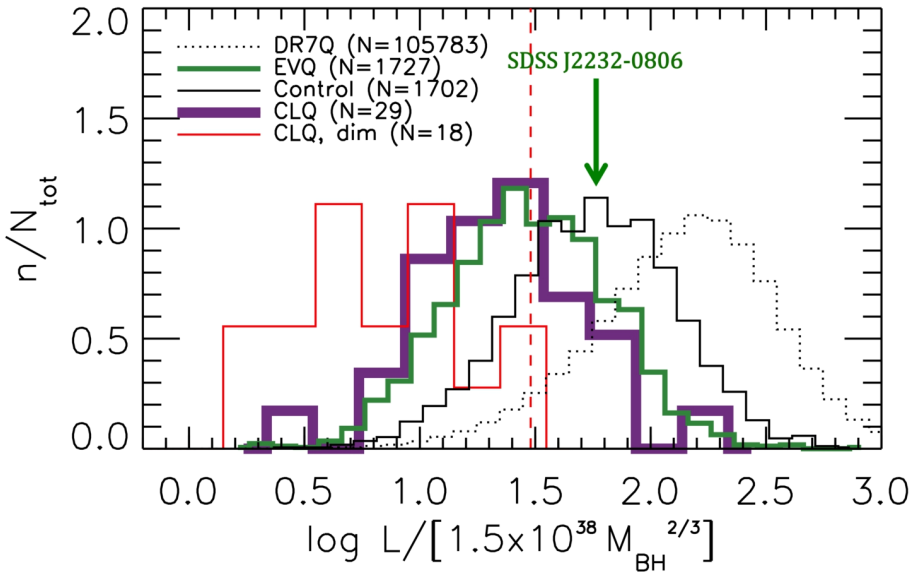

Figure 6.10: Distributions of mass-scaled bolometric luminosities (similar to the Eddington ratio) of different quasar samples. 'DR7Q' is the distribution of all SDSS-DR7 quasars; 'EVQ' are the extremely variable quasar sample of MacLeod et al. (2019); 'Control' is their control sample of less-variable, non-EVQs; 'CLQ' are their changing-look quasars ($L/M_{\rm BH}^{2/3}$ is calculated using the bolometric luminosity in their bright state); 'CLQ, dim' are changing-look quasars with $L/M_{\rm BH}^{2/3}$ calculated using the bolometric luminosity in their dim state. The same quantity calculated for SDSS J2232−0806 is indicated by the green arrow. The red dashed line indicates the critical value of $L/M_{\rm BH}^{2/3}$ in the disk-wind model of Elitzur & Ho (2009), below which the BLR disappears. Adapted from MacLeod et al. (2019).

Whereas optically variable AGN are typically 'bluer-when-brighter' (e.g. Rumbaugh et al. 2018, Wilhite et al. 2005) I do not see strong evidence of that behaviour in the optical monitoring of SDSS J2232−0806. Having corrected the longer-wavelength fluxes for host galaxy contamination, I show in Figure 6.6 that the fractional variabilities in the blue and red are similar (i.e. there is no significant colour change). In Figure 6.3 I show that the shape of the RMS spectrum is very similar to that of the mean spectrum at the shorter wavelengths less affected by host galaxy contamination. I note that Wilhite et al. (2005) used a sample of higher-redshift quasars than SDSS J2232−0806 ($z > 0.5$) so they probed further into the rest frame UV than I do. The authors show that there is a spectral break in the variability of their sample around 2500 Å in the rest frame, with wavelengths shorter than this being more strongly variable. I may not see evidence of a spectral shape change in SDSS J2232−0806 because these spectra do not sample below 2500 Å. Furthermore, in SDSS J2232−0806 it can be seen that changes in the red and blue optical continuum (predominantly emitted from larger/smaller radii, respectively) appear to occur in tandem. No evidence is found for a delay in the variations between the red and blue optical emission, which would be indicative of a heating/cooling front propagating through the disc such as in the model described by Ross et al. (2018).

6.6 Conclusions

The recent optical photometric and spectroscopic monitoring campaign on the hypervariable AGN SDSS J2232−0806 has recorded one dimming and brightening episode with a factor ≈ 3 flux change over four years. Whilst the observed variability of the source is modest compared to that seen in changing-look AGN, it is extreme compared to the broader AGN population. I have been able to demonstrate that variable obscuration does not explain the observed spectral changes, nor does it fit the observed timescales for variability in the optical or near-infrared. An intrinsic change in the AGN luminosity is therefore a likelier explanation, although the

observed changes are much more rapid than the theoretical accretion disc viscous timescale. SDSS J2232−0806 is one of a growing number of objects which challenge our models of viscous accretion discs. Whilst I am unable to determine the cause of the intrinsic luminosity change, X-ray and UV monitoring of future episodes should greatly improve our understanding of the processes at work.

Chapter 7

Summary and future work

Research into quasars and other active galaxies has been ongoing for more than half a century. However, many fundamental questions remain unanswered. These include the origin of jets (which have relevance in providing mechanical feedback into the host galaxy and wider environment); the role of SMBH spin; and rapid, large-amplitude variability (which poses a serious challenge to our current models of SMBH accretion). I hope that the work I have presented in the preceding chapters represents some small steps in advancing our understanding of the AGN phenomenon.

In this thesis I have conducted in-depth multiwavelength studies of individual, extreme AGN. Chapters 4 and 5 presented studies of the γ-ray emitting narrow-line Seyfert 1 galaxies (γ-NLS1s) 1H 0323+342 and PKS J1222+0413. These are the lowest and highest redshift examples, respectively, of this rare group of AGN. Although these is a great desire within the community to learn more about these sources, only around 20 are currently known (see Table 1.2). The fact that γ-NLS1s are so rare makes any new work on single targets a step forward in our general understanding of these sources. In Chapter 6, I conducted an investigation into the nature of the variability of the hypervariable AGN SDSS J2232−0806 nicknamed the 'Big Dipper' after the dramatic fall-and-rise of its luminosity. I demonstrated that the variability was likely to be intrinsic to the AGN (rather than due to external obscuration) and placed the source in the context of other hypervariable AGN and 'changing-look'

quasars.

7.1 Synopsis of findings

7.1.1 γ-ray emitting NLS1s

I made two multiwavelength studies exploring the disc-jet connection in the γ-NLS1s 1H 0323+342 and PKS J1222+0413. I performed a spectral and temporal analysis of the 80 ks *XMM-Newton* X-ray observation of 1H 0323+342, allowing me to discern different variability behaviour in the soft and hard X-ray bands of the RMS spectrum. I interpreted the spectral break as a transition between accretion flow-dominated and jet-dominated emission. Larsson et al. (2018) adopted this interpretation in their analysis of the X-ray spectrum of the γ-NLS1 FBQS J1644+2619. I detected two weak, narrow emission lines in the X-ray spectrum with energies consistent with Fe Kα and Fe XXVI (but see Section 7.2.1 below). Unfortunately, the much shorter *XMM-Newton* observation of PKS J1222+0413 ($\approx$ 4 ks of good time intervals) did not permit such detailed analyses to be made.

I took a novel approach to modelling the SEDs: I first determined the accretion flow parameters from infrared to X-ray data to measure the ambient AGN photon field with which the jet interacts. I then self-consistently incorporated this photon field within the jet model to replicate the full broad-band SED. This approach takes advantage of the wealth of multiwavelength data available for these sources. I contest that this method is more physically-motivated than the standard one of making broad assumptions about the photon field. As discussed below, the parameter space of jet models is already complex, and this approach goes some way towards removing a number of uncertainties.

Assuming that astrophysical jets are scale-invariant, we would expect γ-NLS1s to simply be scaled-down FSRQs. It should therefore be possible to predict the jet SEDs of γ-NLS1s by scaling the mean properties of FSRQ blazars by mass and

mass accretion rate. I tested such simple jet scaling relations for 1H 0323+342 and PKS J1222+0413 and found that the resultant jet SEDs vastly overpredicted the data. The discrepancy was much greater in the case of 1H 0323+342, likely because it has a SMBH mass an order of magnitude lower than PKS J1222+0413, whose mass (2×10^8 $M_\odot$) is similar to those of FSRQ and BL Lac-type blazars. I was able to fit the observed SEDs by adjusting the jet parameters. This resulted in jets of lower power; the total jet power of both sources was approximately half of the accretion disc luminosity. This is in contrast to what has been found for FSRQs and BL Lacs, which on average have jet powers that are greater than the accretion powers[1] (Ghisellini et al. 2014).

If scaling by the mass and mass accretion rate alone cannot correctly predict jet SEDs, then perhaps another parameter plays a role in governing relativistic jets. Conceivably, this parameter could be the SMBH spin. The accretion flow models I applied to the SEDs of 1H 0323+342 and PKS J1222+0413 both disfavoured high-spin solutions, which were found to overpredict the observed soft X-ray emission. Of course, the assumption of energy conservation is hardwired into the model, and the SMBH spin could be higher if some of the accretion power were lost between the optical and X-ray emission regions (for example in a wind).

7.1.2 The hypervariable AGN SDSS J2232−0806

In my study of the 'Big Dipper', I showed that:

- Changes in the Balmer decrement and continuum colours were inconsistent with a simple reddening model.
- The variability behaviour of the Mg II emission line is different to that of the broad Balmer lines (as well as the Balmer continuum and He II).

[1] Note that Ghisellini et al. (2014) compare the jet power to the accretion power $\dot{M}c^2$, having folded out the radiative efficiency η.

- The timescales for an external obscurer crossing our line-of-sight are far too long to explain the observed lightcurve.

- *WISE* records a drop in infrared luminosity approximately a year after a strong decline in the optical luminosity. I demonstrated that this is consistent with infrared emission from surrounding hot dust reverberating with the nuclear optical continuum.

I concluded that the likeliest explanation was an intrinsic change in the luminosity of the accretion disc. Such systematic changes in the disc luminosity ought to be governed by changes in the mass accretion rate, and the appropriate timescale for this is the viscous one. However, the viscous timescales predicted by thin disc models are of the order 10^4–10^5 years. Some AGN demonstrably vary on much shorter timescales than this, which poses a serious challenge to our models of SMBH accretion. New models and ideas have been presented as potential explanations for the observed behaviour (Noda & Done 2018; Ross et al. 2018; Dexter & Begelman 2019). The discovery of many more highly-variable AGN in large transient surveys (see Section 7.2.3 below) will further help us to confront this problem.

7.2 Future work

7.2.1 A long, hard look at 1H 0323+342, and future studies of γ-NLS1s

In Chapter 4, I detected two narrow emission lines in the X-ray spectrum of 1H 0323+342. A subsequent analysis by Paliya et al. (2019) of several X-ray observations of the source suggests that, in fact, the emission is due to a single, broad Fe Kα line (see Figure 7.1) and that the apparent double line features seen in some spectra are due to noise.

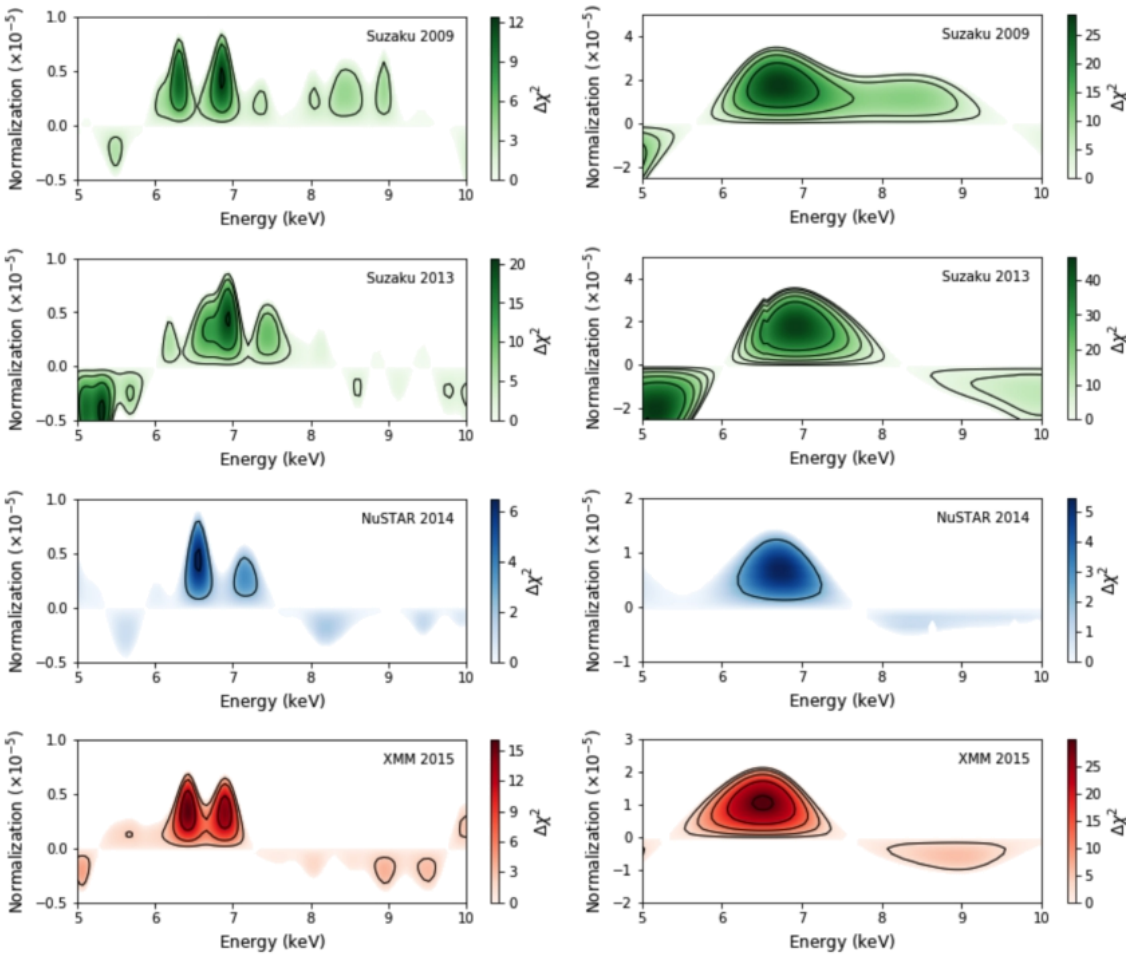

Figure 7.1: Fits of double or single Fe K lines to X-ray spectra of 1H 0323+342. Horizontal cross-sections show the improvement in the fit statistic with line energy (equivalent to my Figure 4.7). Left-hand panels show scans for a narrow Gaussian line of width $\sigma = 0.01$ keV and right-hand panels for width $\sigma = 0.5$ keV. From Paliya et al. (2019).

In Chapter 4, I suggested that the *XMM-Newton* X-ray band sampled both accretion flow and jet emission of 1H 0323+342. However, it is possible that this X-ray emission originates solely from the corona, if it has a much harder spectral index than is typically seen in NLS1s. Such a model was presented in Landt et al. (2017) and Chapter 4.

In 2018 August–September, a long ($\approx$ 300 ks) joint *XMM-Newton*/*NuSTAR* campaign on 1H 0323+342 was conducted (PI: E. Kara). They aim to explore whether the Fe Kα line and the soft X-ray excess, or both, reverberate with the harder X-ray continuum emission. If short-timescale lags exist between these components and the hard continuum, this would demonstrate that the continuum originates from the corona, rather than the more distant jet. They have detected a single, broad Fe Kα line (Mundo et al. in preparation), consistent with the suggestion of Paliya et al. (2019) that my detection of two narrow lines in the 2015 *XMM-Newton* spectrum is due to limited data quality. If the line is relativistically broadened, this would imply a high SMBH spin. As noted in Section 4.6, previous attempts to determine the spin of this source have given contrary results. This new data set may lead to a more robust determination of the SMBH spin, and provide a test of whether high spin is necessary to launch a powerful jet.

My analysis of the soft X-ray spectrum of 1H 0323+342 suggested the presence of another absorber in addition to the standard Galactic ISM. I tested models including both neutral and ionised absorbers both in the Milky Way and intrinsic to 1H 0323+342, but the results were inconclusive (see Chapter 4 and Appendix A). Whilst it was found that the S/N of the *XMM-Newton* RGS spectrum of 1H 0323+342 was too low to be much use (see Figure A.3), Mehdipour & Costantini (2019) claim to detect two distinct wind components with different ionisation parameters and outflow velocities from the same data. Another one of the aims of the 2018 *XMM-Newton* campaign is to search for evidence of a wind or ultra-fast outflow. The detection of an intrinsic, absorbing wind could resolve the problems I and others have faced interpreting the X-ray spectrum of this source.

In Chapters 4 and 5, I faced difficulties in comparing the results of my jet models with those of other groups. A detailed, direct comparison of results is not always possible (or applicable) when different groups use different modelling codes with different input and output parameters. Additionally, the physics of jet emission is very complex; the models have many free parameters and therefore there is much degeneracy the parameter space. As noted by myself and others, it is not credible to claim to have found the unique solution. I have collected together jet model parameters from various groups' fits to the SED of 1H 0323+342 and quote these in Table 7.1. The likely causes of some of the differences in parameters were discussed in Section 4.6.7. From Table 7.1 it can be seen that a range of jet powers is determined by different models ostensibly modelling the same SED. The lowest and highest jet powers listed were even produced by the same author, with Paliya et al. (2014) determining $\log P_{\rm j} = 44.06$ and Paliya et al. (2019) 45.82. In Figure 7.2, I show fitted SEDs for these models; it is apparent that there are differences in the spectral decomposition. Abdo et al. (2009b), Paliya et al. (2014) and Yao et al. (2015a) all attribute the infrared emission to the jet, which has strong synchrotron and synchrotron self-Compton components. In the model of Yao et al. (2015a), the hard X-ray emission is attributed to SSC processes, rather than external Compton scattering. My analysis of the *Spitzer* infrared spectrum suggested a thermal contribution to this band so my model, and the later model of Paliya et al. (2019), have much lower synchrotron and SSC peaks. Since synchrotron emission is polarised, polarimetry studies would help to determine the relative jet and torus contributions in this band and put the spectral decompositions on firmer footing. The JET model on which my work is based is publicly available as a local model for the XSPEC spectral-fitting package and the routine is set out in Gardner & Done (2018). Most other groups use their own, private, jet modelling codes. Without knowing how the physics is implemented within their software, teasing out the root cause of differences between models is very challenging. Progress towards consensus in the community could be made if other groups shared their code and efforts were made between groups to compare

and contrast code outputs.

In Chapters 4 and 5 I noted that because of degeneracies in the parameter space, and different assumptions made in the modelling, there is uncertainty in the jet parameters determined. I have attempted, wherever possible, to limit the 'acceptable' range of parameters on observational or theoretical grounds. The ambient photon fields of 1H 0323+342 and PKS J1222+0413 are well-determined observationally from their well-sampled multiwavelength datasets. I applied these photon fields self-consistently within the jet model, which removes some of the need to make further assumptions about the energy densities of seed photons. As discussed previously, some of the jet parameters are more uncertain than others. The injected electron distribution parameters are reasonably well-determined, since the shape of the distribution influences the shape of the synchrotron and external Compton humps, both of which are sampled by the multiwavelength data. For the two γ-NLS1s I have studied, it was not necessary to make major changes to the injected electron distribution from the mean FSRQ values of Ghisellini et al. (2010) in order to fit the data. Less certain are the precise values of the magnetic field B, the power injected into the electrons $P_{\rm rel}$ and the bulk Lorentz factor $\Gamma_{\rm BLF}$. These parameters in turn influence the calculated power in the jet. However, the blazar-like nature of the jets implies a low inclination angle i of the jet axis to the line of sight. Under the assumption $\Gamma_{\rm BLF} = 1/i$, a small inclination angle implies a high $\Gamma_{\rm BLF} \sim 15$. B and $P_{\rm rel}$ influence the energy densities of the magnetic field and relativistic particles, respectively. Assuming approximate equipartition between the two necessitates balancing U_B and U_e by adjusting B and $P_{\rm rel}$ and using $\Gamma_{\rm BLF}$ as a normalisation for the output SED. Finding a near-equipartition solution which fits the observed SED therefore places some restrictions on the possible combinations of these three key parameters. Because I tested simple scaling relations for the jet parameters B and $P_{\rm rel}$ it is still possible to compare my fitted values (obtained by best matching the observed SED) with those predicted by the scalings. These parameters can therefore be assessed in *relative* terms, even if their *absolute* values are less certain. The jet power is uncertain because it is

Table 7.1: A comparison of jet model parameters and powers determined for 1H 0323+342

Parameter	Units	Model value				
		Abdo+09	Paliya+14	Yao+15	This work	Paliya+19
$\log(M_{\rm BH})$	[$M_\odot$]	7.0	7.30	7.25	7.30	7.30
$Z_{\rm diss}$	[$R_{\rm g}$]	1300	1250	?[2]	1280	24100
i	[deg]	3.0	10	10	4.77	3.0
$\Gamma_{\rm BLF}$		12.0	7.0	2.7	12.0	8.0
B	[G]	30	7.0	1.9	8.0	1.05
$\gamma_{\rm min}$		?	15	130	1	1
$\gamma_{\rm brk}$		60	150	1073	300	89
$\gamma_{\rm max}$		6000	2000	8000	3000	2000
s_1		-1.0	1.2	-1.8	1.50	1.8
s_2		3.1	4.9	5.0	2.70	4.9
$\log(P_{\rm rel})$	[erg/s]	41.00	?	?	41.00	?
$\log(P_{\rm rad})$	[erg/s]	42.80	41.29	43.85	42.51	43.94
$\log(P_{\rm e})$	[erg/s]	42.70	?	43.43	42.74	43.34
$\log(P_B)$	[erg/s]	43.30	?	42.63	42.70	43.42
$\log(P_{\rm p})$	[erg/s]	44.30	44.06	43.66	45.01	45.82
$\log(P_{\rm j})$	[erg/s]	44.36	44.06[1]	44.17	45.01	45.82
$P_{\rm j}/L_{\rm AD}$		0.16	0.11	0.08	0.52	3.3
$U_{\rm e}/U_B$		0.25	?	6.3	1.1	0.83

Notes: (1) I have assumed here that the total jet power, which is not stated explicitly, is dominated by the kinetic power; (2) The dissipation region here is inside the BLR radius, but the precise value is not given. Sources: Abdo et al. (2009b); Paliya et al. (2014); Yao et al. (2015a); this work (Chapter 4); Paliya et al. (2019).

often dominated by the kinetic power in the bulk motion of protons. It therefore depends on the number of protons carried by the jet, which is unknown. The standard assumption is that there is one proton per radiating electron, although if the jet emission originates predominantly from an electron-positron plasma the ratio could be different. Ghisellini et al. (2010) investigate this issue and determine that the role of pairs is negligible, justifying the assumption of one proton per electron. Since this is a standard assumption, it does not in itself prevent a comparison of jet powers between models. In spite of the inherent uncertainties in the jet modelling, I emphasise that my approach follows that of Ghisellini & Tavecchio (2009) and Ghisellini et al. (2010) (on whose work the jet emission code is based) so it is still valid to assess my results in relation to theirs.

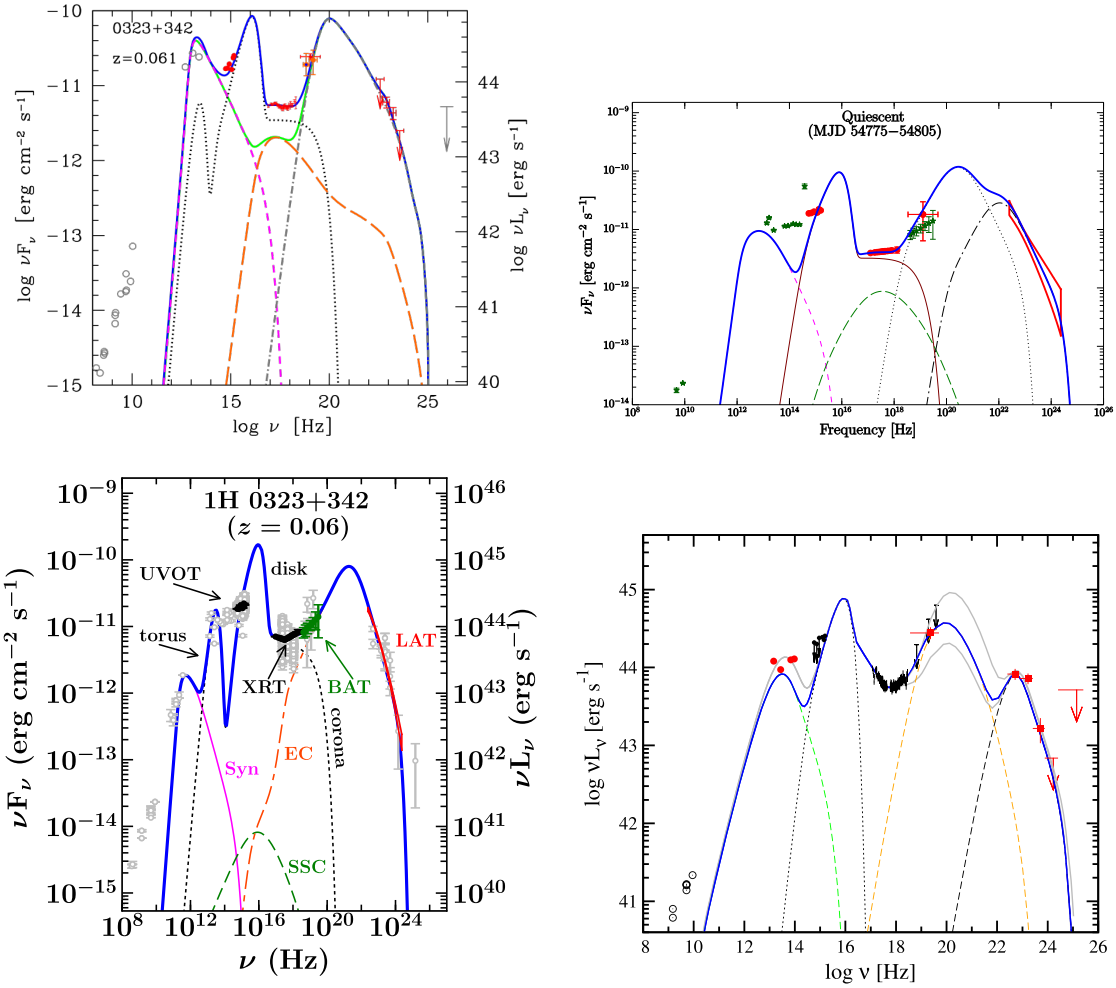

Figure 7.2: Different groups' jet models applied to the SED of 1H 0323+342. *Clockwise from top left:* From Abdo et al. (2009b); Paliya et al. (2014); from Yao et al. (2015a); from Paliya et al. (2019).

My proposal to gain new X-ray spectra of six recently-discovered γ-NLS1s was approved for the current *XMM-Newton* cycle (2019 May – 2020 April). These sources have fainter X-ray and γ-ray emission than many of the other γ-NLS1s and the current X-ray data is of poor quality. These new observations will expand the set of γ-NLS1s with useful high-energy data. With new X-ray spectra I will be able to parameterise their high-energy spectra for the first time, and explore the disc-jet connection in a larger set of sources.

7.2.2 Future high-energy and multimessenger studies of SMBHs

The site of the γ-ray emitting region in blazar jets remains an open question. In Chapter 5 I showed that it was possible to fit the SED of PKS J1222+0413 with an EC-disc model, with the site relatively close to the SMBH. Yao et al. (2015a) had previously shown that EC-BLR and EC-torus solutions, with more distant dissipation regions, were both possible. Zheng et al. (2017) attempted to locate the γ-ray emission region of 36 blazars and concluded that the distances they computed were all consistent with being at the very edge of, or beyond, the BLR. According to Romano et al. (2018), the prospects for detecting γ-NLS1s at very high energies with the Cherenkov Telescope Array (CTA: see Section 3.5.2) are good. The CTA data will hopefully give us new insights into the location of the high-energy emission site, since if the emission region is very near to the SMBH, and compact, then it will be opaque to high-energy γ-rays. The simulations of Romano et al. (2018) show that, in principle, it will be possible to determine whether the γ-ray originates inside or outside of the BLR. The CTA observations will hopefully then remove some degeneracies in our models.

As mentioned in Section 1.1.8, IceCube Collaboration et al. (2018) have claimed the detection of a neutrino from a blazar, suggesting the presence of relativistic hadrons within blazar jets. Further discoveries (or non-discoveries) of blazar neutrino emission

will help us to understand the content of jets and their associated energy budgets.

Athena (Barcons et al. 2015) is a future ESA X-ray telescope that is under development. It is currently planned to launch in the early 2030s. *Athena* will be around one hundred times more sensitive than the current workhorses of X-ray astronomy, *XMM-Newton* and *Chandra*. It will operate in the same band as these missions (0.2–12 keV), and is being designed to deliver a large effective area around the 6 keV region containing iron line emission. Simulations suggest that with *Athena*'s exquisite sensitivity, it will be possible to distinguish prograde, retrograde and non-spinning SMBHs from the shape of the iron line profile. Additionally, in the timing domain, the measurement of short lags between changes in the iron line emission and the X-ray continuum may also imply high SMBH spin, and provide further tests of general relativity. The versatility of X-ray observations, utilising both spectral and timing analyses, could therefore provide independent tests of this key parameter. *Athena* therefore has the potential to reveal the spin distribution of supermassive SMBHs thereby addressing important unanswered questions about the powering of relativistic jets.

7.2.3 Variability studies

7.2.3.1 Prospects for future work on the 'Big Dipper' and other hypervariable AGN

The observing campaign on the 'Big Dipper' I presented in Chapter 6 was fortunate to have recorded a dramatic dimming and brightening event of the source. There is some evidence that similar events have occurred in its past. The source appears to have been in a relatively bright state when observed photographically in 1988 but was in a deep minimum in the SDSS observation of 2000. The Catalina lightcurve suggests another dip occurred between 2005–2007 (see Figure 6.1). As noted by MacLeod et al. (2019), past hypervariable behaviour is an indicator of future events.

Future monitoring of this source is desirable as other interesting episodes of variability may be captured.

New X-ray and UV observations would be highly beneficial in further investigating the nature of the variability. Sampling both sides of the peak of the accretion disc emission peak the would enable a parameterisation of the changing energetics during a variability episode and a determination of whether SDSS J2232−0806 undergoes spectral state changes as seen in e.g. Mrk 1018 (Noda & Done 2018). The ability of UV and X-rays to probe the innermost regions would enable a determination of whether some 'collapse' of the UV emission occurs as seen in e.g. SDSS J110057.70−005304.5 (Ross et al. 2018).

During the writing of this thesis, the first data from the Zwicky Transient Facility (ZTF) was released. New ZTF data for the 'Big Dipper' is shown in Figure 6.1, where it is clear that the high cadence of the observations (and improvement of photometric quality over Catalina) will be highly valuable in monitoring this, and other, variable sources. The ZTF is acting as a pathfinder for the forthcoming Large Synoptic Survey Telescope (LSST, Ivezic et al. 2008) which will generate an order of magnitude more data. The LSST is an 8.4 m optical telescope currently under construction in Chile, with the survey expected to begin in 2020. One of its main science goals is to find optically transient AGN. LSST will issue warnings when transients are detected, allowing observers to rapidly respond and obtain spectroscopic or multiwavelength data of the source. By increasing the known population of hypervariable AGN, it will be possible to gain new insights into the mechanisms behind their dramatic changes. This incredibly large survey will also enable us to address whether hypervariable AGN are a unique population or if all AGN exhibit such extreme behaviour if you look at them for long enough.

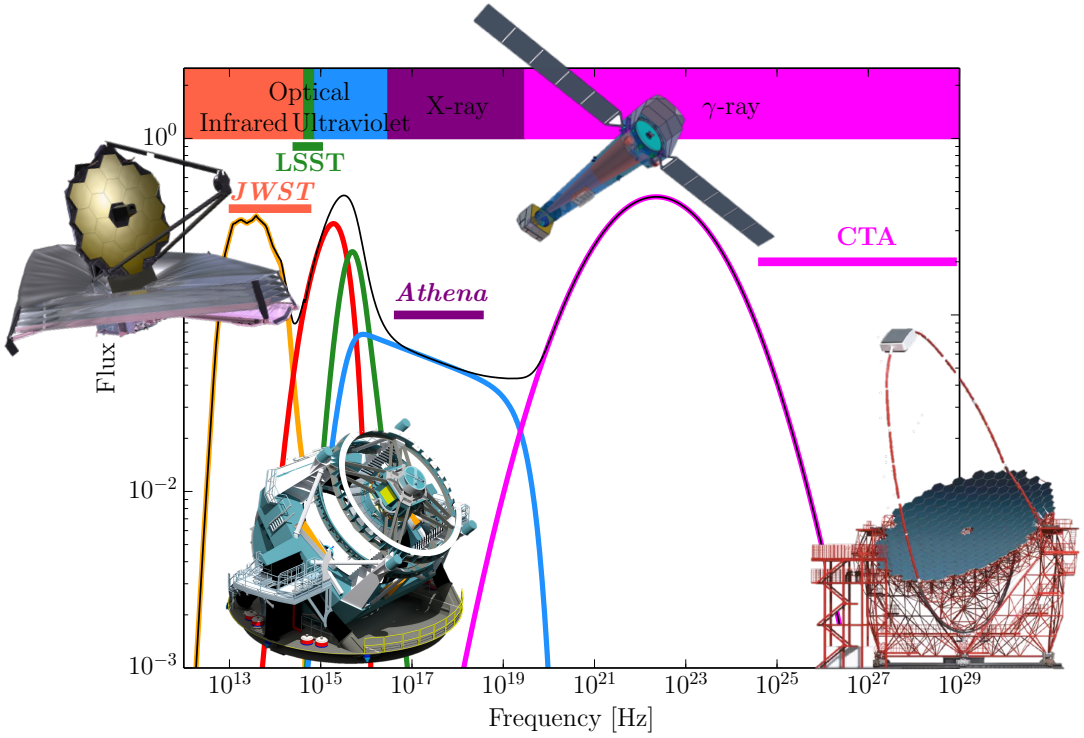

Figure 7.3: An illustration of future astronomical observatories (the *James Webb Space Telescope*, Large Synoptic Survey Telescope, *Athena* and the Cherenkov Telescope Array) and their wavelength coverage on a mock AGN SED.

Appendix A

Complexity in the X-ray spectrum of 1H 0323+342

After fitting the *XMM-Newton* EPIC X-ray spectra (see Section 4.4.2.1) some structure in the residuals, particularly at ~ 0.5 and ~ 6 keV, hinted at additional complexity not modelled by the smooth continuum components. I tested the possibility that reflection of the coronal emission off an ionised, optically thick medium could produce these features. I added a reflection component (REFLIONX, Ross & Fabian 2005) to the continuum model and tied the photon index of its input spectrum to that of the corona, $\Gamma_{\rm ref} = \Gamma_{\rm cor}$. The Fe abundance was fixed to the Solar value. Initially I blurred this reflection with a relativistic convolution code (KDBLUR, Laor 1991) but the blurring was minimal and was not required by the model, so this component was removed. The reflection component is weak and so its parameters are poorly determined. However, it takes up some of the upturn at the very hard end of the spectrum, so the jet makes less of a contribution which in turn means the corona photon index is much flatter. Whilst the addition of reflection is a significant improvement over the simpler, smooth continuum model with $\Delta\chi^2 = 40$ for two additional free parameters, it does not entirely account for the residuals as seen in Figure A.1. However, it is clear that some of the improvement to the fit comes from a Fe reflection feature.

The obvious bump in the residuals at ~ 0.5 keV is very similar to a feature seen in the *XMM-Newton* EPIC spectrum of the prototypical narrow-line blazar I Zw 1 obtained by Gallo et al. (2004). A narrow feature around this energy is also evident in the higher-resolution RGS1 spectrum of 1H 0323+342 (see Fig. A.1). In Gallo et al. (2004), the authors tested the possibilies of O VII emission or an absorption line or edge. These features all had success in minimising the residuals but the data from their 20 ks observation (including the RGS spectra) were not of sufficient quality to conclusively determine the nature of the extra component. I test the three possibilities in the data by adding either a Gaussian emission line (ZGAUSS), Gaussian absorption line (GABS) or absorption edge (ZEDGE) to the continuum model. For consistency, I can compare the inclusion of these features with the improvement of fit in the RGS data. I use only the first-order spectra of RGS1&2 and include a cross-normalisation parameter in the model. The two spectra were rebinned to a minimum of 20 counts per bin so that χ^2 statistics could be used in XSPEC. Because of its limited spectral range, I model the continuum simply with PHABS $\times$ (BBODY + POWERLAW); the resulting fit is shown in Fig. A.1. All three different components improve the fit of the model to the EPIC spectra with F-test probabilities $> 99.99\%$. However, only the Gaussian emission line gives such a good improvement in the RGS spectral model. The energy of this line is a little lower (higher) in the EPIC (RGS) spectral model than that expected for O VII emission at 22 Å ≈ 0.56 keV rest frame. Alternatively, a broad absorption feature could be consistent with unresolved transition array absorption of Fe M-shell ions seen at 16–17 Å (0.73–0.77 keV) (Netzer 2004). The absorption line energy obtained from the EPIC spectra is again a little too low, but the 0.75 ± 0.02 keV line in the RGS model is consistent with Fe M-shell UTA absorption. In both EPIC and RGS spectra, the model absorption edge energies are lower than the ≈ 0.73 keV expected for the O VII absorption edge. The likeliest scenario is the presence of a narrow O VII emission line.

As stated in § 6.3.1.1, if I adopted the Dickey & Lockman (1990) ('D&L90') Galactic

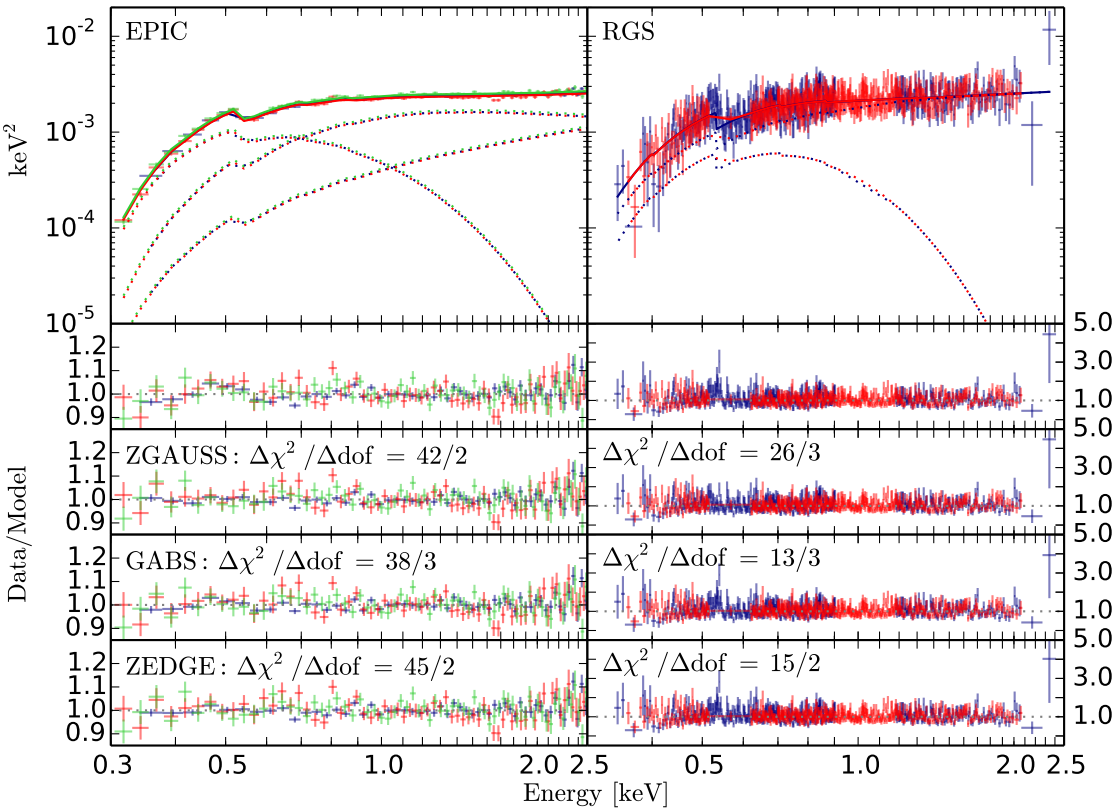

Figure A.1: Complexity in the *XMM* EPIC and RGS soft X-ray spectra. Top panels show the smooth continuum model (COMPTT + NTHCOMP + POWERLAW) and its data / model ratios in the second panels. Data / model ratios for three alternative additional components are shown in the third to bottom panels. The components are an emission line (ZGAUSS), an absorption line (GABS) or an absorption edge (ZEDGE).

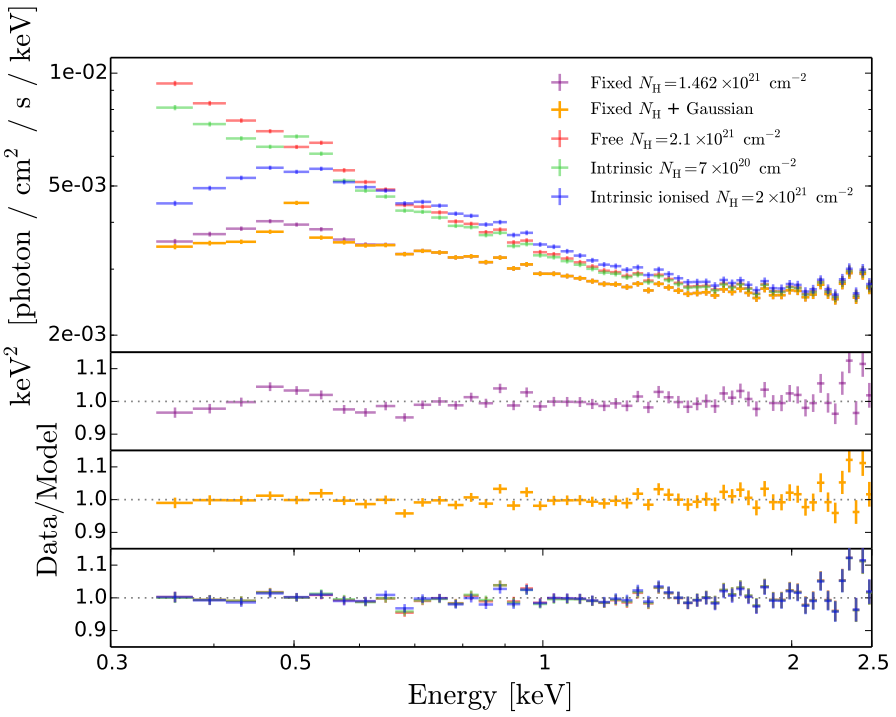

Figure A.2: Upper panel: *XMM-Newton* EPIC pn 0.3 – 2.5 keV spectra deabsorbed through my preferred model with differing absorbing columns. Purple crosses: column fixed to the Galactic value 1.462×10^{21} cm^{-2}; orange crosses: as before but with a narrow Gaussian emission line added at 0.53 keV; red crosses: as before but with the Galactic column allowed to vary in the fit resulting in the value 2.1×10^{21} cm^{-2}; green crosses: Galactic column fixed to 1.462×10^{21} cm^{-2} and an additional intrinsic column fit to the value 4×10^{20} cm^{-2}; blue crosses: Galactic column fixed to 1.462×10^{21} cm^{-2} and an intrinsic, partially ionised, partial covering fraction absorber with 2×10^{21} cm^{-2}. Lower panels: data/model ratios resulting from the fits.

column $N_{\rm H}^{\rm Gal} = 1.46 \times 10^{21}$ cm^{-2}, the deabsorbed *XMM-Newton* EPIC X-ray spectra turned down towards lower energies and did not smoothly connect with the OM photometry. The same downturn can be seen even when accounting for the likely O VII emission at ≈ 0.6 keV (see Figure A.2). I achieved a significant improvement in the fit ($\Delta\chi^2 = 162$ for one additional free parameter), and a corrected shape in the deabsorbed spectra, if I allowed the $N_{\rm H}^{\rm Gal}$ to be a free parameter in my fits and increase to a value $\approx 2.2 \times 10^{21}$ cm^{-2}.

I tested the other X-ray data for evidence of this additional absorprion. I added the *Swift* XRT spectra recorded between 2 August and 29 September 2015; the

co-added spectrum contains 8724 counts. A sum of two power-laws model with $\Gamma_1 = 2.2^{+0.2}_{-0.1}$ and $\Gamma_2 = 1.0^{+0.3}_{-0.4}$ has $\chi^2_\nu = 357/260 = 1.37$ if the Galactic column is fixed to 1.46×10^{21} cm^{-2}. Allowing the Galactic column to be a free parameter, I find the fit improves by $\Delta\chi^2 = 18$ with an F-test probability of 99.97%. The Galactic column in this model is very high at $\left(4.0^{+0.9}_{-0.8}\right) \times 10^{21}$ cm^{-2} and the soft photon index is very steep, $\Gamma_1 = 4.9 \pm 0.7$, but clearly these parameters are poorly constrained by the limited quality of the spectrum. I note that the shapes of the deabsorbed, co-added *Swift* XRT spectra with and without the additional column agree with the corresponding *XMM-Newton* EPIC spectra. I fitted a blackbody plus power-law model fitted to the *XMM-Newton* RGS spectra (taken contemporaneously with the EPIC spectra, see Figure A.3) and recorded a C-statistic 2138 with the D&L90 value of $N_{\rm H}^{\rm Gal}$. Increasing the Galactic column to 2.1×10^{21} cm^{-2} worsens the C-statistic to 2211. However, I note that above ≈ 30 Å (below ≈ 0.4 keV) the count rates in many channels are consistent with zero. Therefore, there is not such strong evidence for a higher Galactic column in the *Swift* XRT data and no evidence in the *XMM-Newton* RGS spectrum.

It is unlikely that the neutral atomic hydrogen column on the line-of-sight towards 1H 0323+342 is truly this much higher than found by D&L90. Whilst it is known that there are small-scale ($\sim$ 1–3 arcsecond), low column density structures which may have been unseen or unresolved by H I 21 cm surveys (Ben Bekhti et al. 2009), I am unaware of such clumps having been detected with column densities as high as implied by my fits ($N_{\rm H} > 10^{20}$ cm^{-2}). If such a neutral absorber were in the Milky Way I would also expect to see additional reddening in the optical/UV data. However, I find no evidence of additional redenning in the optical / UV data. I measured the equivalent width (EW) of the Na I D absorption line in the Keck spectrum of 2016 February to be EW = 0.891 Å assuming its profile to be similar as that of the broad Hβ emission line. Using this measurement, I obtain an estimate of the extinction $A_V = 0.483^{+0.098}_{-0.081}$ using the $E(B-V)$-EW(Na I D) relation of Poznanski et al. (2012) and assuming the typical Milky Way $R_V = 3.1$. This value is

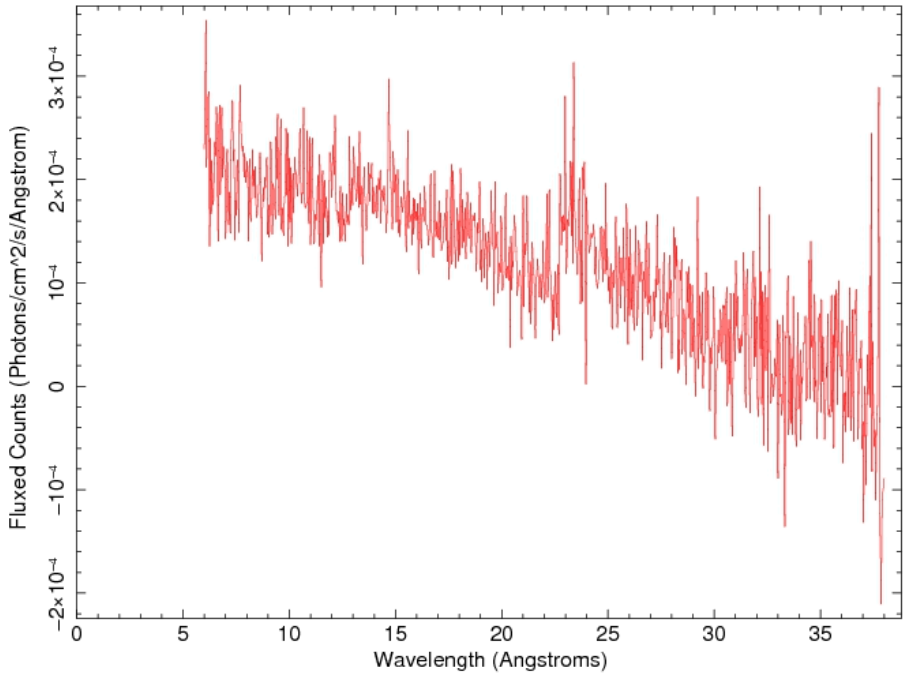

Figure A.3: The *XMM-Newton* RGS spectrum of 1H 0323+342. Note that the counts at longer wavelengths are consistent with zero.

slightly lower than the $A_V = 0.706$ I derived from the D&L90 value of the Galactic H I column.

If the absorber were intrinsic to the AGN, it is possible that there was some occultation of the compact X-ray source but not the more extended optical/UV emission (e.g. Risaliti 2007; Zhang et al. 2017). I modelled the *XMM-Newton* EPIC spectra with Galactic plus intrinsic columns. For the intrinsic column I tried both neutral (ZPHABS) and partially-ionised (ZXIPCF) models. The neutral, intrinsic column improves the fit by $\Delta\chi^2 = 104$ for one additional free parameter (a lesser improvement than the additional Galactic column) and I find $N_{\rm H}^{\rm int} = (8 \pm 1) \times 10^{20}$ cm^{-2}. With the ZXIPCF model I obtain a very low ξ value, indicating weakly ionised material, and a high column $N_{\rm H}^{\rm int} = (2 \pm 1) \times 10^{21}$ cm^{-2}. The improvement in the fit is only $\Delta\chi^2 = 11$ for three additional free parameters and this additional ionised intrinsic absorber did not correct the shape of the deabsorbed spectra (see Figure A.2). In the RGS spectrum, adding a lowly ionised absorber at the redshift of 1H 0323+342 improved the C-statistic by only 0.2 for three additional parameters and the fitted

column density $N_{\rm H}^{\rm int} = 5.2 \times 10^{17}$ cm^{-2} was incredibly small.

Despite extensive modelling, I have been unable to find a physically plausible model with a column density fixed at the D&L90 value which both reduces the residuals and also gives a corrected shape of the deabsorbed soft spectrum that fits the UV data. I adopted the increased neutral Galactic column as being the simplest model solution which improved the fits and the shape on the intrinsic spectrum.

As I showed in § 4.5.1.1, this allows me to fit an energy-conserving accretion disc model which reproduces the optical/UV to hard X-ray data and returns parameters typical of a NLS1. My jet models would not be substantially changed if I had proceeded with an X-ray spectrum deabsorbed through the D&L90 column density value.

In 2018 August–September, a series of six X-ray/UV observations of 1H 0323+342 was taken with *XMM-Newton*. The total exposure time of this campaign was over 300 ks. Preliminary analysis of the X-ray spectra has attributed the sharp feature at ≈ 0.6 keV to the O VII emission feature (E. Kara, private correspondence). A full analysis (Mundo et al., in preparation) will hopefully shed more light on the rest of the frustratingly ambiguous complexity.

Appendix B

Optical spectral fitting of SDSS J2232−0806

In the following pages, I present the results from fitting the eleven optical spectra of SDSS J2232−0806, as described in Chapter 6.

Table B.1: Balmer, [O III] and [N II] emission line measurements

					Hα				
Date	Scale	$\Delta v_{\rm vb}$	$W_{\rm b}$	$W_{\rm n}$	$f_{\rm vb}$ $\times 10^{-15}$	$f_{\rm b}$ $\times 10^{-14}$	$f_{\rm n}$ $\times 10^{-15}$	$f_{\rm tot}$ $\times 10^{-14}$	$EW_{\rm vb+b}$
2013-06-10	1.446	$+800 \pm 700$	4460 ± 50	480 ± 10	3 ± 2	5.05 ± 0.08	1.5 ± 0.1	5.5 ± 0.2	570 ± 20
2013-08-07	1.584	$+1900 \pm 700$	4530 ± 60	550 ± 10	3 ± 1	5.20 ± 0.08	1.8 ± 0.1	5.7 ± 0.2	750 ± 30
2013-09-09	1.046	$+1300 \pm 800$	4280 ± 50	510 ± 10	9 ± 2	5.4 ± 0.1	1.81 ± 0.08	6.5 ± 0.2	850 ± 30
2014-07-23	1.173	$+800 \pm 700$	4200 ± 60	480 ± 10	6 ± 2	4.97 ± 0.09	1.59 ± 0.09	5.7 ± 0.2	1130 ± 50
2014-12-16	1.076	$+2000 \pm 500$	4300 ± 50	570 ± 20	5 ± 4	4.2 ± 0.1	1.7 ± 0.1	4.8 ± 0.4	1070 ± 90
2016-07-09	1.344	$\leqslant 700$	4600 ± 100	490 ± 10	3 ± 2	4.8 ± 0.1	1.47 ± 0.06	5.3 ± 0.2	600 ± 30
2016-10-22	0.706	$+1800 \pm 500$	4510 ± 40	540 ± 10	3 ± 1	4.86 ± 0.05	1.48 ± 0.05	5.3 ± 0.1	610 ± 10
2017-07-27	1.022	$+1800 \pm 8000$	4500 ± 100	470 ± 10	4 ± 3	5.2 ± 0.1	1.43 ± 0.07	5.7 ± 0.3	970 ± 60
2017-10-11	1.152	$+1900$	3670 ± 90	700 ± 200	1.2 ± 0.3	5 ± 1	1.7 ± 0.4	7 ± 1	1200 ± 300
2017-11-24	1.316	$+1900$	4000 ± 500	500 ± 100	2.1 ± 0.7	6 ± 1	1.1 ± 0.4	8 ± 1	1100 ± 200
2018-07-05	1.093	$+1800 \pm 800$	4560 ± 80	490 ± 30	4 ± 3	4.5 ± 0.1	1.5 ± 0.1	5.1 ± 0.3	660 ± 40

Table B.1: Balmer, [O III] and [N II] emission line measurements (continued)

	[NII] λ6583	Hβ						[OIII] λ5007	
Date	f $\times 10^{-16}$	$f_{\rm vb}$ $\times 10^{-15}$	$f_{\rm b}$ $\times 10^{-14}$	$f_{\rm n}$ $\times 10^{-16}$	$f_{\rm tot}$ $\times 10^{-14}$	EW$_{\rm vb+b}$	BD$_{\rm vb+b}$	f $\times 10^{-15}$	EW
2013-06-10	5.7 ± 0.1	3 ± 1	1.46 ± 0.09	2.3 ± 0.1	1.8 ± 0.1	112 ± 8	3.0 ± 0.3	3.2 ± 0.5	21 ± 3
2013-08-07	6.5 ± 0.2	3 ± 1	1.58 ± 0.04	2.7 ± 0.2	1.9 ± 0.1	150 ± 10	2.9 ± 0.2	3.5 ± 0.1	28 ± 8
2013-09-09	6.0 ± 0.1	3 ± 2	1.32 ± 0.05	2.7 ± 0.1	1.7 ± 0.2	170 ± 20	3.8 ± 0.5	3.7 ± 0.2	40 ± 20
2014-07-23	5.7 ± 0.1	3 ± 1	1.21 ± 0.05	2.4 ± 0.1	1.6 ± 0.1	250 ± 20	3.6 ± 0.3	3.4 ± 0.6	56 ± 9
2014-12-16	6.6 ± 0.2	3 ± 1	0.83 ± 0.03	2.6 ± 0.2	1.2 ± 0.1	190 ± 20	4.0 ± 0.5	3.3 ± 0.8	50 ± 10
2016-07-09	5.7 ± 0.2	3 ± 1	1.32 ± 0.09	2.2 ± 0.1	1.6 ± 0.2	120 ± 10	3.2 ± 0.3	3.1 ± 0.4	24 ± 3
2016-10-22	6.4 ± 0.2	3 ± 1	1.34 ± 0.06	2.20 ± 0.08	1.7 ± 0.1	110 ± 10	3.2 ± 0.3	3.3 ± 0.2	23 ± 2
2017-07-27	5.4 ± 0.1	3 ± 1	1.41 ± 0.08	2.1 ± 0.1	1.7 ± 0.2	180 ± 20	3.3 ± 0.3	3.2 ± 0.5	35 ± 5
2017-10-11	8 ± 2	5 ± 2	1.3 ± 0.1	2.5 ± 0.6	1.8 ± 0.2	150 ± 20	3.7 ± 0.7	2.5 ± 0.6	22 ± 6
2017-11-24	6 ± 2	5 ± 2	1.3 ± 0.2	1.6 ± 0.6	1.7 ± 0.3	160 ± 20	4.4 ± 1.0	1.8 ± 0.5	16 ± 4
2018-07-05	5.7 ± 0.4	3 ± 1	1.19 ± 0.09	2.2 ± 0.2	1.5 ± 0.2	120 ± 10	3.3 ± 0.4	3.4 ± 0.8	29 ± 6

'Scale' is the flux scaling factor applied to each spectrum, including both internal and absolute scalings (see Section 6.2.2.2 in the text). Subscripts 'vb', 'b' and 'n' refer to the very broad, broad and narrow emission line components, respectively and 'tot' is the total. $\Delta v_{\rm vb}$ is the velocity offset (in km s^{-1}) of the very broad emission line components relative to the narrower components; positive values indicate a redward offset. Fluxes f in erg s^{-1} cm^{-2}; widths 'W' are FWHM in km s^{-1} and equivalent widths 'EW' are in Å. 'BD' is the Balmer decrement $^{\rm H\alpha}/_{\rm H\beta}$.

Table B.2: Mg II emission line measurements

Date	W_{vb}	f_{vb} $\times 10^{-14}$	W_b	f_b $\times 10^{-14}$	W_{tot}	f_{tot} $\times 10^{-14}$	EW_{tot}
2013-06-10	9000 ± 800	2.2 ± 0.5	3300 ± 300	1.5 ± 0.2	4200 ± 400	3.7 ± 0.5	51 ± 8
2013-08-07	9000 ± 1000	2.0 ± 0.6	3100 ± 500	1.5 ± 0.3	3900 ± 500	3.5 ± 0.7	60 ± 10
2013-09-09	10000 ± 600	2.4 ± 0.3	3400 ± 100	1.9 ± 0.1	4100 ± 200	4.3 ± 0.3	80 ± 10
2014-07-23	9000 ± 700	1.5 ± 0.3	3600 ± 200	2.0 ± 0.2	4000 ± 200	3.5 ± 0.4	100 ± 10
2014-12-16	8400 ± 600	2.1 ± 0.3	3100 ± 200	1.4 ± 0.1	4000 ± 300	3.5 ± 0.3	110 ± 10
2016-07-09	9000 ± 1000	1.9 ± 0.5	3300 ± 400	1.3 ± 0.2	4200 ± 500	3.2 ± 0.6	50 ± 10
2016-10-22	11000 ± 500	2.4 ± 0.3	3400 ± 200	1.7 ± 0.1	4300 ± 200	4.0 ± 0.3	59 ± 7
2017-07-27	9900 ± 700	2.0 ± 0.3	3600 ± 200	2.0 ± 0.1	4200 ± 200	4.0 ± 0.3	73 ± 9
2017-10-11	14000 ± 1300	3.2 ± 0.5	3500 ± 200	2.3 ± 0.2	4200 ± 300	5.5 ± 0.5	100 ± 10
2017-11-24	11000 ± 1700	2.9 ± 0.7	3300 ± 300	1.8 ± 0.3	4200 ± 500	4.7 ± 0.7	110 ± 20
2018-07-05	9000 ± 1000	2.0 ± 0.6	3300 ± 400	1.5 ± 0.3	4200 ± 500	3.5 ± 0.7	60 ± 10

Subscripts 'vb' and 'b' refer to the very broad and broad emission line components, respectively and 'tot' is the total. Fluxes f in erg s^{-1} cm^{-2}; widths 'W' are FWHM in km s^{-1} and equivalent widths 'EW' are in Å.

Appendix C

A large sample of optical/X-ray quasars

In this appendix, I present some ongoing work based on a large sample of X-ray detected optical quasars I have assembled using recently-published catalogues. I describe the selection of the sample and present some preliminary results based on the optical spectral analysis, and discuss some limitations. Future work on the sample will explore the multiwavelength properties of the sources, and investigate correlations between parameters to reveal the drivers behind their diversity.

C.1 Introduction

Chapters 4, 5 and 6 presented in-depth studies of individual AGN. The three sources investigated are extreme AGN: 1H 0323+342 and PKS J1222+0413 because of their dual NLS1-blazar nature and the Big Dipper because of its hypervariability. Whilst interesting sources, it is difficult to extrapolate the findings made to the general AGN population. An alternative route to investigating AGN is through large population studies. The ultimate goal of this project is to assemble multiwavelength SEDs with data straddling the peak of the accretion disc emission. From the SED the energetics and bolometric luminosities of the AGN may be determined. Correlations between

optical and X-ray spectral parameters can be sought, following the approaches of Jin et al. (2012a,b,c) and Collinson et al. (2015, 2017).

Jin et al. (2012a) selected a sample of 51 low-redshift ($z < 0.4$) Type 1 SDSS quasars with Hβ or Hα in their optical spectrum. These sources were chosen to have high-quality X-ray spectra with a minimum of 2000 counts in an EPIC detector and which were found to be free from sharp absorption features that suggest the presence of a warm absorber. Jin et al. (2012b) introduced the novel optical to X-ray correlation spectrum (OCXS) technique. The rest-frame 3700–6700 Å optical spectra were divided into 1000 bins and each of these bins were correlated against the hard X-ray luminosities ($L_{2-10\mathrm{keV}}$). The broad Balmer lines were found to correlate more strongly with $L_{2-10\mathrm{keV}}$ than the underlying optical continuum. The narrow line cores of the Balmer lines were found to have a much weaker correlation with $L_{2-10\mathrm{keV}}$ than the broad components, in contrast with the [O III]$\lambda\lambda 4959, 5007$ narrow lines, which were strongly correlated. Some differences were found in the OCXSs of NLS1s and BLS1s, although the sample sizes of the subgroups were small. Such an analysis would benefit from a larger sample size.

Collinson et al. (2015) presented a sample of 11 $z \sim 2$ AGN with SDSS optical spectra and *XMM-Newton* X-ray and optical/UV data. Because of the high redshift, the data sampled spectral regions near to the peak of the accretion disc emission and the turnover (or flattening of the disc emission peak) was observed in five sources, resulting in strong constraints on the bolometric luminosity determined from SED modelling. It was found that the bolometric luminosities estimated from proxies (i.e. the optical 5100 Å or X-ray 2–10 keV luminosity) could be discrepant with those determined by SED modelling by large factors (ten or more in extreme cases). Further work by Collinson et al. (2017) explored placing limits on the outer accretion disc radius and supermassive black hole (SMBH) spin. The latter was found to be degenerate with orientation and accretion rate and was therefore challenging to determine precisely. Since they chose to measure the SMBH masses from Hα or Hβ, they required near-infrared spectra, which placed a strong limitation of the sample

size. Consequently, whilst comparisons could be made between individual sources, population studies were not possible in this work.

Recently, Lawther et al. (2017) presented first results cataloguing the optical to X-ray SEDs of $z \approx 2$ (spanning the range $1.5 \leqslant z \lesssim 4$) quasars with optical spectra from MMT and SDSS. They have requested that UV/X-ray data for their optical quasar sample be obtained with *Swift*. Their first paper included the analysis of 44 out of 133 sources so far observed by *Swift* (all of which were radio-loud). Only 23 of their sources were detected in X-rays by *Swift*, and therefore detailed modelling or analysis of the broadband SED could not be conducted. By construction, all of the AGN in my sample will be detected in X-rays by *XMM-Newton*. So, unlike Lawther et al. (2017), very faint X-ray AGN (undetected by *XMM-Newton*) will not be included in my sample which will be biased towards brighter and unobscured sources. The greater X-ray sensitivity of *XMM-Newton* will enable me to make a more robust characterisation of the X-ray spectral parameters for a much larger sample.

The main aims of this project are to:

- Determine SMBH masses from the Hα, Hβ and Mg II broad emission lines, using the single epoch virial method. Comparisons can then be made between the different scaling relations used.

- Characterise the X-ray spectra of the sources, determining spectral slopes. In some sources, it will be possible to detect a break in the spectral shape. A comparison of fit statistics of single and double power-law models will enable a determination of the fraction of sources in which a soft X-ray excess can be detected.

- Assemble multiwavelength SEDs. The optical, UV and X-ray data sample both sides of the peak of the accretion disc emission. By applying an energy-conserving accretion flow model, I will be able to parameterise the energetics

across the unseen far and extreme ultraviolet band. This will enable a determination of the bolometric luminosity and (coupled with a measurement of the SMBH mass) the Eddington ratio. Photometric data from infrared catalogues will allow for a and estimations of the dust temperatures and covering factors.

- Explore the correlations of optical, UV and X-ray properties. With a large sample size, I will be able bin objects by (e.g.) mass, accretion rate, luminosity and investigate how the spectral parameters vary in relation to these fundamental properties.

C.2 Sample selection

Much of my analysis will depend on the determination of the mass of the SMBH in the quasar. Single epoch virial scaling relations allow an estimate of the SMBH mass to be made from a measurement of a broad emission line width and a specific luminosity (usually sampling the quasar continuum). Scaling relations have been calculated for several broad emission lines; the best-calibrated and most often used is for the Balmer line Hβ at 4861 Å in the quasar rest frame. However, this line is within the BOSS spectrograph range only for $z \lesssim 1$. My sample can be extended to higher redshift if I instead sample the Mg II emission line at 2798 Å (rest frame) and use scaling relations developed for that line.

C.2.1 The parent catalogues

C.2.1.1 Optical spectra: SDSS-DR14Q

The Quasar Catalog of the Fourteenth SDSS Data Release (SDSS-DR14Q, Pâris et al. 2018) contains 526356 quasars. Each quasar has been the subject of least one optical spectroscopic observation recorded on or before 2016 December 5. The catalogue also contains SDSS photometric data from imaging observations. Multiwavelength

data from *ROSAT*, *XMM-Newton*, *GALEX*, 2MASS, *WISE*, UKIDSS and FIRST are included, where available. The *XMM-Newton* data are taken from the 3XMM-DR7 catalogue (see below). 14736 of the SDSS-DR14Q quasars (≈ 3 per cent) have an X-ray source detection within a 5 arcsecond matching radius. The catalogue lists the soft and hard X-ray fluxes and luminosities of the quasars. In the case of sources with multiple X-ray observations, the quoted values are the weighted average of all detections. However, the catalogue does not contain optical/UV photometry recorded with the *XMM-Newton* Optical Monitor (OM).

C.2.1.2 X-ray spectra: 3XMM-DR7

The high sensitivity and large field of view of *XMM-Newton* mean that, as well as the proposed science target of an observation, the instruments also detect many other sources serendipitously. Typically, *XMM-Newton* detects 70 serendipitous X-ray sources per pointing. These data provide a valuable resource to investigate Galactic and extragalactic X-ray sources and are therefore catalogued by the *XMM-Newton* Survey Science Centre consortium. The 3XMM-DR7 catalogue, being the Seventh Data Release of the Third *XMM-Newton* Serendipitous Source Catalog (Rosen et al. 2016), contains 727790 X-ray detections pertaining to 499266 unique sources from observations made up to 2016 December 15.

C.2.1.3 Optical and ultraviolet photometry: XMM-SUSS4.1

I take *XMM-Newton* optical/UV photometric data from the fourth *XMM-Newton* Serendipitous Ultraviolet Source Survey (SUSS: Page et al. 2012) catalogue, XMM-SUSS4.1. This catalogue, released in 2018 January, contains data from observations made up to 2017 July. The OM has a smaller field of view than the *XMM-Newton* EPIC X-ray detectors (17×17 arcmin cf. EPIC's $\approx 30 \times 30$ arcmin) and has therefore covered a smaller fraction of the sky. This means that not all X-ray sources will have a match in the OM catalogue.

C.2.2 Source selection criteria

To make an estimate of the SMBH mass, I require spectral coverage of at least one of the emission lines Hα, Hβ or Mg II. Hα or Hβ will be visible in the spectra of low-redshift sources and the Mg II emission line will be visible in the wavelength range of the BOSS spectrograph up to $z \lesssim 2.5$. I therefore consider only the SDSS quasars with $z \leqslant 2.5$. Of the 14736 quasars with an *XMM-Newton* X-ray detection, 12839 are at $z \leqslant 2.5$ which I take as my initial optical quasar sample.

Before I cross-match to the 3XMM-DR7 catalogue, I clean it by excluding the sources which:

- have a poor source summary flag (SUM_FLAG $\geqslant 3$);
- are flagged as 'CONFUSED' (i.e. with a nonzero probability of being associated with more than one distinct source);
- were observed with a high background.

The cleaned catalogue then contains 582587 X-ray detections from 404541 unique sources.

I perform a cross-match to find all 'clean' X-ray detections within 5 arcseconds of the optical quasar coordinates. This was the search radius used by Pâris et al. (2018) in their matching of SDSS-DR14Q to perform their catalogue cross matching with 3XMM-DR7. The number of *XMM-Newton* X-ray detections as a function of search radius is shown in Figure C.1. I find a total of 12461 quasars, of which 3744 have multiple X-ray detections. I then match these with sources in the OM catalog. This matching requires that the OM source is within 1 arcsecond of the optical quasar coordinates and that the observation ID of the OM record matches that of the X-ray observation (i.e. the OM and EPIC data were recorded simultaneously). 3486 quasars meet these criteria.

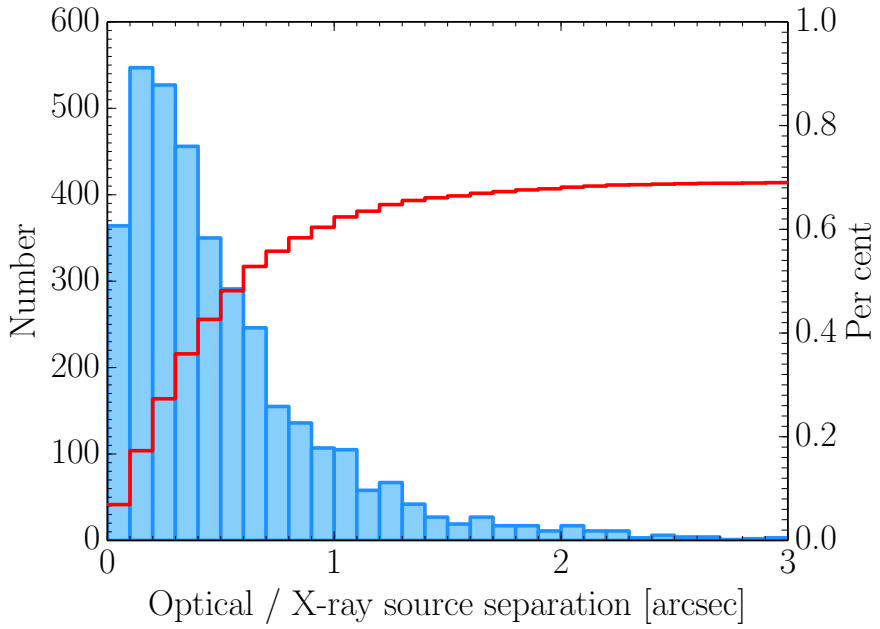

Figure C.1: The number of selected *XMM-Newton* X-ray detections matched to SDSS optical quasars as a function of source separations. The blue bars show the number of matches within each 0.1″-wide annulus and the red line shows the cumulative total as a percentage of all SDSS-DR14Q quasars.

At $z \gtrsim 0.4$, the OM photometry may be compromised by the strong Lyα λ1216 UV emission line and Lyα forest absorption blueward of 912 Å (rest frame). To determine which OM filters would be free of Lyα emission and absorption, I calculated the quasar redshifts for which the red wing of Lyα would fall just outside of the effective bandpass of each filter. Then, for each redshift bin I require an OM detection in one of the following:

- $z < 0.40$: any filter;
- $0.40 \leqslant z < 0.55$: V, B, U, UVW1 or UVM2 filters;
- $0.55 \leqslant z < 0.90$: V, B, U or UVW1 filters;
- $0.90 \leqslant z < 1.35$: V, B, or U filters;
- $1.35 \leqslant z < 1.95$: V or B filters;
- $1.95 \leqslant z < 2.50$: V filter only.

1452 quasars have at least one useful OM photometry point.

I wish to obtain reasonable constraints on the X-ray spectral parameters of these quasars, for which I require relatively high-quality X-ray spectra. I therefore make a quality cut on the number of X-ray counts recorded by an EPIC detector (either pn, MOS1 or MOS2) in the 0.2–12 keV band. The number of sources as a function of X-ray counts is shown in Figure C.2; the number of counts refers to the maximum recorded in any detector over all observations. The distribution peaks at ≈ 250 counts and only 16% of detections are made with 1000 counts or more. I chose to make a cut at 250 counts, which includes approximately half of the clean detections (664 of 1452 AGN).

Likewise, in order to make a reasonable determination of the optical spectral parameters, I wish to have good-quality spectra. I calculated the median pixel-by-pixel S/N in each of the 664 spectra; the distribution is shown in Figure C.2. By making a visual inspection of the spectra at the low end of the S/N distribution, I decided reject sources with optical spectral S/N < 3 (10%). Examples of spectra below this threshold are shown in Figure C.3. The sample then consists of 598 AGN which meet all of the above criteria.

C.3 Optical spectral fitting

To fit the optical spectra I use the Interactive Data Language (IDL) package QSFit (Calderone et al. 2017). This package was written with the purpose of creating a standardised and reproducible procedure to perform AGN optical spectral analysis. The routine fits the known principal optical/ultraviolet emission lines, the Balmer continuum, Fe II complexes and host galaxy and accretion disc continuum emission. For the emission lines it returns key parameters including the integrated luminosity, FWHM, EW and velocity offset. The AGN continuum is evaluated at several (rest frame) wavelengths including 3000 and 5100 Å, which are commonly used in virial SMBH mass relations. Given a measured colour excess, $E(B-V)$, the spectra

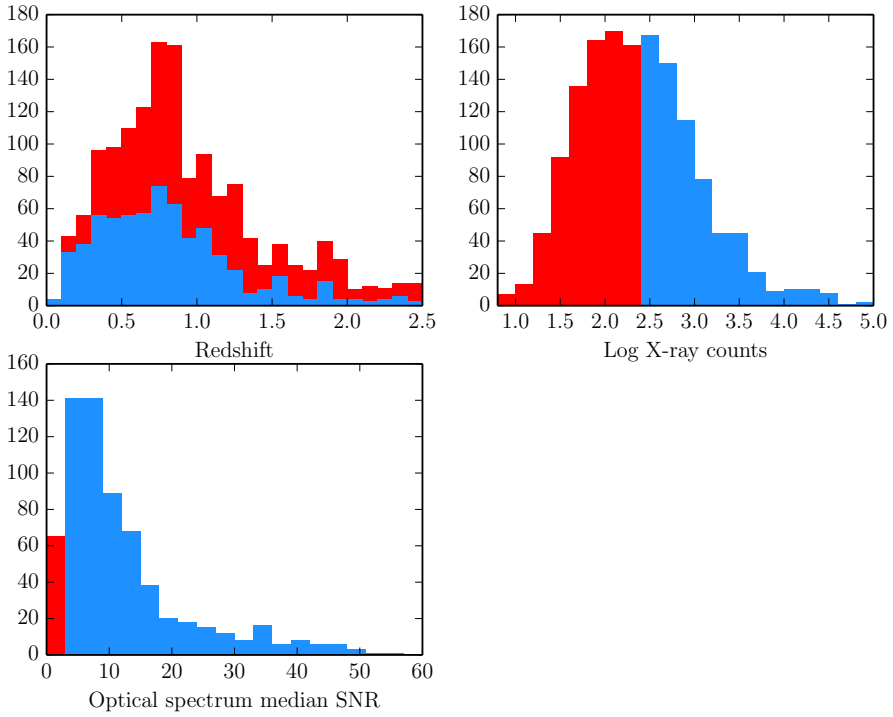

Figure C.2: Properties of the selected sample are shown in blue. Shown in red are rejected sources with optical spectral SNR < 3 and fewer than 250 0.2–12 keV X-ray counts in any EPIC detector.

are corrected for Galactic reddening using the curves of Cardelli et al. (1989) and O'Donnell (1994). (No automatic correction is made for internal reddening.)

I use QSFit to fit the SDSS spectra of the 598 selected AGN. I take values of $E(B-V)$ from Schlafly & Finkbeiner (2011), available from IRSA[1]. The coverage of the Hα and Hβ and Mg II emission lines are shown in Table C.1. QSFit is unable to determine useful emission line parameters from the spectra of two sources which, so far, have passed my quality controls: SDSS J123107.84+254734.0 and SDSS J124806.14+082232.7. Both are high-z in which Hα and Hβ have been shifted out of the observed spectral range. In the case of SDSS J123107.84+254734.0 the Mg II line is at the very end of the spectrum, so QSFit does not attempt to model it. In the case of SDSS J124806.14+082232.7 the Mg II line is very weak, and no modelled emission line is associated with it during the fit.

Table C.1 shows that Hα is measured in only 22 per cent of spectra, since it is

[1] https://irsa.ipac.caltech.edu/applications/DUST/

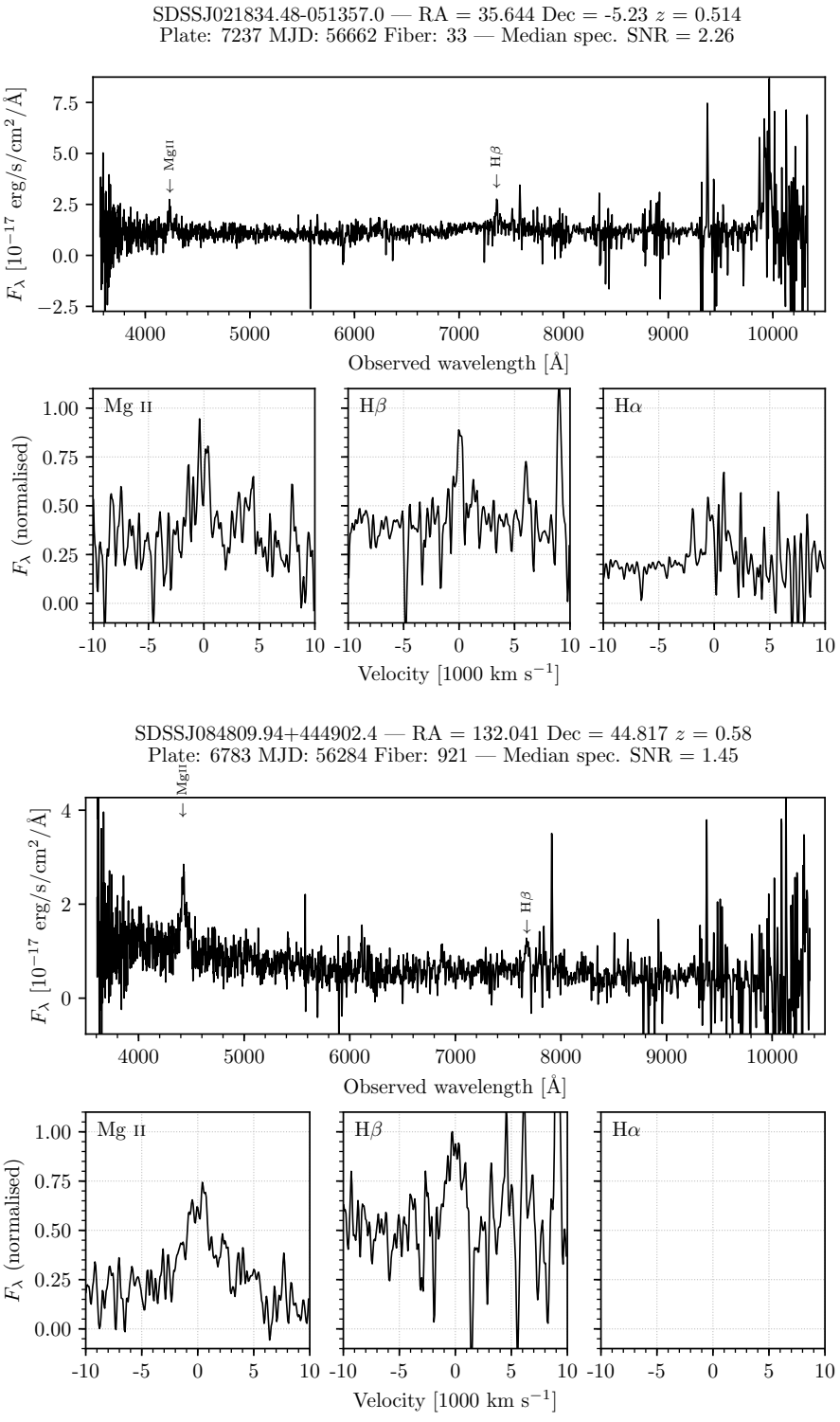

Figure C.3: Examples of low S/N optical spectra (median S/N < 3) of AGN which were not included in the sample.

Table C.1: Coverage of emission lines in optical spectra

	Emission lines	Number	Per cent
Individual lines:			
	Hα	134	22
	Hβ	403	67
	Mg II	476	80
Combinations of lines:			
A)	Hα and Hβ (not Mg II)	84	14
B)	Hα, Hβ and Mg II	49	8
C)	Hβ and Mg II (not Hα)	235	39
D)	Mg II only	192[a]	32
E)	Hβ only	35[b]	6
F)	Hα only	1[c]	0.17
G)	None of Hα, Hβ or Mg II	2[d]	0.32
	Total	598	100

Notes: (a) The spectrum of the source SDSS J141328.87+435808.1 is missing Hβ. (b) The spectrum of the source SDSS J015950.24+002340.8 is missing Hα. (c) The spectrum of the source SDSS J113109.48+311405.4 is missing Hβ. (d) None of the the emission lines suitable for SMBH mass estimates could be measured in the spectra of SDSS J124806.14+082232.7 or SDSS J123107.84+254734.0.

shifted out of the wavelength range of the SDSS spectrographs at ≈ 0.5. Hβ and Mg II have much better coverage, being present in 67 and 80 per cent of spectra, respectively. The fits to some lines are better than others, and QSFit creates a bitmask for each line to flag problems with the fitting. In the following I consider a 'good' measurement to have been made when the bitmask does not contain flags indicating the line luminosity or FWHM (or their associated uncertainties) are zero or NaN, the relative uncertainty on the luminosity is greater than 1.5 or the relative uncertainty on the FWHM is greater than 2.0. For the time being, I ignore flags warning of problems with the velocity offset determination.

The distributions of FWHMs for the key broad and narrow emission lines are shown in Figure C.4. The parameters of the distributions are given in Table C.2. Table C.2 indicates that the fractions of good fits are lower for the narrow lines than the broad lines. In many cases the narrow Hβ line FWHM was close to, or at, the maximum

Table C.2: Emission line FWHMs from spectral fits

Line	N	min	max	median	σ
H$\alpha_{\rm br}$	129 (96%)	1376	8987	3733	1482
H$\beta_{\rm br}$	370 (92%)	1222	14616	4697	2879
Mg II$_{\rm br}$	455 (96%)	1840	14752	4652	2454
H$\alpha_{\rm na}$	73 (54%)	312	794	512	152
H$\beta_{\rm na}$	121 (30%)	301	794	487	138
[O III]λ5007	265 (77%)	300	797	463	119

Note: Values are shown for the subset of spectra for which a reliable fit of the line was made. 'N' gives the number of sources used to make the determination of the distribution. N as a percentage of the total number of spectra in which the line is present is given in parentheses. The distributions are shown in Figure C.4.

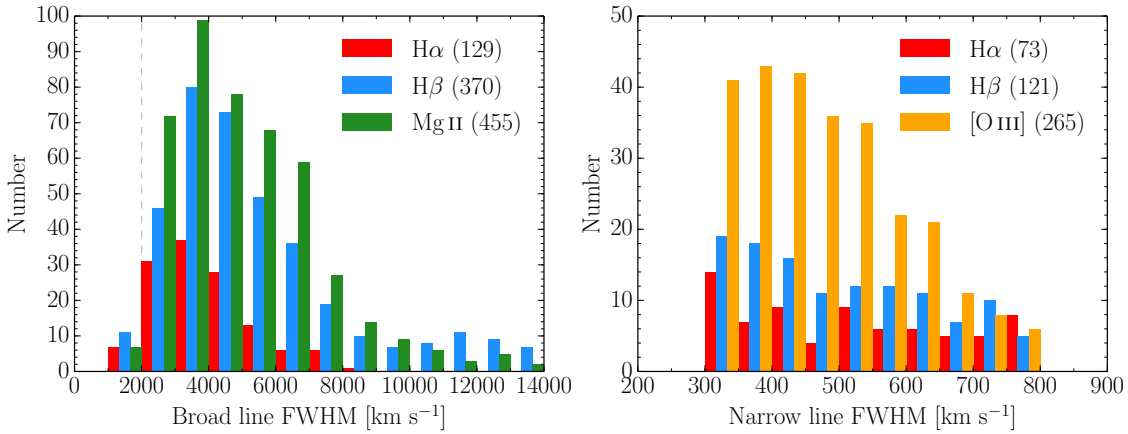

Figure C.4: Distributions of broad and narrow emission line FWHMs determined by QSFit. Only values for lines with a reliable measurement are shown. The total number of reliable measurements is indicated by the legend.

permitted value of 900 km s^{-1}, raising a quality flag.

The spectra of around 60 per cent of sources contain more than one of the Hα, Hβ or Mg II broad emission lines. For these sources, the FWHMs of the lines determined by QSFit can be compared. Scatter plots of the FWHMs and histograms of the FWHM ratios are shown in Figure C.5. It can be seen that the FWHMs of Hα and Hβ are generally in good agreement. The median of the FWHM(Hα)/FWHM(Hβ) ratio is 0.92, suggesting that Hβ is generally slightly broader than Hα. The distribution of FWHM(Hβ)/FWHM(Mg II) also indicates that Hβ is generally broader than Mg II. The FWHM of Mg II is also correlated with that of Hβ, but with greater scatter. Qualitatively, these results are similar to those of Mejía-Restrepo et al. (2016), who

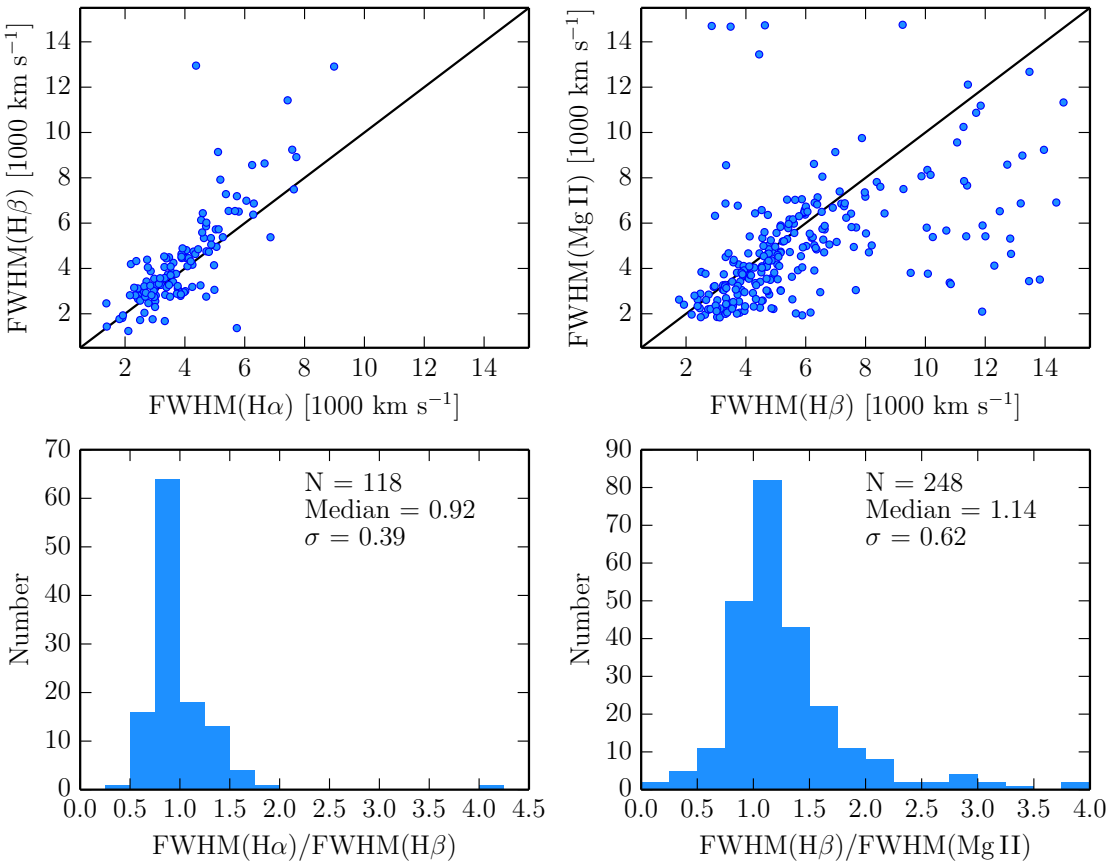

Figure C.5: A comparison of broad emission line FWHMs determined by QSFit. Upper panels show the scatter, lower panels show the distribution of FWHM ratios.

also found a strong correlation between the FWHMs of Hα and Hβ, and a more scattered correlation between the FWHMs of Hβ and Mg II. Additionally, they found that Mg II was $\sim$ 30 per cent narrower than Hβ and that Hα was $\sim$ 7 per cent narrower. Both Greene & Ho (2005) and Osterbrock & Shuder (1982) have previously found Hβ to be, on average, broader than Hα in samples of AGN.

C.3.0.1 Types of AGN within the sample

My selection criteria (requiring a reasonable median optical spectral S/N, X-ray detection with greater than 250 counts in a detector, and simultaneous optical/UV photometry) will bias my sample against low-luminosity and Type 2 AGN. Nonetheless, a few of these types of source will be present, particularly at low redshifts. Initially, I attempted to search for Type 2, Type 1.9 and NLS1 AGN by inspecting

the sources with FWHM(Hβ) $<$ 2000 km s^{-1}. It can be seen from Figure C.4 that there are very few of these within the sample. Expanding the search to include all sources with FWHM(Hβ) $<$ 2000 km s^{-1} *within error*, I find 27 sources. Visually inspecting these sources, I found one Type 2 AGN (SDSS J085612.23+375819.0), a Type 1.9 (SDSS J105421+572544.2)[2] and a LINER (SDSS J131202.25−010955.2). Two other sources with broad Hα, very weak AGN continuum and very low-contrast broad Hβ also appear to be Type 1.9s, but QSFit fits a broad Hβ line without flagging any problems. Among these 27 sources, I find four 'genuine' NLS1s which QSFit determines have FWHM(Hβ) $<$ 2000 km s^{-1} and which have a ratio [O III]λ5007/Hβ $<$ 3 and strong Fe II emission; these are shown in Figure C.7. Five other NLS1 candidates are also identified, which meet the second two criteria but have FWHM(Hβ) $>$ 2000 km s^{-1} (although consistent with 2000 km s^{-1} within error). I visually inspected the spectra of the low-redshift portion of the sample (with both Hα and Hβ observed) and selected several sources which appeared to be NLS1s, but which were not identified as such from the QSFit results. Indeed, the results indicated that the FWHMs of both Hα and Hβ were greater than 2000 km s^{-1}, even considering the errors. However, a few of these had a quality flag on the narrow Hβ component, indicating it was at (or close to) the maximum allowed value. If the narrow Hβ component is wide then it will take up a greater proportion of the core of the line profile, making the broad Hβ component lower in amplitude and wider.

The apparent lack of NLS1s within the sample is striking. The frequency of NLS1s in predominantly optically-selected AGN samples is $\sim$ 15 per cent (Komossa 2008, Rakshit et al. 2017) and perhaps as high as 20 per cent (Zhou et al. 2006). 12 of the 51 Type 1 AGN studied by Jin et al. (2012a) were NLS1s. For a sample of this size, I would therefore expect to find around 90 NLS1s. Based on the QSFit results, I can confidently identify 4 (1 per cent of those in which broad Hβ is well-measured). The reason for this is likely to be the approach taken by the QSFit

[2]This source has a FWHM(Hβ) $= 9318 \pm 7527$ km s^{-1}, so it was selected as a narrow-line source within error. Although the contrast of Hβ against the continuum is very poor (hence the large, poorly-determined FWHM) Hα is well-measured with FWHM(Hα) $= 2446 \pm 265$ km s^{-1}.

algorithm to performing the emission line profile decomposition. Calderone et al. (2017) compared their fit results to those of Shen et al. (2011), and found that while many of the determined quantities were in very good agreement, one of the main differences was in the emission line widths. Their comparison for broad Hβ is shown in Figure C.8; looking at this figure it is perhaps unsurprising that I find very few NLS1s. The decomposition of broad- and narrow-line profiles can be a subtle art and Calderone et al. (2017) argue that (given that the physical processes resulting in the broad emission lines and broadband continuum are not yet fully understood) no one method may be preferred over another. Encouragingly, when QSFit was applied to the Shen et al. (2011) sample they were able to reproduce several well-known empirical relations including the Baldwin effect for C IV and the main Eigenvector 1 correlations. So, in spite of the differences in the absolute parameter values determined by different software, the relationships between key parameters still hold. (See also Section C.6.)

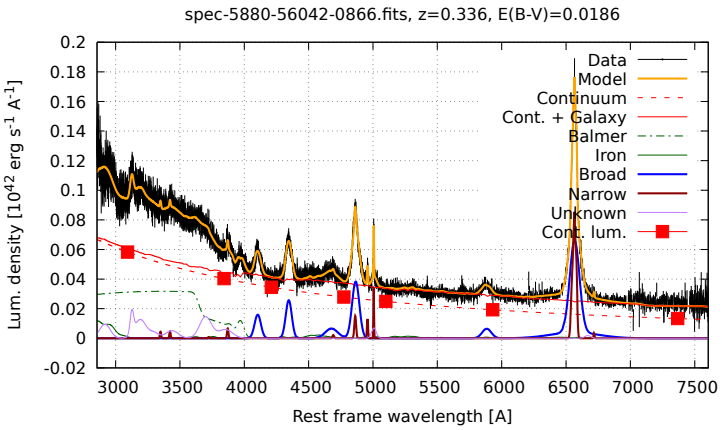

SDSS J021020.43−034226.1: A Seyfert 1

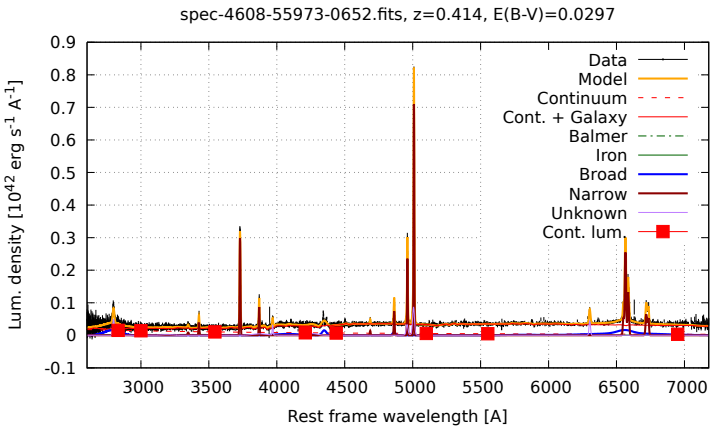

SDSS J085612.23+375819.0: A Seyfert 2

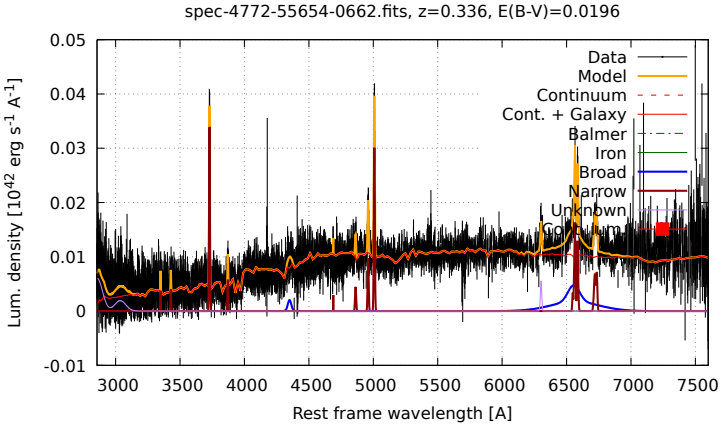

SDSS J103016.32+053421.0: A Seyfert 1.9

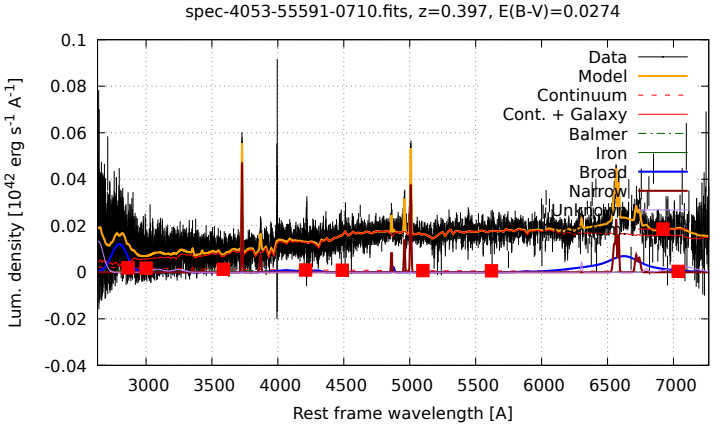

SDSS J131202.25−010955.2: A LINER

Figure C.6: Examples of AGN types within the sample.

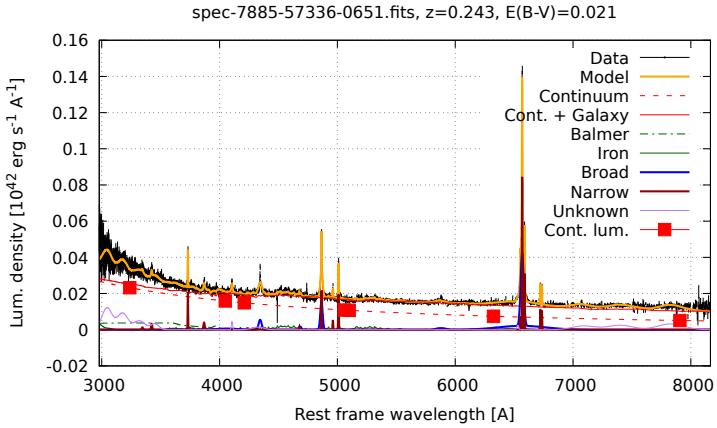

SDSS J021020.43−034226.1: FWHM(Hβ) = 1440 ± 40

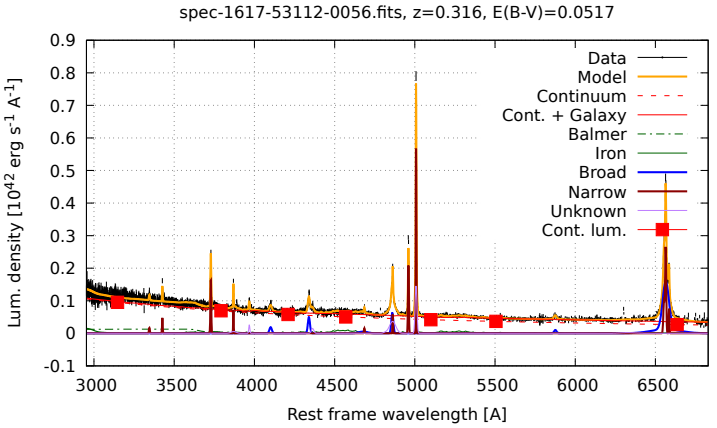

SDSS J112014.85+063341.1: FWHM(Hβ) = 1241 ± 140

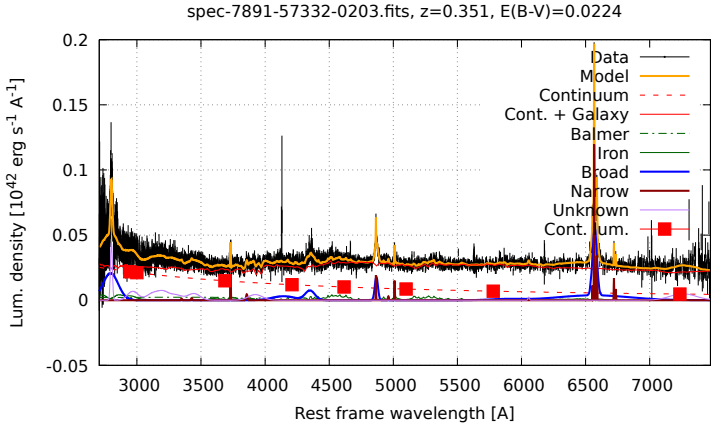

SDSS J020235.88−050625.3: FWHM(Hβ) = 1767 ± 85

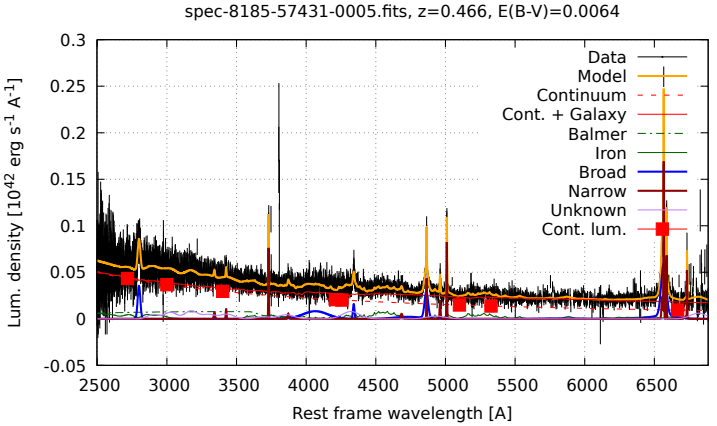

SDSS J105248.04+572116.7: FWHM(Hβ) = 1930 ± 1300

Figure C.7: Genuine NLS1s in the sample.

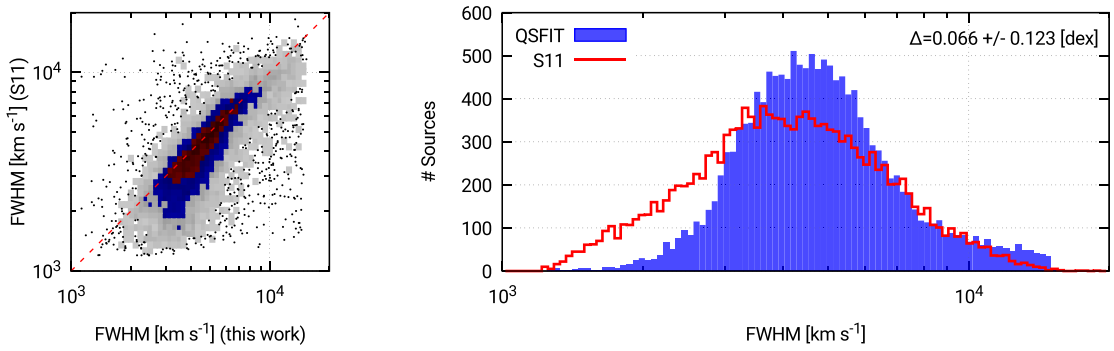

Figure C.8: Distributions of broad line FWHM(Hβ) determined by QSFit and Shen et al. (2011) (S11). A discrepancy is apparent at lower values, with the S11 fitting procedure finding many more narrow-line sources than QSFit. From Calderone et al. (2017).

C.4 Determinations of SMBH masses

C.4.1 Some problematic spectra

For some sources, although the emission line is covered in the spectrum, no (useful) measurement of the Hα, Hβ or Mg II broad emission lines was made. Or, in some cases a useful broad emission line has been measured, but no measurement of the nearby AGN continuum was made. For example, the source SDSS J103016.32+053421.0 appears to be a Seyfert 1.9 (see Figure C.6): it has broad Hα but not Hβ and the continuum emission is dominated by starlight rather than the AGN accretion disc.

26 (8) sources have a Hβ (Mg II) FWHM which has hit the upper limit of the permitted range (15000 km s^{-1}). The broad Hα FWHM is well-constrained in all spectra in which it is measured. Additionally, 41 sources have a reliable measurement of the FWHM of either Hα or Hβ, but do not have a robust measurement of the AGN continuum luminosity at $L_{5100\text{Å}}$. One such case is SDSS J103016.32+053421.0, mentioned above. All of these 41 sources have a quality flag of 1 or 2 on the luminosity measurement, indicating that the value or its uncertainty are zero or NaN, or that the fractional uncertainty on $L_{5100\text{Å}}$ exceeds 1.5, respectively. Similarly, 14 sources

have a measurement of the FWHM of Mg II but do not have a robust measurement of $L_{3000\text{Å}}$. Many of these are at the very end of my redshift range, such that the rest frame 3000 Å is at the very end of the observed spectrum and suffers from poor quality.

Following a more thorough examination of these sources, it may be possible to determine their SMBH masses by (e.g.) making a crude estimate of the continuum luminosity, or using virial relations which rely on the emission line luminosity (rather than the continuum luminosity), or refining the fitting routine. For now, I proceed only with those sources which have good measurements of an emission line FWHM and corresponding continuum luminosity.

C.4.2 SMBH masses for 573 AGN

A mass estimate is possible for 573 of the 598 AGN (96 per cent). These 573 have good measurements of an emission line FWHM and nearby AGN continuum luminosity. To determine SMBH masses from the FWHMs of Hα and Mg II (with $L_{5100\text{Å}}$ and $L_{3000\text{Å}}$, respectively) I use the relations of Mejía-Restrepo et al. (2016). I determine the SMBH mass from FWHM(Hβ) and $L_{5100\text{Å}}$ using the relation of Bentz et al. (2013). 118 sources have a good mass estimate from *both* Hα and Hβ; mass estimates for these sources are shown in Figure C.9. The correlation between the two estimates is good, with little scatter. For 207 sources it is possible to make a mass estimate using both Hβ and Mg II. In Figure C.9 it can be seen that there is a much greater scatter that was the case comparing estimates based on Hα and Hβ. In 42 of the 207 sources (20 per cent) with a mass measured from Hβ and Mg II, the two mass estimates are discrepant by more than 0.25 dex, the reported 1σ scatter in the relation. In many cases, this is due to the poor quality of the spectrum; fits to some of the spectra giving the most discrepant estimates ($|\log(M_{\text{BH}}^{\text{H}\beta}) - \log(M_{\text{BH}}^{\text{Mg II}})| > 1$ dex) are shown in Figure C.10.

In the lower panels of Figure C.9 I show comparisons of mass estimates made using

either the continuum or line luminosities. For the mass estimate using the Hβ luminosity, I take the relation of Greene et al. (2010b) and for the Hα luminosity, I take the relation of Mejía-Restrepo et al. (2016). As in Figure 2.1, I find that masses estimated from the line luminosities are systematically lower than those using the continuum luminosity. The discrepancies are similar to those seen in Figure 2.1, with a median difference of ≈ 0.13 dex for Hβ and ≈ 0.20 dex for Hα. Whether these differences are simply a result of imperfect calibrations between the relations, or result from underlying physics, can be explored in future work.

C.5 Source luminosities

QSFit calculates the monochromatic luminosities at 5100 and 3000 Å in the source rest-frame, accounting for Galactic reddening using provided colour excess values and converting flux to luminosity by obtaining the source redshift from the SDSS spectrum fits file header. For low-redshift sources, subtraction of a fitted host galaxy template is performed where appropriate so that the quoted luminosities at 5100 and 3000 Å are uncontaminated. The distributions of $L_{5100\text{Å}}$ and $L_{3000\text{Å}}$ are shown in Figure C.11. I have included only sources with a good measurement of the luminosity (i.e. the bitmask does not contain a flag indicating that the wavelength is out of the spectral range, or a measurement uncertainty which is zero, NaN or a relative uncertainty greater than 1.5).

The 3XMM-DR7 catalogue provides X-ray fluxes in several energy bands, which can trivially be converted to luminosities using the redshift determined from the spectrum of the optical counterpart. However, the fluxes are calculated from the recorded counts, and do not account for X-ray absorption in the ISM. Luminosities calculated from the catalogue fluxes will therefore be somewhat than the intrinsic source luminosities, depending on the Galactic neutral hydrogen column density along the line of sight, and the spectral shape of the source. Without modelling the X-ray spectrum of each source to determine its shape, a proper correction for X-ray

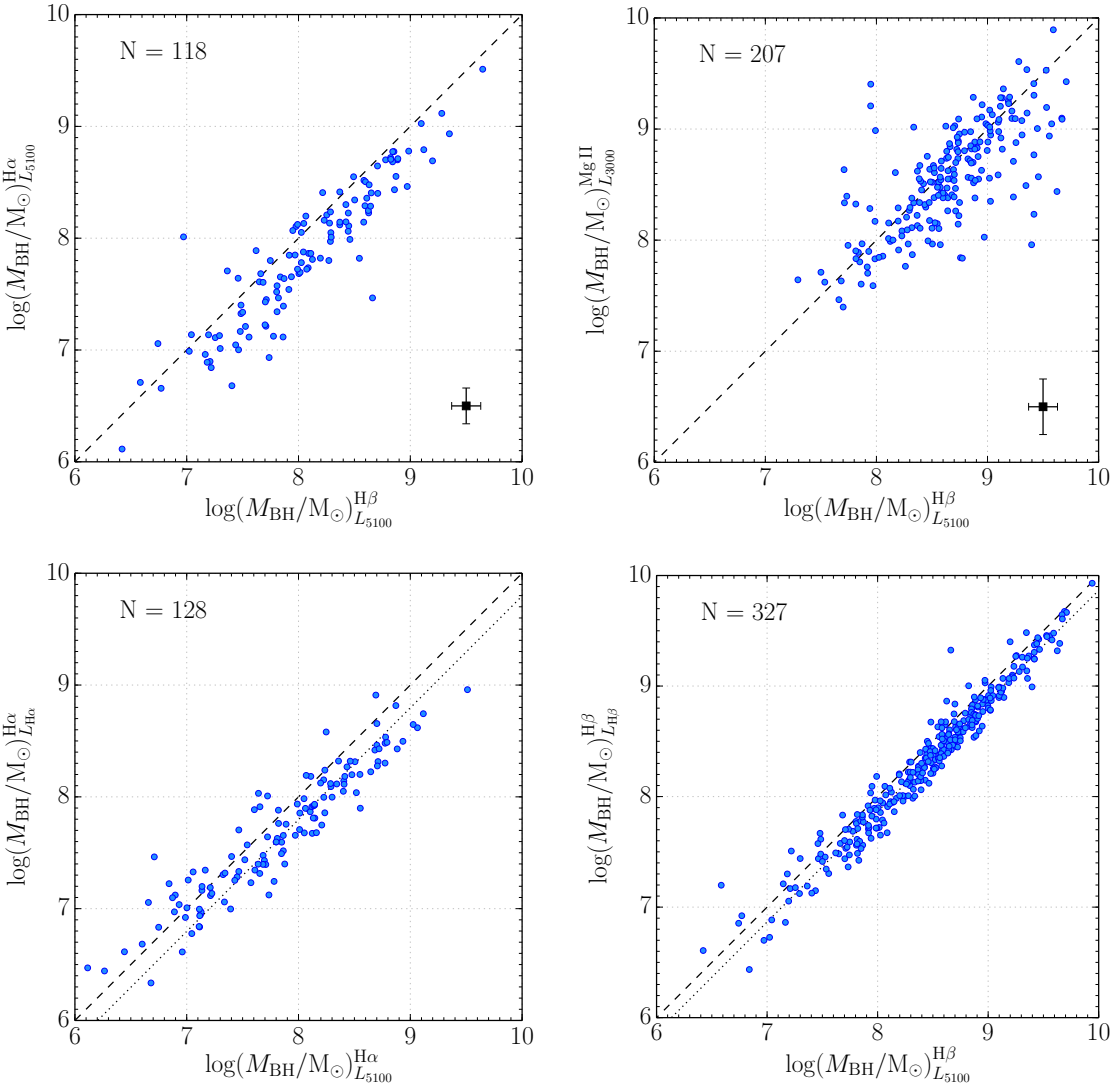

Figure C.9: *Upper panels – Left*: For 118 sources with reliable measurements of the FWHM of broad Hα and Hβ and $L_{5100\text{Å}}$. *Right*: For 207 sources with reliable measurements of the FWHM of broad Hβ and Mg II and $L_{5100\text{Å}}$ and $L_{3000\text{Å}}$. The error-bar in the bottom right corner indicates the magnitude of the reported 1σ scatter in the relations. *Lower panels – Left*: A comparison of mass estimates using FWHM(Hβ) and either $L_{5100\text{Å}}$ or $L_{\text{H}\beta}$. *Right*: A comparison of mass estimates using FWHM(Hα) and either $L_{5100\text{Å}}$ or $L_{\text{H}\alpha}$. Masses estimated from the line luminosities are systematically lower than those using the continuum luminosity $L_{5100\text{Å}}$. The one-to-one relation is shown as a dashed line and the median ratio as a dotted line.

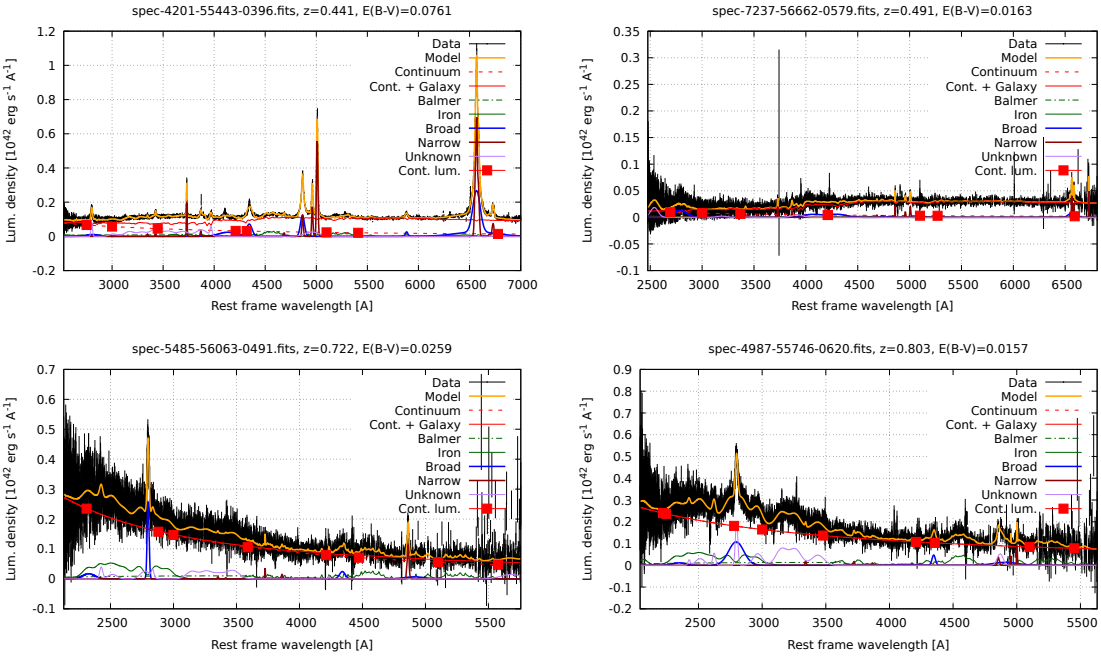

Figure C.10: Examples of fits to spectra in which the SMBH mass determined from FWHM(Hβ) and $L_{5100\text{Å}}$ is discrepant with that determined from FWHM(Mg II) and $L_{3000\text{Å}}$ by more than a factor of 10.

absorption cannot be made. This being said, absorption will have a modest effect for typical values of Galactic $N_{\rm H}$ outside of the Galactic plane. The luminosities shown in Figure C.11 therefore act as a rough guide to the real X-ray luminosity distribution of the sample.

Collinson et al. (2015) cautioned against the use of single-parameter proxies in determining the bolometric luminosities of AGN. However, these provide an efficient method to estimate the distribution of luminosities (and Eddington fractions) for large AGN samples. I use the bolometric correction factors of McLure & Dunlop (2004):

$$L_{\rm bol} = 9.8 \times L_{5100\text{Å}}, \text{ and} \tag{C.5.1}$$

$$L_{\rm bol} = 5.9 \times L_{3000\text{Å}}. \tag{C.5.2}$$

More robust estimates of the bolometric luminosities will be made after performing multiwavelength SED modelling of the sources in the sample. These can then be compared to $L_{5100\text{Å}}$ and $L_{3000\text{Å}}$ (and $L_{2-10keV}$) as was done by Collinson et al. (2015).

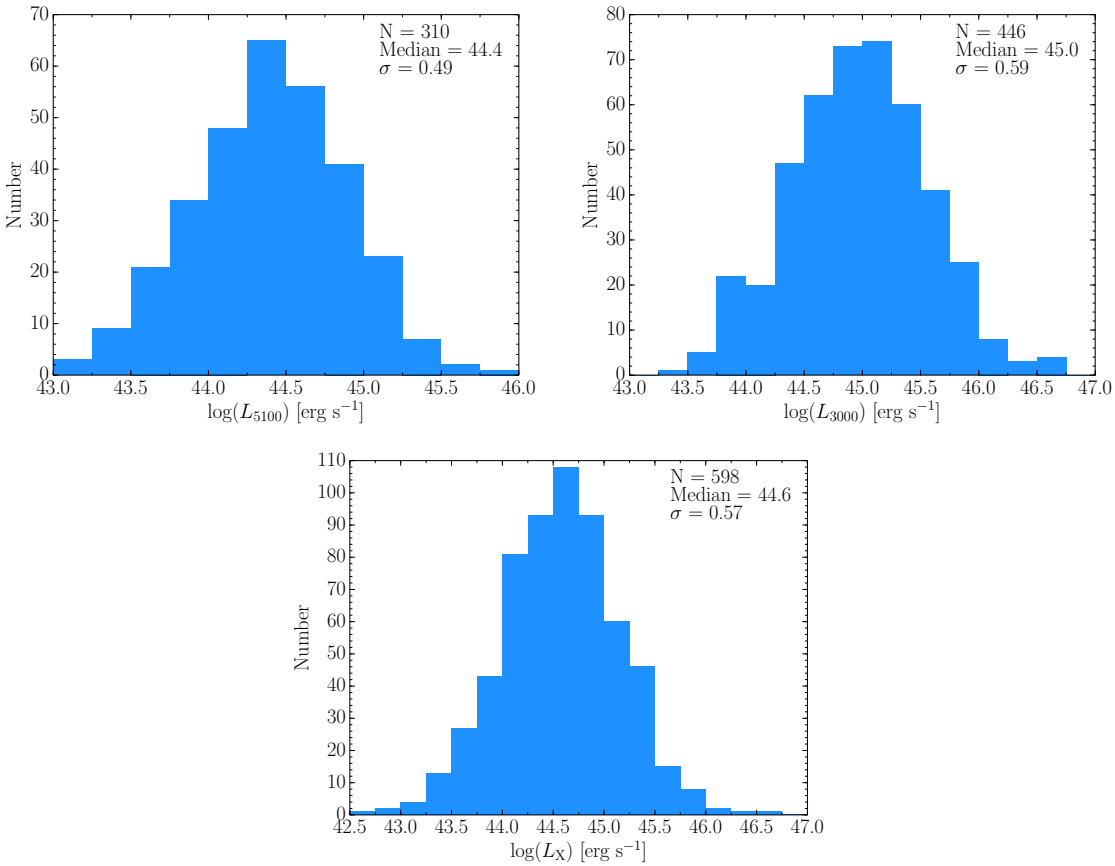

Figure C.11: Optical, ultraviolet and X-ray luminosities of the sample. The distributions for sources with good measurements of $L_{5100\text{Å}}$ and $L_{3000\text{Å}}$ are shown above. The text inset indicates the total number (N) of measurements, and the median and standard deviation of the distributions. All 598 sources have an X-ray flux measurement, by selection. Here I show the distribution of the EPIC band 8 (0.2–12.0 keV) luminosities.

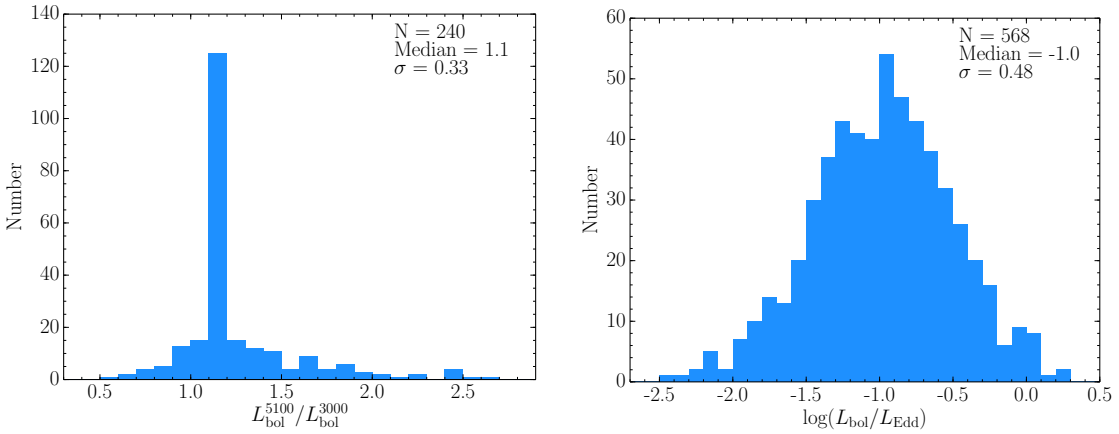

Figure C.12: *Left:* For sources which have both a well-determined $L_{5100\text{Å}}$ and $L_{3000\text{Å}}$, the ratio of bolometric luminosities determined from each is shown. *Right:* For all sources with either a well-determined $L_{5100\text{Å}}$ and $L_{3000\text{Å}}$ and an estimate of $M_{\rm BH}$, the distribution of Eddington ratios is shown.

However, this task is beyond the scope of this current work.

The sample was matched to the FIRST radio source database, using a 10 arcsecond matching radius. 92 sources have a match in FIRST and their rest-frame 1.4 GHz radio luminosities were calculated using the method of Alexander et al. (2003) and assuming a radio spectral index of $\alpha = 0.5$. The distribution of radio luminosities is shown in Figure fig:bs-radio. The flux ratios obtained from FIRST were compared to those from NVSS. Generally there is very good agreement between the two surveys, but several sources are reported as being brighter in NVSS than in FIRST. This may be because the radio emission in these sources is extended (see Section 3.1.2). 75 of these are of sufficiently low redshift that the optical luminosities at 4400 Å could be determined from the optical spectra. For these sources, their radio loudness was computed and the distribution is shown in Figure C.13. 10 of these sources were radio quiet ($R < 10$) and the remainder were radio-loud. Therefore, the fraction of radio-loud sources within the sample is ≈ 10 per cent, which is typical of the broad AGN population.

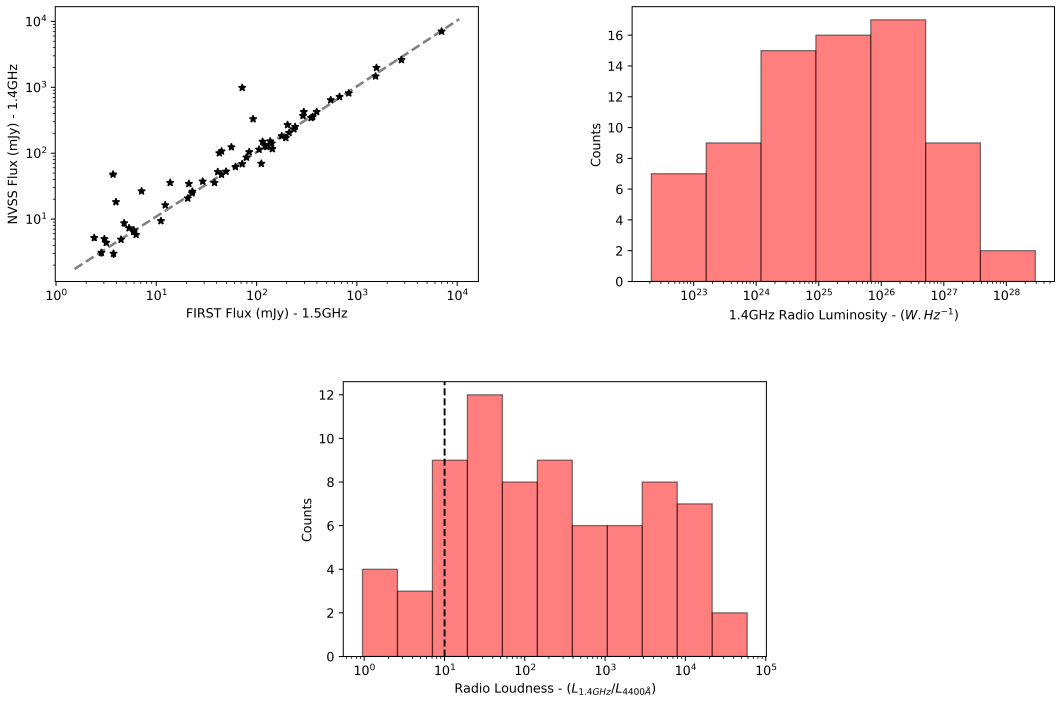

Figure C.13: *Top left:* For the subset of sources with NVSS and FIRST 21 cm radio flux densities, a comparison of the vales from the two surveys is shown. *Top right:* The radio luminosity distribution, calculated from the rest-frame 21 cm FIRST flux densities. *Bottom:* The radio loudness distribution for 75 sources which have both a FIRST radio detection and rest-frame optical 4400 Å luminosity determination. The vertical dashed line indicates the division between radio-quiet and radio-loud sources.

C.6 The quasar main sequence

For a subset of the sample, it is possible to use the optical spectral fitting results to investigate one of the main Eigenvector 1 relations: the anticorellation between broad FWHM(Hβ) and the strength of Fe II emission. 216 of the sources in my sample have a good measurements of both the broad Hβ line and the EW of optical Fe II emission. For these, I calculate $R_{\rm Fe\,II}$ as the ratio of the sum of broad and narrow optical Fe II EWs to the EW of broad Hβ. I note that Boroson & Green (1992) measured the EW of optical Fe II emission in the range 4434-4684 Å whereas QSFIT measures the EW of the whole optical Fe II complex from $\approx$ 3500–7000 Å. The $R_{\rm Fe\,II}$ values I compute from my fit results will therefore be greater than those found by Boroson & Green (1992), nonetheless a qualitative comparison can be made. 215 of these sources also have an Eddington fraction determined from their bolometric luminosity and mass. The points in Figure C.14 have been coloured in sequence by their Eddington ratio from red (low) to blue (high). The best-fit slope is calculated by the Theil-Sen method (Theil 1992) which computes the median of all slopes between points and is therefore less sensitive to outliers. An anti-correlation between FWHM(Hβ) and $R_{\rm Fe\,II}$ is found, with the best-fitting linear relation having a slope ≈ -0.3. Tentatively, it appears that there is a sequence of Eddington ratios along this relation, with the high $L/L_{\rm Edd}$ sources (blue points) concentrated towards lower FWHM(Hβ) and higher $R_{\rm Fe\,II}$; conversely, the lower high $L/L_{\rm Edd}$ sources (red points) extend to lower values of $R_{\rm Fe\,II}$ and have generally higher FWHM(Hβ). Such a trend would be expected if $L/L_{\rm Edd}$ is a main driver of Eigenvector 1.

C.7 Summary

I have assembled a sample of 598 SDSS quasars with an *XMM-Newton* X-ray and optical/UV photometric detection. I have ensured reasonable data quality by selecting only those sources with a median S/N greater than 3 in their optical spectrum, 250

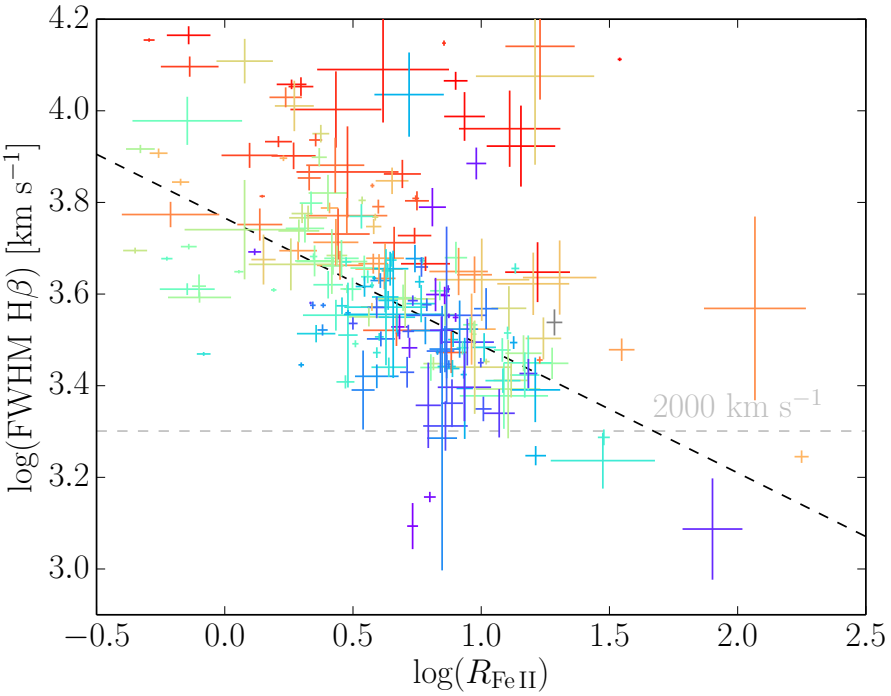

Figure C.14: FWHM(Hβ) versus $R_{\rm Fe\,II}$ for the 216 sources in the sample which have good measurements of both. Points are coloured in sequence by their Eddington ratio from red (low) to blue (high). One source does not have a determined Eddington ratio and is shown in grey.

X-ray counts (or greater) recorded in a single observation by an EPIC detector and at least one photometric point which is unaffected by Lyα emission or absorption.

The analysis presented in this appendix has focussed on the optical spectral properties. The only criterion I use to select the SDSS quasars (other than redshift) is a moderate S/N cut. The selected sources include a small number of Type 2 / 1.9 AGN. Very few NLS1s are found, which is likely to be because of the approach to the line profile decomposition of the algorithm used in QSFit.

A preliminary analysis indicates that the sample covers a range of optical emission line widths, optical and X-ray luminosities, SMBH masses and Eddington fractions. I will therefore be able to split the sample into bins of these and other parameters to make comparisons between their multiwavelength properties. A comparison of optical emission line properties suggests that results from previous studies can be reproduced with this sample, including the relative widths of the lines and one of

the main Eigenvector 1 relations. Future work will involve the analysis of the X-ray spectra and multiwavelength SEDs of this sample, leading to a refinement of the measures presented in this appendix. The sample itself may be refined, with future work focussing on the subset of unobscured Type 1 AGN.

Bibliography

Abazajian K. N., et al., 2009, ApJS, 182, 543

Abbott B. P., et al., 2016, Physical Review Letters, 116, 061102

Abdo A. A., et al., 2009a, ApJ, 699, 976

Abdo A. A., et al., 2009b, APJ, 707, L142

Abdollahi S., et al., 2017, ApJ, 846, 34

Acero F., et al., 2015, ApJS, 218, 23

Acero F., et al., 2016, ApJS, 223, 26

Ahn C. P., et al., 2012, ApJS, 203, 21

Alexander D. M., et al., 2003, AJ, 125, 383

Almeyda T., Robinson A., Richmond M., Vazquez B., Nikutta R., 2017, ApJ, 843, 3

Angelakis E., et al., 2015, A&A, 575, A55

Angelakis E., et al., 2019, preprint, (arXiv:1902.04404)

Antonucci R., 1993, ARA&A, 31, 473

Antonucci R. R. J., Miller J. S., 1985, ApJ, 297, 621

Arnaud K. A., 1996, in Jacoby G. H., Barnes J., eds, Astronomical Society of the Pacific Conference Series Vol. 101, Astronomical Data Analysis Software and Systems V. p. 17

Atwood W. B., et al., 2009, ApJ, 697, 1071

Baldi R. D., Capetti A., Robinson A., Laor A., Behar E., 2016, MNRAS, 458, L69

Baldwin J. A., Ferland G. J., Korista K. T., Hamann F., LaCluyzé A., 2004, ApJ, 615, 610

Barcons X., Nandra K., Barret D., den Herder J.-W., Fabian A. C., Piro L., Watson

M. G., the Athena Team 2015, in Journal of Physics Conference Series. p. 012008, doi:10.1088/1742-6596/610/1/012008

Bardeen J. M., Press W. H., Teukolsky S. A., 1972, ApJ, 178, 347

Baron D., Stern J., Poznanski D., Netzer H., 2016, ApJ, 832, 8

Barthelmy S. D., et al., 2005, Space Sci. Rev., 120, 143

Barvainis R., 1992, ApJ, 400, 502

Baumgartner W. H., Tueller J., Markwardt C. B., Skinner G. K., Barthelmy S., Mushotzky R. F., Evans P. A., Gehrels N., 2013, ApJS, 207, 19

Becker R. H., White R. L., Helfand D. J., 1995, ApJ, 450, 559

Beckmann V., Shrader C., 2012, in Proceedings of "An INTEGRAL view of the high-energy sky (the first 10 years)" - 9th INTEGRAL Workshop and celebration of the 10th anniversary of the launch (INTEGRAL 2012). 15-19 October 2012. Bibliotheque Nationale de France, Paris, France. Published online at http://pos.sissa.it/cgi-bin/reader/conf.cgi?confid=176, id 69. (arXiv:1302.1397)

Bellm E. C., et al., 2019, PASP, 131, 018002

Ben Bekhti N., Richter P., Winkel B., Kenn F., Westmeier T., 2009, A&A, 503, 483

Bentz M. C., Peterson B. M., Netzer H., Pogge R. W., Vestergaard M., 2009, ApJ, 697, 160

Bentz M. C., et al., 2013, ApJ, 767, 149

Bianchi S., Guainazzi M., Matt G., Fonseca Bonilla N., 2007, A&A, 467, L19

Biretta J. A., Sparks W. B., Macchetto F., 1999, ApJ, 520, 621

Blandford R. D., McKee C. F., 1982, ApJ, 255, 419

Blandford R. D., Payne D. G., 1982, MNRAS, 199, 883

Blandford R. D., Rees M. J., 1974, MNRAS, 169, 395

Blandford R. D., Znajek R. L., 1977, MNRAS, 179, 433

Blandford R., Meier D., Readhead A., 2018, preprint, (arXiv:1812.06025)

Bohlin R. C., Savage B. D., Drake J. F., 1978, ApJ, 224, 132

Boller T., Brandt W. N., Fink H., 1996, A&A, 305, 53

Boller T., Brandt W. N., Fabian A. C., Fink H. H., 1997, MNRAS, 289, 393

Bolton C. T., 1972, Nature, 235, 271

Bondi H., Hoyle F., 1944, MNRAS, 104, 273

Boroson T. A., Green R. F., 1992, ApJS, 80, 109

Bowyer S., Byram E. T., Chubb T. A., Friedman H., 1965, Science, 147, 394

Brenneman L. W., Reynolds C. S., 2006, ApJ, 652, 1028

Bridle A. H., Hough D. H., Lonsdale C. J., Burns J. O., Laing R. A., 1994, AJ, 108, 766

Briel U. G., Pfeffermann E., 1986, Nuclear Instruments and Methods in Physics Research A, 242, 376

Bruce A., et al., 2017, MNRAS, 467, 1259

Bruhweiler F., Verner E., 2008, ApJ, 675, 83

Burrows D. N., et al., 2000, in Flanagan K. A., Siegmund O. H., eds, Proc. SPIEVol. 4140, X-Ray and Gamma-Ray Instrumentation for Astronomy XI. pp 64–75, doi:10.1117/12.409158

Burtscher L., et al., 2013, A&A, 558, A149

CTA Consortium Ong R. A., 2019, preprint, (arXiv:1904.12196)

Calderone G., Ghisellini G., Colpi M., Dotti M., 2012, MNRAS, 424, 3081

Calderone G., Ghisellini G., Colpi M., Dotti M., 2013, MNRAS, 431, 210

Calderone G., Nicastro L., Ghisellini G., Dotti M., Sbarrato T., Shankar F., Colpi M., 2017, MNRAS, 472, 4051

Calderone G., D'Ammando F., Sbarrato T., 2018, in Revisiting Narrow-Line Seyfert 1 Galaxies and their Place in the Universe. Online at https://pos.sissa.it/cgi-bin/reader/conf.cgi?confid=328. p. 44

Cannon R. D., 1975, Proceedings of the Astronomical Society of Australia, 2, 323

Capellupo D. M., Netzer H., Lira P., Trakhtenbrot B., Mejía-Restrepo J., 2015, MNRAS, 446, 3427

Cardelli J. A., Clayton G. C., Mathis J. S., 1989, ApJ, 345, 245

Carilli C. L., Perley R. A., Dhawan V., Perley D. A., 2019, APJ, 874, L32

Carpenter J. M., et al., 2008, ApJS, 179, 423

Celotti A., Padovani P., Ghisellini G., 1997, MNRAS, 286, 415

Chambers K. C., et al., 2016, preprint, (arXiv:1612.05560)

Chang K., Refsdal S., 1979, Nature, 282, 561

Clark G. W., 1965, Physical Review Letters, 14, 91

Cohen R. D., 1983, ApJ, 273, 489

Collin S., Joly M., 2000, New Astron. Rev., 44, 531

Collin S., Kawaguchi T., Peterson B. M., Vestergaard M., 2006, A&A, 456, 75

Collinson J. S., Ward M. J., Done C., Landt H., Elvis M., McDowell J. C., 2015, MNRAS, 449, 2174

Collinson J. S., Ward M. J., Landt H., Done C., Elvis M., McDowell J. C., 2017, MNRAS, 465, 358

Collinson J. S., et al., 2018, MNRAS, 474, 3565

Condon J. J., Cotton W. D., Greisen E. W., Yin Q. F., Perley R. A., Taylor G. B., Broderick J. J., 1998, AJ, 115, 1693

Croton D. J., et al., 2006, MNRAS, 365, 11

Crummy J., Fabian A. C., Gallo L., Ross R. R., 2006, MNRAS, 365, 1067

Curtis H. D., 1918, Publications of Lick Observatory, 13, 31

Cushing M. C., Vacca W. D., Rayner J. T., 2004, PASP, 116, 362

Czerny B., Zycki P. T., 1994, APJ, 431, L5

Czerny B., Panda S., Śniegowska M., Kozlowski S., Nikolajuk M., Du P., You B., 2018, in Revisiting narrow-line Seyfert 1 galaxies and their place in the Universe. 9-13 April 2018. Padova Botanical Garden, Italy. p. 30 (arXiv:1806.06741)

D'Ammando F., Orienti M., Larsson J., Giroletti M., 2015, MNRAS, 452, 520

D'Ammando F., Orienti M., Finke J., Larsson J., Giroletti M., Raiteri C., 2016, Galaxies, 4, 11

D'Ammando F., Acosta-Pulido J. A., Capetti A., Raiteri C. M., Baldi R. D., Orienti M., Ramos Almeida C., 2017, MNRAS, 469, L11

D'Ammando F., Acosta-Pulido J. A., Capetti A., Baldi R. D., Orienti M., Raiteri C. M., Ramos Almeida C., 2018, MNRAS, 478, L66

Davidson K., Kinman T. D., 1978, ApJ, 225, 776

Davis S. W., Laor A., 2011, ApJ, 728, 98

Dermer C. D., Cerruti M., Lott B., Boisson C., Zech A., 2014, ApJ, 782, 82

Dexter J., Begelman M. C., 2019, MNRAS, 483, L17

Diamond-Stanic A. M., Rieke G. H., Rigby J. R., 2009, ApJ, 698, 623

Dickey J. M., Lockman F. J., 1990, ARA&A, 28, 215

Donato D., Perkins J. S., 2011, The Astronomer's Telegram, 3452

Done C., Davis S. W., Jin C., Blaes O., Ward M., 2012, MNRAS, 420, 1848

Done C., Jin C., Middleton M., Ward M., 2013, MNRAS, 434, 1955

Draine B., 1989, in Allamandola L. J., Tielens A. G. G. M., eds, IAU Symposium Vol. 135, Interstellar Dust. p. 313

Drake A. J., et al., 2009, ApJ, 696, 870

Edelson R., et al., 2017, ApJ, 840, 41

Edelson R., et al., 2019, ApJ, 870, 123

Edge D. O., Shakeshaft J. R., McAdam W. B., Baldwin J. E., Archer S., 1959, Mem. RAS, 68, 37

Einstein A., 1915a, Sitzungsberichte der Königlich Preußischen Akademie der Wissenschaften (Berlin), pp 778–786

Einstein A., 1915b, Sitzungsberichte der Königlich Preußischen Akademie der Wissenschaften (Berlin), pp 844–847

Elias J. H., Rodgers B., Joyce R. R., Lazo M., Doppmann G., Winge C., Rodríguez-Ardila A., 2006, in Society of Photo-Optical Instrumentation Engineers (SPIE) Conference Series. p. 626914, doi:10.1117/12.671765

Elitzur M., Ho L. C., 2009, APJ, 701, L91

Elvis M., et al., 2012, ApJ, 759, 6

Enard D., 1989, Ap&SS, 160, 45

Event Horizon Telescope Collaboration et al., 2019, APJ, 875, L1

Falomo R., Kotilainen J. K., Carangelo N., Treves A., 2003, ApJ, 595, 624

Fanaroff B. L., Riley J. M., 1974, MNRAS, 167, 31P

Fausnaugh M. M., 2017, PASP, 129, 024007

Ferrarese L., Merritt D., 2000, APJ, 539, L9

Flewelling H. A., et al., 2016, arXiv e-prints,

Foschini L., 2011, in Narrow-Line Seyfert 1 Galaxies and their Place in the Universe. p. 24 (arXiv:1105.0772)

Foschini L., 2014, in International Journal of Modern Physics Conference Series. p. 1460188 (arXiv:1310.5822), doi:10.1142/S2010194514601884

Foschini L., 2017, Frontiers in Astronomy and Space Sciences, 4, 6

Foschini L., Maraschi L., Tavecchio F., Ghisellini G., Gliozzi M., Sambruna R. M., 2009, Advances in Space Research, 43, 889

Foschini L., et al., 2015, A&A, 575, A13

Fossati G., Maraschi L., Celotti A., Comastri A., Ghisellini G., 1998, MNRAS, 299, 433

Francis P. J., Hewett P. C., Foltz C. B., Chaffee F. H., Weymann R. J., Morris S. L., 1991, ApJ, 373, 465

Fuhrmann L., et al., 2016a, Research in Astronomy and Astrophysics, 16, 176

Fuhrmann L., et al., 2016b, A&A, 596, A45

Gallo L. C., Boller T., Brandt W. N., Fabian A. C., Vaughan S., 2004, A&A, 417, 29

Gardner E., Done C., 2014, MNRAS, 438, 779

Gardner E., Done C., 2018, MNRAS, 473, 2639

Gaskell C. M., 2017, MNRAS, 467, 226

Gaskell C. M., Shields G. A., Wampler E. J., 1981, ApJ, 249, 443

Gebhardt K., et al., 2000, APJ, 539, L13

Gehrels N., et al., 2004, ApJ, 611, 1005

Gezari S., et al., 2017, ApJ, 835, 144

Ghez A. M., et al., 2008, ApJ, 689, 1044

Ghisellini G., Tavecchio F., 2009, MNRAS, 397, 985

Ghisellini G., Tavecchio F., 2015, MNRAS, 448, 1060

Ghisellini G., Tavecchio F., Chiaberge M., 2005, A&A, 432, 401

Ghisellini G., Maraschi L., Tavecchio F., 2009, MNRAS, 396, L105

Ghisellini G., Tavecchio F., Foschini L., Ghirlanda G., Maraschi L., Celotti A., 2010, MNRAS, 402, 497

Ghisellini G., Tavecchio F., Maraschi L., Celotti A., Sbarrato T., 2014, Nature, 515, 376

Ghisellini G., Righi C., Costamante L., Tavecchio F., 2017, MNRAS, 469, 255

Giacconi R., Gursky H., Paolini F. R., Rossi B. B., 1962, Physical Review Letters, 9, 439

Gierliński M., Done C., 2004, MNRAS, 349, L7

Gillessen S., Eisenhauer F., Trippe S., Alexander T., Genzel R., Martins F., Ott T., 2009, ApJ, 692, 1075

Giommi P., et al., 2012, A&A, 541, A160

Goodrich R. W., 1989, ApJ, 342, 224

Goodrich R. W., 1995, ApJ, 440, 141

Gordon K. D., Clayton G. C., Misselt K. A., Landolt A. U., Wolff M. J., 2003, ApJ, 594, 279

Graham M. J., et al., 2019, preprint, (arXiv:1902.01945)

Gravity Collaboration et al., 2018, A&A, 615, L15

Greene J. E., Ho L. C., 2005, ApJ, 630, 122

Greene J. E., et al., 2010a, ApJ, 721, 26

Greene J. E., et al., 2010b, ApJ, 723, 409

Greenhill L. J., Jiang D. R., Moran J. M., Reid M. J., Lo K. Y., Claussen M. J., 1995, ApJ, 440, 619

Hambly N. C., et al., 2001, MNRAS, 326, 1279

Hao H., et al., 2010, APJ, 724, L59

Harrison F. A., et al., 2010, in Space Telescopes and Instrumentation 2010: Ultraviolet to Gamma Ray. p. 77320S, doi:10.1117/12.858065

Harrison F. A., et al., 2013, ApJ, 770, 103

Heinz S., Sunyaev R. A., 2003, MNRAS, 343, L59

Helfand D. J., White R. L., Becker R. H., 2015, ApJ, 801, 26

Herbig G. H., Vacca W. D., 2008, AJ, 136, 1995

Ho L. C., 2002, ApJ, 564, 120

Hopkins P. F., Hernquist L., Cox T. J., Kereš D., 2008, ApJS, 175, 356

IceCube Collaboration et al., 2018, Science, 361, eaat1378

Ingram A., van der Klis M., Middleton M., Altamirano D., Uttley P., 2017, MNRAS, 464, 2979

Ivezic Z., et al., 2008, Serbian Astronomical Journal, 176, 1

Izumi T., Wada K., Fukushige R., Hamamura S., Kohno K., 2018, ApJ, 867, 48

Jagoda N., Austin G., Mickiewicz S., Goddard R., 1972, IEEE Transactions on Nuclear Science, 19, 579

Jansen F., et al., 2001, A&A, 365, L1

Jin C., Ward M., Done C., Gelbord J., 2012a, MNRAS, 420, 1825

Jin C., Ward M., Done C., 2012b, MNRAS, 422, 3268

Jin C., Ward M., Done C., 2012c, MNRAS, 425, 907

Jin C., Done C., Ward M., 2017a, MNRAS, 468, 3663

Jin C., Done C., Ward M., Gardner E., 2017b, MNRAS, 471, 706

Kalberla P. M. W., Burton W. B., Hartmann D., Arnal E. M., Bajaja E., Morras R., Pöppel W. G. L., 2005, A&A, 440, 775

Kaspi S., Smith P. S., Netzer H., Maoz D., Jannuzi B. T., Giveon U., 2000, ApJ, 533, 631

Katebi R., et al., 2018, preprint, (arXiv:1811.03694)

Kawaguchi T., Mori M., 2010, APJ, 724, L183

Kellermann K. I., Sramek R., Schmidt M., Shaffer D. B., Green R., 1989, AJ, 98, 1195

Kerr R. P., 1963, Physical Review Letters, 11, 237

Khachikian E. Y., Weedman D. W., 1974, ApJ, 192, 581

Kim D., Im M., Kim M., 2010, ApJ, 724, 386

King A., 2003, APJ, 596, L27

King A. R., Kolb U., 1999, MNRAS, 305, 654

Kishimoto M., Antonucci R., Blaes O., Lawrence A., Boisson C., Albrecht M., Leipski C., 2008, Nature, 454, 492

Koliopanos F., 2017, in Proceedings of the XII Multifrequency Behaviour of High Energy Cosmic Sources Workshop. 12-17 June, 2017 Palermo, Italy (MULTIF2017) Online at https://pos.sissa.it/cgi-bin/reader/conf.cgi?confid=306, id.51. p. 51 (arXiv:1801.01095)

Komossa S., 2000, New Astron. Rev., 44, 483

Komossa S., 2008, in Revista Mexicana de Astronomia y Astrofisica Conference Series. pp 86–92 (arXiv:0710.3326)

Komossa S., Voges W., Xu D., Mathur S., Adorf H.-M., Lemson G., Duschl W. J., Grupe D., 2006, AJ, 132, 531

Kubota A., Done C., 2018, MNRAS, 480, 1247

LaMassa S. M., Heckman T. M., Ptak A., Martins L., Wild V., Sonnentrucker P., 2010, ApJ, 720, 786

LaMassa S. M., et al., 2015, ApJ, 800, 144

Lähteenmäki A., Järvelä E., Ramakrishnan V., Tornikoski M., Tammi J., Vera R. J. C., Chamani W., 2018, A&A, 614, L1

Lakićević M., Popović L. Č., Kovačević-Dojčinović J., 2018, MNRAS, 478, 4068

Lamer G., Uttley P., McHardy I. M., 2003, MNRAS, 342, L41

Landt H., Bentz M. C., Ward M. J., Elvis M., Peterson B. M., Korista K. T., Karovska M., 2008, ApJS, 174, 282

Landt H., Buchanan C. L., Barmby P., 2010, MNRAS, 408, 1982

Landt H., Bentz M. C., Peterson B. M., Elvis M., Ward M. J., Korista K. T., Karovska M., 2011a, MNRAS, 413, L106

Landt H., Elvis M., Ward M. J., Bentz M. C., Korista K. T., Karovska M., 2011b, MNRAS, 414, 218

Landt H., Ward M. J., Peterson B. M., Bentz M. C., Elvis M., Korista K. T.,

Karovska M., 2013, MNRAS, 432, 113

Landt H., Ward M. J., Elvis M., Karovska M., 2014, MNRAS, 439, 1051

Landt H., et al., 2017, MNRAS, 464, 2565

Laor A., 1991, ApJ, 376, 90

Laor A., 2000, APJ, 543, L111

Laor A., Netzer H., 1989, MNRAS, 238, 897

Larsson J., D'Ammando F., Falocco S., Giroletti M., Orienti M., Piconcelli E., Righini S., 2018, MNRAS, 476, 43

Law N. M., et al., 2009, PASP, 121, 1395

Lawrence A., 1991, MNRAS, 252, 586

Lawrence A., 2018, Nature Astronomy, 2, 102

Lawrence A., et al., 2007, MNRAS, 379, 1599

Lawrence A., et al., 2016, MNRAS, 463, 296

Lawther D., Vestergaard M., Raimundo S., Grupe D., 2017, MNRAS, 467, 4674

Leighly K. M., 1999, ApJS, 125, 317

León Tavares J., et al., 2014, ApJ, 795, 58

Lister M., 2018, in Revisiting narrow-line Seyfert 1 galaxies and their place in the Universe. 9-13 April 2018. Padova Botanical Garden, Italy. p. 22 (arXiv:1805.05258)

Lister M. L., et al., 2016, AJ, 152, 12

Lu K.-X., Zhao Y., Bai J.-M., Fan X.-L., 2019, MNRAS, 483, 1722

Lyutyj V. M., Oknyanskij V. L., Chuvaev K. K., 1984, Pisma v Astronomicheskii Zhurnal, 10, 803

MacKenty J. W., Kimble R. A., O'Connell R. W., Townsend J. A., 2008, in Space Telescopes and Instrumentation 2008: Optical, Infrared, and Millimeter. p. 70101F, doi:10.1117/12.790039

MacLeod C. L., et al., 2012, ApJ, 753, 106

MacLeod C. L., et al., 2016, MNRAS, 457, 389

MacLeod C. L., et al., 2019, ApJ, 874, 8

Madejski G. ., Sikora M., 2016, ARA&A, 54, 725

Magnier E. A., et al., 2013, ApJS, 205, 20

Magorrian J., et al., 1998, AJ, 115, 2285

Mainzer A., et al., 2014, ApJ, 792, 30

Maiolino R., Marconi A., Salvati M., Risaliti G., Severgnini P., Oliva E., La Franca F., Vanzi L., 2001, A&A, 365, 28

Marchesini E. J., et al., 2016, A&A, 596, A10

Marconi A., Hunt L. K., 2003, APJ, 589, L21

Margala D., Kirkby D., Dawson K., Bailey S., Blanton M., Schneider D. P., 2016, ApJ, 831, 157

Marscher A. P., 2009, preprint, (arXiv:0909.2576)

Marscher A. P., Jorstad S. G., 2010, preprint, (arXiv:1005.5551)

Marshall F. J., Clark G. W., 1984, ApJ, 287, 633

Martin D. C., et al., 2005, APJ, 619, L1

Marton G., et al., 2016, in Jablonka P., André P., van der Tak F., eds, IAU Symposium Vol. 315, From Interstellar Clouds to Star-Forming Galaxies: Universal Processes?. p. E53 (arXiv:1510.08325), doi:10.1017/S1743921316008152

Marton G., et al., 2017, preprint, (arXiv:1705.05693)

Marziani P., Sulentic J. W., Zwitter T., Dultzin-Hacyan D., Calvani M., 2001, ApJ, 558, 553

Marziani P., et al., 2018, Frontiers in Astronomy and Space Sciences, 5, 6

Mason K. O., et al., 2001, A&A, 365, L36

McHardy I. M., Koerding E., Knigge C., Uttley P., Fender R. P., 2006, Nature, 444, 730

McHardy I. M., et al., 2014, MNRAS, 444, 1469

McHardy I. M., et al., 2018, MNRAS, 480, 2881

McLure R. J., Dunlop J. S., 2001, MNRAS, 327, 199

McLure R. J., Dunlop J. S., 2004, MNRAS, 352, 1390

Mehdipour M., Costantini E., 2019, A&A, 625, A25

Mejía-Restrepo J. E., Trakhtenbrot B., Lira P., Netzer H., Capellupo D. M., 2016,

MNRAS, 460, 187

Mejía-Restrepo J. E., Lira P., Netzer H., Trakhtenbrot B., Capellupo D. M., 2018, Nature Astronomy, 2, 63

Michell J., 1784, Philosophical Transactions of the Royal Society of London Series I, 74, 35

Miyoshi M., Moran J., Herrnstein J., Greenhill L., Nakai N., Diamond P., Inoue M., 1995, Nature, 373, 127

Molina M., Malizia A., Bassani L., Ursini F., Bazzano A., Ubertini P., 2019, MNRAS, 484, 2735

Mor R., Netzer H., 2012, MNRAS, 420, 526

Moretti A., et al., 2005, in Siegmund O. H. W., ed., Proc. SPIEVol. 5898, UV, X-Ray, and Gamma-Ray Space Instrumentation for Astronomy XIV. pp 360–368, doi:10.1117/12.617164

Netzer H., 2004, ApJ, 604, 551

Netzer H., 2013, The Physics and Evolution of Active Galactic Nuclei. Cambridge University Press

Netzer H., Shemmer O., Maiolino R., Oliva E., Croom S., Corbett E., di Fabrizio L., 2004, ApJ, 614, 558

Noda H., Done C., 2018, MNRAS, 480, 3898

Novikov I. D., Thorne K. S., 1973, in Dewitt C., Dewitt B. S., eds, Black Holes (Les Astres Occlus). pp 343–450

O'Donnell J. E., 1994, ApJ, 422, 158

Oh K., et al., 2018, ApJS, 235, 4

Ojha V., Krishna G., Chand H., 2019, MNRAS, 483, 3036

Oke J. B., et al., 1995, PASP, 107, 375

Onken C. A., Ferrarese L., Merritt D., Peterson B. M., Pogge R. W., Vestergaard M., Wandel A., 2004, ApJ, 615, 645

Osterbrock D. E., Ferland G. J., 2006, Astrophysics of gaseous nebulae and active galactic nuclei, 2nd edn. University Science Books, Mill Valley, CA

Osterbrock D. E., Pogge R. W., 1985, ApJ, 297, 166

Osterbrock D. E., Shuder J. M., 1982, ApJS, 49, 149

Owen F. N., Laing R. A., 1989, MNRAS, 238, 357

Packham C., Radomski J. T., Roche P. F., Aitken D. K., Perlman E., Alonso-Herrero A., Colina L., Telesco C. M., 2005, APJ, 618, L17

Padovani P., 2017, Nature Astronomy, 1, 0194

Paerels F., et al., 2001, ApJ, 546, 338

Page M. J., et al., 2012, MNRAS, 426, 903

Pahari M., McHardy I. M., Mallick L., Dewangan G. C., Misra R., 2017, MNRAS, 470, 3239

Paliya V. S., Sahayanathan S., Parker M. L., Fabian A. C., Stalin C. S., Anjum A., Pandey S. B., 2014, ApJ, 789, 143

Paliya V. S., Ajello M., Rakshit S., Mandal A. K., Stalin C. S., Kaur A., Hartmann D., 2018, APJ, 853, L2

Paliya V. S., Parker M. L., Jiang J., Fabian A. C., Brenneman L., Ajello M., Hartmann D., 2019, ApJ, 872, 169

Paresce F., 1984, in Kondo Y., Bruhweiler F. C., Savage B. D., eds, NASA Conference Publication Vol. 2345, NASA Conference Publication.

Pâris I., et al., 2018, A&A, 613, A51

Park D., et al., 2012, ApJ, 747, 30

Parker M. L., et al., 2016, MNRAS, 461, 1927

Pei L., et al., 2017, ApJ, 837, 131

Perley R. A., Willis A. G., Scott J. S., 1979, Nature, 281, 437

Peterson B. M., 1993, PASP, 105, 247

Peterson B. M., 1997, An Introduction to Active Galactic Nuclei. Cambridge University Press

Peterson B. M., Horne K., 2006, Reverberation mapping of active galactic nuclei. p. 89

Peterson B. M., et al., 2004, ApJ, 613, 682

Pilbratt G. L., et al., 2010, A&A, 518, L1

Pinto C., Kaastra J. S., Costantini E., de Vries C., 2013, A&A, 551, A25

Planck Collaboration et al., 2011, A&A, 536, A1

Planck Collaboration et al., 2016a, A&A, 594, A13

Planck Collaboration et al., 2016b, A&A, 594, A26

Plotkin R. M., Markoff S., Trager S. C., Anderson S. F., 2011, MNRAS, 413, 805

Polletta M., et al., 2007, ApJ, 663, 81

Porquet D., Reeves J. N., O'Brien P., Brinkmann W., 2004, A&A, 422, 85

Poznanski D., Prochaska J. X., Bloom J. S., 2012, MNRAS, 426, 1465

Rakshit S., Stalin C. S., Chand H., Zhang X.-G., 2017, ApJS, 229, 39

Reeves J. N., O'Brien P. T., Ward M. J., 2003, APJ, 593, L65

Remillard R. A., McClintock J. E., 2006, ARA&A, 44, 49

Richards J. L., et al., 2011, ApJS, 194, 29

Risaliti G., 2007, in Ho L. C., Wang J.-W., eds, Astronomical Society of the Pacific Conference Series Vol. 373, The Central Engine of Active Galactic Nuclei. p. 458 (arXiv:astro-ph/0701108)

Romano P., Vercellone S., Foschini L., Tavecchio F., Landoni M., Knödlseder J., 2018, MNRAS, 481, 5046

Roming P. W. A., et al., 2005, Space Sci. Rev., 120, 95

Rosen S. R., et al., 2016, A&A, 590, A1

Ross R. R., Fabian A. C., 2005, MNRAS, 358, 211

Ross N. P., et al., 2018, MNRAS, 480, 4468

Ruan J. J., et al., 2016, ApJ, 826, 188

Ruan J. J., Anderson S. F., Eracleous M., Green P. J., Haggard D., Macleod C., Runnoe J. C., Sobolewska M., 2019, in AAS/High Energy Astrophysics Division. p. 106.44

Rumbaugh N., et al., 2018, ApJ, 854, 160

Runnoe J. C., et al., 2016, MNRAS, 455, 1691

Sahnow D. J., et al., 2010, in Space Telescopes and Instrumentation 2010: Optical,

Infrared, and Millimeter Wave. p. 773139, doi:10.1117/12.858058

Salpeter E. E., 1964, ApJ, 140, 796

Sanders D. B., Soifer B. T., Elias J. H., Madore B. F., Matthews K., Neugebauer G., Scoville N. Z., 1988, ApJ, 325, 74

Schlafly E. F., Finkbeiner D. P., 2011, ApJ, 737, 103

Schlegel D. J., Finkbeiner D. P., Davis M., 1998, ApJ, 500, 525

Schmidt M., 1963, Nature, 197, 1040

Schmidt K. B., Rix H.-W., Shields J. C., Knecht M., Hogg D. W., Maoz D., Bovy J., 2012, ApJ, 744, 147

Schödel R., Merritt D., Eckart A., 2009, A&A, 502, 91

Schultz G. V., Wiemer W., 1975, A&A, 43, 133

Schwarzschild K., 1916, Sitzungsberichte der Königlich Preußischen Akademie der Wissenschaften (Berlin), 1916, pp 189–196

Schweitzer M., et al., 2008, ApJ, 679, 101

Seyfert C. K., 1943, ApJ, 97, 28

Shakura N. I., Sunyaev R. A., 1973, A&A, 24, 337

Shapley H., Curtis H. D., 1921, Bulletin of the National Research Council, Vol. 2, Part 3, No. 11, p. 171-217, 2, 171

Shen Y., et al., 2011, ApJS, 194, 45

Shen Y., et al., 2016, ApJ, 818, 30

Sheng Z., Wang T., Jiang N., Yang C., Yan L., Dou L., Peng B., 2017, APJ, 846, L7

Shlosman I., Begelman M. C., 1987, Nature, 329, 810

Shu X. W., Yaqoob T., Wang J. X., 2010, ApJS, 187, 581

Shuder J. M., Osterbrock D. E., 1981, ApJ, 250, 55

Shull J. M., Danforth C. W., Tilton E. M., Moloney J., Stevans M. L., 2017, ApJ, 849, 106

Siebenmorgen R., Haas M., Krügel E., Schulz B., 2005, A&A, 436, L5

Sikora M., Begelman M. C., 2013, APJ, 764, L24

Sikora M., Begelman M. C., Rees M. J., 1994, ApJ, 421, 153

Sikora M., Rutkowski M., Begelman M. C., 2016, MNRAS, 457, 1352

Silk J., Rees M. J., 1998, A&A, 331, L1

Skrutskie M. F., et al., 2006, AJ, 131, 1163

Smith J. D. T., et al., 2007, PASP, 119, 1133

Smith R. A. N., Page M. J., Branduardi-Raymont G., 2008, A&A, 490, 103

Snowden S. L., et al., 1997, ApJ, 485, 125

Sol H., Pelletier G., Asseo E., 1989, MNRAS, 237, 411

Steele I. A., et al., 2004, in Oschmann Jr. J. M., ed., Proc. SPIEVol. 5489, Ground-based Telescopes. pp 679–692, doi:10.1117/12.551456

Stern D., et al., 2018, ApJ, 864, 27

Strüder L., et al., 2001, A&A, 365, L18

Sturm E., et al., 2005, APJ, 629, L21

Sulentic J. W., Zwitter T., Marziani P., Dultzin-Hacyan D., 2000, APJ, 536, L5

Sun M., et al., 2015, ApJ, 811, 42

Svoboda J., Guainazzi M., Merloni A., 2017, A&A, 603, A127

Telfer R. C., Zheng W., Kriss G. A., Davidsen A. F., 2002, ApJ, 565, 773

Theil H., 1992, A Rank-Invariant Method of Linear and Polynomial Regression Analysis. Springer Netherlands, Dordrecht, pp 345–381, doi:10.1007/978-94-011-2546-8_20

Thorne K. S., 1974, ApJ, 191, 507

Titarchuk L., 1994, ApJ, 434, 570

Torrealba J., Chavushyan V., Cruz-González I., Arshakian T. G., Bertone E., Rosa-González D., 2012, Rev. Mex. Astron. Astrofis., 48, 9

Turner M. J. L., et al., 2001, A&A, 365, L27

Urry C. M., Padovani P., 1995, PASP, 107, 803

Vacca W. D., Cushing M. C., Rayner J. T., 2003, PASP, 115, 389

Vanden Berk D. E., et al., 2001, AJ, 122, 549

Vernet J., et al., 2011, A&A, 536, A105

Véron-Cetty M.-P., Véron P., Gonçalves A. C., 2001, A&A, 372, 730

Véron-Cetty M.-P., Joly M., Véron P., 2004, A&A, 417, 515

Vestergaard M., Peterson B. M., 2005, ApJ, 625, 688

Voges W., et al., 1999, A&A, 349, 389

Wandel A., Peterson B. M., Malkan M. A., 1999, ApJ, 526, 579

Wang F., et al., 2016, ApJ, 824, 149

Wang J., Xu D. W., Wei J. Y., 2018, ApJ, 858, 49

Webster B. L., Murdin P., 1972, Nature, 235, 37

Werner M. W., et al., 2004, ApJS, 154, 1

White R. L., Becker R. H., Helfand D. J., Gregg M. D., 1997, ApJ, 475, 479

White R. L., et al., 2000, ApJS, 126, 133

Wilhite B. C., Vanden Berk D. E., Kron R. G., Schneider D. P., Pereyra N., Brunner R. J., Richards G. T., Brinkmann J. V., 2005, ApJ, 633, 638

Willingale R., Starling R. L. C., Beardmore A. P., Tanvir N. R., O'Brien P. T., 2013, MNRAS, 431, 394

Wilms J., Allen A., McCray R., 2000, ApJ, 542, 914

Wotta C. B., Lehner N., Howk J. C., O'Meara J. M., Prochaska J. X., 2016, ApJ, 831, 95

Wright E. L., et al., 2010, AJ, 140, 1868

Yang H., et al., 2018a, MNRAS, 477, 5127

Yang Q., et al., 2018b, ApJ, 862, 109

Yao S., Yuan W., Komossa S., Grupe D., Fuhrmann L., Liu B., 2015a, AJ, 150, 23

Yao S., Yuan W., Zhou H., Komossa S., Zhang J., Qiao E., Liu B., 2015b, MNRAS, 454, L16

Yao S., Komossa S., Liu W.-J., Yi W., Yuan W., Zhou H., Wu X.-B., 2019, MNRAS, 487, L40

York D. G., et al., 2000, AJ, 120, 1579

Yuan W., Zhou H. Y., Komossa S., Dong X. B., Wang T. G., Lu H. L., Bai J. M., 2008, ApJ, 685, 801

Zel'dovich Y. B., 1965, Soviet Ast., 9, 221

Zhang F., Yu Q., Lu Y., 2017, ApJ, 845, 88

Zheng Y. G., Yang C. Y., Zhang L., Wang J. C., 2017, ApJS, 228, 1

Zhou H., Wang T., Yuan W., Lu H., Dong X., Wang J., Lu Y., 2006, ApJS, 166, 128

Zhou H., et al., 2007, APJ, 658, L13

Zhu D., Sun M., Wang T., 2017, ApJ, 843, 30

Zuo W., Wu X.-B., Liu Y.-Q., Jiao C.-L., 2012, ApJ, 758, 104

Życki P. T., Done C., Smith D. A., 1999, MNRAS, 309, 561

den Herder J. W., et al., 2001, A&A, 365, L7

van Groningen E., Wanders I., 1992, PASP, 104, 700